

# UC Berkeley

## UC Berkeley Electronic Theses and Dissertations

### Title

Synthesis and Characterization of Redox-Active Metal–Organic Frameworks

### Permalink

<https://escholarship.org/uc/item/0nt0j9wc>

### Author

Torres, Rodolfo M.

### Publication Date

2019

Peer reviewed|Thesis/dissertation

Synthesis and Characterization of Redox-Active Metal–Organic Frameworks

by

Rodolfo M. Torres

A dissertation submitted in partial satisfaction of the

requirements for the degree of

Doctor of Philosophy

in

Chemistry

in the

Graduate Division

of the

University of California, Berkeley

Committee in charge:

Professor Jeffrey R. Long, Chair

Professor Omar M. Yaghi

Professor Nitash P. Balsara

Summer 2019



## Abstract

### Synthesis and Characterization of Redox-Active Metal–Organic Frameworks

by

Rodolfo M. Torres

Doctor of Philosophy in Chemistry

University of California, Berkeley

Professor Jeffrey R. Long, Chair

This dissertation documents efforts to use a variety of synthetic approaches to generate new redox-active metal–organic frameworks and improve the properties of known frameworks. Chapter 1 introduces the field of metal–organic frameworks and discusses observed redox activity of metal nodes and organic linkers. Additionally, the application of the Langmuir-Freundlich gas adsorption model and the use of IAST selectivity calculations to quantify and predict gas sorption in metal–organic frameworks are discussed. Chapter 2 discusses the successful targeted synthesis of the templated, mixed-metal framework Fe–Zn(dobdc) with proposed short-range order in the metal distribution. This ordered system demonstrates thermal stability for O<sub>2</sub> adsorption compared to both monometallic Fe<sub>2</sub>(dobdc) and nontemplated Fe~Zn(dobdc) via a suite of in situ techniques. Chapter 3 documents the first isolation of the highly oxygen-sensitive framework Fe<sup>II</sup>(H<sub>2</sub>gallate)·2H<sub>2</sub>O. This unusual material exhibits remarkable permanence of crystallinity upon exposure to air as shown by single-crystal-to-single-crystal diffraction experiments. Isothermal gas adsorption measurements reveal an unparalleled selectivity for ethylene over ethane stemming from size exclusivity in narrow framework pores. The redox activity of this system is leveraged to tune gas sorption properties in a mixed-valent isomer: Fe<sup>II/III</sup>(H<sub>x</sub>gallate). Chapter 4 details efforts to apply several different solvent-free synthetic approaches to the synthesis of both iron- and early transition metal-containing frameworks. Melt based reactions are used to obtain a layered two-dimensional solid, Fe(bzimid)<sub>2</sub>, as well as the crystalline metallocene-derived materials Cr–bzimid and V–bzimid. A high-temperature metal-powder-based synthetic route is successfully applied for the first time for an iron-based metal–organic framework in the case of Fe(imid)<sub>2</sub>. Additionally, air- and solvent-free ball milling is shown to increase reaction yields for metal–gallate frameworks and provide evidence of redox activity in the gallate linker. Lastly, Appendix A details the design and use of the Breen adapter, a glass tube adapter with important uses in the field of metal–organic frameworks.

*Para mis padres, Estela Ana Gavosto y Rodolfo Humberto Torres*

# Table of Contents

Dedication .....	i
Table of Contents .....	ii
List of Figures .....	iv
List of Tables .....	vii
Acknowledgements .....	viii
<b>Chapter 1: Redox-Active Metal–Organic Frameworks .....</b>	<b>1</b>
1.1 Introduction .....	1
1.2 Redox-Activity in Metal–Organic Frameworks .....	2
1.3 Redox-Active Metals .....	3
1.4 Redox-Active Ligands .....	4
1.5 Gases in Redox-Active Frameworks .....	6
1.6 Modeling Gas Sorption .....	7
1.7 References .....	11
<b>Chapter 2: Improving O<sub>2</sub> Adsorption Properties of a Redox-Active Open Metal Site via Templating Mixed-Metal Distribution.....</b>	<b>16</b>
2.1 Introduction .....	16
2.2 Experimental .....	17
2.3 Results and Discussion .....	19
Synthesis of Bimetallic Frameworks .....	19
Characterization of Bimetallic Frameworks .....	22
O <sub>2</sub> Stability Experiments.....	29
2.4 Conclusions and Outlook .....	33
2.5 Acknowledgments.....	33
2.6 References and Supplementary Materials.....	34
<b>Chapter 3: Synthesis and Characterization of Iron–Gallate Frameworks .....</b>	<b>50</b>
3.1 Introduction .....	50
3.2 Experimental .....	52
3.3 Results and Discussion .....	53
Synthesis of Fe <sup>III</sup> (H <sub>2</sub> gallate)·2H <sub>2</sub> O .....	53
Synthesis of Fe <sup>II</sup> (H <sub>2</sub> gallate)·2H <sub>2</sub> O .....	55
Single-Crystal Diffraction of Fe <sup>II</sup> (H <sub>2</sub> gallate)·2H <sub>2</sub> O and Fe <sup>III</sup> (H <sub>2</sub> gallate)·xH <sub>2</sub> O .....	58
Oxidation of Fe <sup>II</sup> (H <sub>2</sub> gallate).....	63
Activation and Gas Adsorption Properties of Fe <sup>II</sup> (H <sub>2</sub> gallate).....	66
Activation and Gas Adsorption Properties of Oxidized Iron–Gallate .....	77
3.4 Conclusions and Outlook .....	82
3.5 Acknowledgments.....	83
3.6 References and Supplementary Materials.....	83

<b>Chapter 4: Solvent-Free Synthetic Routes Towards Redox-Active Metal–Organic Frameworks.....</b>	<b>86</b>
4.1 Introduction.....	86
4.2 Experimental.....	90
4.3 Results and Discussion .....	91
Ferrocene-Based Melt Reactions .....	91
Expanding Melt Reactions Beyond Ferrocene .....	93
“Minimalist” Chemical Reactions .....	96
Mechanochemistry Reactions .....	99
4.4 Conclusions and Outlook.....	103
4.5 Acknowledgments.....	104
4.6 References and Supplementary Materials.....	104
<b>Appendix A: The Breen Sealed-Tube Adapter .....</b>	<b>108</b>
A.1 Design .....	108
A.2 Application to Metal–Organic Frameworks .....	109
A.3 Acknowledgements.....	110

## List of Figures

### Chapter 1

Figure 1.1	Inorganic structural motifs in metal–organic frameworks.....	1
Figure 1.2	Redox-active metal site in metal–organic frameworks.....	4
Figure 1.3	Redox-active ligands in metal–organic frameworks.....	5
Figure 1.4	Structures of metal sites that reduce O <sub>2</sub> .....	6
Figure 1.5	Structures of gases binding in redox-active frameworks .....	7

### Chapter 2

Figure 2.1	Structural diagram for templating strategy in Fe–Zn(dobdc) .....	20
Figure 2.2	Statistical prediction for randomized metal distribution in a bimetallic system....	22
Figure 2.3	DRIFTS spectra of activated and O <sub>2</sub> dosed Fe–Zn(dobdc) .....	24
Figure 2.4	Variable temp DRIFTS and Van’t Hoff plots for O <sub>2</sub> dosed Fe–Zn(dobdc).....	25
Figure 2.5	Example O <sub>2</sub> and N <sub>2</sub> isotherms for Fe–Zn(dobdc) and Fe <sub>2</sub> (dobdc) .....	26
Figure 2.6	50 K vs. 5 K Mössbauer spectra comparison for Fe–Zn(dobdc) and Fe <sub>2</sub> (dobdc)..	28
Figure 2.7	Variable temperature magnetic susceptibility for Fe–Zn(dobdc) and Fe~Zn(dobdc) normalized by iron content .....	29
Figure 2.8	DRIFTS spectra of O <sub>2</sub> dosed frameworks at elevated temperatures.....	30
Figure 2.9	O <sub>2</sub> gas sorption cycling experiments.....	32
Figure 2.S1	N <sub>2</sub> gas sorption isotherms for Fe–Zn(dobdc) at 159, 178, and 195 K with fits .....	37
Figure 2.S2	O <sub>2</sub> gas sorption isotherms for Fe–Zn(dobdc) at 159, 178, and 195 K with fits .....	38
Figure 2.S3	N <sub>2</sub> gas sorption isotherms for Fe~Zn(dobdc) at 159, 178, and 195 K with fits.....	39
Figure 2.S4	O <sub>2</sub> gas sorption isotherms for Fe~Zn(dobdc) at 159, 178, and 195 K with fits.....	40
Figure 2.S5	N <sub>2</sub> gas sorption isotherms for Fe <sub>2</sub> (dobdc) at 159, 178, and 195 K with fits .....	41
Figure 2.S6	O <sub>2</sub> gas sorption isotherms for Fe <sub>2</sub> (dobdc) at 159, 178, and 195 K with fits .....	42
Figure 2.S7	DRIFTS spectra of activated and O <sub>2</sub> dosed Fe–Zn(dobdc) .....	44
Figure 2.S8	DRIFTS spectra of activated and O <sub>2</sub> dosed Fe–Zn(dobdc) .....	44
Figure 2.S9	Mössbauer spectra for Fe–Zn(dobdc) at 50 K .....	45
Figure 2.S10	Mössbauer spectra for Fe–Zn(dobdc) at 5 K .....	45
Figure 2.S11	Mössbauer spectra for Fe~Zn(dobdc) at 50 K .....	46

Figure 2.S12	Mössbauer spectra for Fe~Zn(dobdc) at 5 K .....	46
Figure 2.S13	Mössbauer spectra for Fe <sub>2</sub> (dobdc) at 50 K .....	47
Figure 2.S14	Mössbauer spectra for Fe <sub>2</sub> (dobdc) at 5 K .....	47
Figure 2.S15	50 K vs. 5 K Mössbauer spectra comparison for Fe~Zn(dobdc).....	48
Figure 2.S16	Variable temperature magnetic susceptibility for Fe~Zn(dobdc), Fe~Zn(dobdc), and Fe <sub>2</sub> (dobdc).....	49

### Chapter 3

Figure 3.1	Chemical and crystal structures of M(H <sub>2</sub> gallate).....	50
Figure 3.2	Optical Microscope image of iron–gallate crystals .....	54
Figure 3.3	Comparison of PXRD pattern for iron–gallate crystals and predicted pattern .....	54
Figure 3.4	Mössbauer spectra for iron–gallate crystals.....	55
Figure 3.5	Comparison of PXRD patterns for ferrous– and ferric–gallate .....	57
Figure 3.6	Mössbauer spectra for ferrous–gallate .....	57
Figure 3.7	SEM micrograph of Fe <sup>II</sup> (H <sub>2</sub> gallate)·2H <sub>2</sub> O .....	58
Figure 3.8	Single-crystal structure of Fe <sup>II</sup> (H <sub>2</sub> gallate)·2H <sub>2</sub> O.....	59
Figure 3.9	Comparison of chirality in Fe <sup>II</sup> (H <sub>2</sub> gallate)·2H <sub>2</sub> O and Fe <sup>III</sup> (Hgallate)·2H <sub>2</sub> O .....	60
Figure 3.10	Structure of single iron site with labeled oxygen substituents.....	61
Figure 3.11	Space filling model of Fe <sup>II</sup> (H <sub>2</sub> gallate)·2H <sub>2</sub> O pore .....	62
Figure 3.12	Comparison of PXRD patterns for Fe <sup>II</sup> (H <sub>2</sub> gallate)·2H <sub>2</sub> O, Fe <sup>III</sup> (Hgallate)·2H <sub>2</sub> O, and Fe <sup>II/III</sup> (H <sub>x</sub> gallate).....	64
Figure 3.13	Mössbauer spectra for Fe <sup>II/III</sup> (H <sub>2</sub> gallate) .....	65
Figure 3.14	Structural diagram of electronic pathways in iron–gallate .....	66
Figure 3.15	Comparison of PXRD patterns for Fe <sup>II</sup> (H <sub>2</sub> gallate)·2H <sub>2</sub> O, Fe <sup>III</sup> (Hgallate)·2H <sub>2</sub> O, and activated Fe <sup>II</sup> (H <sub>2</sub> gallate).....	67
Figure 3.16	Mössbauer spectra for activated Fe <sup>II</sup> (H <sub>2</sub> gallate) .....	68
Figure 3.17	195 K CO <sub>2</sub> gas sorption isotherm for Fe <sup>II</sup> (H <sub>2</sub> gallate) .....	69
Figure 3.18	BET Surface area calculation of 195 K CO <sub>2</sub> gas sorption isotherm for Fe <sup>II</sup> (H <sub>2</sub> gallate) .....	71
Figure 3.19	303, 313, and 323 K C <sub>2</sub> H <sub>6</sub> gas sorption isotherm for Fe <sup>II</sup> (H <sub>2</sub> gallate) with fits .....	72
Figure 3.20	303, 313, and 323 K C <sub>2</sub> H <sub>4</sub> gas sorption isotherm for Fe <sup>II</sup> (H <sub>2</sub> gallate).....	73
Figure 3.21	Comparison of fitting models for C <sub>2</sub> H <sub>4</sub> in Fe <sup>II</sup> (H <sub>2</sub> gallate) .....	73

Figure 3.22	303, 313, and 323 K C <sub>2</sub> H <sub>2</sub> gas sorption isotherm for Fe <sup>II</sup> (H <sub>2</sub> gallate).....	74
Figure 3.23	Comparison of C <sub>2</sub> H <sub>6</sub> and C <sub>2</sub> H <sub>4</sub> gas sorption isotherm for Fe <sup>II</sup> (H <sub>2</sub> gallate).....	75
Figure 3.24	Comparison of predicted isotherms of C <sub>2</sub> H <sub>6</sub> and C <sub>2</sub> H <sub>4</sub> in Fe <sup>II</sup> (H <sub>2</sub> gallate) and Co(H <sub>2</sub> gallate) at 298 K.....	76
Figure 3.25	Comparison of PXRD patterns for activated Fe <sup>II</sup> (H <sub>2</sub> gallate)·2H <sub>2</sub> O and Fe <sup>II/III</sup> (H <sub>x</sub> gallate).....	77
Figure 3.26	195 K CO <sub>2</sub> and 77 K N <sub>2</sub> gas sorption isotherms for Fe <sup>II/III</sup> (H <sub>x</sub> gallate) .....	78
Figure 3.27	C <sub>2</sub> gas adsorption isotherms collected at 313 K for Fe <sup>II/III</sup> (H <sub>x</sub> gallate) .....	79
Figure 3.28	Comparison of C <sub>2</sub> H <sub>4</sub> gas sorption isotherm for Fe <sup>II</sup> (H <sub>2</sub> gallate) and Fe <sup>II/III</sup> (H <sub>x</sub> gallate).....	79
Figure 3.29	Comparison of C <sub>2</sub> H <sub>6</sub> gas sorption isotherm for Fe <sup>II</sup> (H <sub>2</sub> gallate) and Fe <sup>II/III</sup> (H <sub>x</sub> gallate).....	81
Figure 3.30	195 K C <sub>2</sub> H <sub>6</sub> gas sorption isotherm for Fe <sup>II</sup> (H <sub>2</sub> gallate) .....	81
Figure 3.31	Comparison of C <sub>2</sub> H <sub>8</sub> gas sorption isotherm for Fe <sup>II</sup> (H <sub>2</sub> gallate) and Fe <sup>II/III</sup> (H <sub>x</sub> gallate).....	82
Figure 3.S1	Comparison of PXRD patterns for activated Fe <sup>II</sup> (H <sub>2</sub> gallate)·2H <sub>2</sub> O and Fe <sub>2</sub> (gallate) .....	85

## Chapter 4

Figure 4.1	Chemical structures of n-heterocyclic ligands.....	87
Figure 4.2	Crystal structure of Fe(bzimid) <sub>2</sub> .....	93
Figure 4.3	PXRD pattern of Fe <sup>II</sup> (acac) <sub>2</sub> (Himid) <sub>2</sub> .....	94
Figure 4.4	PXRD patterns for Cr–bzimid and V–bzimid.....	95
Figure 4.5	PXRD pattern of Fe(imid) <sub>2</sub> and image of material .....	97
Figure 4.6	Comparison of PXRD patterns of Fe(imid) <sub>2</sub> and Co(imid) <sub>2</sub> .....	98
Figure 4.7	Predicted structure of Fe(imid) <sub>2</sub> .....	98
Figure 4.8	Comparison of PXRD patterns for 90 and 45 min ball milled Fe <sup>II</sup> (H <sub>2</sub> gallate)·2H <sub>2</sub> O and Fe <sub>2</sub> (gallate) .....	100
Figure 4.9	PXRD pattern of ball milled Ni(H <sub>2</sub> gallate)·2H <sub>2</sub> O.....	102
Figure 4.10	ATIR spectra of air-free and in-air ball milled Ni(H <sub>2</sub> gallate)·2H <sub>2</sub> O with images of products.....	103
Figure 4.S1	Wire-frame structural diagram of three-fold helix in Fe(imid) <sub>2</sub> structure .....	107

## Appendix A

Figure A.1	Images of ½” Breen adapter, assembled and disassembled.....	108
Figure A.2	Image of Breen adapter connected to ASAP tube .....	109
Figure A.3	Images of Micromeritics <i>Transeal</i> opened and closed in a Breen adapter .....	110

## List of Tables and Schemes

### Chapter 2

Scheme 2.1	Diagram of reaction pathways/equilibria in Fe–Zn(dobdc) synthesis .....	21
Table 2.1	O <sub>2</sub> and N <sub>2</sub> binding enthalpies on Fe and Zn open metal sites .....	27
Table 2.2	Unit cell volumes for O <sub>2</sub> dosed frameworks at varying temperature.....	31
Table 2.S1	Multisite Langmuir-Freundlich fit parameters for O <sub>2</sub> and N <sub>2</sub> in Fe–Zn(dobdc), Fe~Zn(dobdc), and Fe <sub>2</sub> (dobdc).....	43
Table 2.S2	Ratio of Fe to Zn in Fe–Zn(dobdc) obtained via multiple methods .....	43
Table 2.S3	Ratio of Fe to Zn in Fe~Zn(dobdc) obtained via multiple methods .....	43
Table 2.S4	Mössbauer fitting parameters for Fe–Zn(dobdc), Fe~Zn(dobdc), and Fe <sub>2</sub> (dobdc) at 50 K and 5 K.....	48

### Chapter 3

Table 3.1	Fe–O bond lengths for reported and obtained iron–gallate structures.....	61
Table 3.2	Mössbauer fitting parameters for Fe <sup>II</sup> (H <sub>2</sub> gallate)·2H <sub>2</sub> O, Fe <sup>III</sup> (Hgallate)·2H <sub>2</sub> O, and Fe <sup>II/III</sup> (H <sub>x</sub> gallate).....	65
Table 3.3	Unit cell parameters for Fe <sup>II</sup> (H <sub>2</sub> gallate)·2H <sub>2</sub> O, Fe <sup>III</sup> (Hgallate)·2H <sub>2</sub> O, activated Fe <sup>II</sup> (H <sub>2</sub> gallate), and activated Mg(H <sub>2</sub> gallate).....	67
Table 3.4	Comparison of Mössbauer fitting parameters for Fe <sup>II</sup> (H <sub>2</sub> gallate)·2H <sub>2</sub> O, and activated Fe <sup>II</sup> (H <sub>2</sub> gallate).....	65
Table 3.5	Theoretical surface areas calculated for Fe <sup>II</sup> (H <sub>2</sub> gallate)·2H <sub>2</sub> O and Fe <sup>III</sup> (Hgallate)·2H <sub>2</sub> O.....	70

### Chapter 4

Scheme 4.1	Mechanism of ferrocene-based melt reactions .....	87
Scheme 4.2	Mechanism of “minimalist” chemical reactions .....	89
Scheme 4.3	Generic example of ball milling salt metathesis reaction .....	90
Table 4.1	Elemental analysis for Cr–bzimid and V–bzimid.....	96

# Acknowledgements

I would like to start by acknowledging the teachers and professors who played an integral part in my chemistry education. Professor Jeff Long deserves the first mention as my advisor, mentor, and teacher. I am now forever blessed/cursed with recognizing well-formatted presentations, figures, and publications. He has created an amazing lab environment filled with some of the most passionate and gifted researchers. I would also like to thank Professor Omar Yaghi and Professor Nitash Balsara for being on both my dissertation committee and qualifying exam committee. I also thank Professor Angelica Stacy for being on my qualifying exam committee.

In high school, my chemistry teacher, Jordan Rose, deserves credit for introducing me to the field of chemistry and finally finding a focal point for my intellectually curiosity. The summer before my senior year of high school I had the privilege to be introduced to research in chemistry by Professor Cindy Berrie; her mentorship continued through college, and I thank her for teaching me how to effectively present research. Professor Ward Thompson is a truly passionate educator, who taught me physical chemistry and always gave helpful feedback. Professor Misha Barybin taught me to love inorganic chemistry; I would not be in this field or at this university without his advice and encouragement.

True friendship is an invaluable resource, not only in grad school but in life, and I have been fortunate enough to have several such friends during my time at Berkeley. Through some miracle, Beth Schirmer managed to stay in touch beyond the amber waves of grain. Our conversations have always been a pleasant reprieve from the coastal chaos. To Nicholas Settineri: thank you for getting to know “the guy who talked too much on visiting weekend”, and I hope to see you in Portland soon, I’ll be hosting game night this time. To my oldest Berkeley friend Matt Kapelewski: it is always a blast hanging out with you and it is nice to not be the loudest in a room for a change. I am also thankful for knowing Sudi Jawahery and Sondre Schnell; you don’t get to choose your friends’ friends but given the choice I wouldn’t have changed a thing.

Graduate students, both young and old, in the Long Group have played a critical role in my graduate career. In order of seniority, I would like to thank first my conductivity mentors, Brian Weirs and Mike Aubrey. It may have taken several years for me to fully understand some of your lessons, but I am grateful for your mentorship. Dana Levine deserves recognition for being one of the kindest coworkers I’ve had and also for her vocal talents (I miss karaoke nights). Miguel Gonzalez is one of the most brilliant minds I have ever met; no other grad student was as well versed in all areas of chemistry or as willing to discuss research at length. I expect great things from him. Lucy Darago was the one grad student in lab who reached out to a floundering first year and helped them find their way. I am not sure how I would have survived without her gift for mentoring.

My yearmates in lab, Julia Oktawiec, Mercedes Taylor, and Jon Bachman always made sure lab wasn’t boring. Jon’s efficiency set an example that we all sought to follow, as he managed to leave with a Ph.D. in record time (then come back, then leave, then come back). Mercedes (pronounced like cicadas) was always fun to work with, I’m still finding packing peanuts in my desk. Julia, despite her ovine comments, has been a great coworker and friend over the years and has always been willing to meticulously share any expertise she has.

Seemingly countless graduate students have joined the Long Group in the years after mine. Rebecca Siegelman is a talented, if quiet-spoken, scientist/engineer/jack of all trades; her firm grasp of thermodynamics in gas sorption was a much-appreciated resource. Henry “Unionize” Jiang deserves recognition for managing to fish one of my projects out of an overcrowded incinerator while simultaneously discussing the pros and cons of capitalism. He has almost single-handedly built a cephalopodic instrument that any gas sorption group in the world would kill for, and I thank him for its use and his expertise. Colin Gould has often been a sympathetic ear to any organic obstacles I encountered. Job Chakarawet is by far the most efficient collaborator I’ve had the pleasure of working with. Ryan Murphy is perhaps scientific curiosity personified and I have enjoyed countless chemistry (and recently perhaps more physics oriented) discussions with him since he joined the lab; I hope Gus serves you well. David Jaramillo has been a great

help both in fruitful inorganic discussions and as a sounding board (possibly overused) for my endeavors in gas sorption, that is when he is not busy being mauled by a dog or perfuming the group room with sardines (but not anchovies, because that would be ridiculous...). I thank Eugene Kim for seemingly endless instrumentation assistance, I still can't believe [REDACTED] designed that spacer that way. He also helped rekindle my love of craft beverages, so for that I thank him as well, my wallet does not. Seeing Ever Velasquez's unassailable perseverance in lab helped me push through obstacles in my own research, just don't hand him a glass container. Naomi Biggins and I share a comradery with perpetually mispronounced names, and I thank her for putting up with me desk-squatting in the solitude of Hildebrand.

Being at UC- Berkeley, I've also been fortunate enough to work with several exceptional undergrads. Raymond Yu was always a pleasure to be around and he made my first year in lab much more enjoyable (Raymond if you are reading this send me a beer from your next batch). Jo Melville deserves a place here as the savior of the College of Chemistry, but his wit and our inane discussions are what I will remember most fondly.

Over the years I worked with many brilliant postdocs in the Long group; in alphabetical order, Brandon Barnett, Dominik Halter, Jeff Martell, Megan Jackson, and Ben Snyder, are particularly talented examples and I have always enjoyed my interactions with them.

I have had the pleasure of working with a wide array of talented staff in my tenure at Berkeley. Kristen Stangl is the most capable, pleasant, and friendly administrative staff that I've ever worked with. Hiro Furukawa is an underappreciated scientist, and I thank him for all his nocturnal efforts in lab. I would like to thank all the staff of the College of Chemistry wood shop, machine shop, electrical shop, and facilities for not just their tireless efforts in keeping all the labs running but also for their timely assistance in helping me overcome crucial obstacles. I can't thank the college's resident glassblower, Jim Breen, enough here, so a more appropriate recognition is found in Appendix A.

Often overlooked are those who have no voice, well at least not a verbal one anyways. In a particular order, I would like to thank Willow, Ginger, Chekhov, Maia, and Haiku for the boost to my psychological wellbeing.

I thank my parents, who, apart from bestowing the obvious gift of life, have given me all the support and love I could have ever asked for. I still can't comprehend how they managed to instill in me a desire for higher education and knowledge from such a young age, but here I am now. My mother, Estela Gavosto, has always pushed me to be the best that I can. My father, Rodolfo Torres, whose incredible sense of humor and life views I hope to emulate: "El quien no se ríe de si mismo, llora de si mismo".

I would also like to thank my brother, Juan Martin; I cherish all our similarities and differences. You are an endless fountain of support, empathy, and wit, even if you are too humble to realize it. I hope someday I can repay you for all your time and effort, especially in the darkest times. To my grandparents, uncles, aunts, and cousins in Argentina: you may be far away, but you've always been close in my heart. Perhaps my greatest regret in grad school is not seeing all of you enough and maybe also introducing Silvio to eBay, but I hope to rectify the former soon.

Above all others, one person in particular deserves mention: my partner in crime, Kristen Colwell. With you, grad school truly became an adventure, even if it had to start on the wrong (broken) foot. You have opened my eyes to entire realms of thoughts and experiences not just in science and engineering, but in life. Together we've managed to make it up this mountain (you certainly deserve the credit for finding the final route) and I look forward to hiking up many more with you.

This journey has been a long and arduous one at times, so I feel I must conclude these acknowledgements by asking forgiveness for any deserving person that I may have accidentally omitted in this last mile of my academic marathon and lastly by thanking you, the reader, for, well, you know.

# Chapter 1: Redox-Active Metal–Organic Frameworks

## 1.1 Introduction

In the last few decades the field of metal–organic frameworks has erupted out of the seemingly abyssal chasm between solid-state and molecular inorganic chemistry. Pioneered by Yaghi,<sup>1</sup> Kitagawa,<sup>2</sup> and Férey,<sup>3</sup> these hybrid materials resemble a molecular adaptation of childhood toys: connecting different pieces together in a repeating pattern yields different shapes and structures. While the field of metal–organic frameworks (MOFs), also known as porous coordination polymers (PCPs), porous coordination networks (PCNs), etc., covers a vast range of materials, there are varying definitions of what qualifies as a “MOF”. Therefore, I begin by defining metal–organic frameworks within the context of the materials that I have dedicated my graduate career to studying. As the name implies, metal-containing units are connected by multitopic organic molecules in a crystalline lattice. These metal-containing units may either be isolated metal cations, inorganic clusters,<sup>4</sup> chains,<sup>5,6</sup> or even sheets. The resulting crystalline lattices are typically three-dimensionally connected but in some cases they exist as stacked two-dimensional materials.<sup>7–10</sup>

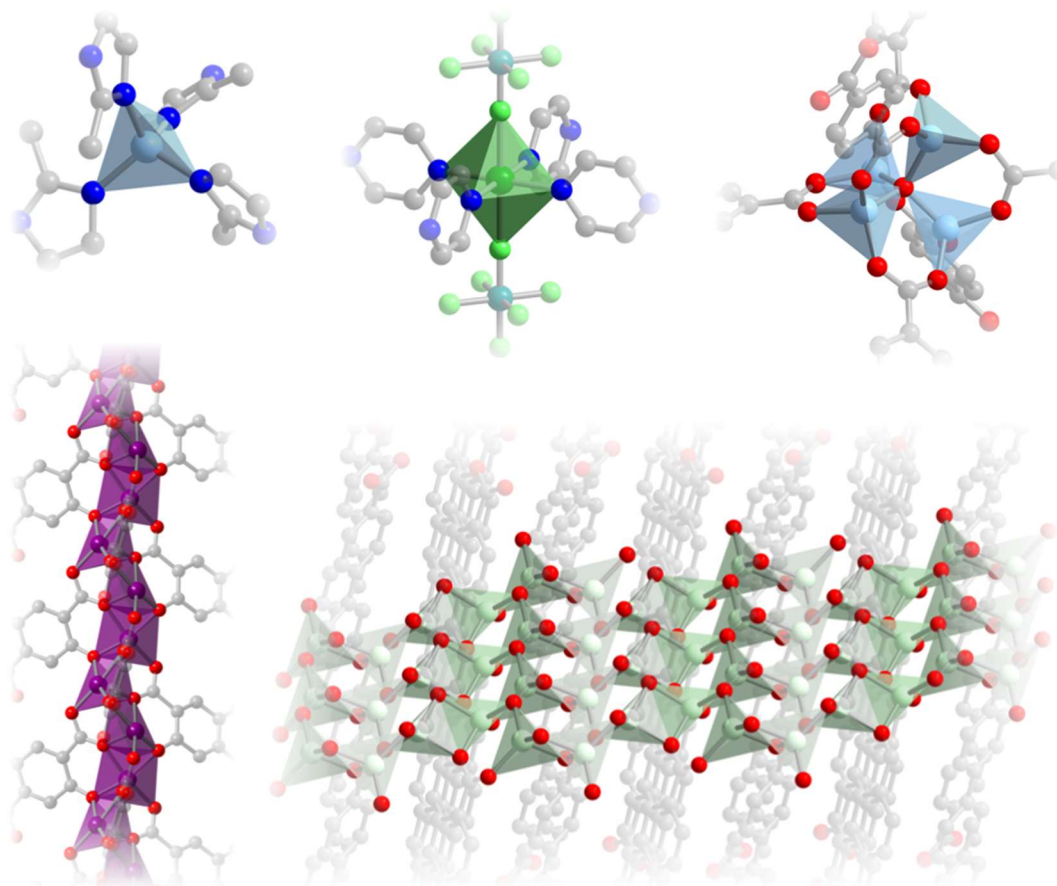


**Figure 1.1.** Example structure motifs in metal–organic frameworks. Mononuclear metal cations in ZIF-8<sup>11</sup> (top left) and SIFSIX-3-Ni<sup>12</sup> (top middle), a tetranuclear cluster in MOF-5<sup>13</sup> (top right), a helical chain in Co<sub>2</sub>(dobdc)<sup>14</sup> (bottom left), and a sheet in ULMOF-2<sup>15</sup> (bottom right).

All metal–organic frameworks exhibit a fundamental and revolutionary feature: porosity.<sup>16</sup> This porosity is often defined as *permanent porosity*, which requires the material to have void space that is typically measured via a gas adsorption technique.<sup>17</sup> For the purposes of this discussion, I am broadening this definition to *accessible porosity*. A coordination solid (the broader category that contains all MOFs) has accessible porosity if guest species (gases, ions, liquids, solids) can be inserted and/or removed while maintaining structural connectivity. The benefit of this porosity is it serves as a new architectural drawing board for inorganic chemists. No longer impeded by rearrangement of ligands in solutions, chemists can now routinely generate high energy conformations of inorganic and/or organic species pinned by the rigidity of the framework scaffold. An example of this is the ability to access coordinatively unsaturated metal sites, where the framework as-synthesized contains metal cations with one or more bound solvent molecules. For some frameworks, this solvent molecule may be removed without framework collapse, allowing for strong polarization of guest molecules. As a result, coordinatively unsaturated metal centers can provide exceptional chemical selectivities for industrial separations,<sup>18–20</sup> new catalytic properties,<sup>21–25</sup> and allow for fundamental study of metal–adsorbate interactions.<sup>26,27</sup> Additionally, a vast range of topologies can be explored from complex and previously unknown networks,<sup>1,28</sup> to unique geometries not found in other porous materials.<sup>29,30</sup> There are innumerable different facets of this rapidly growing field. One particularly intriguing facet is the ability of the inorganic node, the organic linker, or both to undergo redox processes, which can be leveraged to create novel materials and properties. The subsequent sections in this chapter will discuss the basic concepts underlying redox-active metal–organic frameworks.

## 1.2 Redox-Activity in Metal–Organic Frameworks

Many molecular species can be readily oxidized or reduced in solution and have a dissociated/non-coordinating counterion for charge balance.<sup>31</sup> If such species were interconnected into a solid material, any redox chemistry performed on it would require an additional net transfer of charged species to maintain electrostatic equilibrium. It is this interplay between the redox activity of a framework and related guest molecules (oxidants, reductants, counterions, etc.) that defines the field of redox-active metal–organic frameworks.<sup>32</sup> Any metal–organic framework that is capable of maintaining its structural connectivity while changing the charge state of one or more of its components should be considered redox-active. These materials are relatively uncommon and are often highly air-sensitive.<sup>33</sup> Their rarity can be justified from an electrostatic and structural point of view.

Isostructural metal–organic frameworks are seldom reported to exist for the same components in different oxidation states. For example, if a structure is reported with a divalent metal,  $M^{II}$ , then it is uncommon for it to also be reported with the trivalent state,  $M^{III}$ . For a stable material to accommodate a different charged species throughout its structure, it must also incorporate a charge balancing species as well. Most frameworks are incapable of supporting different charge states, either because of an inability to incorporate charge balancing ions due to pore size, an instability to requisite electrochemical potential, or some combination thereof. Many highly reducing frameworks will readily oxidize in air but this is often accompanied with a loss in crystallinity. There are a few examples of materials being post-synthetically reduced concomitantly with alkali cation insertion,<sup>34,35</sup> and there are also examples of frameworks being post-synthetically oxidized, often with the insertion of large charge balancing anions.<sup>36,37</sup> As interest in redox-active metal–organic frameworks has grown over the past decade, there now exist some well-written

reviews on the subject, to which interested readers may refer.<sup>32,38–43</sup> Rather than duplicate these efforts, I would like to highlight and discuss a few relevant areas of the field. While redox-active metals can also often be incorporated into metal–organic frameworks via post-synthetic metal exchange, these species are usually only obtained in low concentrations.<sup>44–48</sup> Such isolated sites can yield interesting phenomena but for the sake of brevity I will not discuss these systems here. The potential applications of redox-active frameworks are particularly exciting for the fields of catalysis<sup>49–52</sup> and energy storage.<sup>53–59</sup> Deploy these materials for industrial application will require de understanding of how to synthesize and use these materials effectively.

### 1.3 Redox-Active Metals

Of known frameworks that exhibit metal-based redox activity, the vast majority are synthesized in a lower oxidation state and can then be post-synthetically oxidized to a higher one. A rational for this bias towards lower oxidation state can be made based on metal ion lability during synthesis. As extended solids, metal–organic frameworks require a moderate degree of reversibility in the formation process in order to exhibit long-range order and thus measurable crystallinity. Metal ions with higher oxidation states (+3 or +4) are in general more kinetically inert<sup>60</sup> and consequentially are less likely to yield crystalline material and more likely to form amorphous solids. Although there are those who study amorphous metal–organic materials (*a*MOFs),<sup>61,62</sup> unless a framework can be isolated as a crystalline solid, it is rarely reported. This skews the distribution of redox-active metal–organic frameworks towards lower oxidation states.

The more common metal-centered redox couples found in metal–organic frameworks are  $V^{III}/V^{IV}$ ,<sup>63,64</sup>  $Cr^{II}/Cr^{III}$ ,<sup>65,66</sup>  $Fe^{II}/Fe^{III}$ ,<sup>34,35,37,43,67</sup>  $Co^{II}/Co^{III}$ ,<sup>68,69</sup> and  $Cu^{I}/Cu^{II}$ .<sup>70–72</sup> Among these,  $Fe^{II/III}$  is by far the most ubiquitous. It appears that  $Fe^{II}/Fe^{III}$  is in a sort of happy medium; ferrous ions are reducing enough to be oxidized by  $O_2$  or other readily accessible oxidants, but not so reducing so as to decompose ligands in solution. While the same can be said for the  $Cu^{I}/Cu^{II}$  redox couple, copper is less amenable to the strongly-bound high-symmetry coordination modes typically found in metal–organic frameworks, and the introduction of a Jahn-Teller distortion upon oxidation from  $Cu^I$  to  $Cu^{II}$ , can induce strain in the crystalline framework.<sup>73–75</sup> Iron, on the other hand, readily adopts tetrahedral and octahedral coordination geometries for both ferrous and ferric oxidation states and can require very little reorganization energy to switch between oxidation states.<sup>76</sup>

It is quite fortuitous that iron is frequently encountered as the redox-active metal in frameworks because it has a naturally-abundant Mössbauer-active isotope:  $^{57}Fe$ . Mössbauer spectroscopy, pioneered by Nobel laureate Rudolph Mössbauer, relies upon the highly chemisensitive excitation and relaxation of nuclei by gamma rays.<sup>77</sup> Gamma rays of a very narrow bandwidth from a source of excited nuclei are passed through a sample. The source is accelerated towards and away from the sample over a range of velocities to utilize the Doppler effect to generate a small but precise range of energies. Nuclei with different chemical environments will absorb gamma rays at slightly different energies, leading to transmission spectra rich with chemical information. Excited nuclei of  $^{57}Fe$ , the electron capture decay product of  $^{57}Co$ , are by far and away the most readily accessible Mössbauer active source.  $^{57}Fe$  Mössbauer spectra can be used to quantify the redox state of iron in a material as well as characterize its chemical environment. The only real limitation to this technique<sup>78</sup> is that strong magnetic interactions at low temperatures as well as less common material geometries can lead to spectra which are difficult to interpret. With that said, neither scenario is frequently encountered in the study of metal–organic frameworks.  $^{57}Fe$  Mössbauer has

thus been frequently used to characterize as-synthesized states of iron frameworks as well as the results of post-synthetic oxidations or reductions.<sup>21,34–37,67</sup>

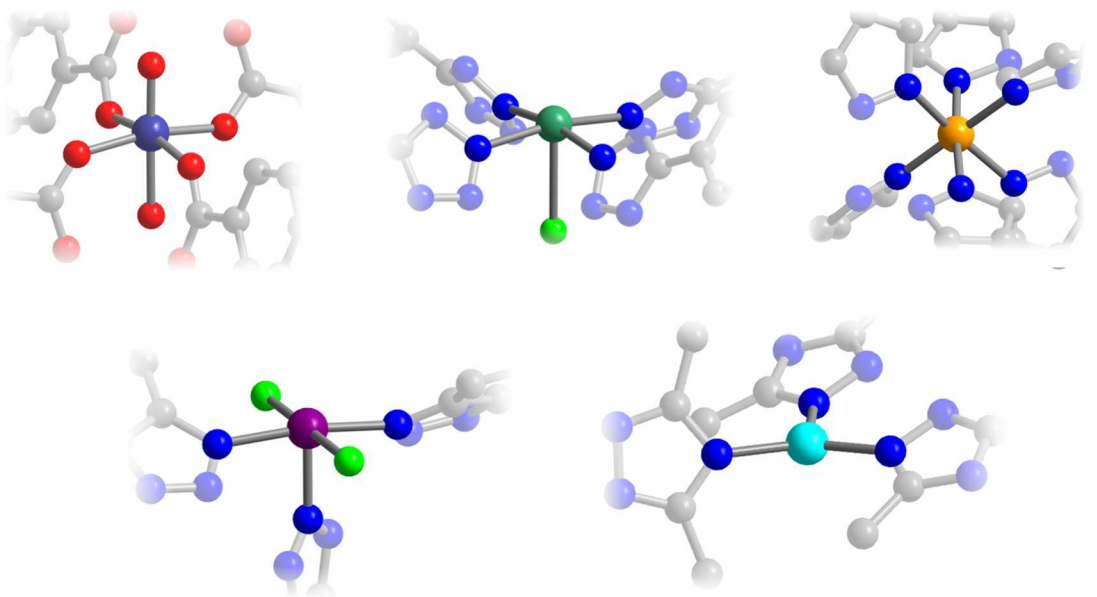


**Figure 1.2:** Examples of redox-active metal centers in metal–organic frameworks.  $V^{III}/V^{IV}$  in MIL-47(V) (top left),<sup>64</sup>  $Cr^{II}/Cr^{III}$  in Cr-BTT (top middle),<sup>65</sup>  $Fe^{III}/Fe^{II}$  in  $Fe_2(bdp)_3$  (top right),<sup>34</sup>  $Co^{II}/Co^{III}$  in  $Co_2Cl_2(bttd)$  (bottom left),<sup>69</sup> and  $Cu^I/Cu^{II}$  in MAF-42 (bottom right).<sup>71</sup>

For non-iron-based frameworks, the redox state of metal sites can be much harder to quantify. Crystallographic information, and elemental analysis can be used to make atomic radii arguments and charge balance justifications, respectively. Additional analytical techniques are required for systems that have some degree of valence ambiguity. To address this question, multiple different X-ray-based techniques such as X-ray photoelectron spectroscopy (XPS) and X-ray adsorption spectroscopy (XAS) can be utilized to infer both oxidation state and coordination environment.<sup>79</sup> However, accurate modeling and interpretation of spectra typically rely upon comparison to known standards and theoretical calculations.<sup>80</sup> This can be particularly challenging for metal–organic frameworks that contain previously unreported chemical environments, such as coordinatively unsaturated metal sites. Magnetic susceptibility measurements can also be used to characterize metal oxidation state, but unless precise material elemental composition is known, it can be difficult to correlate room temperature susceptibility values with metal redox states.<sup>81,82</sup> Additionally, systems that have some ambiguity in the spin state of the components can also be difficult to analyze in this manner.<sup>34</sup>

## 1.4 Redox-Active Ligands

Metal–organic frameworks can also exhibit ligand-based redox activity along with or independently of metal-based redox activity. These ligands universally rely on delocalized  $\pi$ -systems to access different oxidation states. Unlike their metal counterparts, these ligands can be frequently synthesized either as a species that can be reduced or a species that can be oxidized. Generally, these ligands access a new redox state via the formation of a radical. As organic radicals

are typically thermally unstable, solvothermal routes are often incompatible with the formation of a framework with radical-containing ligands. Broadly speaking, redox-active ligands can be sorted into two categories: ligands that communicate electronically with their bound metals and those that do not. The latter are species that have a delocalized  $\pi$ -system connected to metal ions via orthogonal moieties, such as benzoate or azolate species. These systems have demonstrated electrochromic behavior in the case of naphthalene diimide-based linkers<sup>83,84</sup> and tunable electronic conductivity in tetrathiafulvalene-based ligands<sup>85–88</sup> (**Figure 1.3**).

For redox active ligands that communicate electronically with connecting metals, one class of chemical moiety is pervasive: multisubstituted aromatic systems with para and/or ortho electronegative species (O, N, S) to leverage catechol/quinone-type redox states. More commonly incorporated into two-dimensional frameworks, ligands such as 2,5-dichloro-3,6-dihydroxybenzoquinone ( $\text{H}_2\text{Cl}_2\text{dhbq}$ ),<sup>8,89,90</sup> benzenehexathiolate ( $\text{H}_6\text{C}_6\text{S}_6$ ),<sup>91–94</sup> and 2,3,6,7,10,11-hexaminothriphenylene (HITP)<sup>7,95–100</sup> have been utilized to form some of the most conductive metal–organic materials to date, with  $\text{Cu}_3\text{C}_6\text{S}_6$  achieving the highest reported value (**Figure 1.3**).<sup>91</sup> These ligands can often have ambiguous or mixed-valent redox states; this ambiguity stems from redox chemistry that is believed to occur during synthesis. When ligands are introduced in a highly reducing state such as  $\text{H}_6\text{C}_6\text{S}_6$ , it is proposed that the in situ reduction of protons to dihydrogen removes electrons from the ligand, allowing for the formation of materials such as  $\text{Ni}_3([\text{C}_6\text{S}_6]^{3-})_2$ .<sup>93</sup> At the other electrochemical extreme, electron-deficient systems such as  $\text{Cl}_2\text{dhbq}^{2-}$  can be reduced by both metal ions and formate decomposition during solvothermal synthesis.<sup>8</sup> Because of the extensive degree of orbital mixing between the metal  $d$  orbitals and the ligand  $p$  orbitals in these systems it can be quite difficult to assign specific valence states to the ligand.

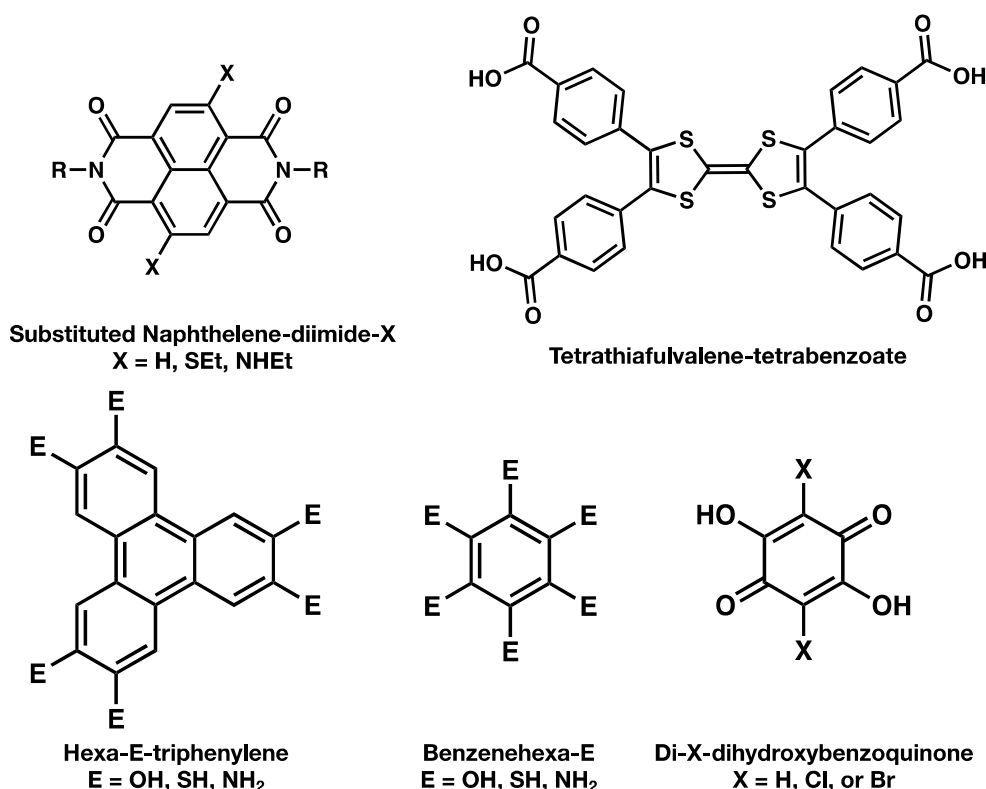


**Figure 1.3:** Example chemical structures of redox-active ligands that have been incorporated into metal–organic frameworks.

## 1.5 Gases in Redox-Active Frameworks

By combining gas sorption measurements with in situ conductivity measurements, metal–organic frameworks can be utilized as electrochemical sensors. In multiple studies, it has been shown that conductive metal–organic frameworks exhibit highly specific changes in conductivity in the presence of different gases.<sup>101,102</sup> Adsorbates bound in these frameworks perturb vibrational modes and/or electronic states, depending on the mechanism of adsorption. These perturbations correlate with changes in measured conductivity that are reproducible for a specific gas at a specific concentration. Utilizing several different conductive frameworks in parallel can allow for more chemiselective detection, as each system responds differently to each adsorbate.

Redox-active frameworks have also received quite a bit of attention in the area of gas separations. Reducing open metal sites have been found to exhibit highly selective chemisorption of O<sub>2</sub> over other gases such as N<sub>2</sub>. Selectivity in these systems is derived from partial or complete inner sphere electron transfer from the metal to O<sub>2</sub> to generate a metal-superoxide species. This phenomenon has been well documented for chromium,<sup>65,66</sup> iron,<sup>67</sup> and cobalt<sup>68</sup> open metal sites (**Figure 1.4**). These adsorbents often suffer from limited thermal stability or cyclability, as the reduced oxygen species that form can often lead to deleterious and irreversible chemistry. The limitations of such adsorbents and a possible route to improving reversibility are discussed in Chapter 2. Additionally, adsorption of other oxidizing gasses such as NO<sup>45,103–105</sup> or Cl<sub>2</sub><sup>69</sup> has also been reported for redox-active frameworks.

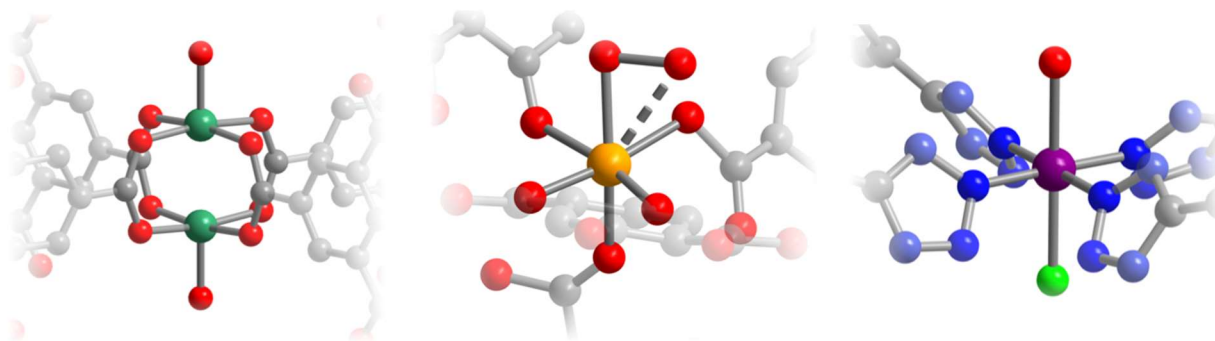


**Figure 1.4:** Example of O<sub>2</sub> adsorption on redox-active open metal site. Cr<sub>3</sub>(btc)<sub>2</sub> (left),<sup>65</sup> Fe<sub>2</sub>(dobdc) (middle)<sup>67</sup>, and Co-BDTriP (right)<sup>68</sup>. In the case of Cr<sub>3</sub>(btc)<sub>2</sub> and Co-BDTriP, only the center of electron density in the O<sub>2</sub><sup>-</sup> species could be resolved.

Selectivities of frameworks can also be altered by reducing or oxidizing the as-synthesized system. This is a relatively unexplored route to creating selective adsorbents, but a few examples have distinguished themselves. Recently, an ethane-selective adsorbent was reported for the separation of ethane/ethylene in the oxidized form of Fe<sub>2</sub>(dobdc). Rather than utilize the open metal sites in Fe<sub>2</sub>(dobdc), Chen et al. suggest that irreversibly bound peroxides in the oxygen exposed Fe<sub>2</sub>(dobdc)O<sub>2</sub> preferentially interact with ethane (**Figure 1.5**).<sup>106</sup> In a different approach, the V<sup>III</sup> framework, MFM-300, can be oxidized to V<sup>IV</sup> without the incorporation of a reduced species.<sup>63</sup> Instead, a charge balancing proton is removed from a bridging hydroxide in the material. This alters both the location and strength of binding sites for CO<sub>2</sub> (**Figure 1.5**). The possible

application of this approach to a new metal–organic framework is further discussed in Chapter 3. Lastly, controlling gas adsorption through the simple change of applied voltage to a material is viewed as the “holy grail” of gas sorption in conductive metal–organic frameworks.<sup>38</sup> At least one tenuous example of this process exists in the reversible adsorption of ethylene onto an amorphous metal–organic material.<sup>107</sup>

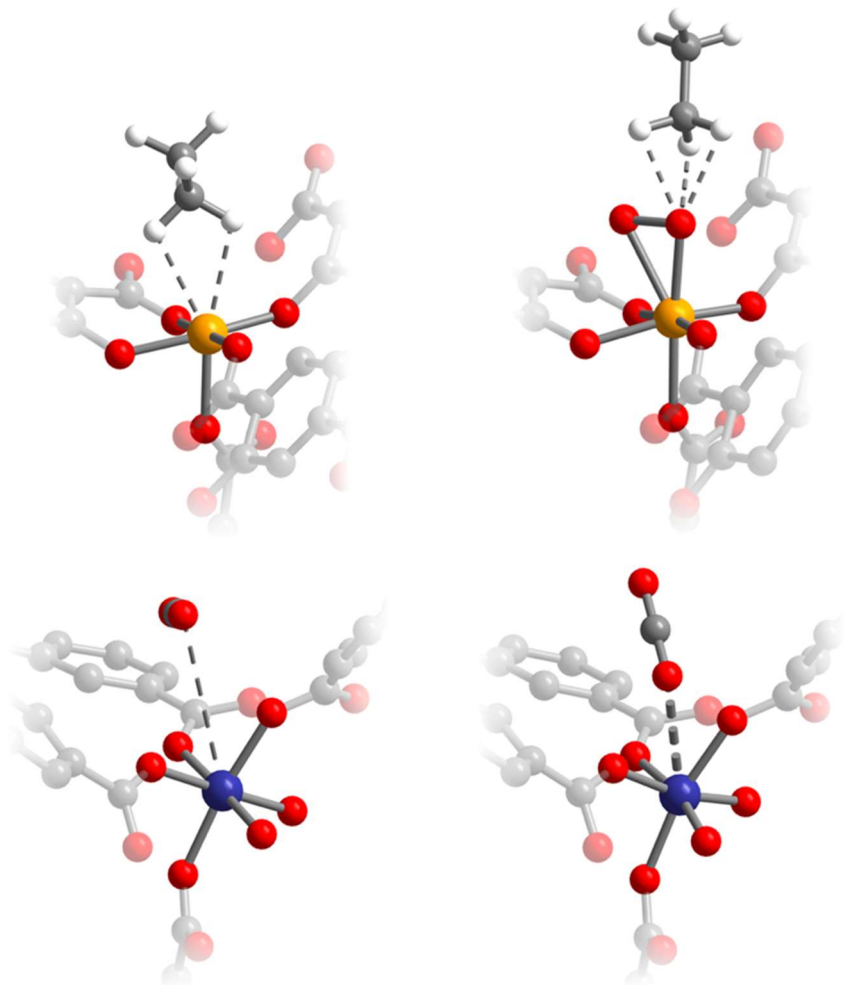


**Figure 1.5:** Examples of changing gas adsorption properties of a framework through redox activity.  $\text{Fe}_2(\text{dobdc})$ <sup>18</sup> exhibits weak binding of ethane as synthesized (top left) but becomes ethane selective when oxidized with  $\text{O}_2$  (top right).<sup>67,106</sup>  $\text{CO}_2$  adsorption in MFM-300<sup>63</sup> changes from weak side-on interaction in the as-synthesized ( $\text{V}^{\text{III}}$ ) form (bottom left) to strong end up interactions in the oxidized state ( $\text{V}^{\text{IV}}$ ) (bottom right).

## 1.6 Modeling Gas Sorption

When it was first demonstrated that metal–organic frameworks could exhibit permanent porosity and adsorb gas molecules in the early 2000s,<sup>13,108,109</sup> the study of adsorption at surfaces had been around for almost a century. While the study of gas sorption in metal–organic frameworks has led to new understandings of adsorption phenomena, in general these 21<sup>st</sup> century materials are analyzed and characterized using 20<sup>th</sup> century models. This is not to say that these models are

necessarily inaccurate or cannot be used to standardize material comparison. In general, these models are most commonly used out of simplicity. However, there are instances where these gas sorption models are applied to scenarios for which they were not designed. These countless number of models and equations present in the literature can and in fact do have entire articles/theses/books written on them. I will therefore limit my discussion here to two common models that have been particularly relevant to my research: the Langmuir-Freundlich adsorption model and ideal adsorbed solution theory (IAST).

First, a brief digression on the statistics (or lack thereof) of gas sorption data and modelling in metal–organic frameworks is required. As recently discussed by Sholl et al. there is a large variation in the reported gas adsorption isotherms for supposedly identical materials.<sup>110</sup> There are at least two clear causes for such variations. First, nearly all reported isotherms for metal–organic frameworks are singular data sets, without repetition of any measurement. As most gas sorption analyzers are very expensive, instrument time is a precious commodity and frequently a limiting factor. Even high throughput analyzers are commonly limited to a single gas/temperature combination across all samples. Because of this, duplicative or multiplicative measurements are often deemed an unnecessary cost. Until instrumentation cost substantially decreases and/or statistical information for isotherm measurements is valued more highly, singular measurements will continue to be the norm.

The second explanation for inconsistencies in reported isotherms stems from material inconsistencies or differences in properties between different batches of the same crystalline phase. This issue may be much more difficult, if not nearly impossible, to address. While molecular species can often exhibit identical properties (NMR shifts, vibrational frequencies, electronic transitions etc.), extended solids can have much larger degrees of variability from sample to sample caused by defects, differences in particle size/shape, etc. Metal–organic frameworks are not excluded from this variability. There is a truly daunting list of reaction variables for metal–organic frameworks syntheses, many of which are almost never reported: heating method and rate, reaction vessel material and/or surface, particle size and shape of solid reagents, order and method of introduction of reagents, etc.<sup>111</sup> If all such reaction parameters were controlled, then the resulting material from duplicate reactions should have identical properties. Even if these as-synthesized materials are identical, materials often undergo multiple additional processing steps before gas sorption measurements are performed. Solvent washes, activation via intrapore solvent removal, and sample manipulation/storage can all impact material properties.

As long as the total amount of inactive sites, metal or ligand vacancies, surface defects, etc. introduced via synthesis and processing remains a small percentage of the material, then only the saturation capacity of gas adsorption measurements will be primarily affected. In general, a small concentration of defects will not perturb the binding enthalpy and entropy of gas molecules in the bulk of the material. However, incomplete reactivation or material degradation between measurements can lead to errors in calculated thermodynamic parameters, as the material is assumed to have the same initial chemical state for each isotherm. While chemists can often disregard exhaustive studies into the variations of chemical and material properties of frameworks as unrewarding, the economic viability and industrial implementation of metal–organic frameworks entirely depend on accurately knowing material properties and consistently reproducing them.

Beyond the inherent pitfalls of solitary measurements, there is not enough discussion or any form of consensus in the metal–organic framework community on how the preferred models should be fit to gas sorption data. Although every area of science must come to consensus with how raw data should be interpreted, refined, modeled etc., I have found this facet of research in metal–organic framework to be particularly eye-opening. When fitting either an isotherm or multiple isotherms simultaneously, there is a seemingly endless list of possible models to use, each with their own caveats, advantages and disadvantages. In general, there is little transparency in how these models are fit to data, yet values derived from them are used to establish hierarchies among metal–organic frameworks as the greatest/highest/largest/best “\_\_\_\_\_”. At a bare minimum, fitted models should be plotted with the raw data. In an ideal scenario, if perhaps a pipe dream, raw data would be explicitly provided in supplemental information to publications, which is not without precedent.

In simple models in gas sorption that can be mathematical reduced to a linear relation, such as BET and Langmuir surface area calculations, data are readily fitted with least-squares linear regression. The quality of these fits can be quantitatively described by the coefficient of determination,  $R^2$ . Widely used across all areas of science,  $R^2$  values are rapidly identified and judged based on their proximity to 1 (often characterized by the number of 9s in the decimal places). A large fallacy can be found, however, in the use of  $R^2$  to evaluate nonlinear fits to gas sorption data.  $R^2$  is frequently used to justify which model best fits a data set, and how good the fit is on a presumed absolute scale. Not only does this term not have any mathematical relation to fits made using a non-least-squares approach, but it can also lead to the selection of the wrong model. Statisticians have shown in an example study that when using  $R^2$  to compare models, it led to the correct model being selected only 28–43% of the time.<sup>112</sup> Instead of  $R^2$ , it would be much more meaningful to utilize a value such as the root mean squared deviation (RMSD) to quantify the goodness of fit for different models to a data set. This value is not without its own limitations, however, as it is data set specific and cannot be used to compare the accuracy of a fit to one data set vs. a different fit to another data set.

The Langmuir-Freundlich adsorption model, as the name implies is a combination of the Langmuir adsorption model with the Freundlich adsorption model. Originally proposed in 1918 by future Nobel laureate Irving Langmuir, the Langmuir model was designed to describe the adsorption of gases on a flat surface.<sup>113</sup> The various derivations of this model have several key assumptions: the adsorbent has a constant and uniform surface with identical and discrete adsorption sites, these sites are each capable of binding only a single adsorbate, and adsorbates do not interact with each other. The simplicity of the Langmuir adsorption model has led to it being applied to a vast array of different fields of research. Even if some of these assumptions are not strictly met, it can still serve as a good first approximation to adsorption phenomena and can often be used to accurately predict adsorption behavior. The multisite form for the Langmuir model may be expressed as follows:

$$q_{total} = \sum_{n=1} q_{sat,n} \cdot \frac{b_n \cdot P}{1 + b_n \cdot P} \quad (1.1)$$

where  $q_{total}$  is the total quantity of gas adsorbed in a material,  $q_{sat,n}$  is the saturation capacity of site of the  $n^{\text{th}}$  site,  $b_n$  is the Langmuir parameter for that site and  $P$  is the pressure of the gas. The Langmuir parameter,  $b_n$ , is often divided into two parts:

$$b_n = b_{n,0} \cdot e^{\frac{-\Delta H_n}{RT}} \quad (1.2)$$

consisting of  $b_{n,0}$ , the preexponential Langmuir parameter, and an exponential component, with  $\Delta H_n$  being the differential enthalpy of gas adsorbing onto site  $n$ ,  $R$  is the gas constant, and  $T$  is temperature. Because of this dependence on temperature, multiple different temperature data sets are required to subdivide the Langmuir parameter. When multiple isotherms are simultaneously fit with a Langmuir model, accurate estimates for the enthalpy of adsorption can be obtained. Enthalpy values obtained from a single temperature data set, are therefore not scientifically meaningful and should be disregarded.

In contrast to the Langmuir model, the Freundlich adsorption model is a purely empirical approximation. Designed by Herbert Freundlich in 1909 to model adsorption in systems where either the surface is not known or is very heterogenous,<sup>114</sup> the Freundlich model is only predictive for the specific temperature/adsorbate combination for which the fitted data were measured. The fairly simplistic model is as follows:

$$q_{total} = J \cdot P^v \quad (1.3)$$

$$q_{total} = \sum_{n=1} q_{sat,n} \cdot \frac{b_n \cdot P^{v_n}}{1 + b_n \cdot P^{v_n}} \quad (1.4)$$

where  $J$  is an empirical constant for the system and  $v$  is the Freundlich parameter, which is also an empirical constant. The Langmuir and the Freundlich models are frequently combined into a single model where the exponential Freundlich parameter is applied to the pressure terms in the Langmuir model, **Equation 1.4**. This combination gives a “fudge factor” to the Langmuir model to help account for surface heterogeneity or other small deviations from the underlying assumption. However, these fitted Freundlich parameters should not deviate dramatically from 1. Because this is a purely empirical parameter, there is no explicit theoretical basis for what constitutes an unreasonable value. For values that are much smaller ( $<0.5$ ) or much larger ( $>2$ ), I am inclined to question whether an additional unmodeled binding site is present in the material or if the material is exhibiting some phenomena that deviates substantially from the assumptions of the Langmuir model. In these cases, the comparison of fit parameters between a system that has Freundlich parameters close to 1 and a system that does not becomes tenuous at best.

Lastly, while publications often report the preexponential Langmuir parameter for Langmuir-Freundlich based fits, this value is not particularly useful, especially when given in the units of pressure to a negative non-integer power. Because the derivation for the Langmuir model has the Langmuir parameter,  $b_n$ , equal to the equilibrium constant for the adsorption process on site  $n$ ,  $K_{eq,n}$ , **Equation 1.4** can be rewritten using **Equation 1.5** and **Equation 1.6**, where  $\Delta G_n$  is the differential Gibb’s free energy of gas adsorbing onto site  $n$ , and  $\Delta S_n$  is the differential entropy of gas adsorbing onto site  $n$ . Using this different form of the multisite Langmuir-Freundlich model shown in **Equation 1.7** to fit isotherms, it is possible to readily obtain the enthalpy and entropy of adsorption for a site.

$$K_{eq,n} = e^{\frac{-\Delta G_n}{RT}} \quad (1.5)$$

$$\Delta G_n = \Delta H_n - T\Delta S_n \quad (1.6)$$

$$q_{total} = \sum_{n=1} q_{sat,n} \cdot \frac{e^{-\frac{\Delta H_n}{RT} + \frac{\Delta S_n}{R}} \cdot P^{v_n}}{1 + e^{-\frac{\Delta H_n}{RT} + \frac{\Delta S_n}{R}} \cdot P^{v_n}} \quad (1.7)$$

As metal–organic frameworks are often proposed to for potential applications in industrial separations, it is requisite to understand how an adsorbent behaves in the presence of a mixture of potential adsorbates. Direct measurement of a multicomponent gas sorption isotherm is an incredibly difficult process. It has been a long-standing goal to be able to predict multicomponent behavior from much more experimentally viable single-component gas sorption isotherms. IAST was proposed by Alan Meyers and John Prausnitz in 1965 to be able to model just such an application.<sup>115</sup> As with all simplifying models, IAST begins with several key assumptions: 1. adsorbates have equal access to the same surface area; 2. adsorption sites are uniform across the adsorbent; and 3. the adsorbates act as an ideal solution. In IAST, adsorbates are modeled as exerting a “spreading pressure” on the surface of an adsorbent and selectivities for one adsorbate over another are determined by finding the point at which their spreading pressures are equal. The spreading pressure,  $\pi$ , for an adsorbate,  $i$ , can be calculated using **Equation 1.8**, where the isotherm for the adsorbate is divided by pressure and integrated with respect to pressure from zero to the partial pressure of the adsorbate,  $P^0$ , and  $A$  is the surface area of the adsorbent. This leads adsorbates with very steep isotherms having large spreading pressures, as there should be a strong driving force for adsorption. Because of its ease of use, IAST is invoked (or at least referenced) in nearly every single gas separation publication.<sup>116</sup> As will be further discussed in Chapter 3, it can often be applied to systems where the assumptions in its derivation are not always strictly followed.

$$\frac{\pi_i A}{RT} = \int_0^{P_i^0} \frac{q_{total,i}}{P} dP \quad (1.8)$$

## 1.7 References

- (1) Yaghi, O. M.; O’Keeffe, M.; Ockwig, N. W.; Chae, H. K.; Eddaoudi, M.; Kim, J. *Nature* **2003**, *423* (6941), 705.
- (2) Kitagawa, S.; Kitaura, R.; Noro, S. Functional Porous Coordination Polymers. *Angew. Chem. Int. Ed.* **2004**, *43* (18), 2334.
- (3) Férey, G. *Chem. Soc. Rev.* **2007**, *37* (1), 191.
- (4) Kalmutzki, M. J.; Hanikel, N.; Yaghi, O. M. *Sci. Adv.* **2018**, *4* (10), 1.
- (5) Rosi, N. L.; Kim, J.; Eddaoudi, M.; Chen, B.; O’Keeffe, M.; Yaghi, O. M. *J. Am. Chem. Soc.* **2005**, *127* (5), 1504.
- (6) Schoedel, A.; Li, M.; Li, D.; O’Keeffe, M.; Yaghi, O. M. *Chem. Rev.* **2016**, *116*, 12466.
- (7) Sheberla, D.; Sun, L.; Blood-Forsythe, M. A.; Er, S.; Wade, C. R.; Brozek, C. K.; Aspuru-Guzik, A.; Dincă, M. *J. Am. Chem. Soc.* **2014**, *136* (25), 8859.
- (8) Ziebel, M. E.; Darago, L. E.; Long, J. R. *J. Am. Chem. Soc.* **2018**, *140* (8), 3040.
- (9) López-Cabrelles, J.; Mañas-Valero, S.; Vitorica-Yrezábal, I.; Bereciartua, P.; Rodríguez-Velamazán, J.; Waerenborgh, J.; Vieira, B.; Davidovikj, D.; Steeneken, P.; van der Zant, H.; Espallargas, G.M.; Coronado, E. *Nat. Chem.* **2018**, *10* (10), 1001.

- (10) Yang, C.; Dong, R.; Wang, M.; Petkov, P.; Zhang, Z.; Wang, M.; Han, P.; Ballabio, M.; Bräuninger, S. A.; Liao, Z.; Zhang, J.; Schwotzer, F.; Zschech, S.; Heine, T.; Feng, X. *Nat. Commun.* **2019**, *10* (1), 3260.
- (11) Morris, W.; Stevens, C. J.; Taylor, R.; Dybowski, C.; Yaghi, O. M.; Garcia-Garibay, M. A. *J. Phys. Chem. C* **2012**, *116* (24), 13307.
- (12) Shekhah, O.; Belmabkhout, Y.; Adil, K.; Bhatt, P. M.; Cairns, A. J.; Eddaoudi, M. *Chem. Commun.* **2015**, *51* (71), 13595.
- (13) Eddaoudi, M.; Kim, J.; Rosi, N.; Vodak, D.; Wachter, J.; O’Keeffe, M.; Yaghi, O. M. *Science* **2002**, *295* (5554), 469.
- (14) Queen, W. L.; Hudson, M. R.; Bloch, E. D.; Mason, J. A.; Gonzalez, M. I.; Lee, J. S.; Gygi, D.; Howe, J. D.; Lee, K.; Darwish, T. A.; James, M.; Peterson, V. K.; Teat, S. J.; Smit, B.; Neaton, J. B.; Long, J. R.; Brown, C. M. *Chem. Sci.* **2014**, *5*, 4569.
- (15) Banerjee, D.; Borkowski, L. A.; Kim, S.; Parise, J. B. *Cryst. Growth Des.* **2009**, *9* (11), 4922.
- (16) Schoedel, A.; Yaghi, O.M. (2016). Porosity in Metal–Organic Compounds. In *Macrocyclic and Supramolecular Chemistry*, R. M. Izatt (Ed.).
- (17) Rowsell, J.; Yaghi, O. M. *Micropor. Mesopor. Mat.* **2004**, *73* (1–2), 3.
- (18) Bloch, E. D.; Queen, W. L.; Krishna, R.; Zadrozny, J. M.; Brown, C. M.; Long, J. R. *Science* **2012**, *335* (6076), 1606.
- (19) Britt, D.; Furukawa, H.; Wang, B.; Glover, G. T.; Yaghi, O. M. *Proc. National Acad. Sci.* **2009**, *106* (49), 20637.
- (20) Dietzel, P. D.; Besikiotis, V.; Blom, R. *J. Mater. Chem.* **2009**, *19* (39), 7362.
- (21) Xiao, D. J.; Bloch, E. D.; Mason, J. A.; Queen, W. L.; Hudson, M. R.; Planas, N.; Borycz, J.; Dzubak, A. L.; Verma, P.; Lee, K.; Bonino, F.; Crocella, V.; Yano, J.; Bordiga, S.; Truhlar, D. G.; Gagliardi, L.; Brown, C. M.; Long, J. R. *Nature Chem.* **2014**, *6*, 590.
- (22) Fu, Y.; Sun, D.; Qin, M.; Huang, R.; Li, Z. *RSC Adv.* **2012**, *2* (8), 3309.
- (23) Yang, D.-A.; Cho, H.-Y.; Kim, J.; Yang, S.-T.; Ahn, W.-S. *Energ. Environ. Sci.* **2011**, *5* (4), 6465.
- (24) Srinivas, G.; Ford, J.; Zhou, W.; Wu, H.; Udovic, T. J.; Yildirim, T. *Chem. Euro. J.* **2011**, *17* (22), 6043.
- (25) Hong, D.; Hwang, Y.; Serre, C.; Férey, G.; Chang, J. *Adv. Funct. Mater.* **2009**, *19* (10), 1537.
- (26) Runčevski, T.; Kapelewski, M. T.; Torres-Gavosto, R. M.; Tarver, J. D.; Brown, C. M.; Long, J. R. *Chem. Commun.* **2016**, *52* (53), 8251.
- (27) Gonzalez, M. I.; Mason, J. A.; Bloch, E. D.; Teat, S. J.; Gagnon, K. J.; Morrison, G. Y.; Queen, W. L.; Long, J. R. *Chem. Sci.* **2017**, *8* (6), 4387.
- (28) Li, M.; Li, D.; O’Keeffe, M.; Yaghi, O. M. *Chem. Rev.* **2014**, *114* (2), 1343.
- (29) Liu, Y.; Kravtsov, V.; Eddaoudi, M. *Angew. Chem. Int. Ed.* **2008**, *47* (44), 8446.
- (30) Alezi, D.; Spanopoulos, I.; Tsangarakis, C.; Shkurenko, A.; Adil, K.; Belmabkhout, Y.; O’Keeffe, M.; Eddaoudi, M.; Trikalitis, P. N. *J. Am. Chem. Soc.* **2016**, *138* (39), 12767.
- (31) Connelly, N. G.; Geiger, W. E. *Chem. Rev.* **1996**, *96* (2), 877.
- (32) D’Alessandro, D. *Chem. Commun.* **2016**, *52* (58), 8957.
- (33) The air-sensitivity of many redox-active systems can be a prohibitive barrier to their study and subsequent publication, leading to a smaller presentation in the literature.
- (34) Aubrey, M. L.; Wiers, B. M.; Andrews, S. C.; Sakurai, T.; Reyes-Lillo, S. E.; Hamed, S. M.; Yu, C.; Darago, L. E.; Mason, J. A.; Baeg, J.; Grandjean, F.; Long, G. J.; Seki, S.; Neaton, J. B.; Yang, P.; Long, J. R. *Nat. Mater.* **2018**, *17*, 625.

- (35) Darago, L. E.; Aubrey, M. L.; Yu, C.; Gonzalez, M. I.; Long, J. R. *J. Am. Chem. Soc.* **2015**, *137* (50), 15703.
- (36) Aubrey, M. L.; Long, J. R. *J. Am. Chem. Soc.* **2015**, *137* (42), 13594.
- (37) Park, J. G.; Aubrey, M. L.; Oktawiec, J.; Chakarawet, K.; Darago, L. E.; Grandjean, F.; Long, G. J.; Long, J. R. *J. Am. Chem. Soc.* **2018**, *140* (27), 8526.
- (38) Sun, L.; Campbell, M. G.; Dincă, M. *Angew. Chem. Int. Ed.* **2016**, *55* (11), 3566.
- (39) Murase, R.; Leong, C. F.; Alessandro, D. *Inorg. Chem.* **2017**, *56*, 14373.
- (40) Bhardwaj, S. K.; Bhardwaj, N.; Kaur, R.; Mehta, J.; Sharma, A. L.; Kim, K.-H.; Deep, A. *J. Mater. Chem. A* **2018**, *6* 14992.
- (41) Calbo, J.; Golomb, M.; Walsh, A. *J. Mater. Chem. A* **2019**, *7*, 16571.
- (42) Murase, R.; Ding, B.; Gu, Q.; Alessandro, D. *Philos. T. R. Soc. A* **2019**, *377* (2149), 20180226.
- (43) Sun, L.; Hendon, C. H.; Park, S. S.; Tulchinsky, Y.; Wan, R.; Wang, F.; Walsh, A.; Dincă, M. *Chem. Sci.* **2017**, *8* (6), 4450.
- (44) Brozek, C. K.; Dincă, M. *J. Am. Chem. Soc.* **2013**, *135* (34), 12886.
- (45) Brozek, C. K.; Miller, J. T.; Stoian, S. A.; Dincă, M. *J. Am. Chem. Soc.* **2015**, *137* (23), 7495.
- (46) Stubbs, A. W.; Braglia, L.; Borfecchia, E.; Meyer, R. J.; Leshkov, Y.; Lamberti, C.; Dincă, M. *ACS Catal.* **2017**, *8* (1), 596.
- (47) Brozek, C.; Ozarowski, A.; Stoian, S.; Dincă, M. *Inorg. Chem. Front.* **2017**, *4* (5), 782.
- (48) Comito, R. J.; Wu, Z.; Zhang, G.; Lawrence, J. A.; Korzyński, M. D.; Kehl, J. A.; Miller, J. T.; Dincă, M. *Angew. Chem. Int. Ed.* **2018**, *57* (27), 8135.
- (49) Ranocchiari, M.; van Bokhoven, J. *Phys. Chem. Chem. Phys.* **2011**, *13* (14), 6388.
- (50) Dhakshinamoorthy, A.; Li, Z.; Garcia, H. *Chem. Soc. Rev.* **2018**, *47* (22), 8134.
- (51) Cui, W.-G.; Zhang, G.-Y.; Hu, T.-L.; Bu, X.-H. *Coordin. Chem. Rev.* **2019**, *387*, 79.
- (52) Remya, V.; Kurian, M. *Int. Nano Lett.* **2019**, *9* (1), 17.
- (53) Zhao, Y.; Song, Z.; Li, X.; Sun, Q.; Cheng, N.; Lawes, S.; Sun, X. *Energy Storage Mater.* **2016**, *2*, 35.
- (54) Mehtab, T.; Yasin, G.; Arif, M.; Shakeel, M.; Korai, R.; Nadeem, M.; Muhammad, N.; Lu, X. *J. Energy Storage* **2019**, *21*, 632.
- (55) Zhang, X.; Chen, A.; Zhong, M.; Zhang, Z.; Zhang, X.; Zhou, Z.; Bu, X.-H. *Electrochem. Energy Rev.* **2019**, *2* (1), 29.
- (56) Xia, W.; Mahmood, A.; Zou, R.; Xu, Q. *Energ. Environ. Sci.* **2015**, *8* (7), 1837.
- (57) Zhao, R.; Liang, Z.; Zou, R.; Xu, Q. *Joule* **2018**, *2*, 2235.
- (58) Zheng, Y.; Zheng, S.; Xue, H.; Pang, H. *J. Mater. Chem. A* **2019**, *7* (8), 3469.
- (59) Miner, E. M.; Dincă, M. *Philos. T. R. Soc. Math Phys. Eng. Sci.* **2019**, *377* (2149), 20180225.
- (60) van Eldik, R.; Hubbard, C. D. *Advances in Inorganic Chemistry: Inorganic Reaction Mechanisms.* **2003**.
- (61) Bennett, T. D.; Cheetham, A. K. *Accounts Chem. Res.* **2014**, *47* (5), 1555.
- (62) Ashworth, C. *Nat. Rev. Mater.* **2017**, *2* (11), 17074.
- (63) Lu, Z.; Godfrey, H. G.; da Silva, I.; Cheng, Y.; Savage, M.; Tuna, F.; McInnes, E. J.; Teat, S. J.; Gagnon, K. J.; Frogley, M. D.; Manuel, P.; Rudić, S.; Ramirez-Cuesta, A.J.; Easun, T.L.; Yang, S.; Schröder, M. *Nat. Commun.* **2017**, *8* (1), 14212.
- (64) Leclerc, H.; Devic, T.; Devautour-Vinot, S.; Bazin, P.; Audebrand, N.; Férey, G.; Daturi, M.; Vimont, A.; Clet, G. *J. Phys. Chem. C* **2011**, *115* (40), 19828.
- (65) Murray, L. J.; Dinca, M.; Yano, J.; Chavan, S.; Bordiga, S.; Brown, C. M.; Long, J. R. *J. Am. Chem. Soc.* **2010**, *132* (23), 7856.

- (66) Bloch, E. D.; Queen, W. L.; Hudson, M. R.; Mason, J. A.; Xiao, D. J.; Murray, L. J.; Flacau, R.; Brown, C. M.; Long, J. R. *Angew. Chem. Int. Ed.* **2016**, *55* (30), 8605.
- (67) Bloch, E. D.; Murray, L. M.; Queen, W. L.; Chavan, S.; Maximoff, S. N.; Bigi, J. P.; Krishna, R.; Peterson, V. K.; Grandjean, F.; Long, G. J.; Smit, B.; Bordiga, S.; Brown, C. M.; Long, J. R. *J. Am. Chem. Soc.* **2011**, *133*, 14814.
- (68) Xiao, D. J.; Gonzalez, M. I.; Darago, L. E.; Vogiatzis, K. D.; Haldoupis, E.; Gagliardi, L.; Long, J. R. *J. Am. Chem. Soc.* **2016**, *138* (22), 7161.
- (69) Tulchinsky, Y.; Hendon, C. H.; Lomachenko, K. A.; Borfecchia, E.; Melot, B. C.; Hudson, M. R.; Tarver, J. D.; Korzyński, M. D.; Stubbs, A. W.; Kagan, J. J.; Lamberti, C.; Brown, C. M.; Dincă, M. *J. Am. Chem. Soc.* **2017**, *139* (16), 5992.
- (70) Denysenko, D.; Grzywa, M.; Jelic, J.; Reuter, K.; Volkmer, D. *Angew. Chem. Int. Ed.* **2014**, *53* (23), 5832.
- (71) Liao, P.-Q.; Zhu, A.-X.; Zhang, W.-X.; Zhang, J.-P.; Chen, X.-M. *Nat. Commun.* **2015**, *6* (1), 6350.
- (72) Tu, B.; Pang, Q.; Xu, H.; Li, X.; Wang, Y.; Ma, Z.; Weng, L.; Li, Q. *J. Am. Chem. Soc.* **2017**, *139*, 7998.
- (73) Sturge, M. D. *Solid State Phys.* **1968**, *20*, 91.
- (74) Liao, Y.; Zhang, L.; Weston, M. H.; Morris, W.; Hupp, J. T.; Farha, O. K. *Chem. Commun.* **2017**, *53* (67), 9376.
- (75) Ingleson, M. J.; Barrio, J.; Bacsá, J.; Dickinson, C.; Park, H.; Rosseinsky, M. J. *Chem. Commun.* **2008**, 1287.
- (76) Hush, N. T. *Faraday Soc.* **1961**, *57* (0), 557.
- (77) Gütlich, P.; Bill, E.; Trautwein, A. X. *Mössbauer Spectroscopy and Transition Metal Chemistry, Fundamentals and Applications*. Springer-Verlag Berlin Heidelberg: Berlin, **2011**.
- (78) Apart from having to obtain expensive synchrotron-generated  $^{57}\text{Co}$  from Russia.
- (79) Senkovska, I.; Bon, V. In *Situ X-ray Diffraction and XAS Methods*. In: *The Chemistry of Metal-organic Frameworks: Synthesis, Characterization, and Applications*. Wiley-VCH Verlag GmbH & Co.: Weinheim, Germany, **2016**.
- (80) van Bokhoven, J. A.; Lamberti, C., Ed. *X-Ray Absorption and X-Ray Emission Spectroscopy: Theory and Applications*. John Wiley & Sons, Ltd., **2016**.
- (81) Kurmoo, M. *Chem. Soc. Rev.* **2009**, *38* (5), 1353.
- (82) Espallargas, G.; Coronado, E. *Chem. Soc. Rev.* **2017**, *47* (2), 533.
- (83) Wade, C. R.; Li, M.; Dincă, M. *Angew. Chem. Int. Ed.* **2013**, *52* (50), 13377.
- (84) AlKaabi, K.; Wade, C. R.; Dincă, M. *Chem* **2016**, *1* (2), 264.
- (85) Narayan, T. C.; Miyakai, T.; Seki, S.; Dincă, M. *J. Am. Chem. Soc.* **2012**, *134* (31), 12932.
- (86) Park, S. S.; Hontz, E. R.; Sun, L.; Hendon, C. H.; Walsh, A.; Voorhis, T.; Dincă, M. *J. Am. Chem. Soc.* **2015**, *137* (5), 1774.
- (87) Xie, L. S.; Dincă, M. *Israel J. Chem.* **2018**, *58* (9–10), 1119.
- (88) Hua, C.; Doheny, P. W.; Ding, B.; Chan, B.; Yu, M.; Kepert, C. J.; Alessandro, D. *J. Am. Chem. Soc.* **2018**, *140* (21), 6622.
- (89) Abrahams, B. F.; Hudson, T. A.; McCormick, L. J.; Robson, R. *Cryst. Growth Des.* **2011**, *11* (7), 2717.
- (90) Luo, T.; Liu, Y.; Tsai, H.; Su, C.; Ueng, C.; Lu, K. *Eur J Inorg. Chem.* **2004**, *21*, 4253.
- (91) Huang, X.; Sheng, P.; Tu, Z.; Zhang, F.; Wang, J.; Geng, H.; Zou, Y.; Di, C.; Yi, Y.; Sun, Y.; Xu, W.; Zhu, D. *Nat. Commun.* **2015**, *6* (1), 7408.

- (92) Huang, X.; Yao, H.; Cui, Y.; Hao, W.; Zhu, J.; Xu, W.; Zhu, D. *ACS Appl. Mater. Inter.* **2017**, *9* (46), 40752.
- (93) Kambe, T.; Sakamoto, R.; Hoshiko, K.; Takada, K.; Miyachi, M.; Ryu, J.-H.; Sasaki, S.; Kim, J.; Nakazato, K.; Takata, M.; Nishihara, H. *J. Am. Chem. Soc.* **2013**, *135* (7), 2462.
- (94) Downes, C. A.; Clough, A. J.; Chen, K.; Yoo, J. W.; Marinescu, S. C. *ACS Appl. Mater. Inter.* **2017**, *10* (2), 1719.
- (95) Campbell, M. G.; Sheberla, D.; Liu, S. F.; Swager, T. M.; Dincă, M. *Angew. Chem. Int. Ed.* **2015**, *54* (14), 4349.
- (96) Campbell, M. G.; Liu, S. F.; Swager, T. M.; Dincă, M. *J. Am. Chem. Soc.* **2015**, *137* (43), 13780.
- (97) Miner, E. M.; Fukushima, T.; Sheberla, D.; Sun, L.; Surendranath, Y.; Dincă, M. *Nat. Commun.* **2016**, *7* (1), 10942.
- (98) Sheberla, D.; Bachman, J. C.; Elias, J. S.; Sun, C.-J.; Shao-Horn, Y.; Dincă, M. *Nat. Mater.* **2016**, *16*, 220.
- (99) Sun, L.; Liao, B.; Sheberla, D.; Kraemer, D.; Zhou, J.; Stach, E. A.; Zakharov, D.; Stavila, V.; Talin, A. A.; Ge, Y.; Allendorf, M.D.; Chen, G.; Léonard, F.; Dincă, M. *Joule* **2017**, *1* (1), 168.
- (100) Miner, E. M.; Wang, L.; Dincă, M. *Chem. Sci.* **2018**, *9* (29), 6286.
- (101) Campbell, M. G.; Dincă, M. *Sensors* **2017**, *17* (5), 1108.
- (102) Aubrey, M. L.; Kapelewski, M. T.; Melville, J. F.; Oktawiec, J.; Presti, D.; Gagliardi, L.; Long, J. R. *J. Am. Chem. Soc.* **2019**, *141*, 5005.
- (103) López-Cabrelles, J.; Romero, J.; Abellán, G.; Giménez-Marqués, M.; Palomino, M.; Valencia, S.; Rey, F.; Espallargas, G. *J. Am. Chem. Soc.* **2019**, *141* (17), 7173.
- (104) Barth, B.; Mendt, M.; Pöppel, A.; Hartmann, M. *Micropor. Mesopor. Mat.* **2015**, *216*, 97.
- (105) Bloch, E. D.; Queen, W. L.; Chavan, S.; Wheatley, P. S.; Zadrozny, J. M.; Morris, R.; Brown, C. M.; Lamberti, C.; Bordiga, S.; Long, J. R. *J. Am. Chem. Soc.* **2015**, *137* (10), 3466.
- (106) Li, L.; Lin, R.-B.; Krishna, R.; Li, H.; Xiang, S.; Wu, H.; Li, J.; Zhou, W.; Chen, B. *Science* **2018**, *362* (6413), 443.
- (107) Mendecki, L.; Ko, M.; Zhang, X.; Meng, Z.; Mirica, K. A. *J. Am. Chem. Soc.* **2017**, *139* (48), 17229.
- (108) Eddaoudi, M.; Moler, D. B.; Li, H.; Chen, B.; Reineke, T. M.; O’Keeffe, M.; Yaghi, O. M. *Accounts Chem. Res.* **2001**, *34* (4), 319.
- (109) Rosi, N. L.; Eckert, J.; Eddaoudi, M.; Vodak, D. T.; Kim, J.; O’Keeffe, M.; Yaghi, O. M. *Science* **2003**, *300* (5622), 1127.
- (110) Park, J.; Howe, J. D.; Sholl, D. S. *Chem. Mater.* **2017**, *29*, 10487.
- (111) Stock, N.; Biswas, S. *Chem. Rev.* **2012**, *112* (2), 933.
- (112) Spiess, A.-N.; Neumeyer, N. *BMC Pharmacol.* **2010**, *10* (1), 6.
- (113) Langmuir, I. *J. Am. Chem. Soc.* **1918**, *40* (9), 1361.
- (114) Freundlich, H. *Kapillarchemie, Eine Darstellung Der Chemie Der Kolloide Und Verwandter Gebiete.* **1909**.
- (115) Myers, A.; Prausnitz, J. *AICHE J.* **1965**, *11* (1), 121.
- (116) Walton, K. S.; Sholl, D. S. *AICHE J.* **2015**, *61* (9), 2757.

# Chapter 2: Improving O<sub>2</sub> Adsorption Properties of a Redox-Active Open Metal Site via Templating Mixed-Metal Distribution

## 2.1 Introduction

The industrial separation of small molecules with similar physical properties consumes an enormous quantity of energy due in part to the heavy reliance on large and costly distillation columns.<sup>1,2</sup> The use of chemiselective adsorbents has often been proposed as an alternative separation method, one which requires adsorbents to have high selectivity, capacity, and stability in order to be industrially viable.<sup>3,4</sup> Metal–organic frameworks have emerged as a promising class of materials for these separations due in part to the possibility of controlling the properties of binding sites to target selective adsorbate-framework interactions.<sup>5–8</sup> Following this strategy, various systems have recently been reported with high selectivities for a variety of important separations such as O<sub>2</sub>/N<sub>2</sub>,<sup>9–11</sup> olefin/paraffin,<sup>12</sup> carbon capture,<sup>13</sup> etc.<sup>14,15</sup> In particular, M<sub>2</sub>(dobdc) (M = Mg, Mn, Fe, Co, Ni, Cu, Zn, Cd; dobdc<sup>4-</sup> = 2,5-dioxido-1,4-benzenedicarboxylate) and isorecticular analogues have been the subject of numerous studies in part because of their privileged status as adsorbents with the highest density of coordinatively-unsaturated metal sites, both volumetrically and gravimetrically.<sup>16–19</sup> This family of frameworks is characterized by a honeycomb lattice of hexagonal one-dimensional pores with salicylate-derived helical metal chains at the vertices. Each of these one-dimensional metal chains consists of octahedral divalent metal cations that can be post-synthetically activated by removing a coordinated solvent molecule, leaving a square pyramidal species with an exposed empty coordination site.<sup>16,20,21</sup> These “open metal sites” found within the M<sub>2</sub>(dobdc) family of frameworks confer some of the highest selectivities and capacities reported in metal frameworks for a variety of small molecules, due to strong selective interactions with guests.<sup>18,22–28</sup>

Fe<sub>2</sub>(dobdc), for example, was one of the first metal–organic frameworks reported to selectively and reversibly adsorb O<sub>2</sub>.<sup>29</sup> Due to the current high cost associated with the cryogenic distillation of O<sub>2</sub> from air (~78% N<sub>2</sub>, ~21% O<sub>2</sub>), there is high demand for a more energy-efficient separation process. While N<sub>2</sub> selective species have had some success industrially, these materials are limited by low selectivity and the economics/logistics of selectively removing the major component of a mixture.<sup>30</sup> Despite the clear incentives, there is a dearth of O<sub>2</sub> selective adsorbents. In Fe<sub>2</sub>(dobdc), selective chemisorption of O<sub>2</sub> occurs via an electron transfer from an Fe<sup>II</sup> open metal site to O<sub>2</sub> forming a Fe<sup>III</sup>–superoxide adduct. Above 220 K, the infinite chains of Fe<sup>III</sup>–superoxides in the framework undergo disproportionation, forming a Fe<sup>III</sup>–peroxide species and an empty Fe<sup>III</sup> open metal site, restricting the reversible process to low temperatures. This thermal limitation presents a major downside to a material designed to alleviate the current dependence on costly cryogenic distillation. The disproportionation in Fe<sub>2</sub>(dobdc)(O<sub>2</sub>)<sub>2</sub> is presumed to occur via a thermally activated electron transfer facilitated by a high degree of electronic communication between adjacent iron cations. Isolation of these highly reducing iron open metal sites from one another by replacing every other site with redox inert metal ions could potentially prevent this deleterious electronic communication and increase the thermal stability of this material. However, this would require not only that the material have multiple metals incorporated into the structure, but also that

these metals be arranged in a specific alternating order to prevent adjacent iron sites from undergoing irreversible disproportionation in the presence of O<sub>2</sub> at elevated temperatures.

Incorporation of multiple metal species into one framework to engender improved or novel properties, is a rapidly expanding area of research in field of metal–organic frameworks. The concept of combining multiple isorecticular metal–organic frameworks into one, sometimes referred to as multivariate- or MTV-MOFs,<sup>31</sup> has been proposed previously for both mixed-metal and mixed-ligand systems.<sup>32–34</sup> The M<sub>2</sub>(dobdc) structural family itself has been the focus of numerous mixed-metal studies due in part to the large variety of isostructural metal analogues.<sup>35–40</sup> Mixed-metal MM'(dobdc) systems have been shown to possess improved catalytic activity,<sup>41–43</sup> exhibit stronger binding of H<sub>2</sub>,<sup>44,45</sup> improved selectivity for 1-hexene over hexane,<sup>46</sup> and tunable binding of water.<sup>47</sup> Additionally, MM'(dobdc) systems are some of the most widely used sacrificial metal–organic framework precursors for bimetallic hierarchical porous carbons.<sup>48–56</sup> However, the goal of local metal arrangement is more elusive. In general, MM'(dobdc) family frameworks are treated as a solid solution of the two metal cations, without large phase segregation,<sup>36</sup> and with no pretext of knowing local metal distribution except in cases of assumed infinite dilution.<sup>57</sup> In fact, the vast majority of bimetallic studies across all metal–organic frameworks do not provide insight into local metal distribution beyond micron-scale energy-dispersive X-ray spectroscopy measurements. The few examples that exist of well characterized local metal distributions rely on systems with discrete, or zero-dimensional, multinuclear structural nodes. These studies utilize in situ techniques such as NMR and X-ray adsorption spectroscopy to differentiate elemental arrangement based on the interactions of a few metal atoms.<sup>58–60</sup>

When a framework has an inorganic building unit that is not zero-dimensional, such as is the case for M<sub>2</sub>(dobdc), the system becomes substantially more complicated. Recently Coskun et al proposed a synthetic route that would generate 50/50 bimetallic systems, MZn(dobdc) (M = Mg or Ni), with alternating metal cations along the helical chains.<sup>61</sup> This route relies on the use of a coordination solid, Zn(H<sub>2</sub>dobdc)(H<sub>2</sub>O)<sub>2</sub>, as an insoluble templating precursor; however, no direct evidence of local ordering was reported. Such unprecedented control of the local ordering of cations within an infinite one-dimensional chain is truly tantalizing; it could be both leveraged and substantiated by designing a material that demonstrates properties that would not arise from a mixed-metal system with either a stochastic or phase-segregated metal distribution. In particular, the O<sub>2</sub> adsorption properties of Fe<sub>2</sub>(dobdc) could be greatly improved in a templated bimetallic system, as electronic isolation of each iron center would prevent the electron transfer step in the superoxide-to-peroxide disproportionation thereby allowing for higher-temperature reversible O<sub>2</sub> adsorption.

## 2.2 Experimental

### Materials and Synthesis

All material syntheses and sample manipulations, unless otherwise stated, were performed under an oxygen-free atmosphere: with an argon Schlenk line, in an argon-filled inert glovebox, or in a water compatible anaerobic glovebox hereafter referred to as the “water box.” This “water box” consists of a standard Vac pressurized glove box retrofitted with a Coy Lab Products unheated catalyst fan box and palladium on alumina catalyst, with an atmosphere of 95/5 N<sub>2</sub>/H<sub>2</sub>, with > 20% relative humidity and up to ppm levels of O<sub>2</sub>. Starting materials FeSiF<sub>6</sub>·6H<sub>2</sub>O and

$\text{Zn}(\text{H}_2\text{dobdc})(\text{H}_2\text{O})_2$  were synthesized according to reported procedures.<sup>62,63</sup>  $\text{Fe}_2(\text{dobdc})$  was synthesized and activated according to reported procedures.<sup>29</sup>

The templated framework **Fe–Zn(dobdc)** was synthesized by first dissolving 1131 mg (3.697 mmol, ~1.1 eq.) of white-green  $\text{FeSiF}_6 \cdot 6\text{H}_2\text{O}$  in the “water box” in 12.5 mL of water, from a Milli-Q water purification system. This colorless solution was added to a light-yellow suspension of 1000 mg (3.361 mmol, ~1 eq.) of finely ground  $\text{Zn}(\text{H}_2\text{dobdc})(\text{H}_2\text{O})_2$  in 225 mL N,N-dimethylformamide (DMF) and 12.5 mL ethanol in a 500 mL Schlenk flask with a stir bar. The reaction flask was sealed, transferred out of the water box and onto a Schlenk line. It was then placed in a preheated 75 °C oil bath while stirring for three hours. Upon heating there is a rapid color change of the suspension from light yellow to orange. Subsequently, the reaction was transferred back into the water box, the reaction mixture was transferred into a 500 mL jar, and the supernatant was decanted. The resulting solid was washed thrice with ~400 mL of DMF at 100 °C and thrice with ~400 mL of methanol at 60 °C. After washing, the solid was filtered and activated under dynamic vacuum at 160 °C for ~16 hours yielding 790 mg (2.5 mmol, 74% yield) of **Fe–Zn(dobdc)**, a seafoam green microcrystalline powder. Fe/Zn ratio obtained from ICP-OES measurements was found to be 0.90/1.10 Fe/Zn.

The nontemplated framework **Fe~Zn(dobdc)** was synthesized by dissolving 896 mg (3.179 mmol, ~1 eq.) of  $\text{Fe}(\text{O}_2\text{CCF}_3)_2$  and 1562 mg (4.770 mmol, ~1.5 eq.) of  $\text{Zn}(\text{O}_2\text{CCF}_3)_2(\text{H}_2\text{O})_2$  in a mixture of 270 mL DMF, 15 mL ethanol, and 15 mL Millipore water in a 500 mL Schlenk flask with a stir bar yielding a yellow solution. To this solution, 630 mg (3.180 mmol, ~1 eq.) of  $\text{H}_4\text{dobdc}$  was added. The reaction flask was sealed, transferred out of the water box and onto a Schlenk line. It was then placed in an oil bath and rapidly heated to 120 °C while stirring for 12 hours. During heating, a dark red-brown precipitate gradually forms. Subsequently, the reaction was transferred back into the water box, the reaction mixture was transferred into a 500 mL jar, and the supernatant was decanted. The resulting solid was washed thrice with ~400 mL of DMF at 100 °C and thrice with ~400 mL of methanol at 60 °C. After washing, the solid was filtered and activated under dynamic vacuum at 160 °C for ~16 hours yielding 430 mg (1.36 mmol, 43% yield) of **Fe~Zn(dobdc)**, a pale yellow-green microcrystalline powder. Fe/Zn ratio obtained from ICP-OES measurements was found to be 0.88/1.12 Fe/Zn.

## DRIFTS Measurements

Diffuse Reflectance Infrared Fourier Transform Spectra were collected using a Bruker Vertex 70 spectrometer equipped with a glowbar source, KBr beamsplitter, and a liquid nitrogen cooled mercury-cadmium-telluride detector. A custom-built diffuse reflectance system with an IR-accessible gas dosing cell was used for all measurements. Sample temperature was controlled by an Oxford Instruments OptistatDry TLEX cryostat, and sample atmosphere was controlled by a Micromeritics ASAP 2020Plus gas sorption analyzer. In a typical experiment, activated framework material was dispersed in dry KBr (~10 wt%) in an argon-filled glovebox and evacuated at room temperature overnight. Spectra were collected *in situ* under UHP-grade  $\text{O}_2$  and  $^{18}\text{O}_2$  (99 atom %  $^{18}\text{O}$ , Sigma-Aldrich) at 4  $\text{cm}^{-1}$  resolution under each temperature and pressure continually until equilibrium was observed.

## Gas Sorption Measurements

Isothermal measurements were performed using a Micromeritics 3Flex Surface Characterization Analyzer. For each framework, ~50 mg of preactivated material was loaded into

a preweighed ½” glass sample tube inside an argon glove box. Each tube was sealed with a Mircomeritics *Transeal* in order to properly perform gas sorption measurements without risking exposure to air. Adsorption measurements were performed with N<sub>2</sub> at 159, 178, and 195 K and with O<sub>2</sub> at 159, 178, 195, and 273 K. A variety of cooling baths were used to maintain temperature: a slurry of frozen ethanol for 159 K, a slurry of frozen acetone for 178 K, a dry ice/isopropanol bath for 195 K, and an ice/water bath for 273 K. In order to ensure no irreversible reaction with O<sub>2</sub>, after collection of isotherms at 159, 178, and 195 K, samples were left under dynamic vacuum in the cooling baths for 12 hours before allowing to warm to ambient temperature.

### **In situ Powder X-ray Diffraction**

High-resolution powder X-ray diffraction patterns were collected at Beamline 17-BM-B at the Advanced Photon Source of Argonne National Laboratory, with an average wavelength of 0.72768 Å. Scattered intensity was recorded by a PerkinElmer a-Si Flat Panel detector. Prior to measurement, samples were packed in borosilicate glass capillaries of 1.0 mm diameter under a N<sub>2</sub> atmosphere. Each capillary was attached to a custom-designed gas-dosing cell equipped with a gas valve, which was then mounted onto the goniometer head and connected to a gas-dosing manifold for in situ diffraction measurements. Sample temperature was controlled by an Oxford CryoSystems Cryo-stream 800.

### **Mössbauer Spectroscopy**

Zero-field <sup>57</sup>Fe Mössbauer spectra were recorded in constant acceleration spectrometer (See Co. Edina, MN) between room temperature and 5 K in a Janis Research Co. cryostat (Willington, MA). Collected spectra were analyzed using the WMOSS software package (See Co. Edina, MN). Isomer shifts are reported relative to  $\alpha$ -iron (30  $\mu$ m foil) at 295 K. For each of the three frameworks: **Fe<sub>2</sub>(dobdc)**, **Fe–Zn(dobdc)**, and **Fe~Zn(dobdc)**, approximately 20–30 mg of activated framework was placed in a nylon washer with an area of ~1.3 cm<sup>2</sup>, and carefully sealed between multiple layers of Scotch packing tape in an argon glovebox. The protected samples were transferred rapidly in air into the spectrometer under a flow of helium and were measured under a small pressure of helium in the cryostat. With the exception of 5 K Fe<sub>2</sub>(dobdc), all other spectra were fit to two Lorentzian doublets.

### **Magnetic Measurements**

Samples were prepared in a N<sub>2</sub> glove box by adding ~25mg of crystalline powder of activated framework to a 5 mm i.d. / 7 mm o.d. quartz tube containing a raised quartz platform. Borosilicate glass wool was added to immobilize the sample in order to prevent crystallite torqueing of the loose powder. The tube was fitted with a Teflon sealable adapter, evacuated on a Schlenk line while submerged in liquid N<sub>2</sub>, and flame-sealed under static vacuum. Magnetic susceptibility measurements were performed using a Quantum Design MPMS-XL SQUID magnetometer.

## **2.3 Results and Discussion**

### **Synthesis of Bimetallic Frameworks**

The templated bimetallic framework **Fe–Zn(dobdc)** was targeted in order to improve the O<sub>2</sub> adsorption properties of **Fe<sub>2</sub>(dobdc)**. A bimetallic system with alternating Fe<sup>II</sup> and Zn<sup>II</sup> ions down the one-dimensional metal chains of this structure family should dramatically increase the barrier for charge transfer between open metal sites by removing any possible orbital overlap thereby

increasing the electron hopping distance. Electronically isolated  $\text{Fe}^{\text{II}}$  sites would therefore be able to reduce  $\text{O}_2$  to superoxide, while subsequent irreversible peroxide formation at high temperatures would be disfavored (**Figure 2.1**). Synthesis of **Fe–Zn(dobdc)** was adapted from the route previously reported by Coskun et al. to generate  $\text{MZn(dobdc)}$  ( $\text{M} = \text{Mg}$  or  $\text{Ni}$ ) with proposed alternating metal ions down the one-dimensional chains.<sup>61</sup> This reported route utilized a solid-to-solid transformation: reacting crystalline  $\text{Zn}(\text{H}_2\text{dobdc})(\text{H}_2\text{O})_2$  as a templating agent with a secondary metal nitrate in a DMF containing solution at  $120\text{ }^\circ\text{C}$  for 3 hours. I designed and optimized a new variation of this synthetic scheme in order to incorporate  $\text{Fe}^{\text{II}}$  ions without oxidation, and to prevent excess or deficient secondary metal ion incorporation towards the realization of a highly-ordered bimetallic phase (**Scheme 2.1**).

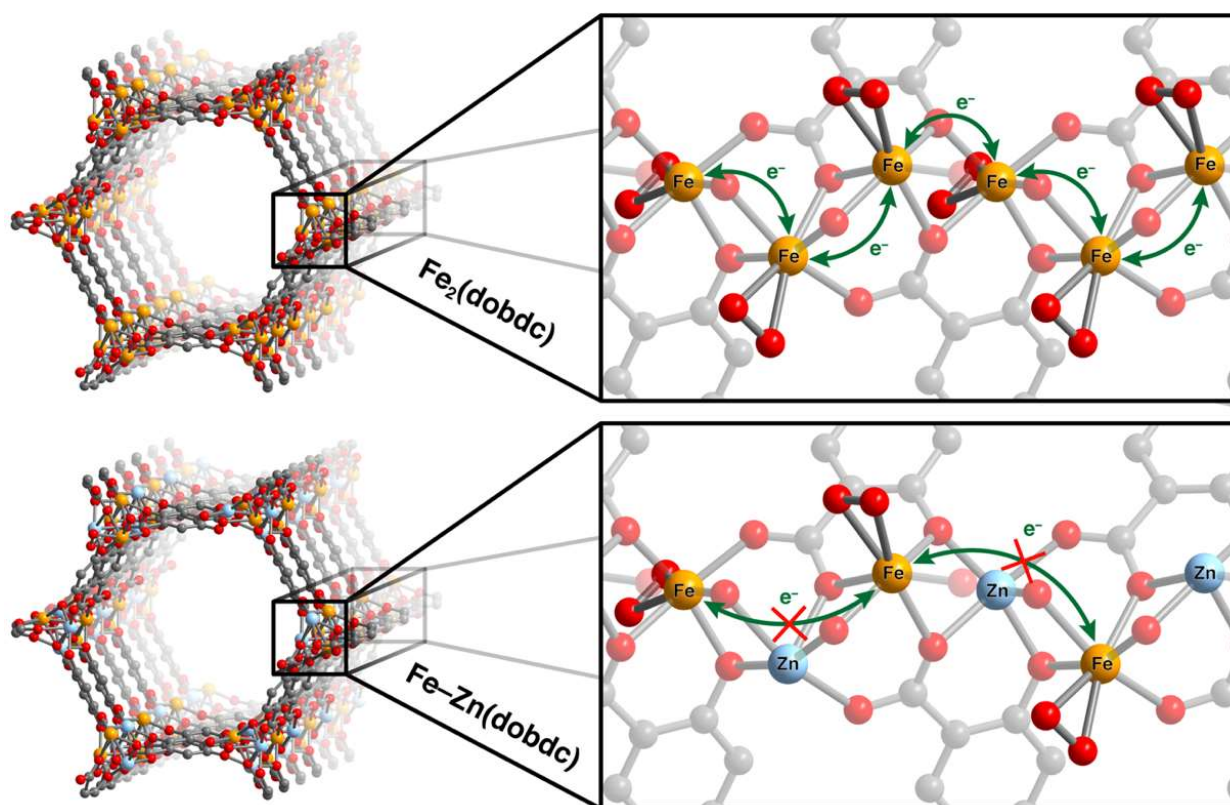


**Figure 2.1:** Crystal structure of  $\text{Fe}_2(\text{dobdc})$  (Top Left) and hypothetical structure of templated  $\text{Fe-Zn(dobdc)}$  (Bottom Left) with view down the  $c$ -axis showing hexagonal 1D pore. (Right) Views of  $\text{O}_2$  dosed helical metal chains down a pore wall with perpendicular ligands removed for clarity. (Top Right) Possible charge transfer pathway between iron-superoxide species in  $\text{Fe}_2(\text{dobdc})$ . (Bottom Right) Proposed elimination of charge transfer between iron-superoxide species in  $\text{Fe-Zn(dobdc)}$  through templated alternating metal distribution.

While the solubility of  $\text{Zn}(\text{H}_2\text{dobdc})(\text{H}_2\text{O})_2$  is very low in most solvents, including DMF, some dissolution must occur in order for the formation of  $\text{Zn}_2(\text{dobdc})$  to occur as was previously reported, as there is no other source of  $\text{Zn}^{2+}$  ions. Free ligand in solution, most likely partially deprotonated, can react with both  $\text{Fe}^{2+}$  and  $\text{Zn}^{2+}$  ions in solution to give non-templated  $\text{Fe}_x\text{Zn}_{2-x}(\text{dobdc})$ . As most of the ions in solution are  $\text{Fe}^{2+}$ , this process will primarily yield all iron



a microcrystalline powder. It is worth noting that because this synthesis necessarily involves the combination of water containing species and O<sub>2</sub> sensitive species, extensive screening of reaction conditions was greatly facilitated by the use of a water-compatible anaerobic glove box.

For the sake of comparison, the synthesis of a nontemplated Fe/Zn bimetallic system was required. A one-pot synthetic approach was chosen as it has been previously proposed to generate a “solid-solution” or random distribution of metals. A completely random distribution of metal sites in a Fe<sub>x</sub>Zn<sub>2-x</sub>(dobdc) system, however, would have very few iron sites isolated by zinc sites on both sides. From a simple probabilistic model of a completely stochastic distribution, the maximum number of isolated iron sites would be capped at ~14.8% (**Figure 2.2**). To directly compare to the templated system **Fe–Zn(dobdc)**, Zn(O<sub>2</sub>CCF<sub>3</sub>)<sub>2</sub> and Fe(O<sub>2</sub>CCF<sub>3</sub>)<sub>2</sub> were reacted in an optimized ratio with H<sub>4</sub>(dobdc) solvothermally to yield a nontemplated Fe<sub>0.88</sub>Zn<sub>1.12</sub>(dobdc), **Fe~Zn(dobdc)**.

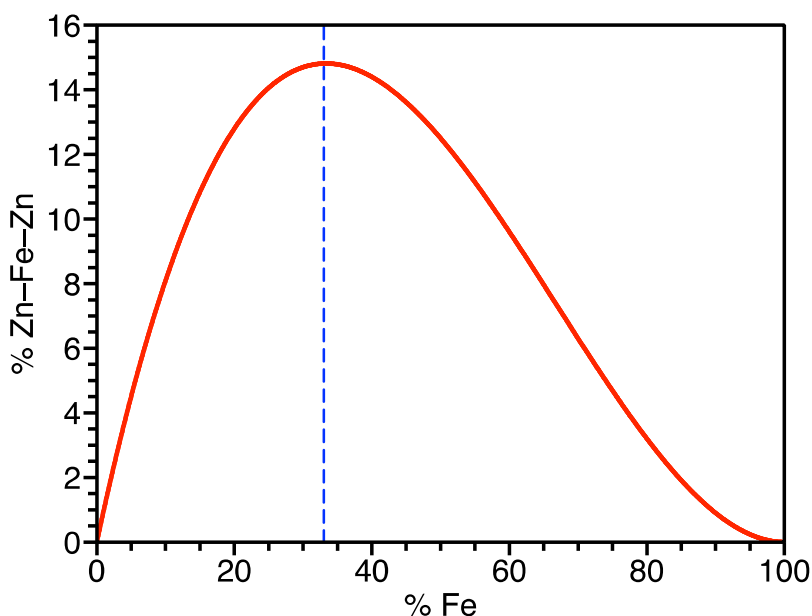


**Figure 2.2:** For a material Fe<sub>2x</sub>Zn<sub>2(1-x)</sub>(dobdc) with completely random distribution, the probability of desired metal distribution Zn–Fe–Zn is calculated as (1-x)×(x)×(1-x), shown in red. The maximum would occur at 1:2 Fe:Zn (dotted blue line).

### Characterization of Bimetallic Frameworks

X-ray powder diffraction of solvent washed and activated **Fe–Zn(dobdc)** confirms that it is isostructural to Fe<sub>2</sub>(dobdc). Pawley refinements in the space group R $\bar{3}$  revealed a unit cell with a volume of 4003 Å<sup>3</sup> in between that of **Fe<sub>2</sub>(dobdc)** under identical conditions (4050 Å<sup>3</sup>) and previously reported Zn<sub>2</sub>(dobdc) (3957 Å<sup>3</sup>). A similarly smaller unit cell volume is also observed in the nontemplated bimetallic system **Fe~Zn(dobdc)** (3991 Å<sup>3</sup>) which has a similar Fe/Zn ratio as the templated framework. I was unable to find any evidence of a supercell or lowered symmetry in **Fe–Zn(dobdc)**. This is to be expected for two reasons: 1. while I propose to generate ordered heterobimetallic chains of alternating –Fe–Zn– units, the reaction mechanism does not impose any ordering of one helical chain with respect to an adjacent one. As such, it is possible to maintain local order within each chain while having disordered Fe/Zn positions over the whole unit cell.

2. among all of published mixed metal  $MM'(dobdc)$  materials, metal ion substitution in the helical chain has not been reported to cause a substantial distortion to the structure so as to induce a change in symmetry.

*In-situ* DRIFTS was used to directly probe the interaction of an iron open metal site with  $O_2$ . Dosing of activated **Fe–Zn(dobdc)** with  $O_2$  at 195 K results in a peak at  $2236\text{ cm}^{-1}$  (**Figure 2.3**). A nearly identical peak is also observed under similar conditions in **Fe–Zn(dobdc)** (**Figure 2.S7**) and **Fe<sub>2</sub>(dobdc)** (**Figure 2.S8**) and is consistent with the previously reported vibrational overtone for superoxide bound to an  $Fe^{III}$  site in  $Fe_2(dobdc)(O_2)_2$ ,  $2238\text{ cm}^{-1}$ . The expected fundamental stretch previously reported at  $1129\text{ cm}^{-1}$  is not readily distinguished due to overlap with shifting framework vibrations as the material is oxidized. In order to unambiguously assign this species, the material was dosed with  $^{18}O_2$ ; a peak at  $2112\text{ cm}^{-1}$  was observed in lieu of the peak at  $2236\text{ cm}^{-1}$ , consistent with an isotopic shift approximated by a simple harmonic oscillator. Using the  $^{18}O_2$ -dosed spectrum as a baseline for the  $^{16}O_2$ -dosed spectrum, vibrational signals resulting from changes in the framework are removed and only signals attributed to adsorbed  $O_2$  species remain (**Figure 2**). The resulting difference spectrum clearly shows the fundamental stretch for both  $^{16}O_2$  and  $^{18}O_2$ ,  $1125$  and  $1063\text{ cm}^{-1}$ , respectively, thereby confirming the mechanism of adsorption in **Fe–Zn(dobdc)** to be analogous of that in  $Fe_2(dobdc)$ .

Variable-temperature infrared spectroscopy is a well-established technique in determining site-specific thermodynamics of adsorption.<sup>65</sup> For **Fe–Zn(dobdc)**, employing the aforementioned isotopic background subtraction yields spectra in which changes in both background and features arising due to framework structural vibrations are cancelled out, allowing  $Fe^{III-16}O_2^-$  and  $Fe^{III-18}O_2^-$  overtones to be clearly observed over a flat baseline and enabling thermodynamic analysis to be applied (**Figure 2.4**). Van't Hoff plots were generated for both  $^{16}O_2$  and  $^{18}O_2$ , yielding enthalpies of adsorption of approximately  $-40\text{ kJ/mol}$  for both. This value is in good agreement with the previously reported value of  $-41\text{ kJ/mol}$  for  $O_2$  in  $Fe_2(dobdc)$ , indicating that the iron sites in **Fe–Zn(dobdc)** retain the low temperature  $O_2$  reactivity exhibited by the monometallic framework. I would like to emphasize that binding enthalpy calculated through this method more accurately represents that of the gas molecules at a specific site because it is directly probing a specific species, as compared to enthalpies calculated by fitting equilibrium gas sorption measurements, which probe the sum of multiple interactions.

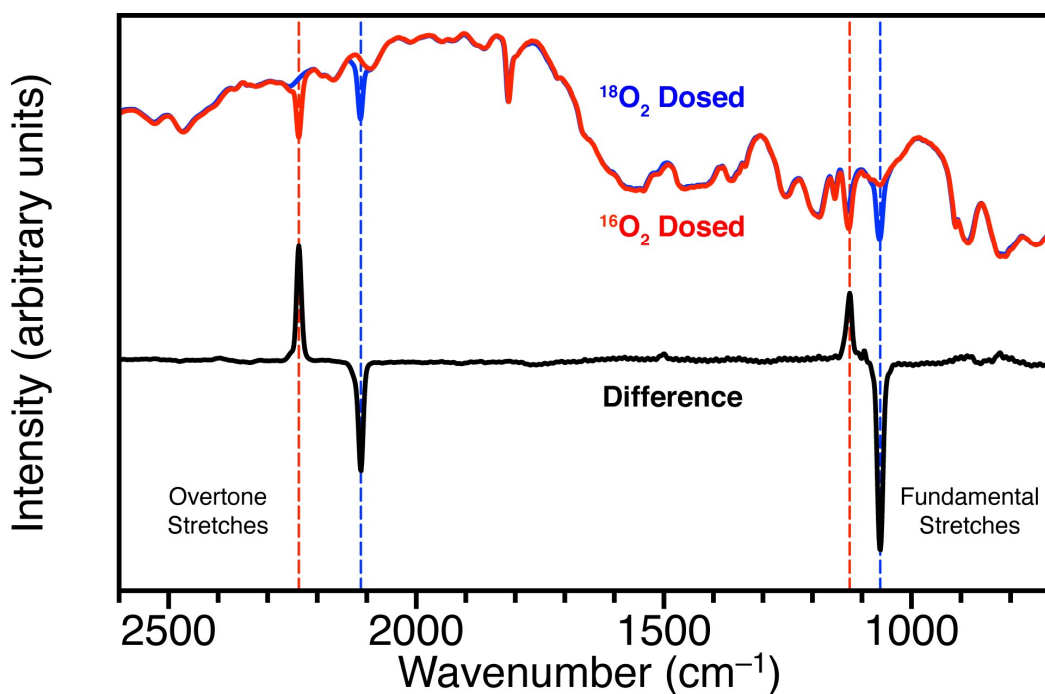
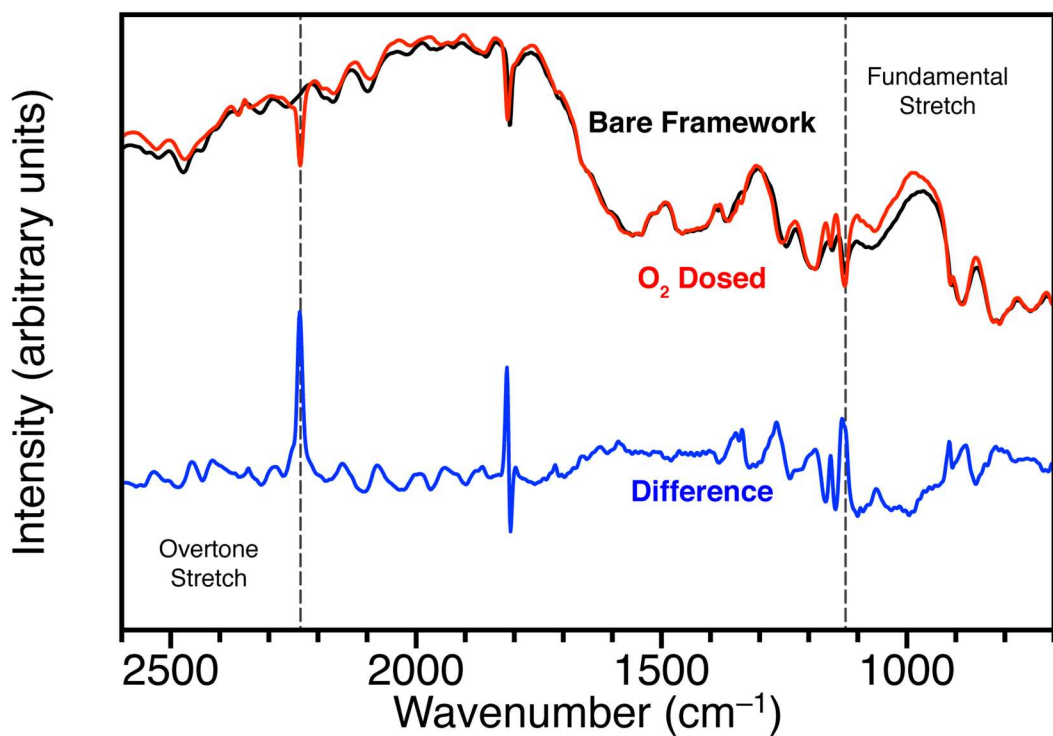


**Figure 2.3:** (Top) DRIFTS spectra of activated  $\text{Fe-Zn(dobdc)}$  in black,  $\text{O}_2$  dosed  $\text{Fe-Zn(dobdc)}$  in red, and a difference spectrum in blue. (Bottom) DRIFTS spectra of  $^{16}\text{O}_2$  dosed  $\text{Fe-Zn(dobdc)}$  in red,  $^{18}\text{O}_2$  dosed  $\text{Fe-Zn(dobdc)}$  in blue, and a difference spectrum in black. Samples were held under 10 mbar  $\text{O}_2$  at 195 K.

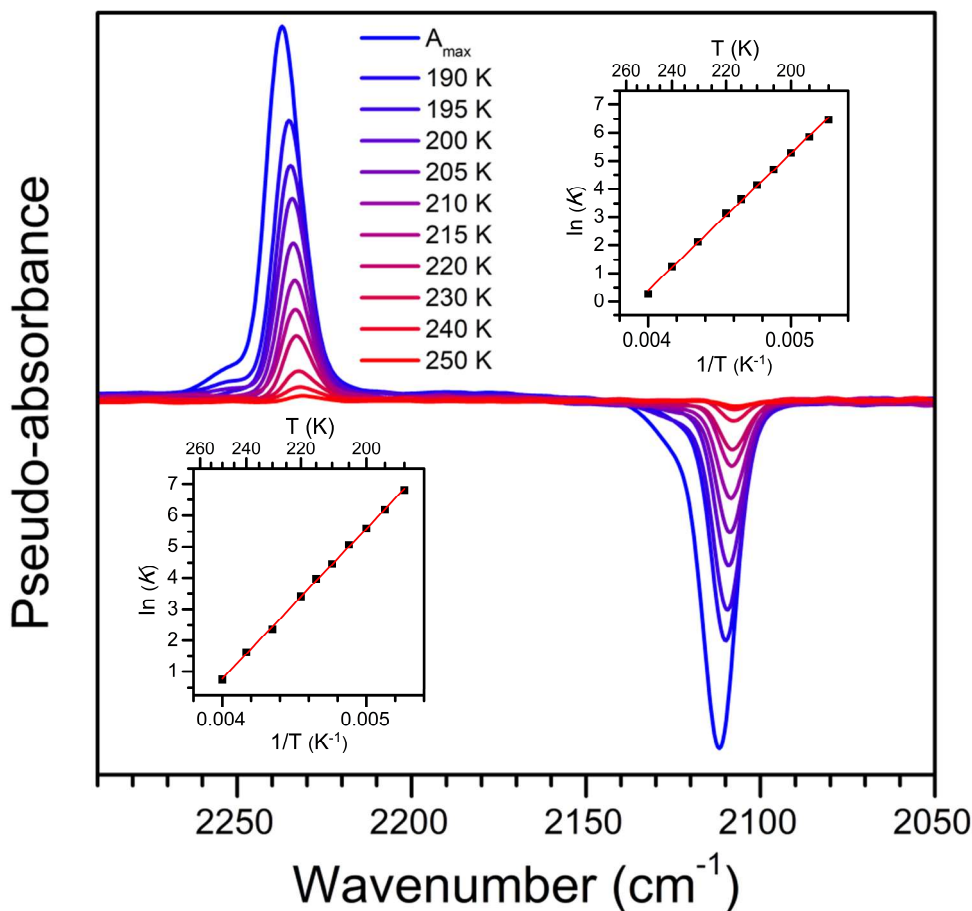


**Figure 2.4:** Variable temperature difference DRIFTS spectra of superoxide overtone stretch for  $^{16}\text{O}_2$  dosed  $\text{Fe-Zn(dobdc)}$  (top left, positive peaks) and  $^{18}\text{O}_2$  dosed  $\text{Fe-Zn(dobdc)}$  (bottom right, negative peaks). Van't Hoff plot insets for equilibrium data comparing peak area to maximum measure for  $^{16}\text{O}_2$  (bottom left inset) and  $^{18}\text{O}_2$  (top right inset).

Gas sorption measurements also suggest that at low temperatures, the iron open metal sites in both templated and nontemplated bimetallic systems behave like those of  $\text{Fe}_2(\text{dobdc})$ .  $\text{N}_2$  and  $\text{O}_2$  isotherms were collected at 195, 178, and 159 K for  $\text{Fe-Zn(dobdc)}$ ,  $\text{Fe-Zn(dobdc)}$ , and  $\text{Fe}_2(\text{dobdc})$  (Figures 2.S1–2.S6).  $\text{Fe-Zn(dobdc)}$ , for example, exhibits strong  $\text{O}_2$  binding and weak nitrogen uptake, consistent with gas sorption behavior seen in  $\text{Fe}_2(\text{dobdc})$  (Figure 2.5). To quantitatively compare each material, data from all three temperatures were simultaneously fit to multisite Langmuir-Freundlich isotherm models (Equation 2.1): three-site for the bimetallic systems and two-site for  $\text{Fe}_2(\text{dobdc})$  (Table 2.S1). Freely refining the ratio of the two strongest binding sites for the bimetallic system yields fits with minimized root mean square deviation exhibited ratios consistent with the ICP-OES measured Fe:Zn ratios (Tables 2.S2 and 2.S3), supporting a model where each unsaturated metal center is represented by a corresponding strong adsorption site. This designation is further supported by the similar  $\text{O}_2$  and  $\text{N}_2$  binding enthalpies calculated across all three modeled iron sites and both modeled zinc sites. Additionally, the enthalpies calculated for the iron sites are consistent with both previously reported values and those

obtained via infrared spectroscopy (**Table 2.1**). Such similarities in site binding enthalpies across all materials suggests that at lower temperatures, each open metal site in either pure or mixed metal  $M_2(\text{dobdc})$  can be treated as isolated units. Previous studies have theoretically demonstrated this invariant behavior for water adsorption in other metal analogs of  $M_2(\text{dobdc})$ .<sup>36</sup>

$$\sum_{n=1} q_{sat_n} \frac{e^{\frac{-\Delta H_n + \Delta S_n}{RT} \cdot P^{\nu_n}}}{1 + e^{\frac{-\Delta H_n + \Delta S_n}{RT} \cdot P^{\nu_n}}} \quad (2.1)$$

Multi-site Langmuir-Freundlich equation used to fit gas sorption isotherms.  $q_{sat}$  : Saturation capacity of site.  $\Delta H$  : Binding enthalpy of gas onto site.  $\Delta S$  : Binding entropy of gas onto site.  $R$  : Gas Constant.  $T$  : Temperature.  $P$  : Pressure.  $\nu$  : Freundlich Parameter

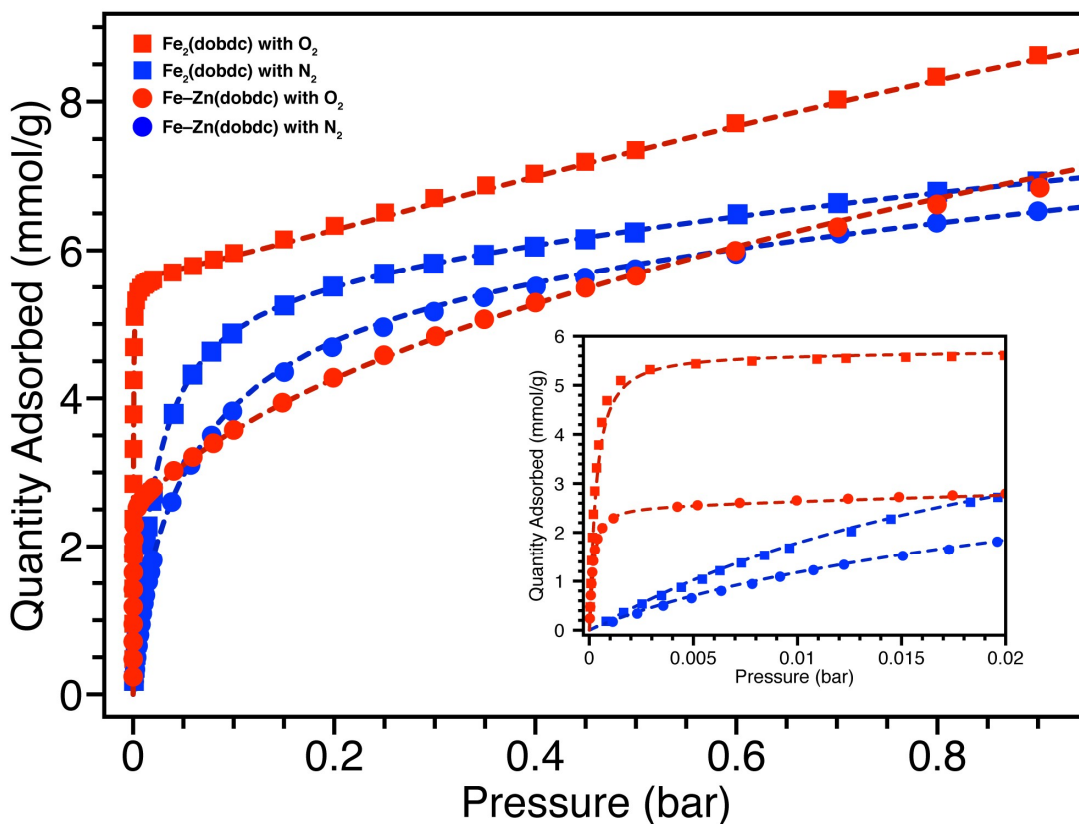


**Figure 2.5:** Gas Sorption isotherms of  $\text{Fe}_2(\text{dobdc})$  (squares) and  $\text{Fe-Zn}(\text{dobdc})$  (circles) for  $\text{O}_2$  (red) and  $\text{N}_2$  (blue) at 178 K with low pressure region magnified (inset). Multisite Langmuir-Freundlich fits from simultaneously fitting multiple temperatures are shown as dashed lines.

**Table 1.1:** Calculated binding enthalpies for O<sub>2</sub> and N<sub>2</sub> onto the open metal sites found in **Fe<sub>2</sub>(dobdc)**, **Fe~Zn(dobdc)**, **Fe–Zn(dobdc)**. \*This work, calculated from gas sorption data. †This work, calculated from DRIFTS data

Open Metal Site	$\Delta H$ for O <sub>2</sub> Binding (kJ/mol)	$\Delta H$ for N <sub>2</sub> Binding (kJ/mol)
Fe in <b>Fe<sub>2</sub>(dobdc)</b>	<b>-39.3*</b> <b>-41.0</b>	<b>-25.5*</b> <b>-23.0</b>
Fe in <b>Fe–Zn(dobdc)</b>	<b>-41.4*</b> <b>-40.0†</b>	<b>-23.6*</b> -
Fe in <b>Fe~Zn(dobdc)</b>	<b>-41.0*</b>	<b>-23.6*</b>
Zn in <b>Fe–Zn(dobdc)</b>	<b>-16.9*</b>	<b>-20.9*</b>
Zn in <b>Fe~Zn(dobdc)</b>	<b>-17.3*</b>	<b>-20.5*</b>

Further evidence for the chemical similarity of the iron open metal sites in these systems can be seen via <sup>57</sup>Fe Mössbauer spectroscopy. Spectra collected for activated samples **Fe–Zn(dobdc)**, **Fe~Zn(dobdc)**, and **Fe<sub>2</sub>(dobdc)** have nearly identical room temperature isomer shifts and quadrupole splittings, indicative of high spin Fe<sup>II</sup> centers (**Table 2.S4** and **Figures 2.S9–2.S15**). On the other hand, low temperature spectra exhibit a clear difference between the monometallic and bimetallic systems. Magnetic interactions in **Fe<sub>2</sub>(dobdc)** lead to broadening of the observed peaks at 5 K due to spin relaxation on the Mössbauer timescale, while the Lorentzian doublets of the bimetallic systems remains approximately constant (**Figure 2.6**).

These differences in magnetic exchange interactions are readily apparent in field cooled magnetic susceptibility measurements performed using a SQUID magnetometer. As was previously reported, **Fe<sub>2</sub>(dobdc)** exhibits weak intrachain ferromagnetic coupling between high spin  $S = 2$  ferrous sites, indicated by a slight rise in the magnetic susceptibility when the material is cooled.<sup>66,67</sup> Such interactions are greatly diminished or entirely absent in both of the bimetallic systems (**Figure 2.S16**). It appears that the insertion of zinc ions in the iron helical chains prevents long-range magnetic ordering. At 300 K, remnant magnetization observed for both bimetallic systems are consistent with the expected values based on molar concentration of iron (3.75 and 3.73 cm<sup>3</sup> K/mol Fe for **Fe–Zn(dobdc)** and **Fe~Zn(dobdc)**, respectively) (**Figure 2.7**). Because there is no large difference between the templated and nontemplated frameworks' magnetic properties, I infer that any difference in metal distribution between the two systems is on a shorter length scale than that required for magnetic ordering in this structure.

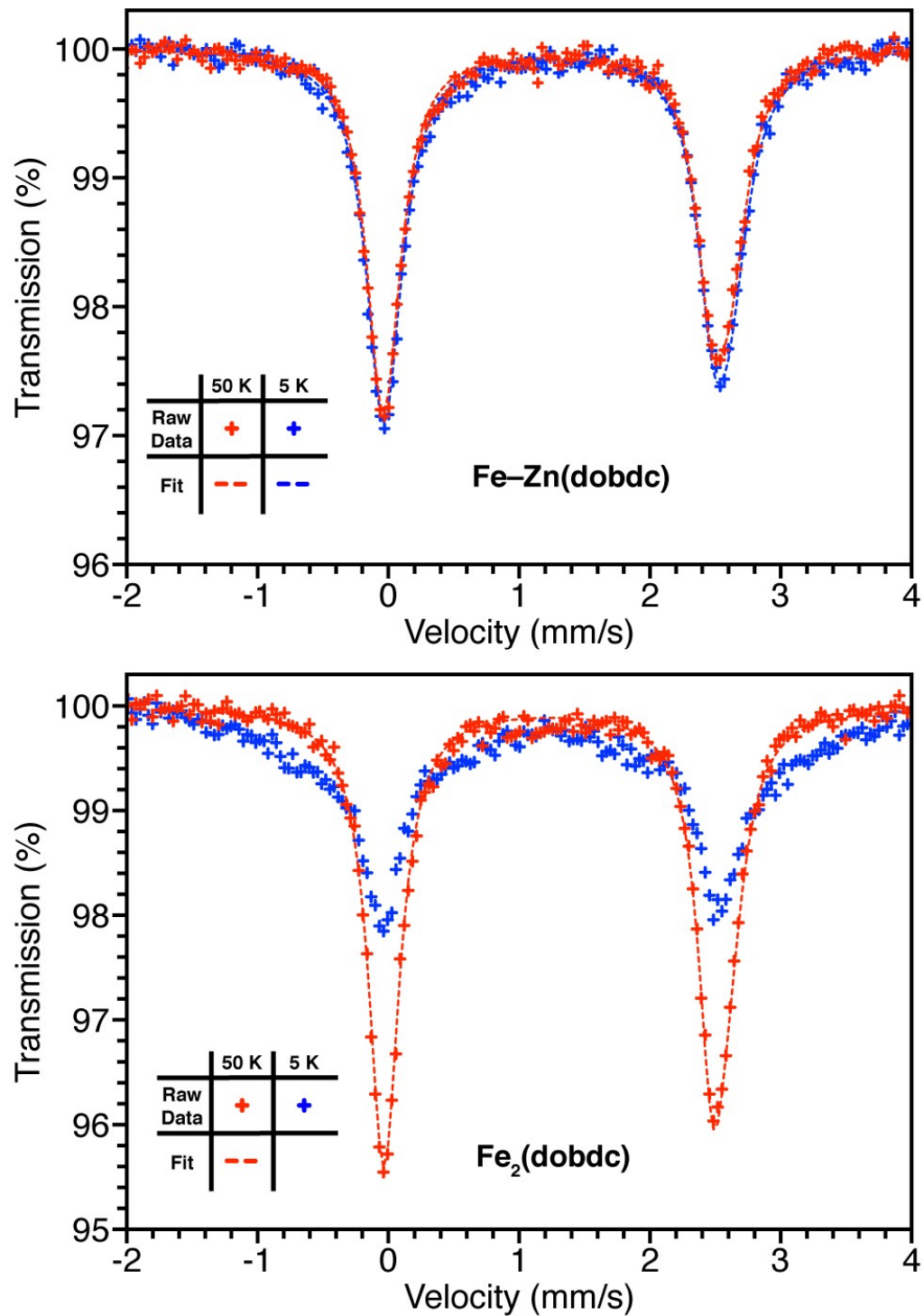


**Figure 2.6:** Mössbauer spectra of activated Fe-Zn(dobdc) (top) and activated Fe<sub>2</sub>(dobdc) (bottom) collected at 50 K and 5 K.

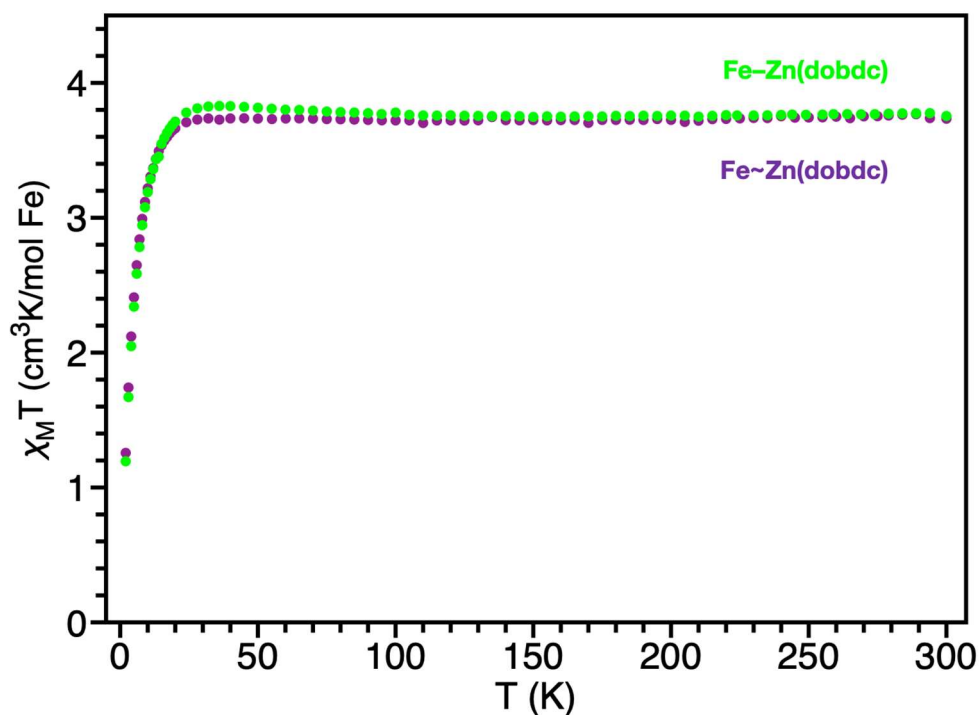


**Figure 2.7:** Variable-temperature magnetic susceptibility normalized per Fe for **Fe-Zn(dobdc)** and **Fe~Zn(dobdc)** collected at 1 kOe

## O<sub>2</sub> Stability Experiments

Multiple *in situ* techniques were utilized to characterize the thermal stability of the synthesized bimetallic materials to O<sub>2</sub> exposure. Previous reports indicate that pairs of the reversible Fe<sup>III</sup>-superoxide species formed when ferrous **Fe<sub>2</sub>(dobdc)** is exposed to O<sub>2</sub> undergo an irreversible disproportionation above 220 K to form a Fe<sup>III</sup>-peroxide species and a Fe<sup>III</sup> open metal site.<sup>29,68</sup> Because the irreversible oxidation of the iron open metal sites occurs via a thermally accessed charge transfer from an adjacent site, it represents a unique property which stems directly from the interactions between adjacent open metal sites. As such, completely isolated iron sites, as would be the case in an alternating -Fe-Zn-Fe-Zn- chain, should behave dramatically different from an all iron system or a material with random Fe/Zn distribution. DRIFTS allowed *in situ* monitoring of both superoxide formation and chemical changes in the framework under O<sub>2</sub> at higher temperatures. **Fe-Zn(dobdc)** was dosed with 1 bar of O<sub>2</sub> at 195 K and the sample was heated to 273 K. No change in the framework vibrations were observed, indicating disproportionation did not occur (**Figure 2.8**). The material was evacuated and dosed again with O<sub>2</sub>, upon which the same superoxide features were observed. Heating further to 300 K resulted in only slight changes in the 1800–1600 cm<sup>-1</sup> region, while leaving the sample overnight resulted in significant changes across the entire spectrum, while no superoxide formation was observed upon cycling. Similar treatment of **Fe<sub>2</sub>(dobdc)** shows dramatic changes in the spectra at just 273 K with significant changes in framework vibrations and broadening of the superoxide overtone (**Figure 2.8**), with no superoxide formation upon evacuation and redosing. **Fe~Zn(dobdc)** exhibits intermediate behavior, indicated by a broadening of the superoxide peak upon dosing at 273 K. The absence of any direct spectroscopic evidence of the peroxide can be explained by deleterious chemical reactivity with the organic linker in the framework. Previous reports have suggested that this ligand is redox-active,<sup>64,69,70</sup> and peroxide derivatives has been previously shown to facilitate

decarboxylation.<sup>71–73</sup> Either of these reactivities on the linker could be responsible for the changes seen in the spectra and would be expected to weaken the structural integrity of the framework.

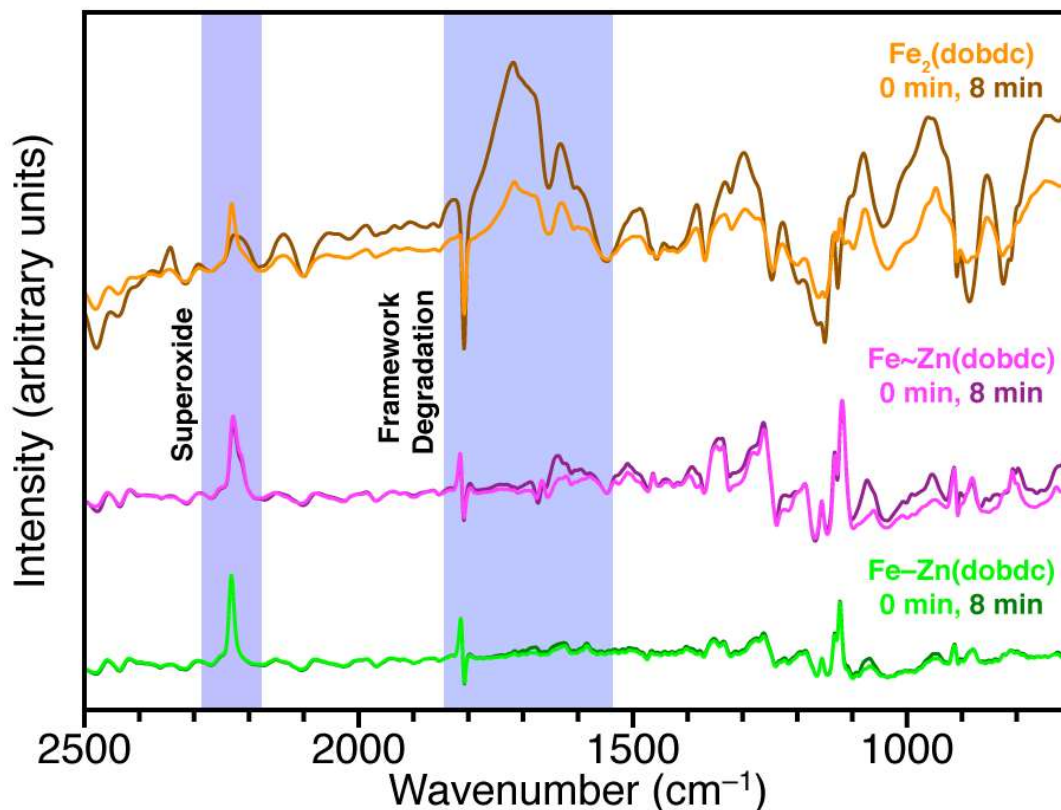


**Figure 2.8:** Consecutive collected DRIFTS spectra for **Fe<sub>2</sub>(dobdc)** (top), **Fe~Zn(dobdc)** (middle), and **Fe-Zn(dobdc)** (bottom) dosed with 1 bar of O<sub>2</sub> at low temperatures and warmed to 273 K. Initial spectra are shown in lighter colors and spectra collected 8 minutes later are shown in dark colors.

*In situ* powder X-ray diffraction studies demonstrated that O<sub>2</sub> adsorption in **Fe-Zn(dobdc)**, **Fe~Zn(dobdc)** and **Fe<sub>2</sub>(dobdc)** at 195 K results in a clear unit cell contraction (Table 2.2). This structural change arises due to oxidation of the framework by adsorbed O<sub>2</sub> to form Fe<sup>III</sup>-superoxide units, causing a contraction in the ligand sphere of the Fe ions. The magnitude of these changes is lessened in the bimetallic frameworks, as the redox inert zinc will not react in this manner. Clear differences arise when all three O<sub>2</sub> dosed samples are warmed to 273 K. A dramatic loss in crystallinity for **Fe<sub>2</sub>(dobdc)** is observed, most likely due to partial framework decomposition in the presence of the peroxide species formed at high temperatures. Remaining crystalline material was found to have a contracted unit cell, as the framework remains oxidized due to the persistence of Fe<sup>III</sup>-peroxide species. This thermal/chemical degradation observed in **Fe<sub>2</sub>(dobdc)** contrasts greatly with the behavior of the bimetallic systems. Although both **Fe-Zn(dobdc)** and **Fe~Zn(dobdc)** undergo unit cell contractions upon O<sub>2</sub> dosing at low temperature, they both exhibit a subsequent unit cell expansion upon heating to 273 K, consistent with partial desorption O<sub>2</sub> and reduction of Fe<sup>III</sup> sites to Fe<sup>II</sup>. Under both conditions **Fe~Zn(dobdc)** displayed a smaller unit cell; We hypothesize that this is due to some peroxide formation in **Fe~Zn(dobdc)** due to local heating upon O<sub>2</sub> adsorption at 195 K and additional peroxide formation upon heating to 273 K. As such,

these results clearly demonstrate the improved resilience of the crystalline structure in the mixed metal materials in contrast to **Fe<sub>2</sub>(dobdc)**.

**Table 2.2:** Unit cell volumes for **Fe<sub>2</sub>(dobdc)**, **Fe~Zn(dobdc)**, **Fe~Zn(dobdc)**, under vacuum at 298 K (Activated), 210 mbar O<sub>2</sub> at 195 K (O<sub>2</sub> Dosed Low T), and 210 mbar O<sub>2</sub> at 273 K (O<sub>2</sub> Dosed High T).

MOF	Fe <sub>2</sub> (dobdc)	Fe~Zn(dobdc)	Fe~Zn(dobdc)
Activated	4050.3(3) Å <sup>3</sup>	4003.0(10) Å <sup>3</sup>	4003.7(2) Å <sup>3</sup>
O <sub>2</sub> Dosed Low T	3916.8(3) Å <sup>3</sup>	3952.0(2) Å <sup>3</sup>	3932.3(3) Å <sup>3</sup>
O <sub>2</sub> Dosed High T	–	3975.2(2) Å <sup>3</sup>	3955.5(2) Å <sup>3</sup>

Cycling gas sorption measurements were employed to directly probe the enhanced reversible high-temperature O<sub>2</sub> adsorption in **Fe~Zn(dobdc)** relative to **Fe~Zn(dobdc)** and **Fe<sub>2</sub>(dobdc)**. For each material, 15 consecutive adsorption/activation cycles were collected at 273 K (**Figure 2.9**). Single point O<sub>2</sub> isotherms were collected at 210 mbar (atmospheric concentration of O<sub>2</sub>) followed by 30 minutes of activation under dynamic vacuum. As expected, **Fe<sub>2</sub>(dobdc)** has an initial uptake of 3.11 mmol/g, close to the expected uptake of 3.27 mmol/g for the irreversible formation of peroxide: Fe<sub>2</sub>(dobdc)(O<sub>2</sub><sup>2-</sup>). Subsequent cycles show a precipitous loss of capacity on the second cycle followed by small, continually decreasing uptake attributed to any residual porosity that the degrading material possess. **Fe~Zn(dobdc)** adsorbed 0.31 mmol/g on the first cycle. The adsorption drops very slightly over the next 4 cycles to 0.27 mmol/g, but then remains invariant within error over the remaining cycles. While this stable reversible uptake is noticeably less than the full low temperature capacity of the material, it is consistent with the thermodynamically predicted adsorption by iron sites in the material. The measured capacity of 0.095 O<sub>2</sub>/Fe (0.27 mmol /g) is only slightly above the expected 0.087 O<sub>2</sub>/Fe; we attribute the additional adsorption to weak binding at the zinc open metal sites or secondary sites. As with the previous O<sub>2</sub> experiments, **Fe~Zn(dobdc)** exhibits intermediate behavior: in this case, the relatively high uptake on the first cycle, 0.92 mmol/g, is followed by a dramatic decrease in adsorption through the remaining cycles. Because the O<sub>2</sub> adsorption in **Fe~Zn(dobdc)** significantly exceeds that expected for reversible binding, it can be inferred that some O<sub>2</sub> must be irreversibly binding through peroxide formation. Thus, subsequent cycles exhibit decreasing capacity while still adsorbing more than expected. This remarkably different behavior exhibited by both bimetallic species, despite having almost identical chemical compositions, is consistent with the proposed difference in metal distribution.

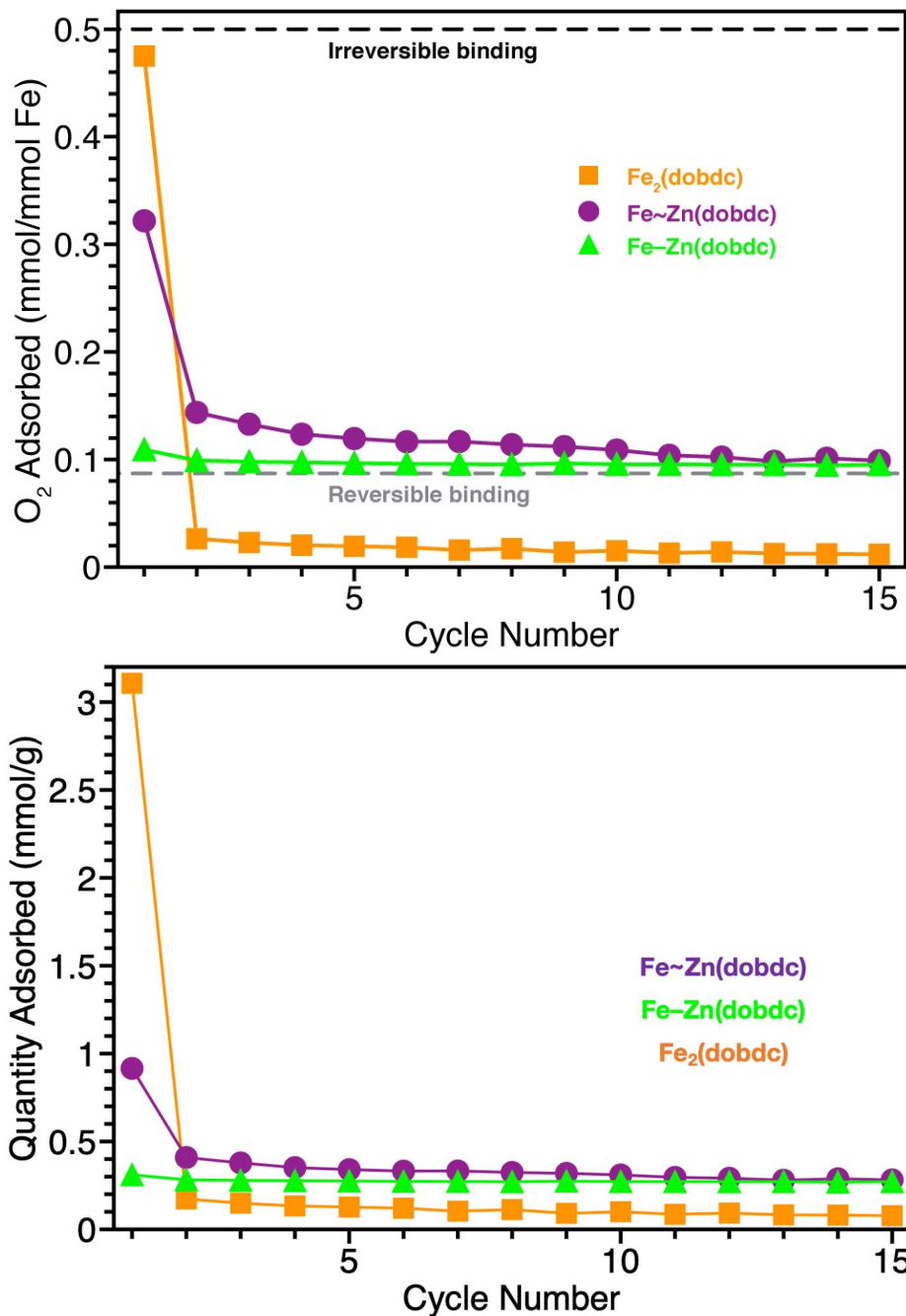


**Figure 2.9:** O<sub>2</sub> adsorption cycling measurements for Fe<sub>2</sub>(dobdc) (orange squares), Fe~Zn(dobdc) (purple circles, and Fe-Zn(dobdc) (green triangles). Scaled by Fe content (mmol/mmol Fe) (top) with expected one-time irreversible uptake for peroxide formation (black dashed line) and expected fully reversible uptake for superoxide formation (grey dashed line) and plotted in mmol/g (bottom).

While the drastic difference between Fe-Zn(dobdc) and Fe~Zn(dobdc) suggests largely isolated iron sites in the templated material, it appears likely that there are a small number of defect sites, possibly from metal exchange occurring during synthesis or zinc ion vacancies in the precursor. These defects lead to the presence of some sequential iron sites and thus some

irreversible binding, which manifests as small decreases in capacity on the initial O<sub>2</sub> cycles. After all these non-isolated iron sites react and disproportionate, O<sub>2</sub> binding on the alternating Fe/Zn metal chain is fully reversible under these conditions, corroborating with observations from *in situ* DRIFTS and PXRD. Intermediate results seen in **Fe~Zn(dobdc)** is consistent with a material with either a completely stochastic distribution or some degree of local phase segregation. In addition to reversible uptake caused by a small percentage of isolated Fe<sup>II</sup> sites, small segments of contiguous Fe<sup>II</sup> sites could also exhibit some degree of reversible O<sub>2</sub> adsorption. For example, I can consider a hypothetical isolated segment of four iron sites (Zn-Fe<sup>II</sup>-Fe<sup>II</sup>-Fe<sup>II</sup>-Fe<sup>II</sup>-Zn). If the two middle iron sites in a contiguous segment of four iron sites bind O<sub>2</sub> and then disproportionate (Zn-Fe<sup>II</sup>-Fe<sup>III</sup>-Fe<sup>III</sup>-Fe<sup>II</sup>-Zn), it would create a substantial energetic and spatial charge-transfer barrier for disproportionation of any superoxide species that form on the two outer sites. Local heating caused by the initial adsorption of O<sub>2</sub> across multiple adsorb/desorb cycles could help overcome this larger charge transfer barrier. Scenarios such as this would be expected to occur over a wide range of segment lengths in a material without an ordered metal distribution. Utilizing a templated synthetic approach, as is the case in **Fe-Zn(dobdc)**, can therefore give rise to a bimetallic material with improved properties and more uniform and homogeneous behavior.

## 2.4 Conclusions and Outlook

I report the design, synthesis, and characterization of a Fe<sup>II</sup> open metal site in the M<sub>2</sub>(dobdc) structural family with greater thermal stability to O<sub>2</sub> binding than Fe<sub>2</sub>(dobdc). The enhanced thermal stability of a Fe<sup>III</sup>-superoxide species above 273 K is achieved via the templated synthesis of a bimetallic framework, **Fe-Zn(dobdc)**. Using a suite of *in situ* and *ex situ* techniques to compare the templated framework to **Fe<sub>2</sub>(dobdc)** and to a nontemplated bimetallic system, **Fe~Zn(dobdc)**, strongly suggests that the distribution of metals in **Fe-Zn(dobdc)** is the origin of its unique behavior. I believe that these results give credence to the alternating metal chain first suggested by Coskun et al. Additionally, application of this templating strategy to the breadth of reported and potential M(H<sub>2</sub>dobdc)(H<sub>2</sub>O)<sub>x</sub> one-dimensional coordination solids could allow for the synthesis of any MM'(dobdc) combination with alternating M/M' chains.<sup>74</sup> Current efforts are underway to utilize this approach in other members of the M<sub>2</sub>dobdc isorecticular family. For example, the O<sub>2</sub> stability of the Fe sites could be further improved by utilizing the more redox stable meta congener of the ligand: H<sub>4</sub>(*m*-dobdc). Lastly, the use of partially reacted and potentially templating precursors of other metal-organic frameworks with continuous nodes could be used to generalize this control over metal distribution and resultant properties.

## 2.5 Acknowledgements

Material synthesis was funded by the U.S. Department of Energy (DoE), Office of Science, Basic Energy Sciences (BSE) (the Center for Gas Separations, an Energy Frontier Research Center, DE-SC0001015) and *in situ* characterization was funded by DoE, BSE: DE-SC0019992. R.M.T. was funded by the National Science Foundation (NSF) Graduate Research Fellowship Program and the University of California-Berkeley Chancellor's Fellowship. Henry Jiang for *in situ* DRIFTS and PXRD measurements, Khetpakorn Chakarawet for <sup>57</sup>Fe Mössbauer measurements, Lucy Darago and Colin Gould for magnetism measurements, and Kristen A. Colwell and Eugene Kim for helpful discussion.

## 2.6 References and Supplementary Figures

- (1) Humphrey, J.; Keller, G. *Separation Process Technology*. McGraw-Hill, New York: 1997.
- (2) Oak Ridge National Laboratory. *Materials for Separation Technologies: Energy and Emission Reduction Opportunities* (2005).
- (3) Sholl, D. S.; Lively, R. P. *Nat. News* **2016**, 532 (7600), 435.
- (4) Ruthven, D. *Principles of Adsorption and Adsorption Processes*. John Wiley & Sons, Inc.: New York, 1984.
- (5) Yaghi, O. M.; O’Keeffe, M.; Ockwig, N. W.; Chae, H. K.; Eddaoudi, M.; Kim, J. *Nature* **2003**, 423 (6941), 705.
- (6) Kitagawa, S.; Kitaura, R.; Noro, S. *Angew. Chem. Int. Ed.* **2004**, 43 (18), 2334.
- (7) Férey, G. *Chem. Soc. Rev.* **2007**, 37 (1), 191.
- (8) Furukawa, H.; Cordova, K. E.; O’Keeffe, M.; Yaghi, O. M. *Science* **2013**, 341 (6149), 1230444.
- (9) Li, Y.; Yang, R. T. *Langmuir* **2007**, 23 (26), 12937.
- (10) Xiao, D. J.; Gonzalez, M. I.; Darago, L. E.; Vogiatzis, K. D.; Haldoupis, E.; Gagliardi, L.; Long, J. R. *J. Am. Chem. Soc.* **2016**, 138 (22), 7161.
- (11) Demir, H.; Stoneburner, S. J.; Jeong, W.; Ray, D.; Zhang, X.; Farha, O. K.; Cramer, C. J.; Siepmann, I. J.; Gagliardi, L. *J. Phys. Chem. C* **2019**, 123, 12935.
- (12) Barnett, B. R.; Gonzalez, M. I.; Long, J. R. *Trends Chem.* **2019**, 1, 159.
- (13) Sumida, K.; Rogow, D. L.; Mason, J. A.; McDonald, T. M.; Bloch, E. D.; Herm, Z. R.; Bae, T.-H.; Long, J. R. *Chem. Rev.* **2012**, 112 (2), 724.
- (14) Li, J.-R.; Sculley, J.; Zhou, H.-C. *Chem. Rev.* **2012**, 112 (2), 869.
- (15) Adil, K.; Belmabkhout, Y.; Pillai, R. S.; Cadiau, A.; Bhatt, P. M.; Assen, A. H.; Maurin, G.; Eddaoudi, M. *Chem. Soc. Rev.* **2017**, 46 (11), 3402.
- (16) Rosi, N. L.; Kim, J.; Eddaoudi, M.; Chen, B.; O’Keeffe, M.; Yaghi, O. M. *J. Am. Chem. Soc.* **2005**, 127 (5), 1504.
- (17) Deng, H.; Grunder, S.; Cordova, K. E.; Valente, C.; Furukawa, H.; Hmadeh, M.; Gándara, F.; Whalley, A. C.; Liu, Z.; Asahina, S.; Kazumori, H.; O’Keefe, M.; Terasaki, O.; Stoddart, J.F.; Yaghi, O.M. *Science* **2012**, 336 (6084), 1018.
- (18) Kapelewski, M. T.; Geier, S. J.; Hudson, M. R.; Stuk, D.; Mason, J. A.; Nelson, J. N.; Xiao, D. J.; Hulvey, Z.; Gilmour, E.; FitzGerald, S. A.; Head-Gordon, M.; Brown, C. M.; Long, J. R. *J. Am. Chem. Soc.* **2014**, 136, 12119.
- (19) McDonald, T. M.; Lee, W.; Mason, J. A.; Wiers, B. M.; Hong, C.; Long, J. R. *J. Am. Chem. Soc.* **2012**, 134 (16), 7056.
- (20) Dietzel, P. D.; Morita, Y.; Blom, R.; Fjellvåg, H. *Angew. Chem. Int. Ed.* **2005**, 44 (39), 6354.
- (21) Dietzel, P. D.; Panella, B.; Hirscher, M.; Blom, R.; Fjellvåg, H. *Chem. Commun.* **2006**, 959.
- (22) Zhou, W.; Wu, H.; Yildirim, T. *J. Am. Chem. Soc.* **2008**, 130 (46), 15268.
- (23) Britt, D.; Furukawa, H.; Wang, B.; Glover, G. T.; Yaghi, O. M. *Proc. National Acad. Sci.* **2009**, 106 (49), 20637.
- (24) Bachman, J. E.; Kapelewski, M. T.; Reed, D. A.; Gonzalez, M. I.; Long, J. R. *J. Am. Chem. Soc.* **2017**, 139, 15363.
- (25) Rosnes, M. H.; Sheptyakov, D.; Franz, A.; Frontzek, M.; Dietzel, P. D.; Georgiev, P. A. *Phys. Chem. Chem. Phys.* **2017**, 19 (38), 26346.

- (26) Gonzalez, M. I.; Kapelewski, M. T.; Bloch, E. D.; Milner, P. J.; Reed, D. A.; Hudson, M. R.; Mason, J. A.; Barin, G.; Brown, C. M.; Long, J. R. *J. Am. Chem. Soc.* **2018**, *140*, 3412.
- (27) Kapelewski, M. T.; Oktawiec, J.; Runčevski, T.; Gonzalez, M. I.; Long, J. R. *Israel J. Chem.* **2018**, *58* (9–10), 1138.
- (28) Kapelewski, M. T.; Runčevski, T.; Tarver, J. D.; Jiang, H. Z. H.; Hurst, K. E.; Parilla, P. A.; Ayala, A.; Gennett, T.; FitzGerald, S. A.; Brown, C. M.; Long, J. R. *Chem. Mater.* **2018**, *30*, 8179.
- (29) Bloch, E. D.; Murray, L. M.; Queen, W. L.; Chavan, S.; Maximoff, S. N.; Bigi, J. P.; Krishna, R.; Peterson, V. K.; Grandjean, F.; Long, G. J.; Smit, B.; Bordiga, S.; Brown, C. M.; Long, J. R. *J. Am. Chem. Soc.* **2011**, *133*, 14814.
- (30) Rege, S. U.; Yang, R. T. *Ind. Eng. Chem. Res.* **1997**, *36* (12), 5358.
- (31) Helal, A.; Yamani, Z. H.; Cordova, K. E.; Yaghi, O. M. *Natl Sci Rev* **2017**, *4*, 296.
- (32) Deng, H.; Doonan, C. J.; Furukawa, H.; Ferreira, R. B.; Towne, J.; Knobler, C. B.; Wang, B.; Yaghi, O. M. *Science* **2010**, *327* (5967), 846.
- (33) Abednatanzi, S.; Derakhshandeh, P.; Depauw, H.; Coudert, F.-X.; Vrielinck, H.; Voort, P.; Leus, K. *Chem. Soc. Rev.* **2019**, *48* (9), 2535.
- (34) Pang, Q.; Tu, B.; Li, Q. *Coordin. Chem. Rev.* **2019**, *388*, 107.
- (35) Wang, L. J.; Deng, H.; Furukawa, H.; Gándara, F.; Cordova, K. E.; Peri, D.; Yaghi, O. M. *Inorg. Chem.* **2014**, *53* (12), 5881.
- (36) Howe, J. D.; Morelock, C. R.; Jiao, Y.; Chapman, K. W.; Walton, K. S.; Sholl, D. S. *J. Phys. Chem. C* **2016**, *121*, 627.
- (37) Marti, R. M.; Howe, J. D.; Morelock, C. R.; Conradi, M. S.; Walton, K. S.; Sholl, D. S.; Hayes, S. E. *J. Phys. Chem. C* **2017**, *121*, 25778.
- (38) Xing, J.; Guo, K.; Zou, Z.; Cai, M.; Du, J.; Xu, C. *Chem. Commun.* **2018**, *54* (51), 7046.
- (39) Zhang, T.; Wang, J.; Zhang, W.; Yang, C.; Zhang, L.; Zhu, W.; Sun, J.; Li, G.; Li, T.; Wang, J. *J. Mater. Chem. A* **2019**, *7* (6), 2845.
- (40) Shen, X.; Zhang, Y.; Ma, P.; Sutrisno, L.; Luo, Z.; Hu, Y.; Yu, Y.; Tao, B.; Li, C.; Cai, K. *Biomaterials* **2019**, *212*, 1.
- (41) Sun, D.; Sun, F.; Deng, X.; Li, Z. *Inorg. Chem.* **2015**, *54* (17), 8639.
- (42) Huang, C.; Liu, R.; Yang, W.; Li, Y.; Huang, J.; Zhu, H. *Inorg. Chem. Front.* **2018**, *8*, 1923.
- (43) Fu, Y.; Xu, L.; Shen, H.; Yang, H.; Zhang, F.; Zhu, W.; Fan, M. *Chem. Eng. J.* **2016**, *299*, 135.
- (44) Botas, J. A.; Calleja, G.; Sánchez-Sánchez, M.; Orcajo, G. M. *Int. J. Hydrogen Energ.* **2011**, *36* (17), 10834.
- (45) Villajos, J.; Orcajo, G.; Martos, C.; Botas, J.; Villacañas, J.; Calleja, G. *Int. J. Hydrogen Energ.* **2015**, *40* (15), 5346.
- (46) Sun, H.; Ren, D.; Kong, R.; Wang, D.; Jiang, H.; Tan, J.; Wu, D.; Chen, S.; Shen, B. *Micropor. Mesopor. Mat.* **2019**, *284*, 151.
- (47) Liu, J.; Zheng, J.; Barpaga, D.; Sabale, S.; Arey, B.; Derewinski, M. A.; McGrail, P. B.; Motkuri, R. *Eur. J. Inorg. Chem.* **2018**, *2018* (7), 885.
- (48) Yan, L.; Cao, L.; Dai, P.; Gu, X.; Liu, D.; Li, L.; Wang, Y.; Zhao, X. *Adv. Funct. Mater.* **2017**, *27* (40), 1703455.
- (49) Qu, C.; Zhao, B.; Jiao, Y.; Chen, D.; Dai, S.; deGlee, B. M.; Chen, Y.; Walton, K. S.; Zou, R.; Liu, M. *ACS Energy Lett.* **2017**, *2*, 1263.
- (50) Sun, D.; Ye, L.; Sun, F.; García, H.; Li, Z. *Inorg. Chem.* **2017**, *56*, 5203.

- (51) Kim, H.; Sohail, M.; Wang, C.; Rosillo-Lopez, M.; Baek, K.; Koo, J.; Seo, M.; Kim, S.; Foord, J. S.; Han, S. *Sci. Rep.* **2019**, *9* (1), 8984
- (52) Sun, W.; Tao, X.; Du, P.; Wang, Y. *Chem. Eng. J.* **2019**, *366*, 622.
- (53) Jia, Z.; Cui, Z.; Tan, Y.; Liu, Z.; Guo, X. *Chem. Eng. J.* **2019**, *370*, 89.
- (54) Zhang, X.-L.; Zhang, D.-X.; Chang, G.; Ma, X.-C.; Wu, J.; Wang, Y.; Yu, H.-Z.; Tian, G.; Chen, J.; Yang, X.-Y. *Ind. Eng. Chem. Res.* **2019**, *58*, 7209.
- (55) Sun, W.; Chen, S.; Wang, Y. *Dalton Trans.* **2019**, *48* (6), 2019.
- (56) Wang, X.; Xiao, H.; Li, A.; Li, Z.; Liu, S.; Zhang, Q.; Gong, Y.; Zheng, L.; Zhu, Y.; Chen, C.; Wang, D.; Peng, Q.; Gu, L.; Han, X.; Li, J.; Li, Y. *J. Am. Chem. Soc.* **2018**, *140*, 15336.
- (57) Xiao, D. J.; Bloch, E. D.; Mason, J. A.; Queen, W. L.; Hudson, M. R.; Planas, N.; Borycz, J.; Dzubak, A. L.; Verma, P.; Lee, K.; Bonino, F.; Crocella, V.; Yano, J.; Bordiga, S.; Truhlar, D. G.; Gagliardi, L.; Brown, C. M.; Long, J. R. *Nature Chem.* **2014**, *6*, 590.
- (58) Liu, Q.; Cong, H.; Deng, H. *J. Am. Chem. Soc.* **2016**, *138*, 13822.
- (59) Bignami, G. P.; Davis, Z. H.; Dawson, D. M.; Morris, S. A.; Russell, S. E.; McKay, D.; Parke, R. E.; Iuga, D.; Morris, R. E.; Ashbrook, S. E. *Chem. Sci.* **2017**, *9* (4), 850.
- (60) Mali, G.; Mazaj, M.; Arcon, I.; Hanzel, D.; Arcon, D.; Jaglicic, Z. *J. Phys. Chem. Lett.* **2019**, *10*, 1464.
- (61) Kim, D.; Coskun, A. *Angew. Chem. Int. Ed.* **2017**, *56* (18), 5071.
- (62) Cotton, A. F.; Daniels, L.M; Murillo, C. A.; Quesada, J. F. *Inorg. Chem.* **1993**, *32* (22), 4861.
- (63) Ghermani, N.; Morgant, G.; d'Angelo, J.; Desmaële, D.; Fraisse, B.; Bonhomme, F.; Dichi, E.; Sgahier, M. *Polyhedron* **2007**, *26* (12), 2880.
- (64) Zou, L.; Feng, D.; Liu, T.-F.; Chen, Y.-P.; Yuan, S.; Wang, K.; Wang, X.; Fordham, S.; Zhou, H.-C. *Chem. Sci.* **2015**, *7* (2), 1063.
- (65) Garrone, E.; Areán, C. *Chem. Soc. Rev.* **2005**, *34* (10), 846.
- (66) Bloch, E. D.; Queen, W. L.; Krishna, R.; Zadrozny, J. M.; Brown, C. M.; Long, J. R. *Science* **2012**, *335* (6076), 1606.
- (67) Borycz, J.; Paier, J.; Verma, P.; Darago, L. E.; Xiao, D. J.; Truhlar, D. G.; Long, J. R.; Gagliardi, L. *Inorg. Chem.* **2016**, *55* (10), 4924.
- (68) Li, L.; Lin, R.-B.; Krishna, R.; Li, H.; Xiang, S.; Wu, H.; Li, J.; Zhou, W.; Chen, B. *Science* **2018**, *362* (6413), 443.
- (69) Cozzolino, A. F.; Brozek, C. K.; Palmer, R. D.; Yano, J.; Li, M.; Dincă, M. *J. Am. Chem. Soc.* **2014**, *136* (9), 3334.
- (70) Aubrey, M. L.; Long, J. R. *J. Am. Chem. Soc.* **2015**, *137* (42), 13594.
- (71) Lamrini, R.; Lacan, P.; Francina, A.; Guilluy, R.; sage; Michon, J.; Becchi, M.; Brazier, J. *Free Radical Bio. Med.* **1998**, *24* (2), 280.
- (72) Gardner, L. K.; Lawrence, G. D. *J. Agr. Food Chem.* **1993**, *41* (5), 693.
- (73) Lamrini, R.; Crouzet, J. M.; Francina, A.; Guilluy, R.; Steghens, J. P.; Brazier, J. L. *Anal. Biochem.* **1994**, *220* (1), 129.
- (74) Ayoub, G.; Karadeniz, B.; Howarth, A. J.; Farha, O.; Đilović, I.; Germann, L. S.; Dinnebier, R. E.; Užarević, K.; Friscic, T. *Chem. Mater.*  
<https://doi.org/10.1021/acs.chemmater.9b01068>.

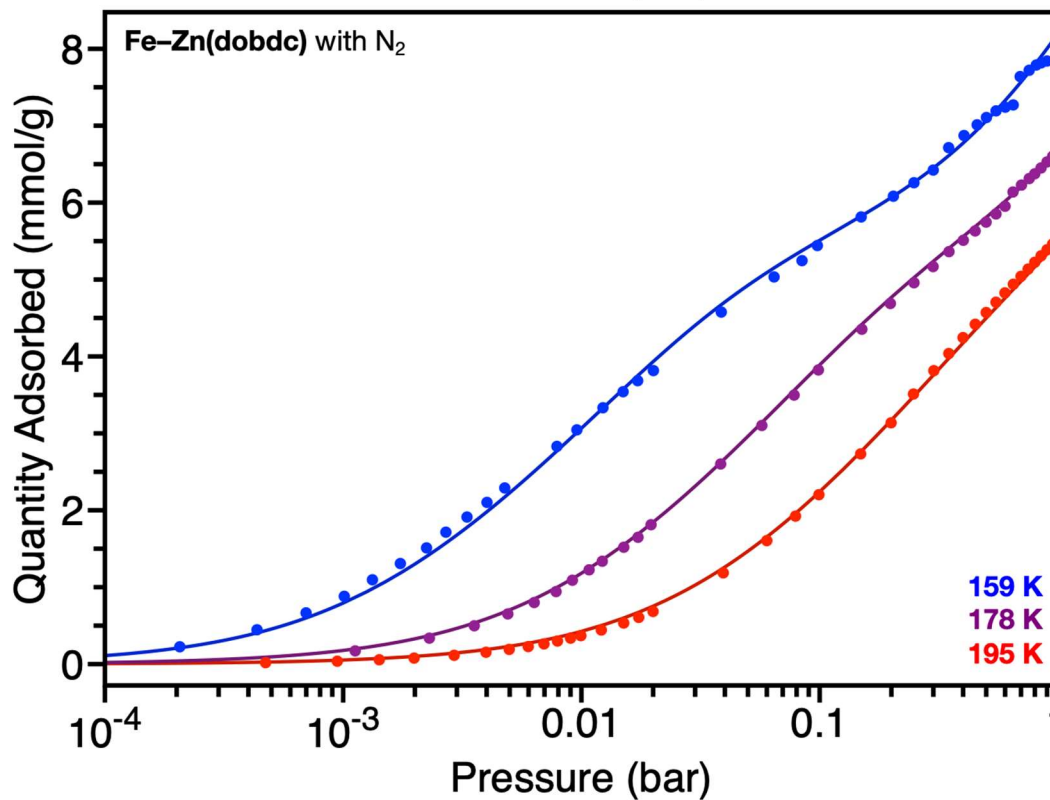
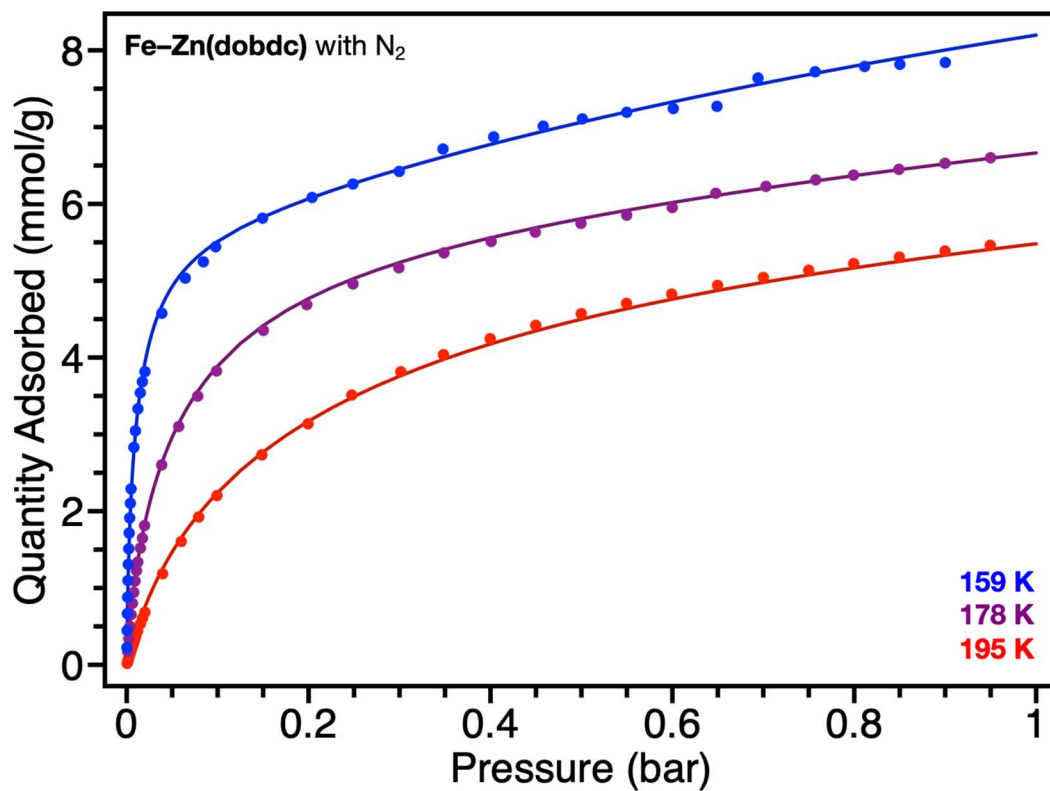


**Figure 2.S1:** Isothermal gas sorption measurement of Fe-Zn(dobdc) with N<sub>2</sub> at 159, 178, and 195 K, fitted with a three-site Langmuir-Freundlich equation, parameters found in Table 2.S1, plotted linearly (top) and logarithmically (bottom).

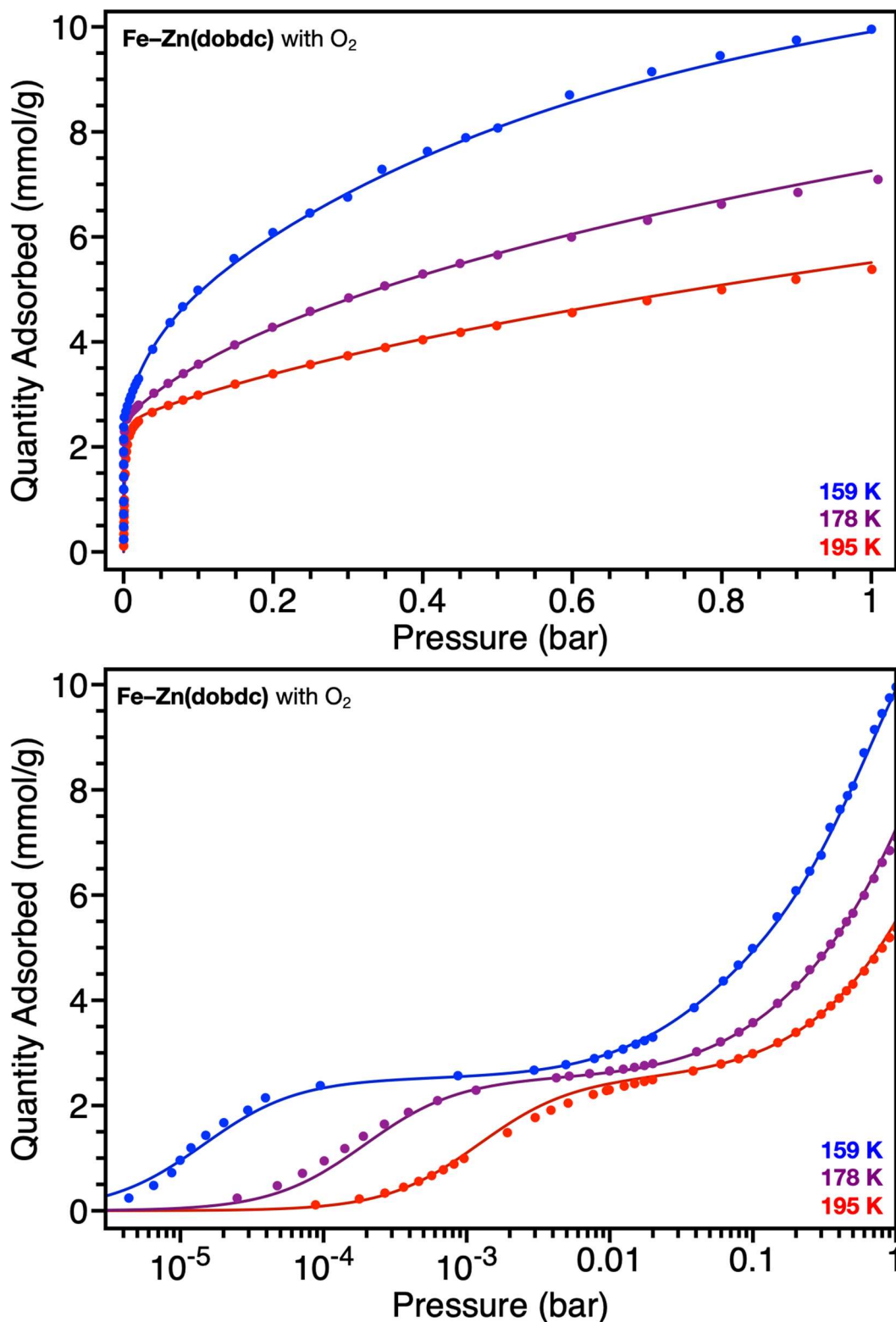


**Figure 2.S2:** Isothermal gas sorption measurement of Fe-Zn(dobdc) with O<sub>2</sub> at 159, 178, and 195 K, fitted with a three-site Langmuir-Freundlich equation, parameters found in Table 2.S1, plotted linearly (top) and logarithmically (bottom).

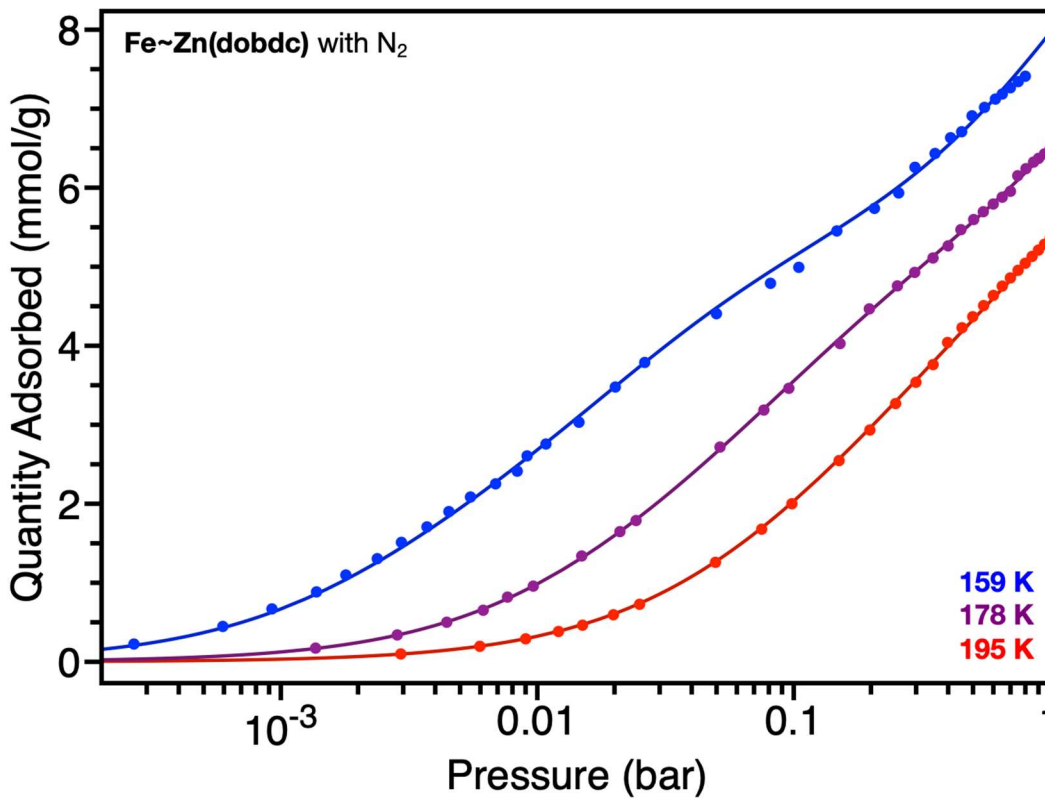
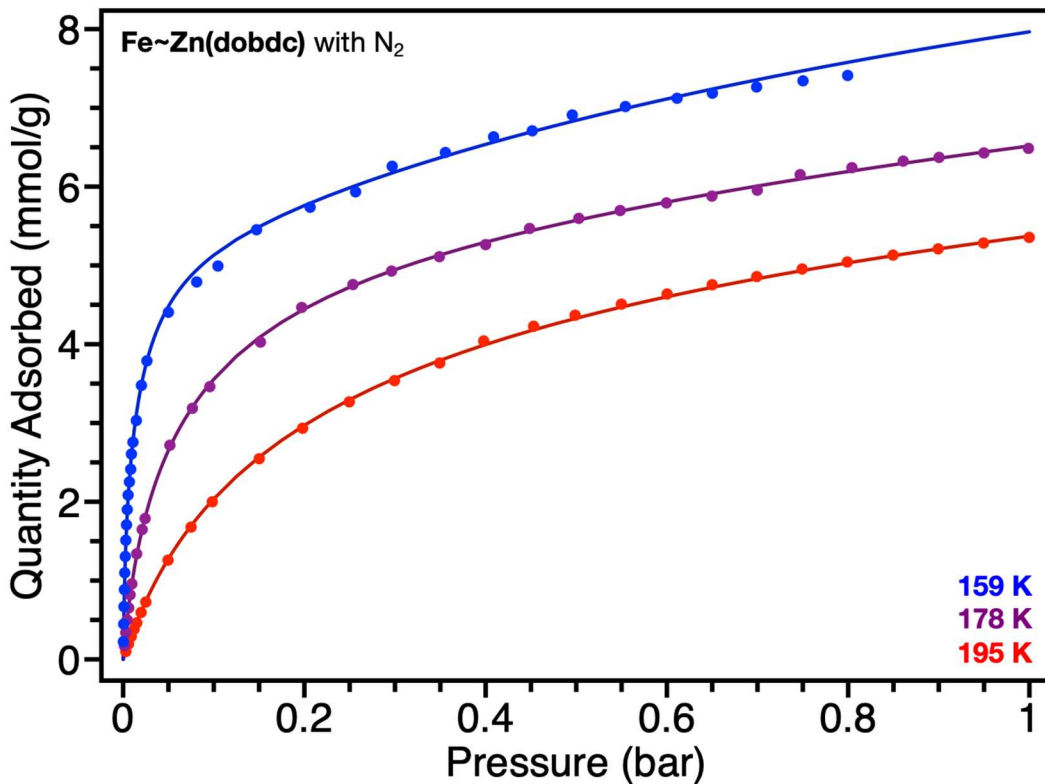


**Figure 2.S3:** Isothermal gas sorption measurement of Fe~Zn(dobdc) with N<sub>2</sub> at 159, 178, and 195 K, fitted with a three-site Langmuir-Freundlich equation, parameters found in Table 2.S1, plotted linearly (top) and logarithmically (bottom).

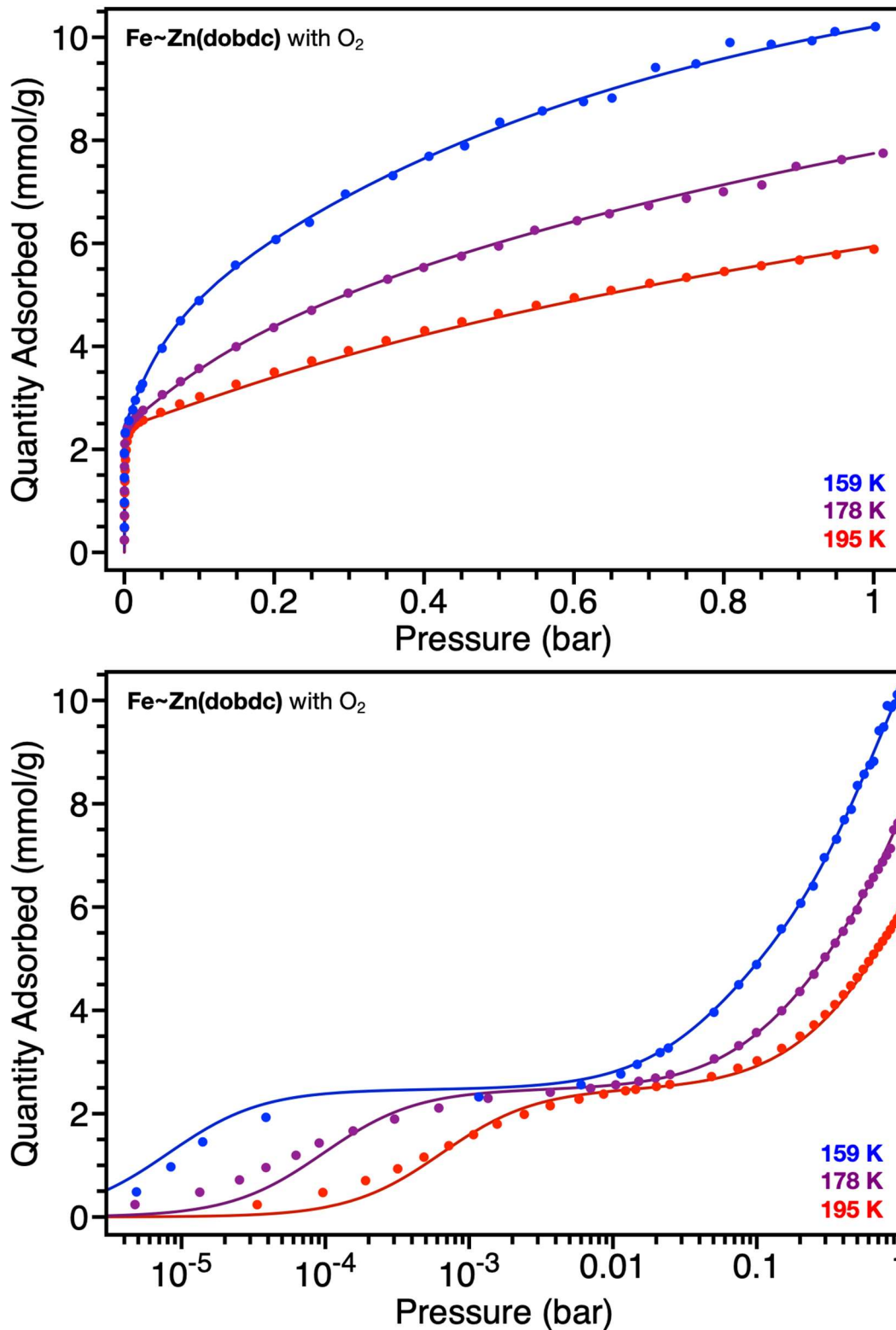


**Figure 2.S4:** Isothermal gas sorption measurement of Fe~Zn(dobdc) with  $O_2$  at 159, 178, and 195 K, fitted with a three-site Langmuir-Freundlich equation, parameters found in Table 2.S1, plotted linearly (top) and logarithmically (bottom).

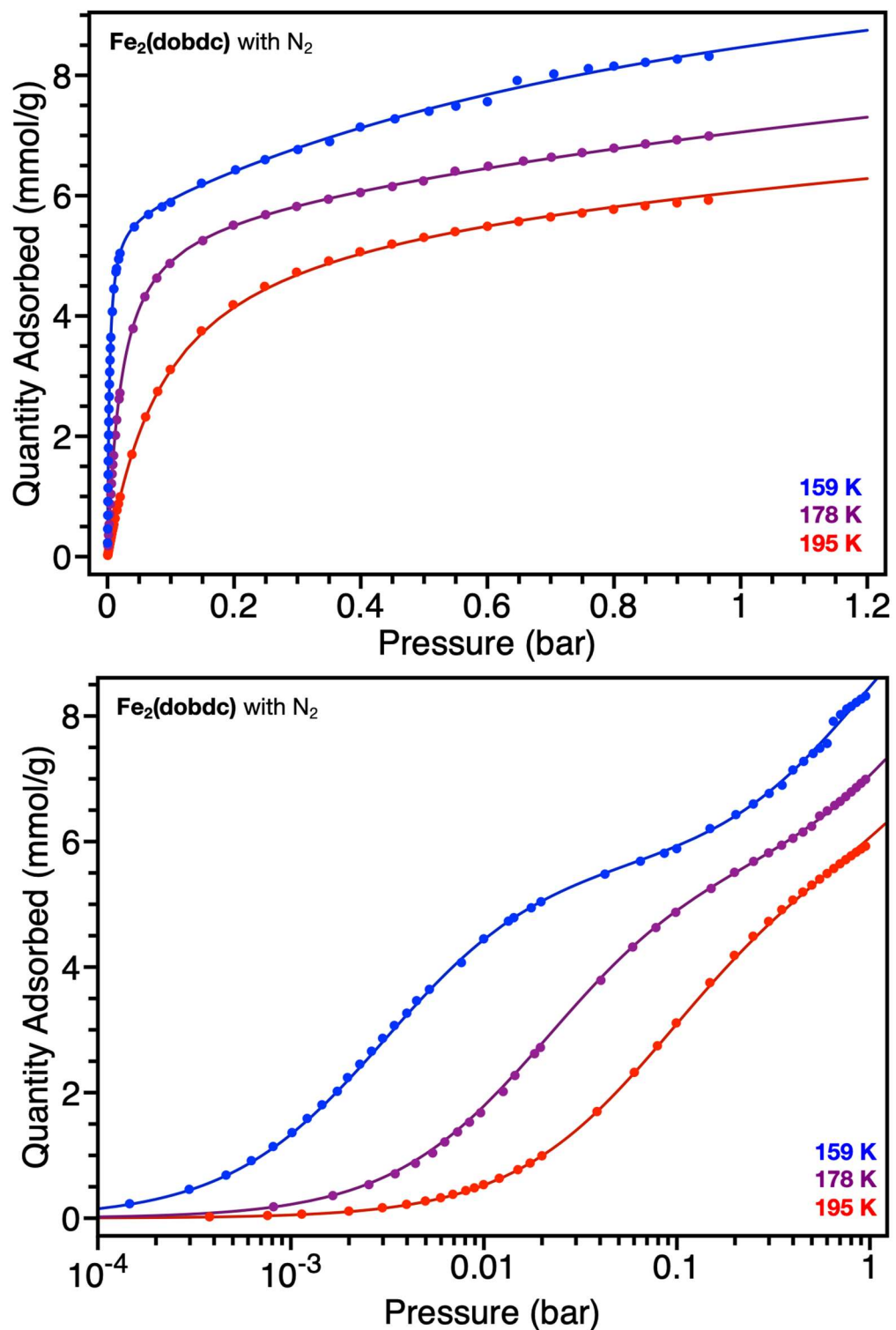


**Figure 2.S5:** Isothermal gas sorption measurement of  $\text{Fe}_2(\text{dobdc})$  with  $\text{N}_2$  at 159, 178, and 195 K, fitted with a two-site Langmuir-Freundlich equation, parameters found in Table 2.S1, plotted linearly (top) and logarithmically (bottom).

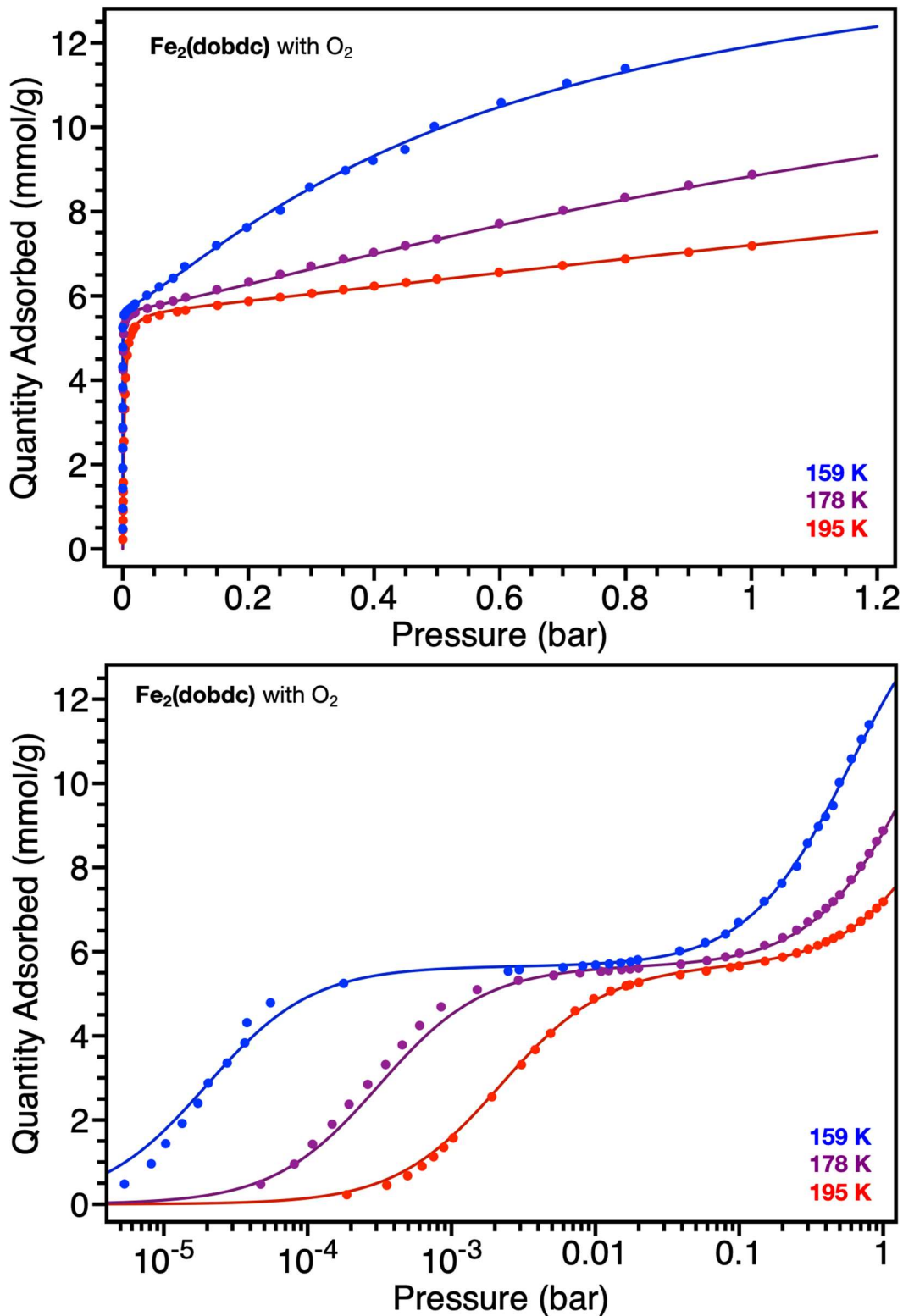


**Figure 2.S6:** Isothermal gas sorption measurement of Fe<sub>2</sub>(dobdc) with O<sub>2</sub> at 159, 178, and 195 K, fitted with a two-site Langmuir-Freundlich equation, parameters found in Table 2.S1, plotted linearly (top) and logarithmically (bottom).

**Table 2.S1:** Parameters for multisite Langmuir-Freundlich equations simultaneously fit to gas sorption data for N<sub>2</sub> or O<sub>2</sub> at 159, 178, and 195 K for the frameworks **Fe–Zn(dobdc)**, **Fe~Zn(dobdc)**, and **Fe<sub>2</sub>(dobdc)**. Site 1 is assigned to Fe<sup>2+</sup> in all the systems and Site 2 is assigned to in the bimetallic frameworks Zn<sup>2+</sup>, due to both the strength of binding and capacity.

Gas	Material	Site	$q_{sat}$ (mmol/g)	$\Delta H$ (kJ/mol)	$\Delta S$ (J/mol K)	$\nu$ (dimensionless)
N <sub>2</sub>	<b>Fe–Zn(dobdc)</b>	1 (Fe <sup>2+</sup> )	2.65	–23.6	–111	1.14
		2 (Zn <sup>2+</sup> )	3.02	–20.9	–88	0.93
		3	7.75	–11.8	–80	1.07
	<b>Fe~Zn(dobdc)</b>	1 (Fe <sup>2+</sup> )	2.44	–23.6	–100	1.01
		2 (Zn <sup>2+</sup> )	2.92	–20.5	–94	1.12
		3	6.40	–11.1	–72	1.10
	<b>Fe<sub>2</sub>(dobdc)</b>	1 (Fe <sup>2+</sup> )	5.67	–25.5	–109	1.06
		2	5.53	–13.0	–81	1.12
	O <sub>2</sub>	<b>Fe–Zn(dobdc)</b>	1 (Fe <sup>2+</sup> )	2.41	–41.4	–139
2 (Zn <sup>2+</sup> )			2.99	–16.9	–83	0.98
3			7.41	–15.1	–91	1.33
<b>Fe~Zn(dobdc)</b>		1 (Fe <sup>2+</sup> )	2.47	–41.0	–128	1.34
		2 (Zn <sup>2+</sup> )	3.13	–17.3	–82	1.18
		3	7.74	–14.1	–86	1.38
<b>Fe<sub>2</sub>(dobdc)</b>		1 (Fe <sup>2+</sup> )	5.65	–39.3	–142	1.18
		2	9.56	–16.2	–97	1.22

**Table 2.S2:** Ratio of Fe to Zn for **Fe–Zn(dobdc)**, normalized to Fe<sub>x</sub>Zn<sub>2-x</sub>(dobdc), calculated from various methods.

Method	Fe	Zn
ICP	0.90	1.10
N <sub>2</sub> Gas Adsorption	0.93	1.07
O <sub>2</sub> Gas Adsorption	0.91	1.09

**Table 2.S3:** Ratio of Fe to Zn for **Fe~Zn(dobdc)**, normalized to Fe<sub>x</sub>Zn<sub>2-x</sub>(dobdc), calculated from various methods.

Method	Fe	Zn
ICP	0.88	1.12
N <sub>2</sub> Gas Adsorption	0.91	1.09
O <sub>2</sub> Gas Adsorption	0.88	1.12

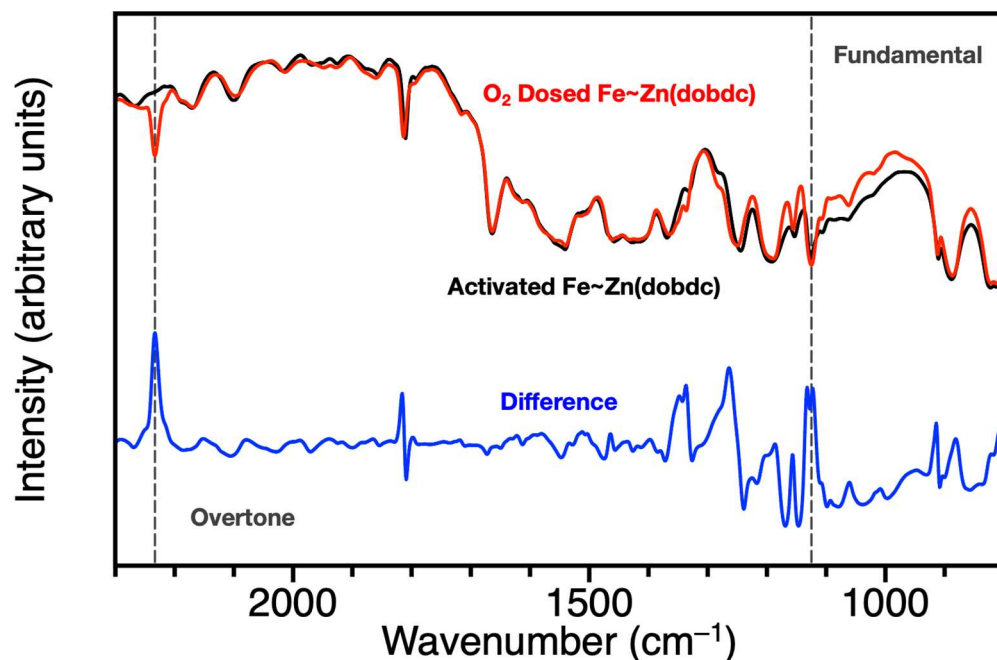


**Figure 2.S7:** DRIFTS measurements of Fe~Zn(dobdc) with activated bare framework in black, O<sub>2</sub> dosed in red and the difference spectrum in blue. The fundamental vibrational stretch for superoxide is obscured by framework vibrations but the overtone stretch at 2233 cm<sup>-1</sup> is clearly visible.

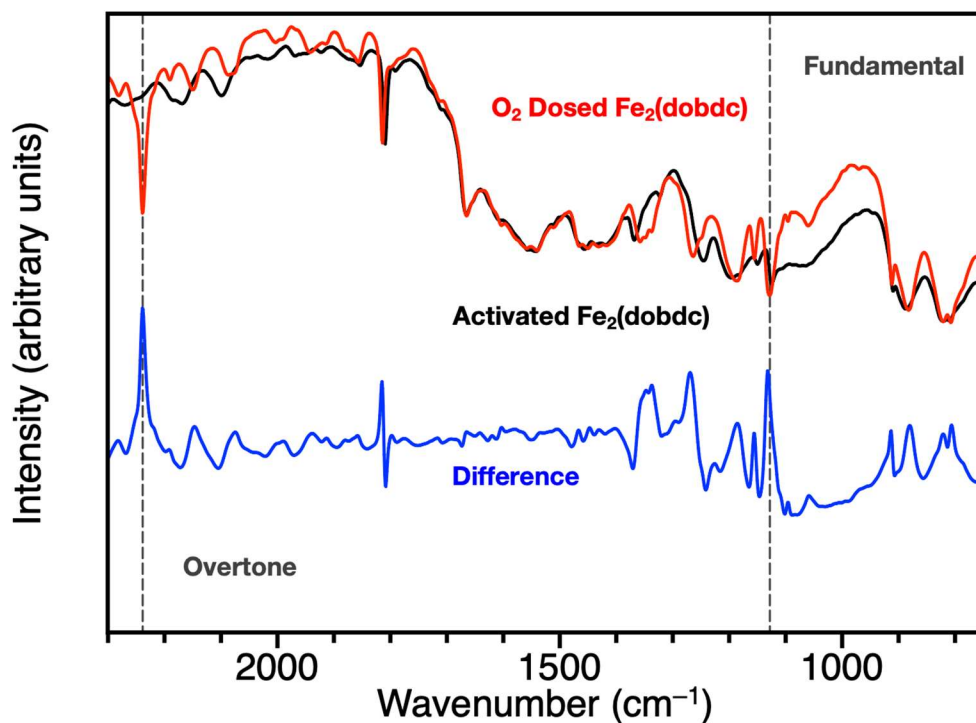


**Figure 2.S8:** DRIFTS measurements of Fe<sub>2</sub>(dobdc) with activated bare framework in black, O<sub>2</sub> dosed in red and the difference spectrum in blue. The fundamental vibrational stretch for superoxide is obscured by framework vibrations but the overtone stretch at 2239 cm<sup>-1</sup> is clearly visible.

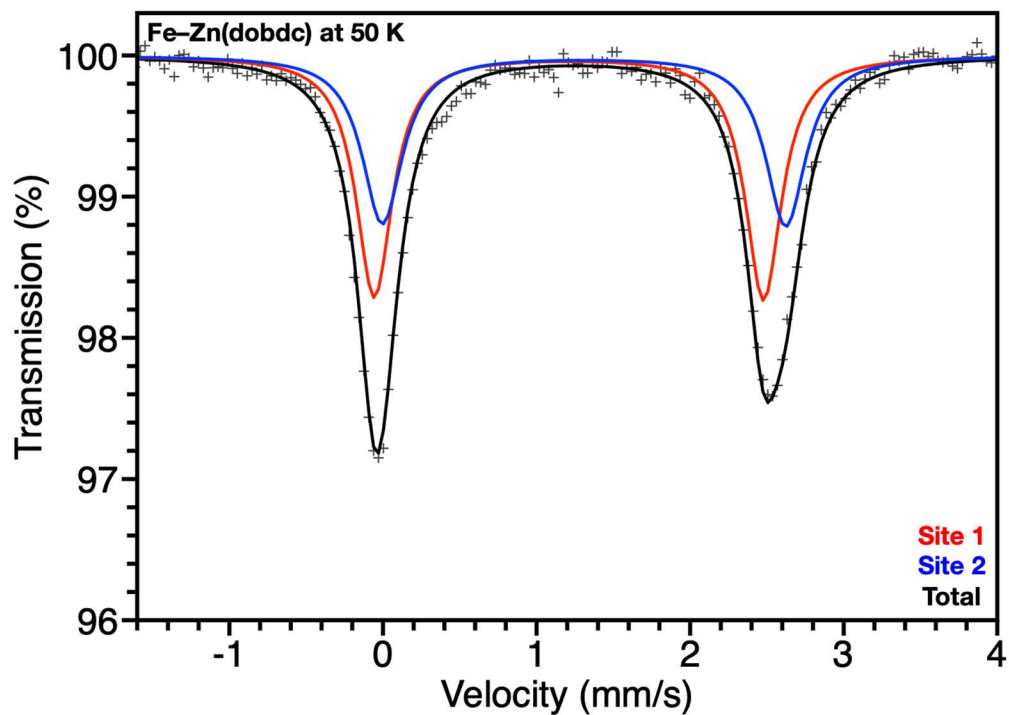


**Figure 2.S9:**  $^{57}\text{Fe}$  Mössbauer spectrum for Fe-Zn(dobdc), collected at 50 K, raw data (+), Site 1 (red), Site 2 (blue), and total fit (black). Parameters for Site 1 and Site 2 found in Table 2.S4.

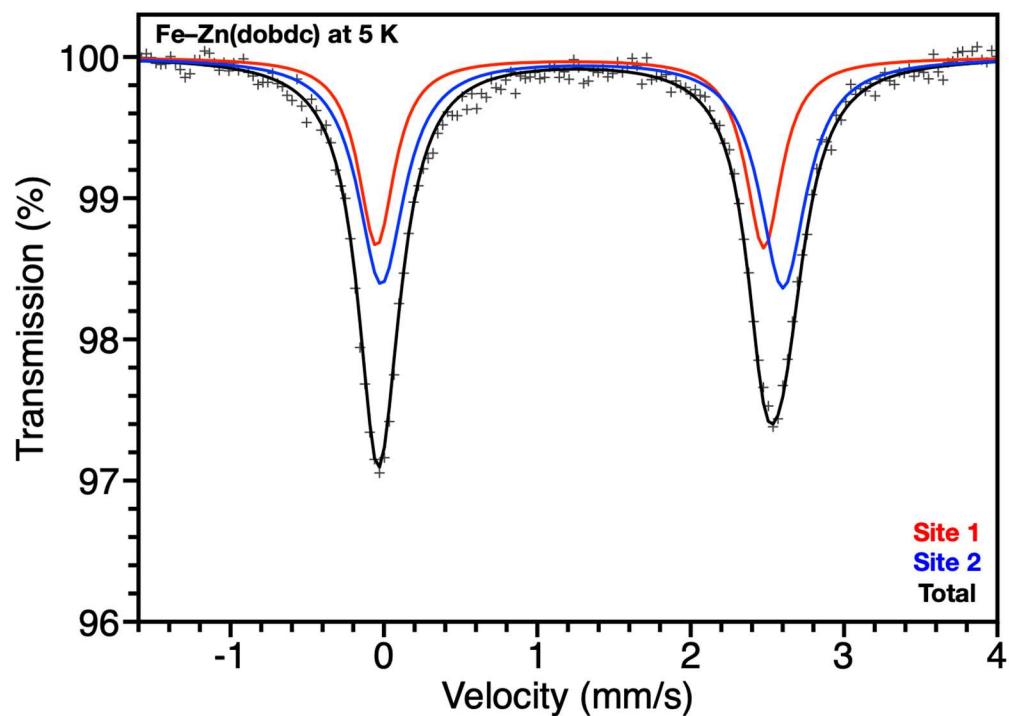


**Figure 2.S10:**  $^{57}\text{Fe}$  Mössbauer spectrum for Fe-Zn(dobdc), collected at 5 K, raw data (+), Site 1 (red), Site 2 (blue), and total fit (black). Parameters for Site 1 and Site 2 found in Table 2.S4.

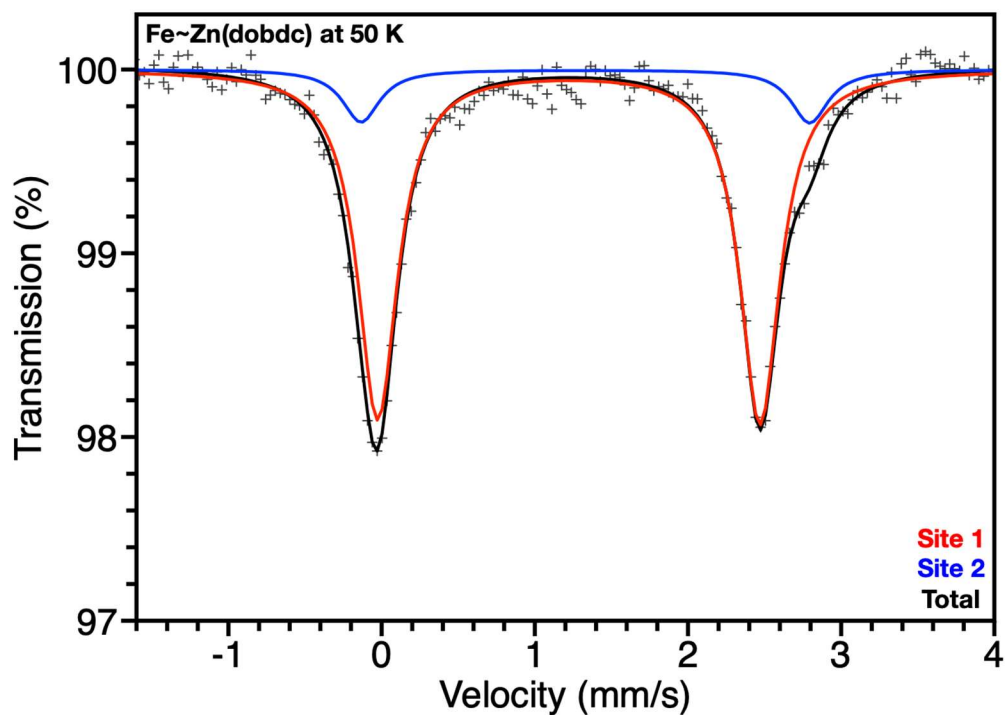


**Figure 2.S11:**  $^{57}\text{Fe}$  Mössbauer spectrum for Fe~Zn(dobdc), collected at 50 K, raw data (+), Site 1 (red), Site 2 (blue), and total fit (black). Parameters for Site 1 and Site 2 found in Table 2.S4.

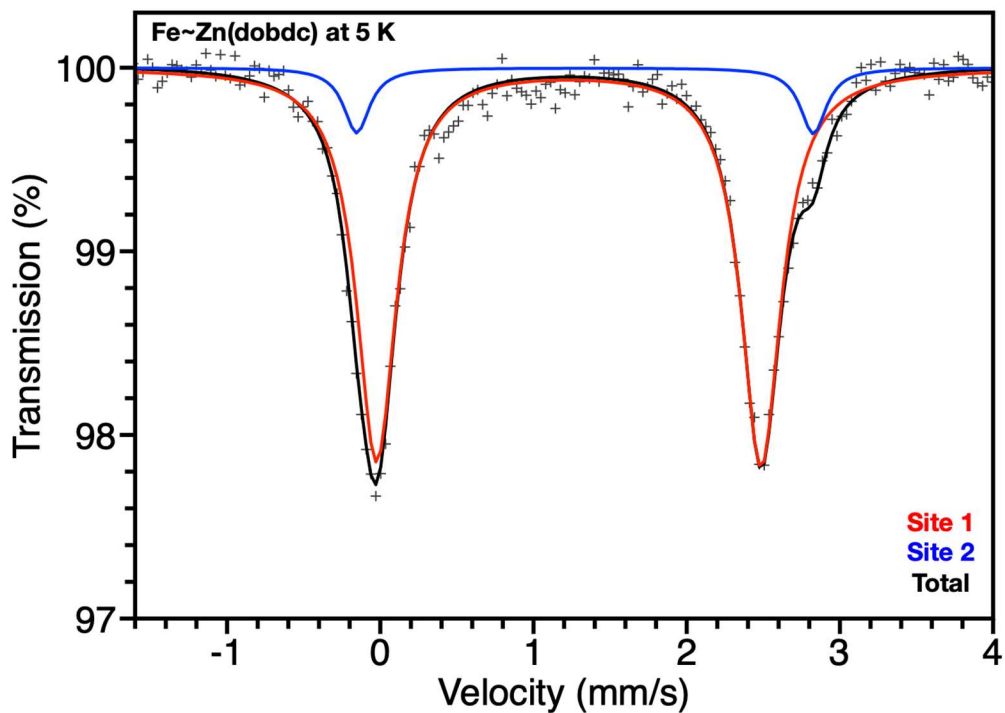


**Figure 2.S12:**  $^{57}\text{Fe}$  Mössbauer spectrum for Fe~Zn(dobdc), collected at 5 K, raw data (+), Site 1 (red), Site 2 (blue), and total fit (black). Parameters for Site 1 and Site 2 found in Table 2.S4.

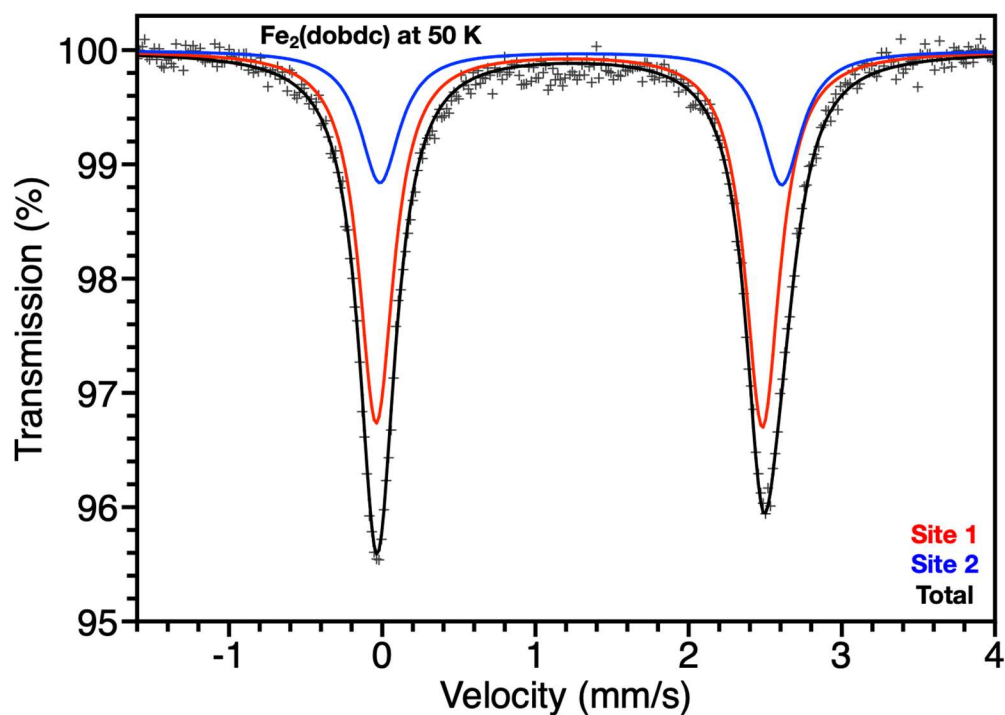


**Figure 2.S13:**  $^{57}\text{Fe}$  Mössbauer spectrum for  $\text{Fe}_2(\text{dobdc})$ , collected at 50 K, raw data (+), Site 1 (red), Site 2 (blue), and total fit (black). Parameters for Site 1 and Site 2 found in Table 2.S4.

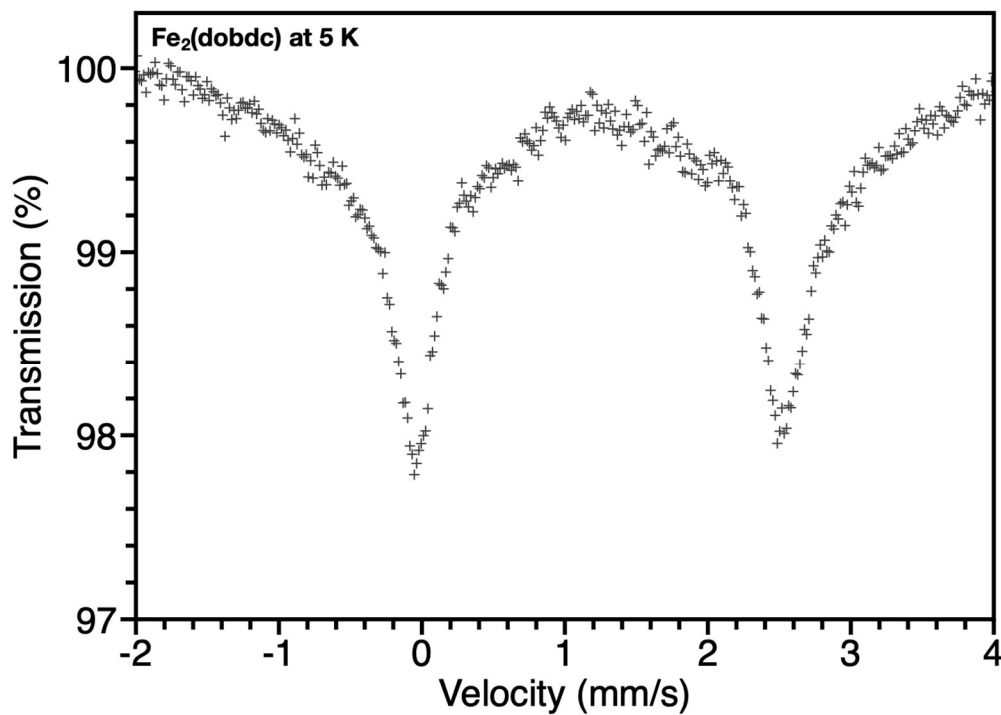


**Figure 2.S14:**  $^{57}\text{Fe}$  Mössbauer spectrum for  $\text{Fe}_2(\text{dobdc})$ , collected at 5 K. The data (+) could not be fitted to Lorentzian doublets due to superparamagnetic broadening.

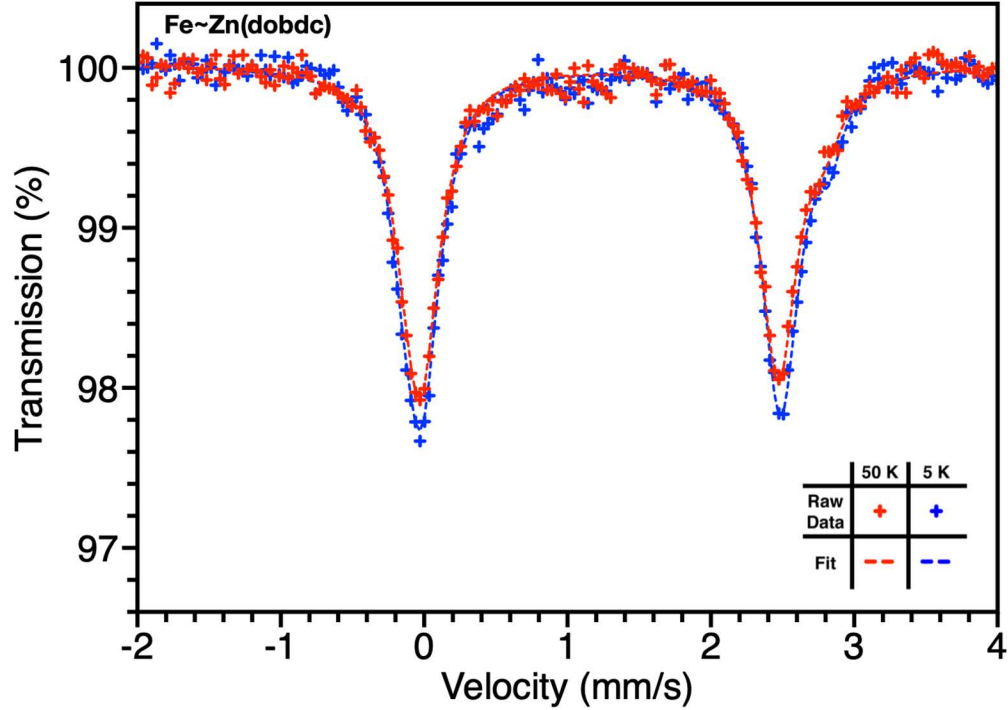


**Figure 2.S15:**  $^{57}\text{Fe}$  Mössbauer spectra for Fe~Zn(dobdc), comparing data from 50 K (red) and 5 K (blue). Similar to Fe–Zn(dobdc), no sign of line broadening is observed.

**Table 2.S4:**  $^{57}\text{Fe}$  Mössbauer spectral fitting parameters for Fe–Zn(dobdc), Fe~Zn(dobdc), and Fe<sub>2</sub>(dobdc), at 50 K and 5 K, with estimated standard deviations given in parentheses.

Material	$T$ (K)	Site	$\delta$ (mm/s)	$\Delta E_Q$ (mm/s)	$\Gamma$ (mm/s)	Area (%)
Fe–Zn(dobdc)	50	1	1.205(8)	2.52(1)	0.29(2)	58(10)
		2	1.31(1)	2.61(2)	0.31(2)	42(10)
	5	1	1.21(1)	2.52(2)	0.29(3)	42(11)
		2	1.29(2)	2.60(2)	0.36(2)	58(13)
Fe~Zn(dobdc)	50	1	1.223(2)	2.493(5)	0.304(8)	88(3)
		2	1.32(1)	2.93(4)	0.25(4)	12(2)
	5	1	1.231(2)	2.509(4)	0.306(6)	90(2)
		2	1.331(9)	2.98(2)	0.20(3)	10(2)
Fe <sub>2</sub> (dobdc)	50	1	1.222(4)	2.819(8)	0.28(1)	70(10)
		2	1.29(1)	2.63(2)	0.32(2)	30(9)
	5	-	-	-	-	-

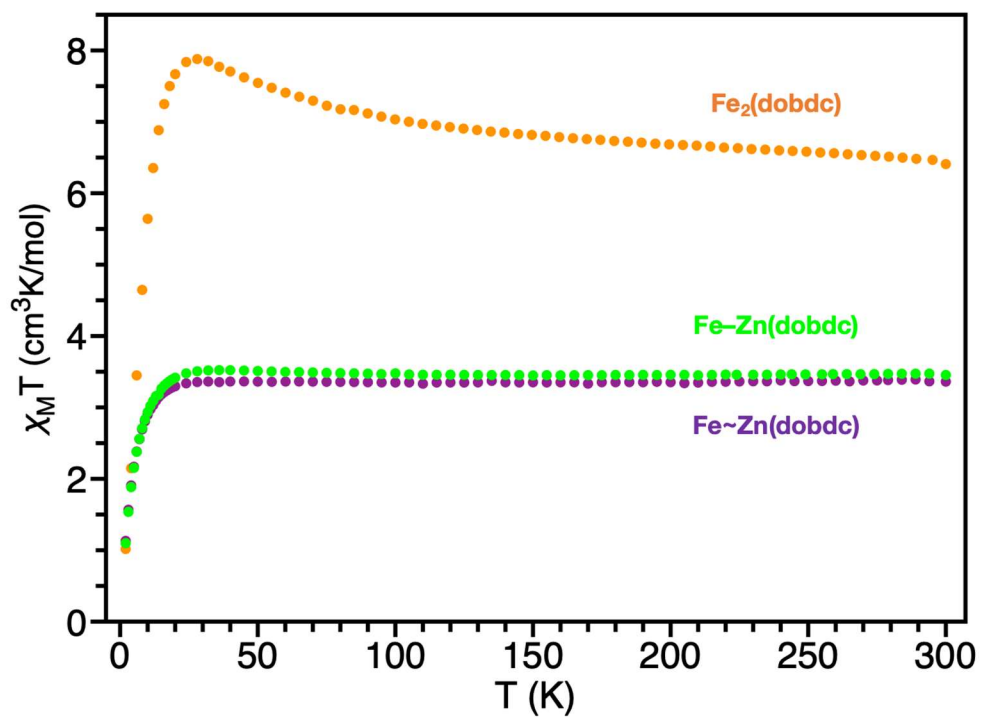


**Figure 2.S16:** Variable-temperature magnetic susceptibility for  $Fe_2(dobdc)$  collected at 10 kOe and for  $Fe-Zn(dobdc)$  and  $Fe\sim Zn(dobdc)$  collected at 1 kOe

# Chapter 3: Synthesis and Characterization of Iron–Gallate Frameworks

## 3.1 Introduction

The series of dense metal–organic frameworks that can be formed with gallic acid (3,4,5-trihydroxybenzoic acid, H<sub>4</sub>gallate) are a unique example of isostructural frameworks in that they are reported with metals in different oxidation states. Frameworks with divalent metal cations have been reported for Mg<sup>2+</sup>, Mn<sup>2+</sup>, Co<sup>2+</sup>, and Ni<sup>2+</sup> with gallic acid being doubly deprotonated: M(H<sub>2</sub>gallate)·2H<sub>2</sub>O, also reported as M(C<sub>7</sub>O<sub>5</sub>H<sub>4</sub>)·2H<sub>2</sub>O and M–gallate (**Figure 3.1**).<sup>1–3</sup> These materials are predated substantially by the Fe<sup>3+</sup> analog, with gallic acid being triply deprotonated: Fe<sup>III</sup>(Hgallate).<sup>4,5</sup> Not only does the crystal structure of this iron framework predate most known metal–organic frameworks, but there is also some evidence that this material could have existed since antiquity.

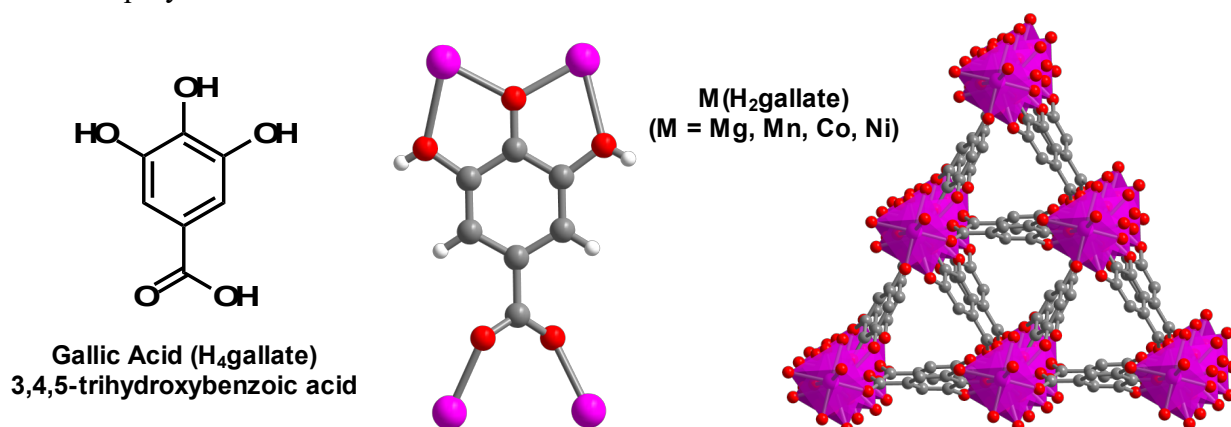


**Figure 3.1:** Chemical structure of gallic acid (left), crystal structure of H<sub>2</sub>gallate incorporated in the M(H<sub>2</sub>gallate) framework with hydroxy groups at positions 3 and 5 still protonated (center), and crystal structure of M(H<sub>2</sub>gallate) shown with view down the *c* axis (right).

Ferric iron–gallate, as is suggested by its original publication name “Eisengallustinte”, is a pitch black material that is derived from components used to make iron gall ink.<sup>5</sup> This ink is typically made from iron sulfate and extracts from oak gall nuts high in gallic acid and gallic-acid-derived tannic acids. Description of the dark coloration that arises when these reactants are mixed extends back to ancient Rome, where it was first reported by Gaius Plinius Secundus, also known as Pliny the Elder, in *Natural History* (77 AD).<sup>6</sup> An early recipe for an iron gall ink dates back to the 5<sup>th</sup> century in *Encyclopedia of Seven Liberal Arts* by Martianus Capella.<sup>7</sup> Iron gall ink has been used extensively as the most common form of ink for writing in the centuries since, falling out of use only in the mid 20<sup>th</sup> century with the development of synthetic dyes. Although this is still a topic of debate in the literature, recent studies have shown that iron gall ink from historic documents exhibits spectroscopic signatures similar to the crystalline framework, Fe<sup>III</sup>(Hgallate), and as the framework is “aged” by heating in air, the spectra become nearly identical.<sup>8–10</sup> The presence of microcrystalline or pseudo-amorphous iron–gallate in iron gall ink would certainly make it the oldest man-made metal–organic framework, although it would still be

predated by naturally occurring oxalate frameworks.<sup>11</sup> Apart from its potential historical significance, iron–gallate deserves particular attention because unlike the other metal analogs, it contains trivalent metal cations rather than divalent ones. The ferrous analog,  $\text{Fe}^{\text{II}}(\text{H}_2\text{gallate})\cdot 2\text{H}_2\text{O}$ , is conspicuously absent from the literature, despite the fact that  $\text{Fe}^{\text{III}}(\text{Hgallate})\cdot 2\text{H}_2\text{O}$  is made from a ferrous salt. If the ferrous congener can be synthesized, it could open multiple areas of study.

The extreme dark color of  $\text{Fe}^{\text{III}}(\text{Hgallate})\cdot 2\text{H}_2\text{O}$ , a visual indicator of low energy electronic transitions, could be derived from intrinsic electronic conductivity.<sup>12</sup> At only  $\sim 3.7$  Å, the Fe–Fe distance in  $\text{Fe}^{\text{III}}(\text{Hgallate})$  is one of the shortest among known metal–organic frameworks and suggests that electronic communication between sites could be possible. Additionally, as discussed in Chapter 1, octahedral iron centers are one of the metal species best suited for electronic conductivity in metal–organic frameworks due to the low reorganizational energy for the  $\text{Fe}^{\text{II/III}}$  redox couple, both for high spin and low spin electronic configurations.<sup>13</sup> Therefore, isolation of  $\text{Fe}^{\text{II}}(\text{H}_2\text{gallate})$  and accessing intermediate oxidation states of iron–gallate could allow for novel fundamental study of electronic conductivity. While studies probing the effect of redox state on conductivity in iron-based metal-organic frameworks have been performed for n-heterocyclic systems, these have required the insertion of large counterions.<sup>14,15</sup> These highly polarizing counterions could lead to decreased charge mobility due to the localization of charge through large polaron formation, as is suspected to be the case in hybrid perovskites.<sup>16</sup> Because gallate frameworks have the highly unusual property of containing protonated metal-bound phenols, these could be leveraged for charge balance; it may be possible to access different oxidation states post-synthetically without having to insert large charge balancing ions. As it is already proven that the gallate framework structure can exist with the ligand in different protonation states, protons could be inserted or removed to achieve charge neutrality under different metal oxidation states. Another possibility to further probe material redox states would be via ligand oxidation, as gallic acid has been shown to be redox active.<sup>17–19</sup>

Recently, metal–gallate frameworks were reported to not only have permanent porosity but also to have high gas adsorption selectivity for ethylene over ethane.<sup>20</sup> The industrial separation of ethylene from ethane is a process that is currently performed using energetically and financially expensive distillation columns, the replacement of which could noticeably impact global energy consumption.<sup>21</sup> In the case of  $\text{Co}(\text{H}_2\text{gallate})$ , the material was reported to have an ideal adsorbed solution theory (IAST) ethylene/ethane selectivity of 52 for a 50/50 ethylene/ethane mixture at 1 bar and 298 K, the highest reported value for any material. Ren et al. extensively studied the adsorption properties of Mg, Co, and  $\text{Ni}(\text{H}_2\text{gallate})$ , all of which showed ethylene selectivity. Notably, the iron framework was absent, ferric or otherwise. While the gas adsorption properties of  $\text{Fe}^{\text{II}}(\text{H}_2\text{gallate})$  could serve as an interesting comparison to the other metal analogues, a comparison of the properties of  $\text{Fe}^{\text{II}}(\text{H}_2\text{gallate})$  and  $\text{Fe}^{\text{III}}(\text{Hgallate})$  could be far more illuminating. Because of the incredibly small nature of the one-dimensional pore in the metal–gallate frameworks, the ethylene/ethane selectivity is attributed to size selective adsorption; it was proposed that ethane is incapable of fitting into a gallate framework pore. Therefore, even small changes in the pore environment, such as those caused by oxidation and/or deprotonation, could lead to dramatic changes in the gas sorption properties of this structure type.

## 3.2 Experimental

### Large scale synthesis of $\text{Fe}^{\text{II}}(\text{H}_2\text{gallate})\cdot 2\text{H}_2\text{O}$

Inside an aqueous compatible glove box, 3.042 g of anhydrous  $\text{FeCl}_2$  beads (24 mmol, 1 eq.), 4.515 g of gallic acid monohydrate (24 mmol, 1 eq.), and 300 mL of deoxygenated aqueous 0.05 M KOH solution were added to a 350 mL heavy walled glass reaction vessel. The vessel was sealed with a Teflon plug and o-ring, transferred out of the glovebox, heated in an oil bath at 120 °C for 24 hours and then transferred back into the glovebox. Filtering the precipitate and washing with water yielded ~650 mg (2.5 mmol, 10.4% yield) of off white  $\text{Fe}^{\text{II}}(\text{H}_2\text{gallate})\cdot 2\text{H}_2\text{O}$ .

### Single crystal synthesis of $\text{Fe}^{\text{II}}(\text{H}_2\text{gallate})\cdot 2\text{H}_2\text{O}$

Inside an argon glove box, 380 mg of anhydrous  $\text{FeCl}_2$  beads (3 mmol, 1 eq.) and 564 mg of anhydrous gallic acid (3 mmol, 1 eq.) were added to a 50 mL solvent bomb. The vessel was sealed, transferred out of the glovebox and cycled onto a Schlenk line. Approximately 30 mL of deoxygenated aqueous 0.05 M KOH solution was transferred via cannula to the solvent bomb. The vessel was sealed and heated in an oil bath at 75 °C for 5 days, yielding <50 mg of off-white single crystals of  $\text{Fe}^{\text{II}}(\text{H}_2\text{gallate})\cdot 2\text{H}_2\text{O}$ .

### Synthesis of $\text{Fe}^{\text{II/III}}(\text{H}_x\text{gallate})$

Inside an aqueous compatible glove box, 382 mg of  $\text{Fe}^{\text{II}}(\text{H}_2\text{gallate})\cdot 2\text{H}_2\text{O}$  (1.47 mmol, 1 eq.) and 200 mg of ferrocenium tetrafluoroborate (0.74 mmol, 0.5 eq.) were combined in a 20 mL scintillation vial with 10 mL of deoxygenated water and a stir bar. After stirring for 24 hours, a black solid was filtered and rinsed with water and methanol before being activated at 120 °C under dynamic vacuum to yield ~240 mg of  $\text{Fe}^{\text{II/III}}(\text{H}_x\text{gallate})$  (1.08 mmol, 73% yield).

### Gas sorption measurements

Isothermal measurements were performed using a Micromeritics 3Flex Surface Characterization Analyzer. For each framework, ~50 mg of preactivated material was loaded into a preweighed ½” glass sample tube inside an argon glove box. Each tube was sealed with a Mircomeritics *Transeal* in order to properly perform gas sorption measurements without risking exposure to air. Adsorption measurements were performed with  $\text{N}_2$  at 77 K, with  $\text{CO}_2$  at 195 K, with  $\text{C}_2$  gasses ( $\text{C}_2\text{H}_6$ ,  $\text{C}_2\text{H}_4$ , and  $\text{C}_2\text{H}_2$ ) at 303, 313, and 323 K. An additional isotherm was performed for  $\text{C}_2\text{H}_6$  in  $\text{Fe}^{\text{II}}(\text{H}_2\text{gallate})\cdot 2\text{H}_2\text{O}$  at 195 K. 77 and 195 K temperatures were achieved using a liquid  $\text{N}_2$  bath and a dry ice/isopropanol bath, respectively. 303, 313, and 323 K temperatures were achieved with a heated/cooled water circulator.

### Mössbauer measurements

Zero-field  $^{57}\text{Fe}$  Mössbauer spectra were recorded in constant acceleration spectrometer (See Co. Edina, MN) between room temperature and 5 K in a Janis Research Co. cryostat (Willington, MA). Collected spectra were analyzed using the WMOSS software package (See Co. Edina, MN). Isomer shifts are reported relative to  $\alpha$ -iron (30  $\mu\text{m}$  foil) at 295 K. For each sample approximately 20–30 mg of material was placed in a nylon washer with an area of ~1.3  $\text{cm}^2$ , and carefully sealed between multiple layers of Scotch packing tape in a glovebox. The protected samples were transferred rapidly in air into the spectrometer under a flow of helium and were measured under a small pressure of helium in the cryostat. All spectra were fit to either one or two Lorentzian doublets.

### 3.3 Results and Discussion

#### Synthesis of $\text{Fe}^{\text{III}}(\text{Hgallate})\cdot 2\text{H}_2\text{O}$

Initial attempts to replicate the reported synthesis<sup>2</sup> of the ferric–gallate framework  $\text{Fe}^{\text{III}}(\text{Hgallate})\cdot 2\text{H}_2\text{O}$  were unsuccessful. This contrasted greatly with the other reported metal analogs: Mg, Co, and  $\text{Ni}(\text{H}_2\text{gallate})\cdot 2\text{H}_2\text{O}$ , all of which were readily synthesized according to reported methods.<sup>2</sup> Addition of ferrous chloride tetrahydrate to a 0.05M potassium hydroxide aqueous solution and an equivalent of gallic acid in air immediately resulted in a dramatic color change of the solution to dark purple/black and rapid precipitation of a black solid. The solution mixture was heated in a Teflon lined bomb at 120 °C as previously reported but across multiple attempts gave only very weakly crystalline material. Attempts to synthesize the desired phase directly from multiple ferric sources, including  $\text{FeCl}_3\cdot 6\text{H}_2\text{O}$ , resulted in the near instantaneous precipitation of amorphous black solid. Additionally, screens performed with  $\text{FeSO}_4\cdot 7\text{H}_2\text{O}$  (the only other readily available pseudo-air stable ferrous source present in lab) also gave amorphous black material. From these results, I inferred that both the valence state and counterion of the metal source were critically important in the formation of the desired phase. It is possible that the iron–gallate framework only forms a crystalline solid with ferrous ions in solution and then becomes oxidized to the ferric solid. I became concerned that the root of my problem was a substantial valence impurity in the  $\text{FeCl}_2\cdot 4\text{H}_2\text{O}$  leading to initial amorphous precipitate. Instead, the use of anhydrous  $\text{FeCl}_2$  beads, that had been stored in a glovebox and were known to have high valence purity, led to substantially increased crystallinity despite the reaction solution visually behaving the same.

In one replicate reaction screen of the reported synthesis but with anhydrous  $\text{FeCl}_2$ , all of the solution in the Teflon lined reactor evaporated, presumably via a leak in the liner, yielding the some of the largest MOF crystals I have ever grown to date: long intergrown black needles up to a millimeter in length (**Figure 3.2**). While these crystals did not diffract sufficiently well enough to obtain a single crystal structure, powder X-ray diffraction indicates that material is isostructural to  $\text{Fe}^{\text{III}}(\text{Hgallate})$  (**Figure 3.3**).  $^{57}\text{Fe}$  Mössbauer spectroscopy also confirmed that these crystals were  $\text{Fe}^{\text{III}}$  (despite using an  $\text{Fe}^{\text{II}}$  salt as the metal source) (**Figure 3.4**). While attempts to replicate this serendipitous result were unsuccessful, the result highlights an interesting flaw of the synthetic scheme. Because the reaction solution contains only one equivalent of base (KOH) per equivalent of gallic acid, the theoretical yield is limited to 33%;  $\text{H}_4\text{gallate}$  must liberate three equivalents of  $\text{H}^+$  in order to form  $\text{Fe}^{\text{III}}(\text{Hgallate})$ . Any further framework formation would acidify the solution, in addition to the acidic protons contributed by the carboxylic acid of gallic acid dissolved in solution. Over the course of a synthesis, as the solution acidifies above a threshold some of the framework will begin to dissolve. This will eventually lead to an equilibrium between acidic solution and incomplete consumption of reagents. At elevated temperatures, the vapor phase in the reaction vessel should become disproportionately gaseous HCl, due to its volatility.<sup>22,23</sup> By allowing some of the acid byproduct to leave in the form of HCl leaking out, this large crystal reaction was able to slowly proceed further to completion.

Additionally, the concentration of the reaction solution further increases the driving force for the formation of a precipitate. While the reaction mixture may start out supersaturated, framework formation should deplete the concentration of reagents below supersaturation; as solvent evaporates, the reaction will again become supersaturated. This contrasts dramatically with typical solvothermal reactions which can proceed to completion by the generation of a large excess of

base via solvent decomposition. Attempts to apply solvothermal routes to the synthesis of  $\text{Fe}^{\text{III}}(\text{Hgallate})$  only yielded amorphous product or, in one case, a different phase with an elemental analysis predicted formula of  $\text{Fe}_2(\text{gallate})$  (Figure 3.S1). In order to improve the synthesis of not only  $\text{Fe}^{\text{III}}(\text{Hgallate})$  but also of the other metal–gallate frameworks (which rely on a similar synthetic scheme), different synthetic routes will need to be explored, see Chapter 4.

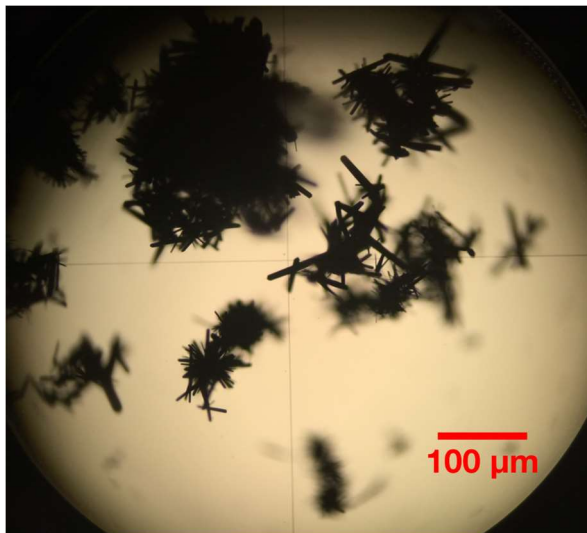


Figure 3.2: Optical microscope image of black needles from iron–gallate screens.

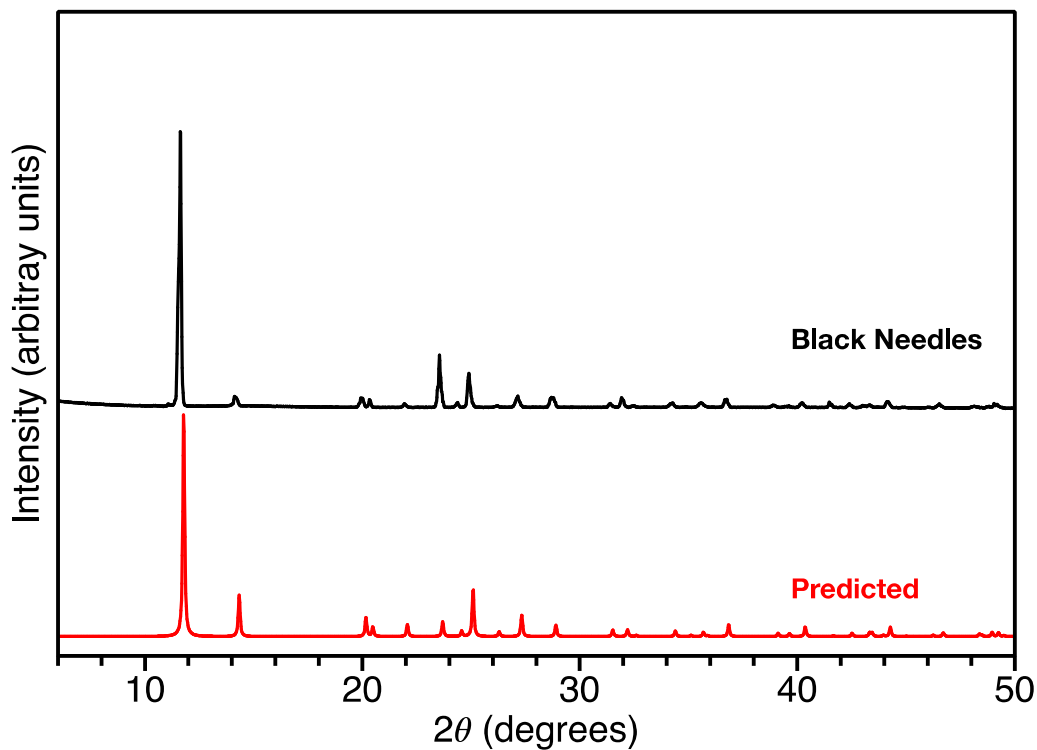
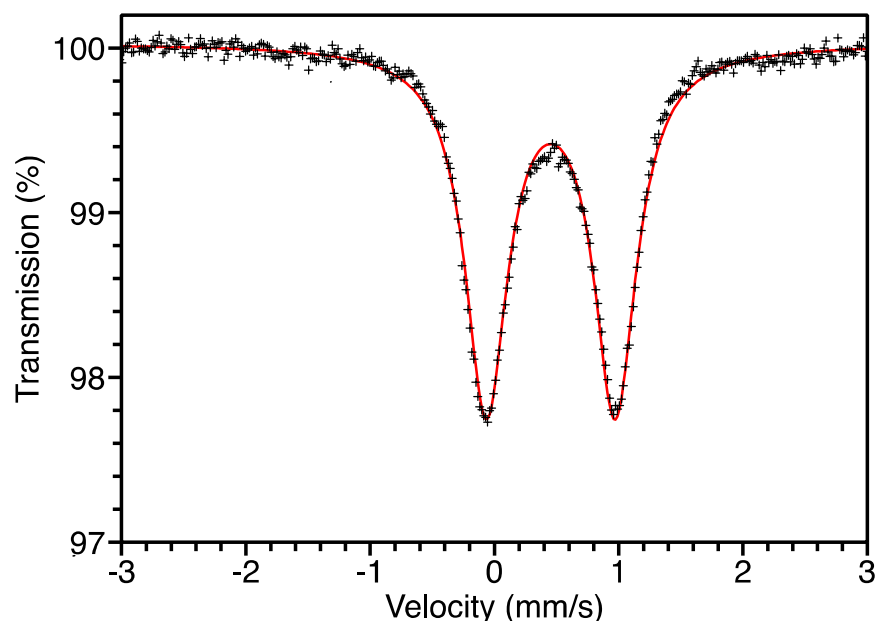


Figure 3.3: Powder X-ray diffraction pattern of large black needles from iron–gallate screens (black, top) matching predicted powder pattern for  $\text{Fe}^{\text{III}}(\text{Hgallate}) \cdot 2\text{H}_2\text{O}$  (red, bottom).



**Figure 3.4:**  $^{57}\text{Fe}$  Mössbauer spectrum for  $\text{Fe}^{\text{III}}(\text{Hgallate})$  collected at 290 K (black crosses), consistent with a single high spin  $\text{Fe}^{\text{III}}$  site (red line).

### Synthesis of $\text{Fe}^{\text{II}}(\text{H}_2\text{gallate})\cdot 2\text{H}_2\text{O}$

Initial results in synthesizing  $\text{Fe}^{\text{III}}(\text{Hgallate})$  implied that ferrous ions were requisite to the formation of the crystalline framework. While there is precedent for iron ions to be incorporated into a crystalline framework concomitant with a change in oxidation state, the only oxidizing species present in the iron-gallate reaction is residual atmospheric  $\text{O}_2$ .<sup>24</sup> Because reduced oxygen species are not present in the crystalline product, it is possible that ferrous-gallate forms initially and is then oxidized to ferric-gallate. It stands to reason that the removal of any appreciable  $\text{O}_2$  concentration from the reaction mixture could lead to the isolation of the unreported ferrous phase:  $\text{Fe}^{\text{II}}(\text{H}_2\text{gallate})\cdot x\text{H}_2\text{O}$ . The largest hurdle initially for this goal was the inability to load and unload the reaction vessel, in this case a Teflon lined reaction bomb, in an anaerobic environment. Because the reaction is performed in aqueous media, it was relegated to the use of a nitrogen filled glove bag. Independent of how much the glove bag was purged prior to use, the reaction mixture always became black and any isolated product was found to match the PXRD pattern for  $\text{Fe}^{\text{III}}(\text{Hgallate})\cdot 2\text{H}_2\text{O}$ . As the reported reaction is expected to proceed at elevated pressures, since water at 120 °C should exceed 2 bar of vapor pressure, I was wary of utilizing typical Schlenk flasks. I turned instead to my experience in sealing glass tubes as reaction vessels for anaerobic syntheses. Standard lab practice at the time was to use a ground glass joint valve or Teflon stopcock valve connected to a  $\frac{1}{2}$ " tube glass tube via a short rubber tube; 1-2 mL of reaction solution was loaded into a  $\frac{1}{2}$ " glass tube inside a glovebox, the "adapter" was attached, the tube was cycled out of the box, freeze-pump-thawed on a Schlenk line, and then flame sealed. I was able to find one sealed tube "adapter" that had been made from a 14/20 ground glass Schlenk adapter that would allow me to transfer solution to the tube via cannula using standard Schlenk technique. By loading  $\text{FeCl}_2$  and gallic acid into a glass tube inside an argon glove box, then transferring the tube with this particular adapter onto my Schlenk line, and finally cannula transferring ~1 mL of deoxygenated 0.05M KOH(aq) solution, I was able for the first time avoid to the dramatic color change the reaction solution normally exhibits. Rather than the usual dark purple/black color, the

reaction mixture was slightly green (presumably from the formation of some ferrous iron hydroxide). When properly sealed and reacted at 120 °C, this tube and subsequent sealed tubes made using this method, formed an off-white solid. Upon exposure to air, the white solid immediately turned black, and PXRD measurements confirmed the material was consistent with the metal–gallate structure type.

In order to possibly improve this synthesis and increase the number of adapters available, I consulted with the College of Chemistry’s in-house professional glass blower, Jim Breen, about the fabrication of better sealed tube adapters. This led to the creation of a substantially improved sealed tube adapter capable of maintaining a much more rigorously air-free seal while also allowing for standard Schlenk chemistry. Due to the numerous uses that have been found for this adapter, I am dubbing it a “Breen adapter”; its uses are further discussed in **Appendix A**. With multiple Breen adapters in hand, I was able to screen more reaction conditions for  $\text{Fe}^{\text{II}}(\text{H}_2\text{gallate})\cdot x\text{H}_2\text{O}$  and improve both crystallinity and yield. I also discovered that crystalline iron–gallate could be obtained at lower temperatures (100 °C and below), opening the door for the possibility of safe Schlenk chemistry and subsequent isolation of valence pure  $\text{Fe}^{\text{II}}(\text{H}_2\text{gallate})$  without the dramatically colorful oxidation. Larger scale reactions (50-200 mL) performed by loading Schlenk flasks with the solid reagents in a glove box and cannula transferring aqueous potassium hydroxide solutions invariably yielded purple/black solutions after heating for 12-16 hours. It appears that this reaction is sensitive enough to trace oxygen that typical greased ground glass seals are not sufficient to prevent evident oxidation while the reaction proceeds.

This problem can be solved (albeit unconventionally) by utilizing either a Schlenk storage flask or a Straus flask as the reaction vessel. With a Teflon-to-glass seal rather than a grease-ground glass based one,  $\text{Fe}^{\text{II}}(\text{H}_2\text{gallate})\cdot x\text{H}_2\text{O}$  can be readily obtained at arbitrary scale. It is possible to transfer this framework into a standard glove box by first performing multiple careful cannula transfers to remove the supernatant and wash the framework with anhydrous methanol while heating to remove any internally bound water. Alternatively, the advent of an aqueous compatible glove box dramatically simplified the synthesis and manipulation of  $\text{Fe}^{\text{II}}(\text{H}_2\text{gallate})\cdot x\text{H}_2\text{O}$ . The entire reaction solution can be prepared, heated (only up to 100 °C), and product isolated in an anaerobic environment. Larger scale syntheses can be performed with a much safer heavy walled Chemglass reaction vessel (CG-1880-42), prepared inside the water box, transferred out, heated in an oil bath behind a blast shield, and transferred back in to the water box without any visual indication of oxidation. PXRD measurements formed on a sealed capillary of  $\text{Fe}^{\text{II}}(\text{H}_2\text{gallate})\cdot x\text{H}_2\text{O}$  exhibit diffraction peaks consistent with  $\text{Fe}^{\text{III}}(\text{H}_2\text{gallate})\cdot 2\text{H}_2\text{O}$  but shifted to lower angle, as expected due to the inclusion of larger  $\text{Fe}^{\text{II}}$  cations (**Figure 3.5**). Additionally,  $^{57}\text{Fe}$  Mössbauer measurements confirm that the material is entirely ferrous in nature, exhibiting only one iron signature (**Figure 3.6**). After my initial isolation of ferrous iron–gallate in July 2015, Wagner and Lerf reported the  $^{57}\text{Fe}$  Mössbauer of a  $\text{Fe}^{\text{II}}$  analog of iron–gallate in August 2015.<sup>10</sup> This material was described as a “blue-green precipitate” and was not isolated nor characterized further: “ $\text{Fe}^{\text{II}}$ gallate oxidizes easily at room temperature to  $\text{Fe}^{\text{III}}$ gallate and could therefore not be obtained in the dried form and no attempts to obtain XRD patterns could be made.”<sup>10</sup> Synthesized via common Schlenk techniques at room temperature, this material was most likely an amorphous or weakly crystalline form of ferrous–gallate with trace oxidation, but this report underscores the difficulty in synthesizing and isolating crystalline ferrous–gallate cleanly.

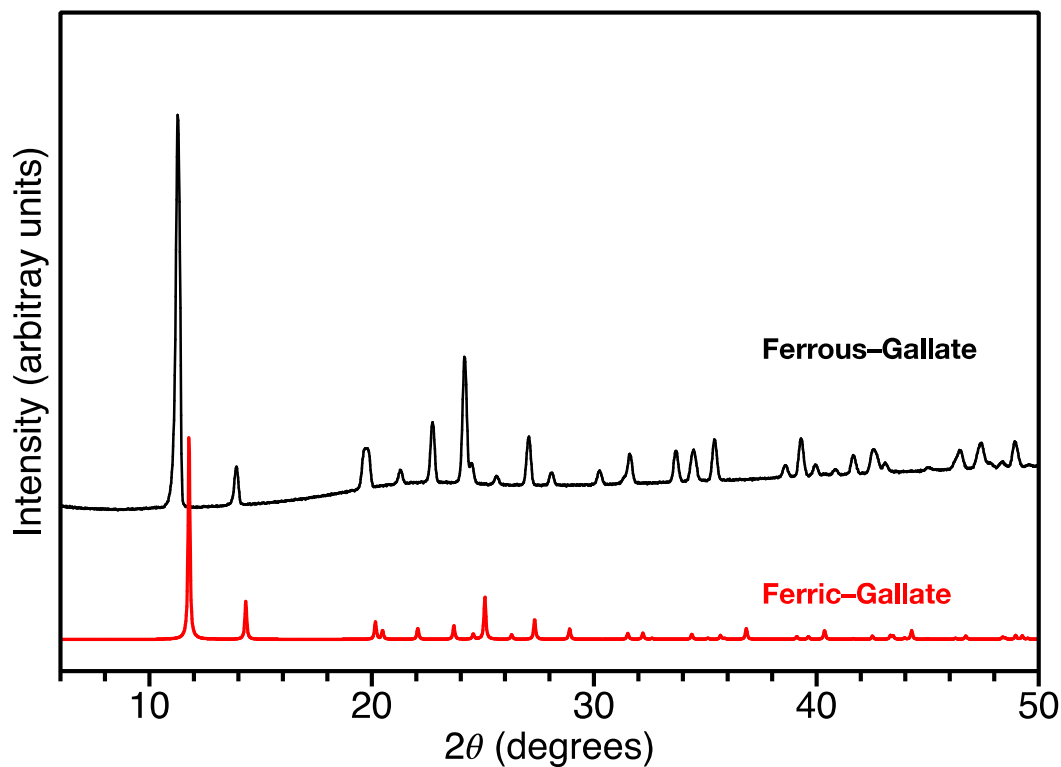


**Figure 3.5:** X-ray powder diffraction pattern of off-white powder presumed to be  $\text{Fe}^{\text{II}}(\text{H}_2\text{gallate}) \cdot x\text{H}_2\text{O}$  (black) matching predicted powder pattern for  $\text{Fe}^{\text{III}}(\text{Hgallate}) \cdot 2\text{H}_2\text{O}$  (red).

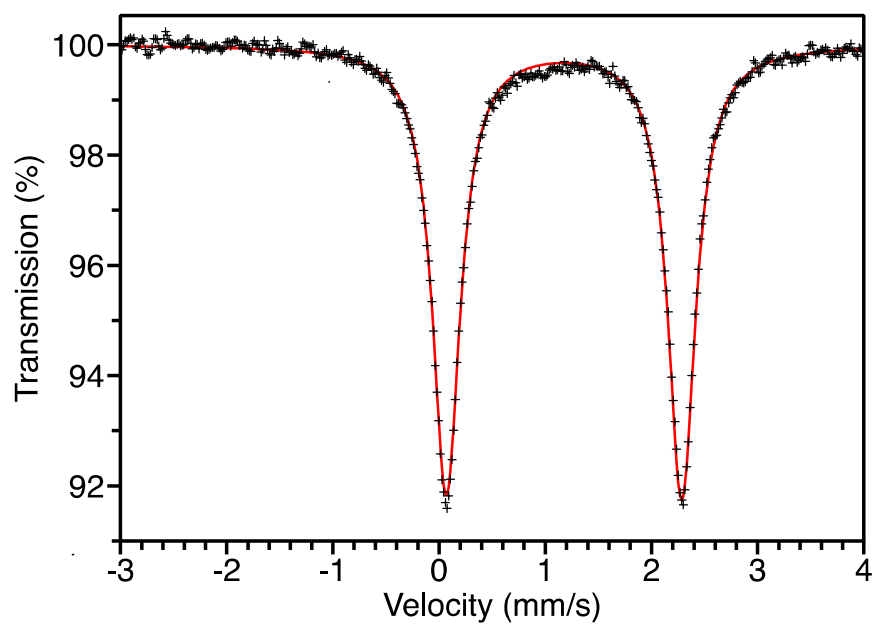


**Figure 3.6:**  $^{57}\text{Fe}$  Mössbauer spectrum for  $\text{Fe}^{\text{II}}(\text{H}_2\text{gallate})$  collected at 295 K (black crosses), consistent with a single high spin  $\text{Fe}^{\text{II}}$  site (red line).

### Single-Crystal Diffraction of $\text{Fe}^{\text{II}}(\text{H}_2\text{gallate})\cdot 2\text{H}_2\text{O}$ and $\text{Fe}^{\text{III}}(\text{H}_2\text{gallate})\cdot x\text{H}_2\text{O}$

By performing the ferrous-gallate reaction for a longer period of time (5 days compared to 1) and at a lower temperature (75 °C compared to 100 °C), I obtained single crystals of sufficiently high quality for diffraction (**Figure 3.7**). A crystal of  $\text{Fe}^{\text{II}}(\text{H}_2\text{gallate})\cdot x\text{H}_2\text{O}$  was quickly removed from solution, encased in paratone oil and solidified/cooled in a cryostream to 100 K to measure a single crystal structure (**Figure 3.8**). The structure of  $\text{Fe}^{\text{II}}(\text{H}_2\text{gallate})\cdot x\text{H}_2\text{O}$  has the chiral space group  $P3_121$ ; this is consistent with the other gallate frameworks which form as a mixture of enantiopure  $P3_121$ , and  $P3_221$  crystals. Unlike other reported structures, however,  $\text{Fe}^{\text{II}}(\text{H}_2\text{gallate})\cdot x\text{H}_2\text{O}$  has a unit cell  $c$  axis length that is nearly twice as long (21.284 Å vs ~10.8 Å). This unit cell doubling appears to be caused by a slight twist in the helical change leading to two distinct iron centers and two distinct gallate ligands in the asymmetric unit. It is not immediately obvious why the material adopts this conformation and other  $\text{M}(\text{H}_2\text{gallate})$  structures do not. These iron sites have bond lengths consistent with high spin  $\text{Fe}^{\text{II}}$  centers, which are drastically different than previously reported iron–gallate structures.<sup>2,5,8</sup> As with other  $\text{M}(\text{H}_2\text{gallate})\cdot 2\text{H}_2\text{O}$  crystal structures, there is a water molecule hydrogen bonding with each protonated phenol on the linker leading to the expected empirical formula of  $\text{Fe}^{\text{II}}(\text{H}_2\text{gallate})\cdot 2\text{H}_2\text{O}$ .

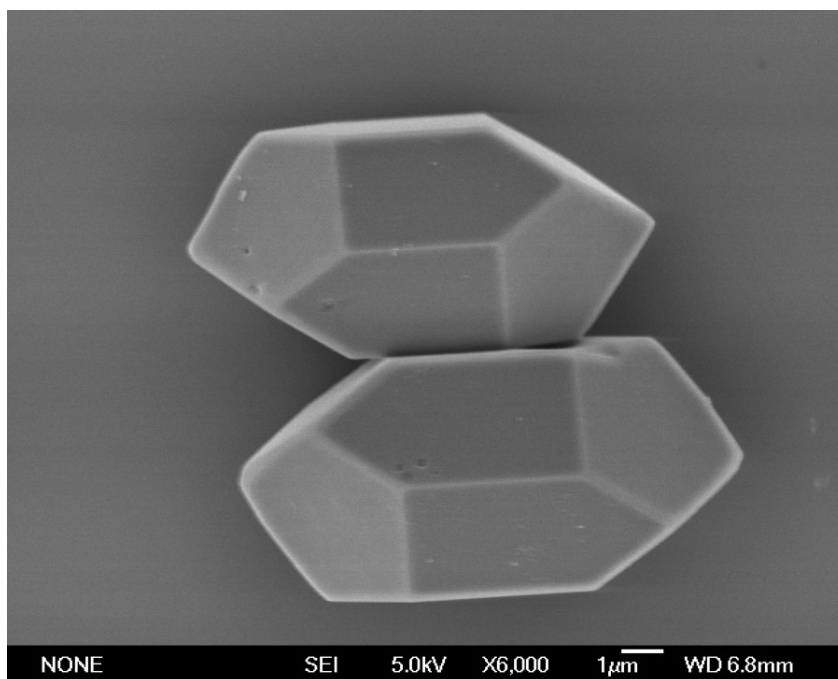


**Figure 3.7:** Scanning electron microscopy image of single crystals of  $\text{Fe}^{\text{II}}(\text{H}_2\text{gallate})\cdot 2\text{H}_2\text{O}$ , exhibiting clearly defined facets consistent with a pentagonal dodecahedron elongated along a 3-fold axis.

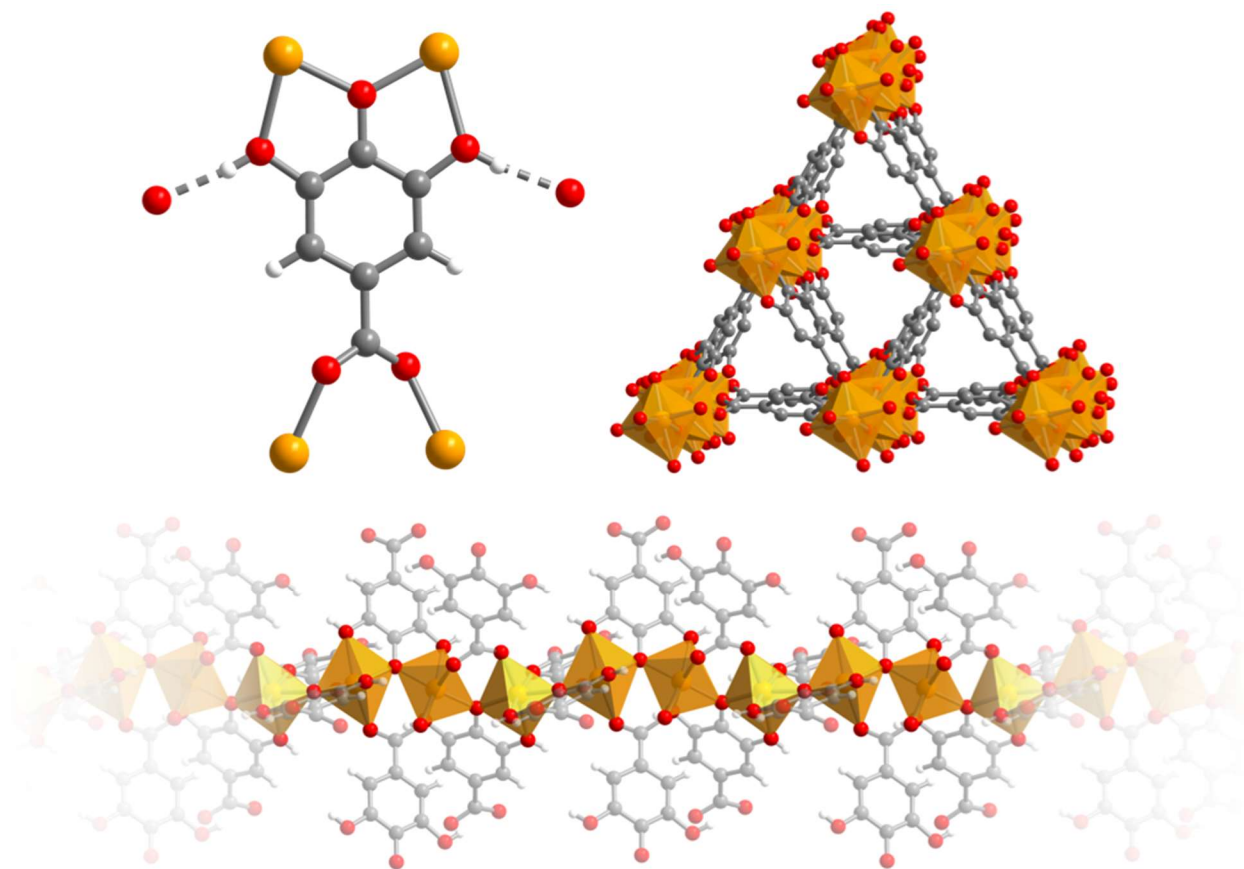


**Figure 3.8:** Single-crystal structure of  $\text{Fe}^{\text{II}}(\text{H}_2\text{gallate})\cdot 2\text{H}_2\text{O}$ : single ligand with two hydrogen bound water oxygen atoms (top left), view of multiple one-dimensional channels down the  $c$  axis (top right), a single vertex sharing chain of octahedral  $\text{Fe}^{\text{II}}$  centers that run along the  $c$  axis (bottom).

Following the initial collection of X-ray diffraction data on  $\text{Fe}^{\text{II}}(\text{H}_2\text{gallate})\cdot 2\text{H}_2\text{O}$ , the crystal was left in air at ambient temperature for three hours. This exposure allowed the crystal to oxidize via the diffusion of  $\text{O}_2$  through the coating of paratone oil. Despite this irreversible reactivity, the crystal maintained single crystallinity and a second X-ray diffraction data set was collected. The  $c$  axis doubled unit cell is no longer observed and the unit cell dimensions are now consistent with other reported  $\text{Fe}^{\text{III}}(\text{Hgallate})\cdot x\text{H}_2\text{O}$  structures. Interestingly, the chirality of the unit cell has changed to  $\text{P}3_221$  from  $\text{P}3_121$  despite using the same crystal for both structures. Closer inspection of the helical metal chain reveals that the handedness has not changed but rather that the repeat distance of the threefold screw axis is different (**Figure 3.9**). This repeat distance is related to two distinct iron centers being present in the asymmetric unit of  $\text{Fe}^{\text{II}}(\text{H}_2\text{gallate})\cdot 2\text{H}_2\text{O}$  compared to just one iron center in that of  $\text{Fe}^{\text{III}}(\text{Hgallate})\cdot x\text{H}_2\text{O}$ . After oxidation the bond lengths of these iron centers are consistent with high spin  $\text{Fe}^{\text{III}}$  and the other reported  $\text{Fe}^{\text{III}}(\text{Hgallate})\cdot x\text{H}_2\text{O}$  structures (**Figure 3.10 and Table 3.1**). Additionally, the water molecules in the pore are now substantially more disordered possibly due to heterogeneity in the protonation state of the linker.

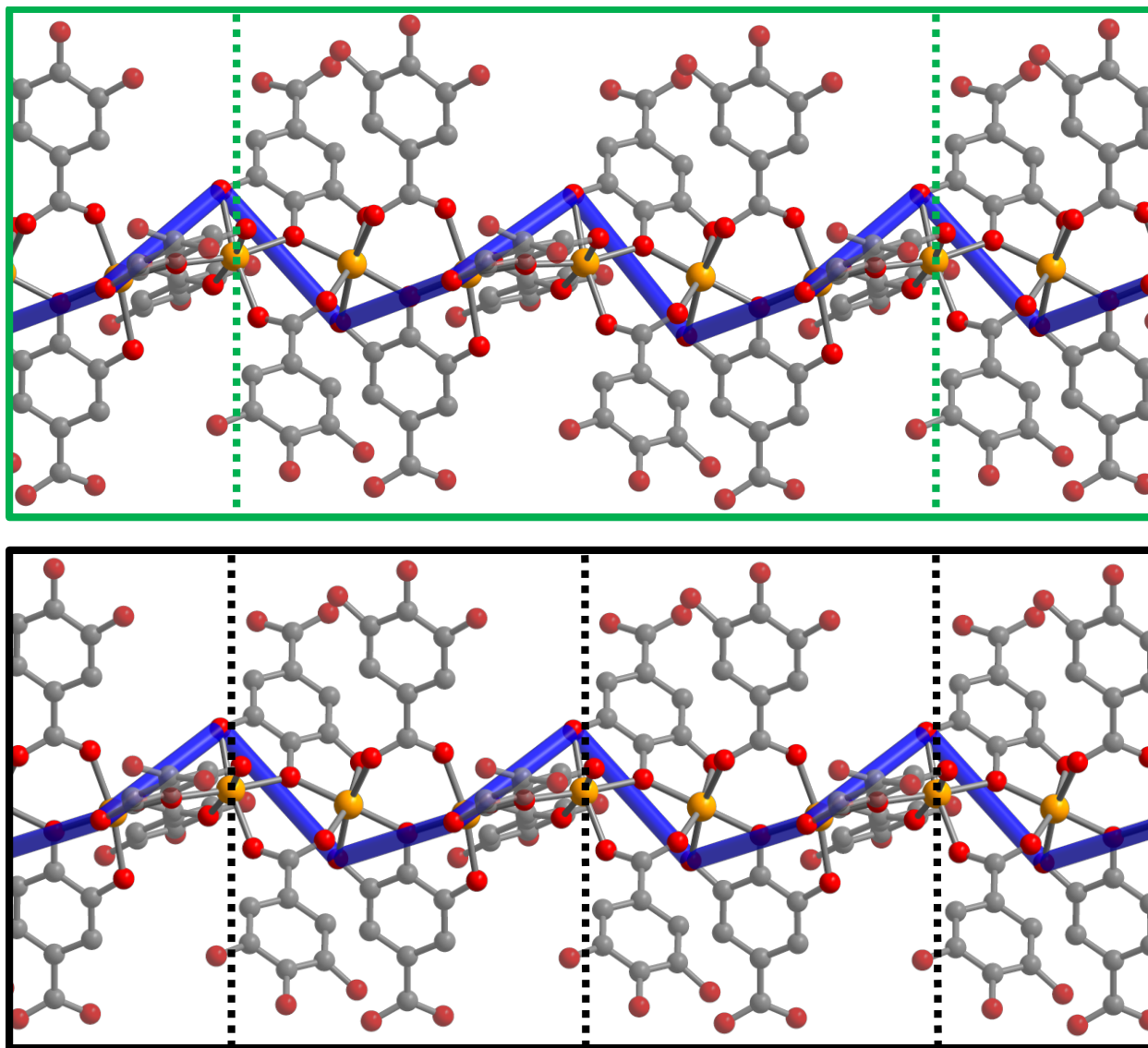


**Figure 3.9:** Side-on view of chiral metal helix along *c* axis of  $\text{Fe}^{\text{II}}(\text{H}_2\text{gallate}) \cdot 2\text{H}_2\text{O}$  (top, green) and  $\text{Fe}^{\text{III}}(\text{Hgallate}) \cdot 2\text{H}_2\text{O}$  (bottom, black) demonstrating the same handedness, with crystallographic *c* cell edges added (dashed lines). Although it is difficult to perceive, the ferrous unit cell is slightly less than twice the length of the ferric unit cell along the *c* axis. For visual clarity of the chiral helix, blue connections are drawn between terminal phenyl groups.

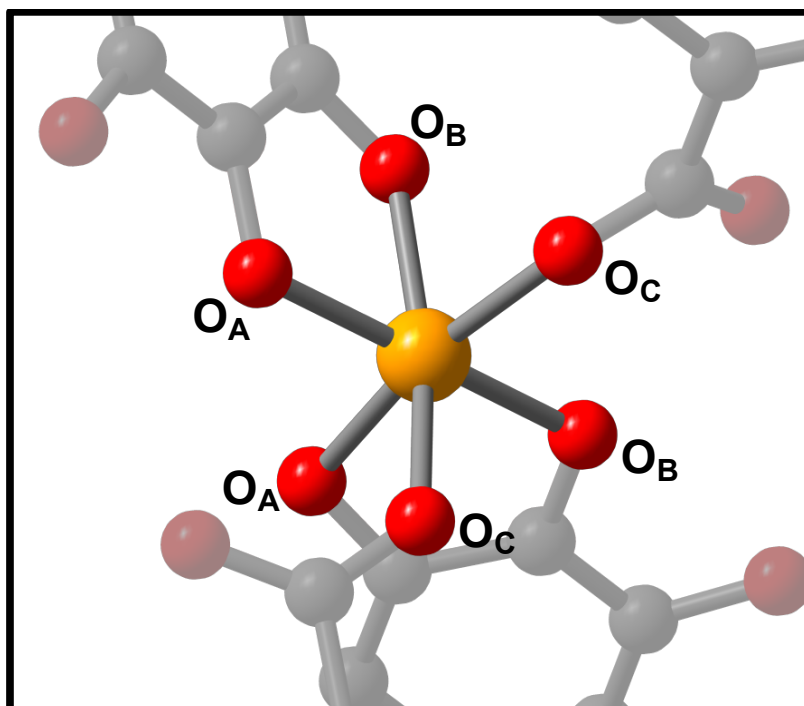


**Figure 3.10:** Single metal site in iron–gallate with oxygen atoms labeled for reference to **Table 3.1:** bridging middle phenol ( $O_A$ ), terminal side phenol ( $O_B$ ), carboxylate ( $O_C$ ). Adjacent metal sites omitted for visual clarity.

**Table 3.1:** Fe–O bond lengths (Å) for published iron–gallate crystal structures and this work (\*), with oxygen labels defined by **Figure 3.10**.

Structure	Fe– $O_A$	Fe– $O_B$	Fe– $O_C$
$\text{Fe}^{\text{II}}(\text{H}_2\text{gallate})\cdot 2\text{H}_2\text{O}^*$ (Site 1)	2.015(9)	2.263(19)	2.100(13)
$\text{Fe}^{\text{II}}(\text{H}_2\text{gallate})\cdot 2\text{H}_2\text{O}^*$ (Site 2)	2.014(8)	2.272(14)	2.101(12)
$\text{Fe}^{\text{III}}(\text{Hgallate})\cdot 2\text{H}_2\text{O}^*$	2.003(5)	2.082(12)	2.023(12)
$\text{Fe}^{\text{III}}(\text{Hgallate})\cdot 2\text{H}_2\text{O}^4$	2.000(4)	2.028(5)	2.006(5)
$\text{Fe}^{\text{III}}(\text{Hgallate})\cdot 2\text{H}_2\text{O}^2$	2.020(4)	1.999(14)	2.022(6)
$\text{Fe}^{\text{III}}(\text{Hgallate})\cdot 2\text{H}_2\text{O}^8$	2.009(10)	2.075(3)	2.041(5)

Structures of oxidized metal–organic frameworks are uncommon but by no means rare. Often, frameworks maintain local crystallinity upon reactivity with oxygen, or another oxidant, but individual crystals fragment, limiting structural characterization to powder diffraction experiments.<sup>25,26</sup> Most reported oxidized structures are achieved via careful oxidation under water-free conditions, as the combination of water and a reactive species such as superoxide often lead to framework degradation. There are a much smaller number of frameworks where crystals were exposed to air for a period of time and an oxidized structure was obtained.<sup>27,28</sup> The Fe<sup>II</sup>(H<sub>2</sub>gallate)-Fe<sup>III</sup>(Hgallate) single-crystal-to-single-crystal oxidation is thus particularly interesting as in addition to being performed in air with structures obtained on the same crystal, there are no open metal sites and there is no obvious sign of incorporation of the oxidizing species. In most other reported structures of oxidized frameworks, reduction occurs at a coordinatively unsaturated metal site. Whether these sites have five-,<sup>26,29,30</sup> four-,<sup>31</sup> three-,<sup>27</sup> or two-coordinate metals,<sup>28</sup> they invariably result in a new oxidation-byproduct species bound in the framework.

While oxygen atoms assigned to water in the ferric structure are much more disordered than in the ferrous material, distances between these sites are either too large or too small to correspond to a reduced O<sub>2</sub> species. Despite the apparent pore filling by water, as evident in a space-filling view of the structure (**Figure 3.11**), the material was still able to oxidize. While it is conceivable that O<sub>2</sub> could diffuse into the solid, it would have to displace water bound via a strong hydrogen bond; this process would be very slow, particularly for a material with one-dimensional pores. The rapid oxidation of this material and the absence of reduced species in the pore implies that the crystal oxidizes on its exterior surface. Via conduction of charges (both protons and electrons) from interior unit cells, the entire material converts from a ferrous solid to a ferric one.

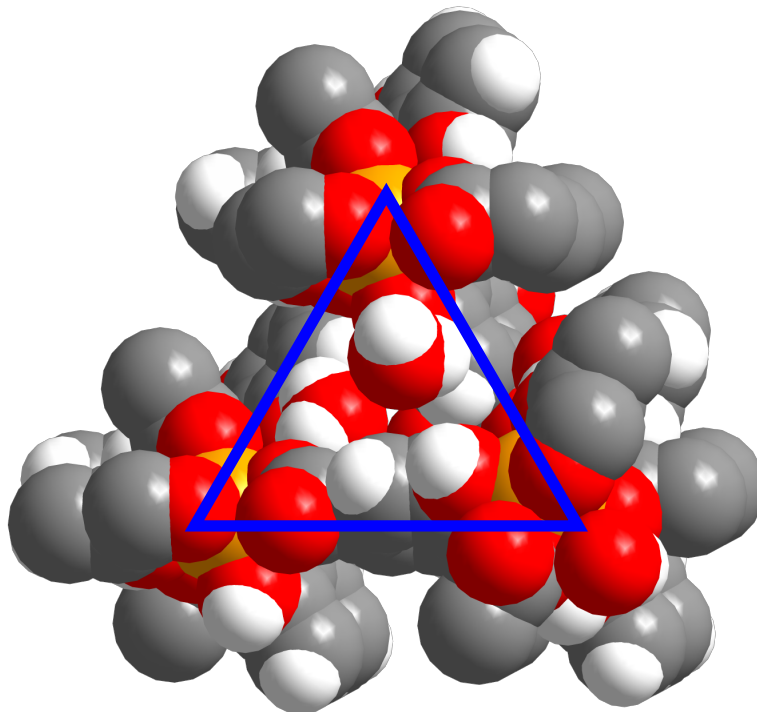


**Figure 3.11:** Space filling model of Fe<sup>II</sup>(H<sub>2</sub>gallate)·2H<sub>2</sub>O, showing a nearly completely blocked triangular pore (blue triangle for clarity).

## Oxidation of Fe<sup>II</sup>(H<sub>2</sub>gallate)

As directly observed by the single crystal diffraction experiments and indirectly via Fe<sup>III</sup>(Hgallate) synthetic attempts, Fe<sup>II</sup>(H<sub>2</sub>gallate) can be oxidized to Fe<sup>III</sup>(Hgallate) without a substantial loss in crystallinity. As becomes immediately apparent upon trying to handle the ferrous framework, it is extremely oxygen sensitive. Even inside a catalyst regulated glove box under “inert” atmosphere, the material must be handled with care. Whether in the process of filtering the framework from the reaction solution or transferring dry powder, a visual color change is readily seen if the glove box atmosphere has even 1 ppm of O<sub>2</sub>. Fe<sup>II</sup>(H<sub>2</sub>gallate)·2H<sub>2</sub>O, which can be synthesized as a pure white powder, will darken gradually through shades of grey to eventually black as it oxidizes. This material can be stored long term without a color change, but only in a sealed glass ampule. Interestingly, this extreme sensitivity is also present for the reactants in solution. A basic solution of FeCl<sub>2</sub> and gallic acid will turn purple in the presence of ppm, or possibly lower, concentrations of oxygen. While I have used this as a litmus test for the presence of oxygen in a water compatible glovebox, it could potentially be used for detecting oxygen in solvents such as methanol that are normally incompatible with typical diagnostics such as titanocene<sup>32</sup> or ketal.<sup>33</sup>

While both the entirely ferrous and entirely ferric states of the iron–gallate framework can be readily accessed, cleanly accessing a mixed-valent state presents an interesting challenge. Oxidation via O<sub>2</sub> is not a viable route, even with carefully controlled dosing, because the oxidation is incredibly rapid and exothermic and readily leads to material heterogeneity. Individual crystallites could oxidize entirely to Fe<sup>III</sup> while others achieve only partial oxidation. Instead a milder, water-friendly oxidant is desired which rules out some common oxidants designed for oxygen/water-free use.<sup>34</sup> The ferrocenium cation, FeCp<sub>2</sub><sup>+</sup>, is an interesting option because it should be capable of at least partial oxidation of Fe<sup>II</sup>(H<sub>2</sub>gallate), it is readily available with a variety of anions, and it is stable to water. Additionally, the use of a larger anion such as BF<sub>4</sub><sup>-</sup> or PF<sub>6</sub><sup>-</sup> should prevent any anion insertion to the material, as the anions should be too large to fit into the pores, especially when taking into account hydration sphere size. If a BF<sub>4</sub><sup>-</sup> were capable of shedding its solvating water molecules and displacing additional water molecules from inside the framework, this process should be dramatically slower than proton diffusion out, which would achieve the same charge balance.

To this end, off-white Fe<sup>II</sup>(H<sub>2</sub>gallate) was oxidized with half an equivalent of FeCp<sub>2</sub>BF<sub>4</sub> dissolved in water (dark blue solution). The solid immediately turned dark/black, and gradually over time the color of the solution lightened. After 24 hours, the supernatant was colorless. Rather than a visible precipitation of yellow/orange ferrocene a dense dark purple/black liquid layer formed at the bottom of the reaction mixture. The oxidized framework can be isolated by filtering the reaction and washing multiple times with water and methanol (to dissolve any residual ferrocene).<sup>35</sup> Interestingly, when methanol is added to the filtrate, the dense dark aqueous solution that formed is destabilized and a yellow precipitate forms while the solution still maintains its dark color. It is highly likely that over the course of the oxidation some amount of the framework deteriorates and dissolves into solution leading to this dark coloration. When Fe<sup>II</sup>(H<sub>2</sub>gallate) is oxidized by an electron, it should eject an equivalent proton, thus acidifying the solution. Under acidic conditions, some of the framework dissolves releasing a mixture of Fe<sup>II</sup> and Fe<sup>III</sup> ions as well as gallic acid into solution.

The isolated partially-oxidized framework, hereafter referred to as  $\text{Fe}^{\text{II/III}}(\text{H}_x\text{gallate})$ , still maintains crystallinity, albeit to a slightly diminished extent (**Figure 3.12**). The first peak position is intermediate to those of  $\text{Fe}^{\text{II}}(\text{H}_2\text{gallate})\cdot 2\text{H}_2\text{O}$  and  $\text{Fe}^{\text{III}}(\text{Hgallate})\cdot 2\text{H}_2\text{O}$ .  $^{57}\text{Fe}$  Mössbauer indicates that the material is mixed valent  $\text{Fe}^{\text{II/III}}$  with two distinct sites: a high spin  $\text{Fe}^{\text{II}}$  and a high spin  $\text{Fe}^{\text{III}}$  (**Figure 3.13**). Surprisingly, these sites are in a 31/69  $\text{Fe}^{\text{II}}/\text{Fe}^{\text{III}}$  ratio, which exceeds the degree of oxidation expected for half an equivalent of  $\text{FeCp}_2\text{BF}_4$  being entirely consumed. Since it seems that some amount of the material dissolved during the chemical oxidation, it is not unreasonable to postulate that more labile  $\text{Fe}^{\text{II}}$  ions would disproportionately be removed compared to more inert  $\text{Fe}^{\text{III}}$  ions. This imbalanced dissolution would leave a material with excess  $\text{Fe}^{\text{III}}$ .<sup>36</sup> The two sites have quadrupole splittings and isomer shifts similar to the valence pure analogues, implying that the chemical environment is maintained during the chemical oxidation and that no other iron containing species are present in appreciable quantity (Table 3.2).

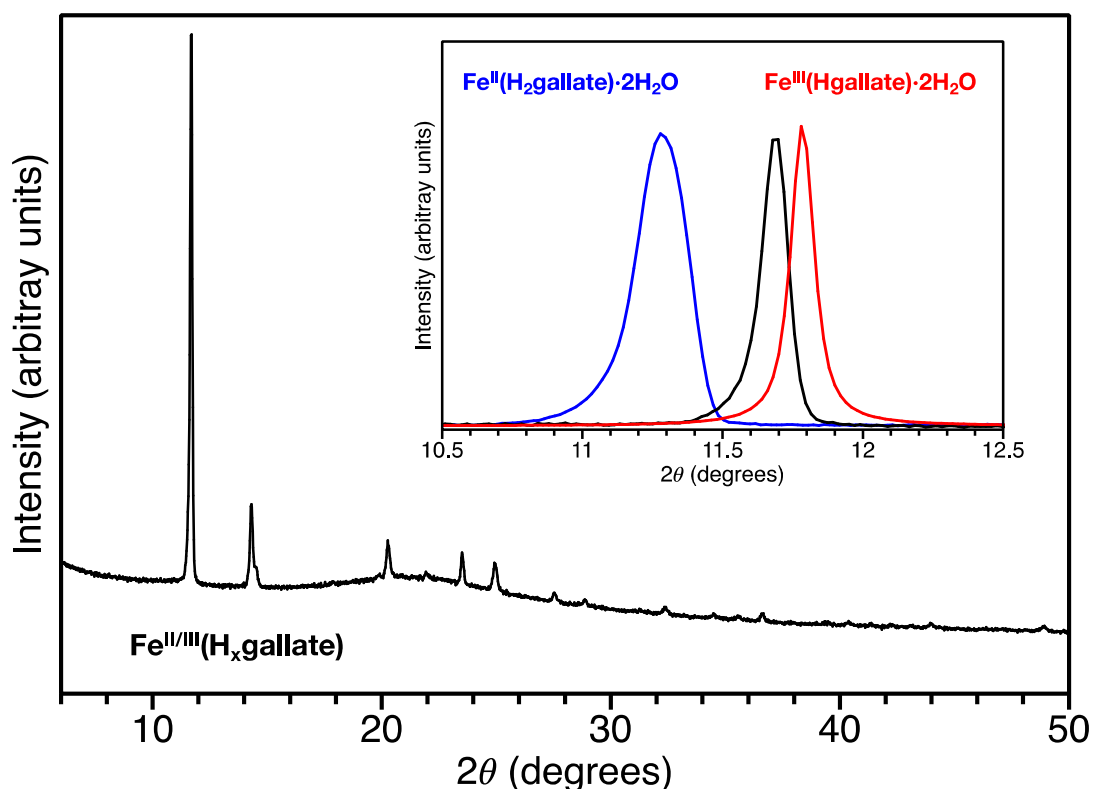


**Figure 3.12:** X-ray powder diffraction pattern of  $\text{Fe}^{\text{II/III}}(\text{H}_x\text{gallate})$  (black), with inset comparing the position of the first diffraction peak to those of  $\text{Fe}^{\text{II}}(\text{H}_2\text{gallate})\cdot 2\text{H}_2\text{O}$  (blue) and  $\text{Fe}^{\text{III}}(\text{Hgallate})\cdot 2\text{H}_2\text{O}$  (red).

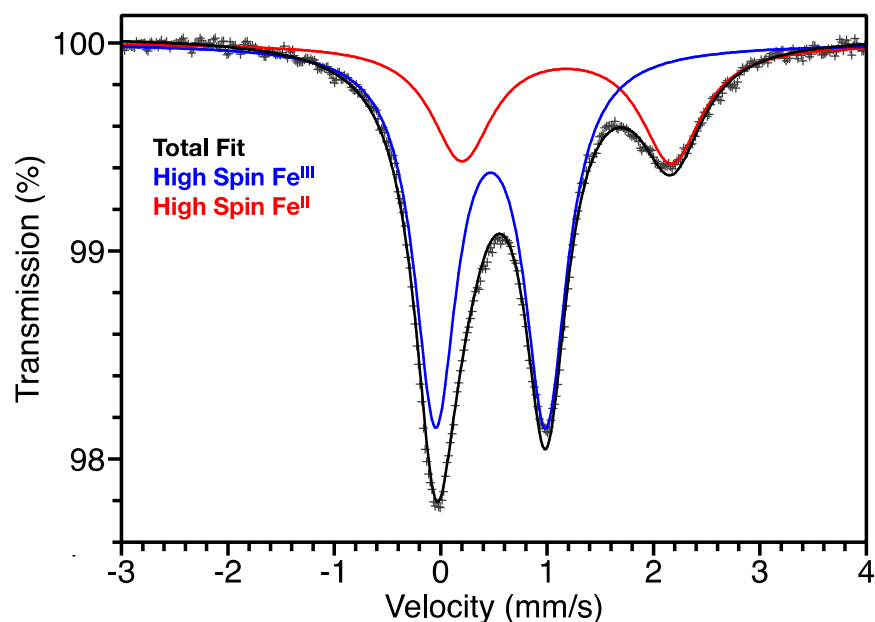


**Figure 3.13:**  $^{57}\text{Fe}$  Mössbauer spectrum for  $\text{Fe}^{\text{II/III}}(\text{H}_x\text{gallate})$  collected at 295 K (grey crosses) fit to two sites: high spin  $\text{Fe}^{\text{III}}$  (blue line), high spin  $\text{Fe}^{\text{II}}$  (red line), and total fit (black line).

**Table 3.2:** Comparison of  $^{57}\text{Fe}$  Mössbauer fitting parameters for  $\text{Fe}^{\text{II}}(\text{H}_2\text{gallate})\cdot 2\text{H}_2\text{O}$ ,  $\text{Fe}^{\text{II/III}}(\text{H}_x\text{gallate})$ , and  $\text{Fe}^{\text{III}}(\text{Hgallate})\cdot 2\text{H}_2\text{O}$ .

	h.s. FeII in $\text{Fe}^{\text{II}}(\text{H}_2\text{gallate})\cdot 2\text{H}_2\text{O}$	h.s. FeII in $\text{Fe}^{\text{II/III}}(\text{H}_x\text{gallate})$	h.s. FeIII in $\text{Fe}^{\text{II/III}}(\text{H}_x\text{gallate})$	h.s. FeIII in $\text{Fe}^{\text{III}}(\text{Hgallate})\cdot 2\text{H}_2\text{O}$
$\delta$ (mm/s)	1.176	1.184	0.469	0.453
$\Delta E_Q$ (mm/s)	2.217	1.970	1.036	1.037
$\Gamma$ (mm/s)	0.319	0.699	0.480	0.417
Area	100%	31%	69%	100%

Despite the close Fe–Fe distance and indirectly observed ability to transport charge through the material (possibly both electrons and protons), attempts to directly measure intrinsic conductivity have been unsuccessful. Because samples of  $\text{Fe}^{\text{II}}(\text{H}_2\text{gallate})$ ,  $\text{Fe}^{\text{II/III}}(\text{H}_x\text{gallate})$  and  $\text{Fe}^{\text{III}}(\text{Hgallate})$ , could only be reproducibly obtained as microcrystalline powder, conductivity measurements were performed on pressed pellets of the frameworks. Both direct current resistance measurements and alternating current impedance measurements showed no appreciable conductivity above the limit of detection of available instrumentation ( $\sim 10^{-9}$ – $10^{-10}$  S/cm). This is likely an unfortunate byproduct of the dimensionality of conductive pathways in the metal–gallate

frameworks. Even though the structure has three-dimensional chemical connectivity, electronic conductivity should only occur via the metal chains along the c axis. Neighboring iron chains are connected to each other via carboxylate groups from the gallate ligand; because the orbitals on carboxylate groups are orthogonal to those of the rest of the ligand, there is no accessible path for electron conductivity across carboxylates connecting separate chains (**Figure 3.14**). Thus, pressed pellet conductivity measurements of one-dimensional conductors, as should be the case for metal–gallate frameworks, suffers from the high tortuosity of conductive pathways through the pellet. This leads to dramatically lower observed conductivities in such materials, especially in the case of metal–organic frameworks which already have dramatically decreased density of conductive pathways.<sup>14</sup> Further elucidation of charge transport phenomena in the iron–gallate structure will rely upon either the use of more sensitive instrumentation and/or obtaining larger enough crystals for single-crystal measurements.

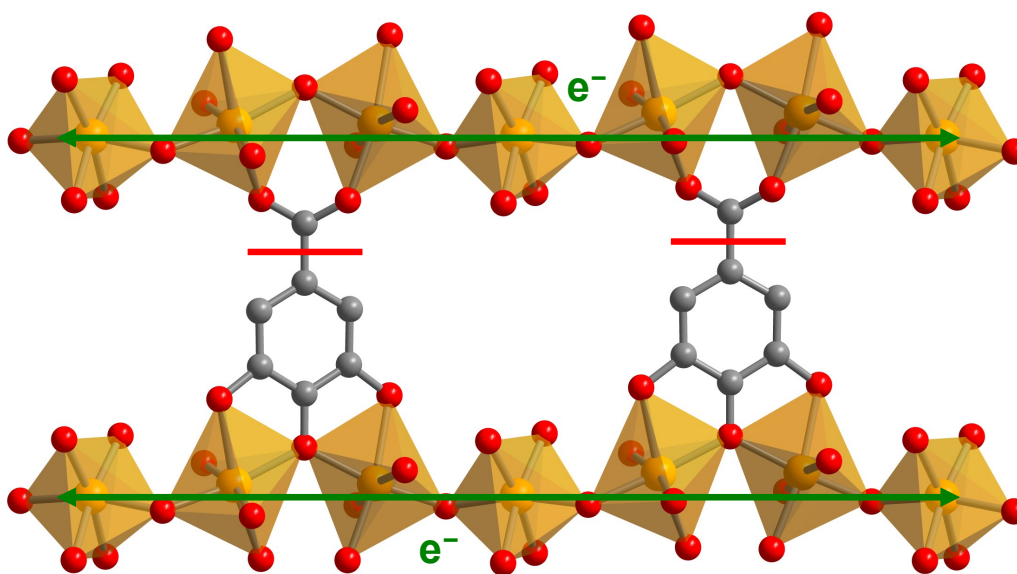


**Figure 3.14:** Crystal structure view of two adjacent vertex sharing iron chains in iron–gallate. Electronic conductivity is proposed to occur only along these parallel chains (green arrows). Multi-dimensional conductivity is prohibited by the lack of electronic communication between the carboxylate and phenyl ring of the ligand, indicated by red lines.

### Activation and Gas Adsorption Properties of $\text{Fe}^{\text{II}}(\text{H}_2\text{gallate})$

An unusual benefit of the incredibly small pore is that the gallate frameworks are not capable of having excess ligand or metal salt left in the pore. Any undesired materials internally incorporated as defects would have no viable path to be removed. Because there is no need to wash out material to increase the porosity, any solvent washes are merely for ease of activation. While it is possible to exchange the water in the pore for methanol, the material can actually be readily activated from the water solvated state. Heating  $\text{Fe}^{\text{II}}(\text{H}_2\text{gallate}) \cdot 2\text{H}_2\text{O}$  at 150 °C under dynamic vacuum for 48 hours yields  $\text{Fe}^{\text{II}}(\text{H}_2\text{gallate})$ . The framework undergoes a slight structural rearrangement as the pores are evacuated (**Figure 3.15**). There is a reversible reduction in symmetry of the framework to  $\text{P3}_1$ , which is consistent with the reported structure change in magnesium–gallate (**Table 3.3**).<sup>37</sup>

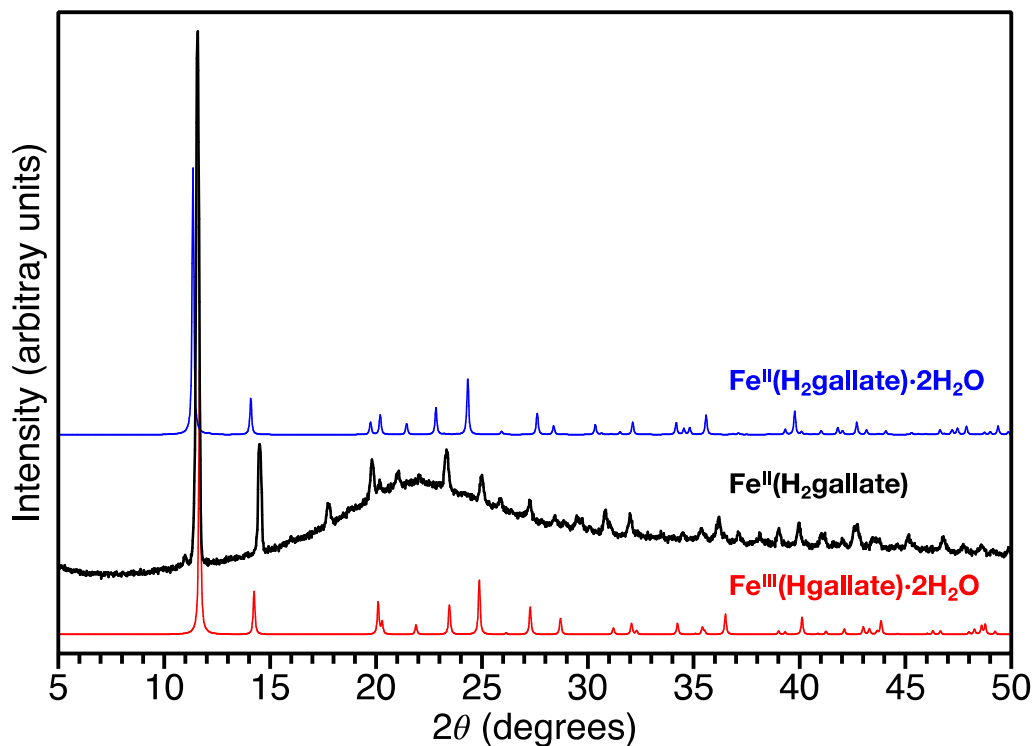


**Figure 3.15:** X-ray powder diffraction pattern of a sealed capillary of activated  $\text{Fe}^{\text{II}}(\text{H}_2\text{gallate})$  (black), compared to predicted patterns for  $\text{Fe}^{\text{II}}(\text{H}_2\text{gallate})\cdot 2\text{H}_2\text{O}$  (blue) and  $\text{Fe}^{\text{III}}(\text{Hgallate})\cdot 2\text{H}_2\text{O}$  (red). New peaks stemming from the reduction in symmetry are visible at  $11^\circ$  and  $18^\circ$ .

**Table 3.3:** Comparison of unit cells parameters for  $\text{Fe}^{\text{II}}(\text{H}_2\text{gallate})\cdot 2\text{H}_2\text{O}$  and  $\text{Fe}^{\text{III}}(\text{Hgallate})\cdot 2\text{H}_2\text{O}$  from single crystal structures,  $\text{Fe}^{\text{II}}(\text{H}_2\text{gallate})$  from powder X-ray diffraction, and previously reported  $\text{Mg}(\text{H}_2\text{gallate})$ .<sup>20</sup>

	$\text{Fe}^{\text{II}}(\text{H}_2\text{gallate})\cdot 2\text{H}_2\text{O}$	$\text{Fe}^{\text{III}}(\text{Hgallate})\cdot 2\text{H}_2\text{O}$	$\text{Fe}^{\text{II}}(\text{H}_2\text{gallate})$	$\text{Mg}(\text{H}_2\text{gallate})$
Space Group	P3 <sub>1</sub> 21	P3 <sub>2</sub> 21	P3 <sub>1</sub>	P3 <sub>1</sub>
<b>a</b> (Å)	8.988	8.748	15.22	15.11
<b>c</b> (Å)	21.284	10.861	10.12	10.30
<b>Volume</b> (Å <sup>3</sup> )	1489	720	2031	2037
<b>Z</b>	6	3	9	9
<b>Volume/Z</b>	248	240	226	226

This structural distortion is also apparent via  $^{57}\text{Fe}$  Mössbauer spectroscopy;  $\text{Fe}^{\text{II}}(\text{H}_2\text{gallate})$  exhibits two equal area high spin  $\text{Fe}^{\text{II}}$  sites, whereas  $\text{Fe}^{\text{II}}(\text{H}_2\text{gallate})\cdot 2\text{H}_2\text{O}$  has only one (**Figure 3.16** and **Table 3.4**). Exposure of this activated phase to air results in an immediate color change to black and gradual conversion of the powder diffraction from that of  $\text{Fe}^{\text{II}}(\text{H}_2\text{gallate})$  to that of  $\text{Fe}^{\text{III}}(\text{Hgallate})\cdot x\text{H}_2\text{O}$ . While it is possible that an activated  $\text{Fe}^{\text{III}}(\text{Hgallate})$  species is transiently existing due to conduction of electrons and protons from the interior of the material to surface reactivity with oxygen, this species is not isolable, as water molecules and/or reduced oxygen species are simultaneously diffusing into the material.

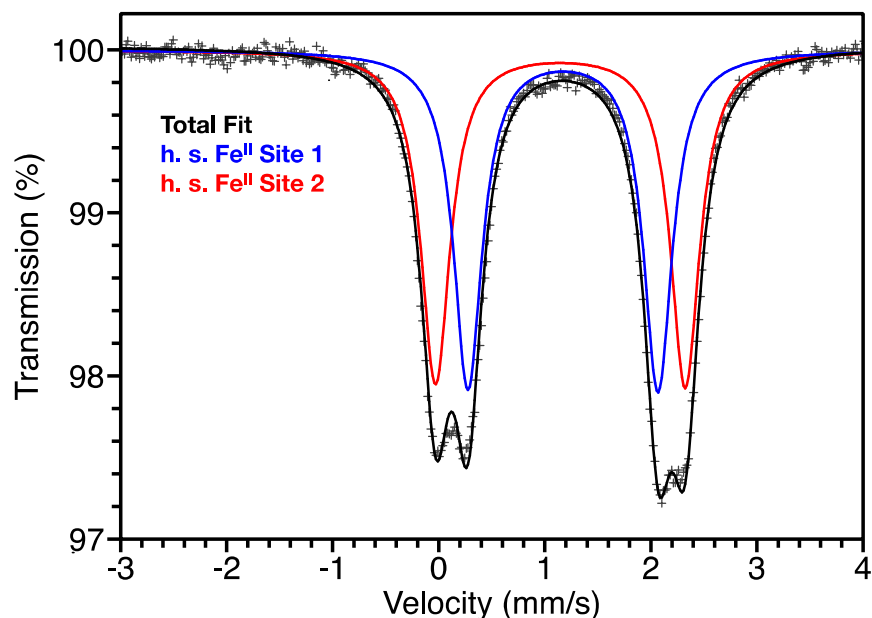


**Figure 3.16:**  $^{57}\text{Fe}$  Mössbauer spectrum for  $\text{Fe}^{\text{II}}(\text{H}_2\text{gallate})$  collected at 295 K (grey crosses) fit to two high spin  $\text{Fe}^{\text{II}}$  sites: Site 1 (blue line, inner doublet), Site 2 (red line, outer doublet), and total fit (black line).

**Table 3.4:** Comparison of  $^{57}\text{Fe}$  Mössbauer fitting parameters for water solvated  $\text{Fe}^{\text{II}}(\text{H}_2\text{gallate})\cdot 2\text{H}_2\text{O}$  and activated  $\text{Fe}^{\text{II}}(\text{H}_2\text{gallate})$ .

	h.s. $\text{Fe}^{\text{II}}$ in $\text{Fe}^{\text{II}}(\text{H}_2\text{gallate})\cdot 2\text{H}_2\text{O}$	h.s. $\text{Fe}^{\text{II}}$ in $\text{Fe}^{\text{II}}(\text{H}_2\text{gallate})$ (Site 1)	h.s. $\text{Fe}^{\text{II}}$ in $\text{Fe}^{\text{II}}(\text{H}_2\text{gallate})$ (Site 2)
$\delta$ (mm/s)	1.176	1.171	1.147
$\Delta E_Q$ (mm/s)	2.217	1.792	2.354
$\Gamma$ (mm/s)	0.319	0.327	0.334
Area	100%	50%	50%

Attempts to obtain a standard 77 K N<sub>2</sub> BET surface area have been unsuccessful, most likely due to the small pores and changing framework geometry from a desolvated and closed phase to a more open and gas accessible phase. Equilibration of N<sub>2</sub> uptake at 77 K in this material is slow enough that cooling bath liquid N<sub>2</sub> levels and small unavoidable leak rates of the instrumentation become problematic. Only the magnesium framework has been previously reported to have a 77K N<sub>2</sub> BET surface area of 330 m<sup>2</sup>/g.<sup>1</sup> This issue of surface area measurements was solved without discussion in the recent publication by Ren et al via their report of surface areas of 559, 475, and 424 m<sup>2</sup>/g for Mg, Co, and Ni, respectively.<sup>20</sup> These surface areas were obtained via BET calculations from 195 K CO<sub>2</sub> isotherms. Carbon dioxide has been used to probe surface area for porous solids long before the rise of metal–organic frameworks.<sup>38</sup> However, its uses in metal–organic framework surface area determinations have been fairly limited due to complications associated with CO<sub>2</sub>–CO<sub>2</sub> interactions. Nevertheless, CO<sub>2</sub> surface areas are still evidence of permanent porosity and correlate qualitatively, if not quantitatively, with material capacity for gas molecules. Isothermal measurement of CO<sub>2</sub> adsorption in Fe<sup>II</sup>(H<sub>2</sub>gallate) cooled to 195 K via a dry ice/isopropanol bath shows steep adsorption, exceeding 5 mmol/g before 5 mbar of pressure (**Figure 3.17**).

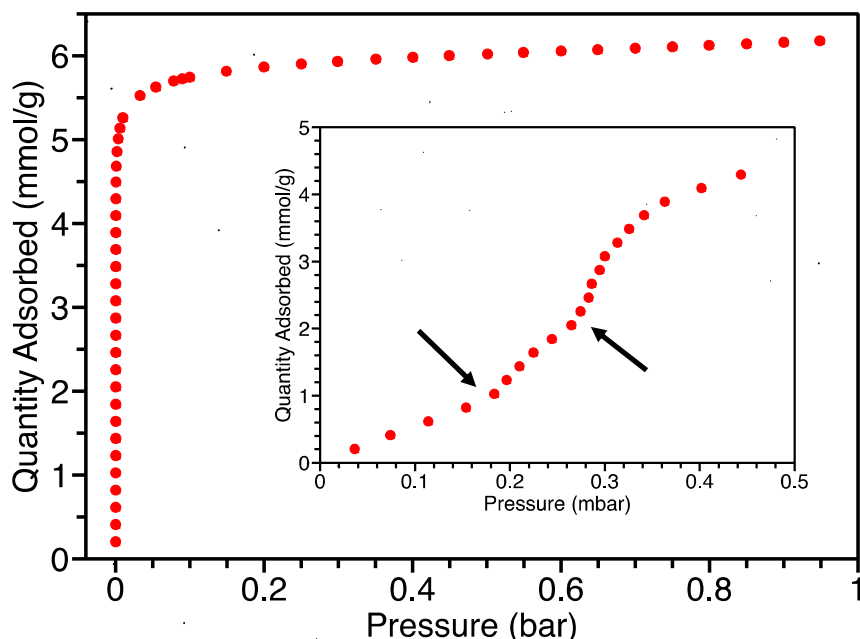


**Figure 3.17:** Fe<sup>II</sup>(H<sub>2</sub>gallate) CO<sub>2</sub> gas adsorption isotherm measured at 195 K with low pressure inset and indicated inflection points consistent with phase changes.

This adsorption does not follow typical Langmuir behavior but is instead consistent with a material undergoing at least one, if not two, phase changes. Magnification of the low-pressure region of the isotherm (0–0.5 mbar) clearly shows two inflection points (**Figure 3.17** inset). In situ powder diffraction combined with gas dosing would definitively confirm a structural change, but in the absence of such measurements, it can be inferred that a material that is capable of undergoing a reversible phase change in the presence of one adsorbate may do so in the presence of another. Such phase changes are well documented in the literature, typically referred to as flexibility, and often occur at different pressures/temperatures for different adsorbates.

While the chemical interactions that dictate a phase change in a material are much more complex than simple mathematical relations, I believe that the phase-change behavior observed in the metal–gallates should follow a transitive relation. Both iron and magnesium gallate exhibit lower crystallographic symmetry in the same manner upon activation. Fe<sup>II</sup>(H<sub>2</sub>gallate) undergoes a phase change at small partial pressures of CO<sub>2</sub> at 195 K. Therefore, Mg(H<sub>2</sub>gallate) may also exhibit a phase change with CO<sub>2</sub>. Such behavior could also present in Co and Ni(H<sub>2</sub>gallate). The low-pressure region of CO<sub>2</sub> measurements obtained by Ren et al.<sup>20</sup> are left unplotted<sup>39</sup> and any discussion of unusual phase change, material flexibility, or strange isotherm behavior is absent. BET adsorption theory cannot be validly applied across phase changes, yet this was used for Mg, Co, and Ni(H<sub>2</sub>gallate).

If such analysis is applied to Fe<sup>II</sup>(H<sub>2</sub>gallate) from 0–10 mbar, a surface area of 471 m<sup>2</sup>/g is obtained with a R<sup>2</sup> of 0.9846 for the linear fit. Despite this surface area being consistent with the isoreticular values, the R<sup>2</sup> is too low; inspection of the lower-pressure region of the fit clearly shows substantial deviation from linearity in the data. If only pressure points after the second inflection point are used, a BET surface area of 450 m<sup>2</sup>/g is obtained with a significantly improved R<sup>2</sup> of 0.9999 (**Figure 3.18**). While the numerical values of these fits only differ slightly, the quality of the fits are dramatically different. This highlights the effect of low-pressure phase transitions on surface area calculations, and the lower value should be regarded as a more accurate representation of the surface area of Fe<sup>II</sup>(H<sub>2</sub>gallate).

A CO<sub>2</sub> Langmuir surface area can also be calculated from the higher-pressure region of this data set, giving 538 m<sup>2</sup>/g. Theoretical surface area calculations for Fe<sup>II</sup>(H<sub>2</sub>gallate), using the Fe<sup>II</sup>(H<sub>2</sub>gallate)·2H<sub>2</sub>O single crystal structure with water molecules removed, show a range of results based on probe size (**Table 3.5**). Using a probe size equal to that of CO<sub>2</sub> (a kinetic radius of 1.65 Å) gives a surface area of 432 m<sup>2</sup>/g, indicating that the BET surface area obtained using data points after the phase changes is a reasonable measurement. Interestingly, if a 1.4 Å size probe (smaller than all gases except He) is used to calculate accessible surface area from the outside of a crystallite, no internal porosity can be accessed. This result suggests that some rearrangement of the framework, whether through thermal motion or phase change, must occur in order for larger gas molecules to access internal porosity.

**Table 3.5:** Theoretical Langmuir surface area calculations, reported in m<sup>2</sup>/g, obtained using Materials Studio models for ferric–gallate and ferrous–gallate using hydrated single-crystal structures with water molecules omitted. Probe radius of 1.65 and 1.82 Å were used to model CO<sub>2</sub> and N<sub>2</sub>, respectively, while a 1.40 Å probe was used as a nonphysical indicator of porosity.

Probe Radius	Fe <sup>II</sup> (H <sub>2</sub> gallate)	Fe <sup>III</sup> (Hgallate)
1.40 Å	544	538
1.65 Å	432	441
1.82 Å	352	363

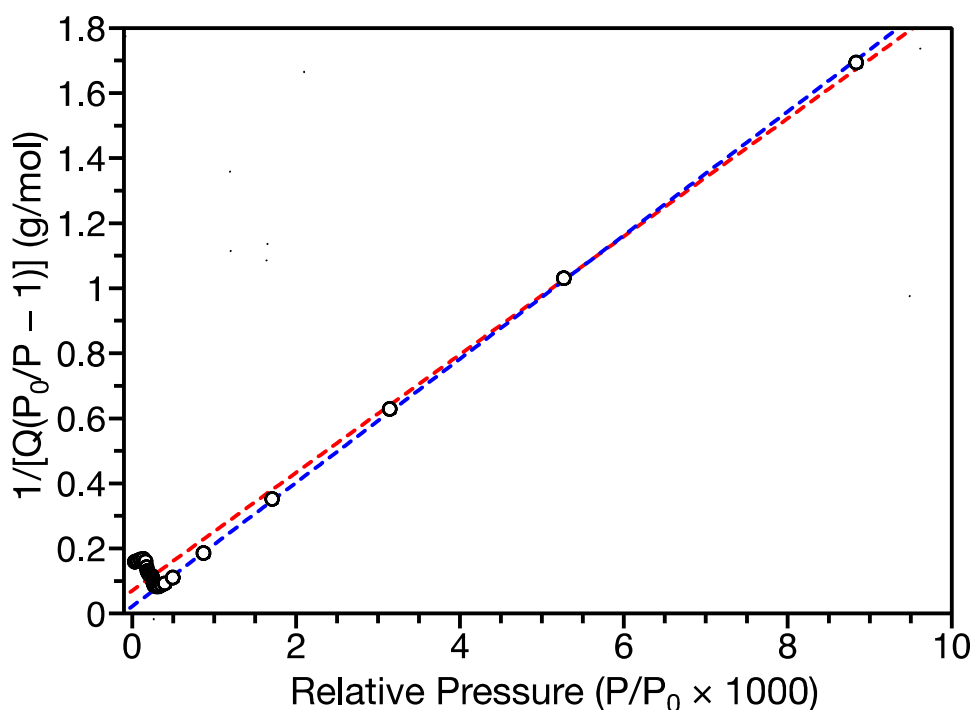


**Figure 3.18:** BET fit of low-pressure region of  $\text{Fe}^{\text{II}}(\text{H}_2\text{gallate})$  195 K  $\text{CO}_2$  isotherm (empty black circles), with fit of the entire low-pressure region including phase transitions (red dashed line) and fit excluding the phase transitions (blue dashed line). Q: quantity adsorbed, P: Pressure,  $P_0$ : saturation pressure of  $\text{CO}_2$  at 195 K.

As Mg, Co, and Ni( $\text{H}_2\text{gallate}$ ) were previously reported to exhibit exceptional ethylene/ethane selectivities, I performed isothermal gas sorption measurements on  $\text{Fe}^{\text{II}}(\text{H}_2\text{gallate})$  for ethylene and ethane, as well as acetylene for complete comparison of the C2 hydrocarbons. Just like its isostructural analogs,  $\text{Fe}^{\text{II}}(\text{H}_2\text{gallate}) \cdot 2\text{H}_2\text{O}$  demonstrates strong adsorption of ethylene with high capacity (3.72 mmol/g at 1 bar and 303 K), while showing nearly minimal adsorption of ethane (0.27 mmol/g at 1 bar and 303 K). Isotherms collected at 303, 313, and 323 K for ethane in  $\text{Fe}^{\text{II}}(\text{H}_2\text{gallate})$  follow simple Langmuir-type adsorption (**Figure 3.19**). Whether ethane is adsorbing weakly inside the pores of the material, merely on the external surface of crystallites, or in structure defects is not immediately apparent. It has been previously postulated that ethane is too large to fit in the pores of Mg, Co, or Ni( $\text{H}_2\text{gallate}$ ). As the ethane uptake across all of these materials is similar, it can be assumed that a similar mechanism of adsorption is occurring and thus  $\text{Fe}^{\text{II}}(\text{H}_2\text{gallate})$  may also be excluding ethane from its pores due to size restrictions.

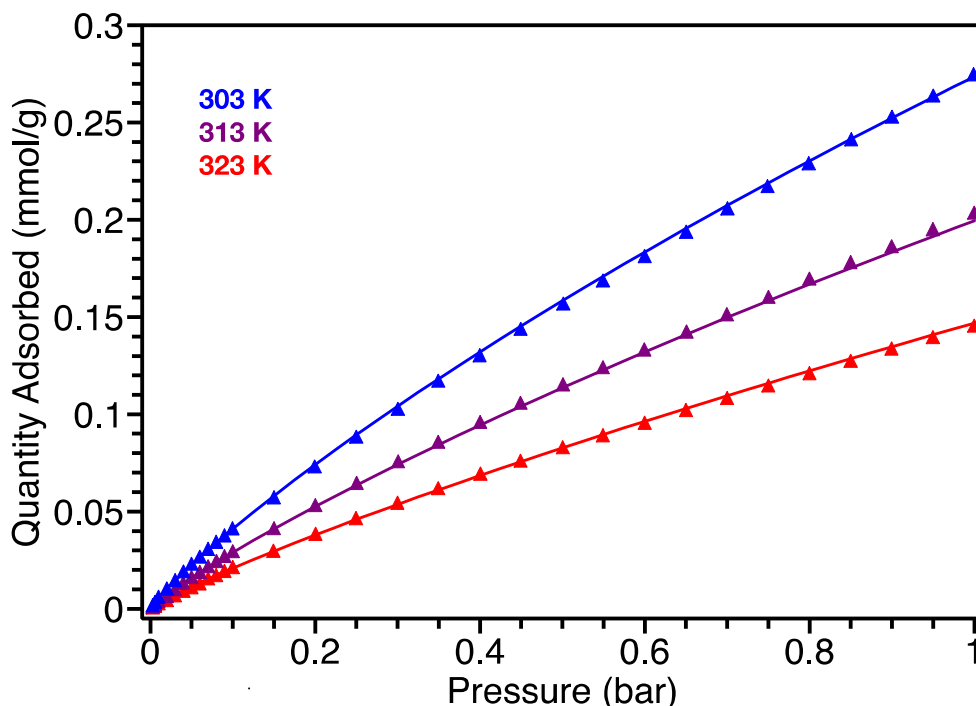


**Figure 3.19:**  $\text{Fe}^{\text{II}}(\text{H}_2\text{gallate})$   $\text{C}_2\text{H}_6$  gas adsorption isotherms (triangles) measured at 303 K (blue, top), 313 K (purple, middle), and 323 K (red, bottom), with dual-site Langmuir-Freundlich fits (solid lines).

Ethylene isotherms, also collected at 303, 313, and 323 K for  $\text{Fe}^{\text{II}}(\text{H}_2\text{gallate})$ , do not follow Langmuir-type adsorption but rather show a clear inflection point indicative of a change in the adsorption process such as a phase change (**Figure 3.20**). It is likely that a similar framework rearrangement is occurring with ethylene as with water and  $\text{CO}_2$ . Fitting  $\text{Fe}^{\text{II}}(\text{H}_2\text{gallate})$  with a dual site Langmuir-Freundlich equation, as was reported for the other metal analogs, clearly does not accurately capture the material's behavior. Instead, low-pressure and high-pressure points sufficiently far from the phase change can be independently fit with Langmuir-Freundlich equations (**Figure 3.21**). The error, calculated as RMSD, of these fits over their pressure ranges is less than one-fourth of the error for the full pressure range fit. Acetylene isotherms for  $\text{Fe}^{\text{II}}(\text{H}_2\text{gallate})$  are similar to ethylene, even showing the same inflection point phenomena, but they have steeper adsorption, greater capacity, and exhibit phase transition at lower pressures (**Figure 3.22**).

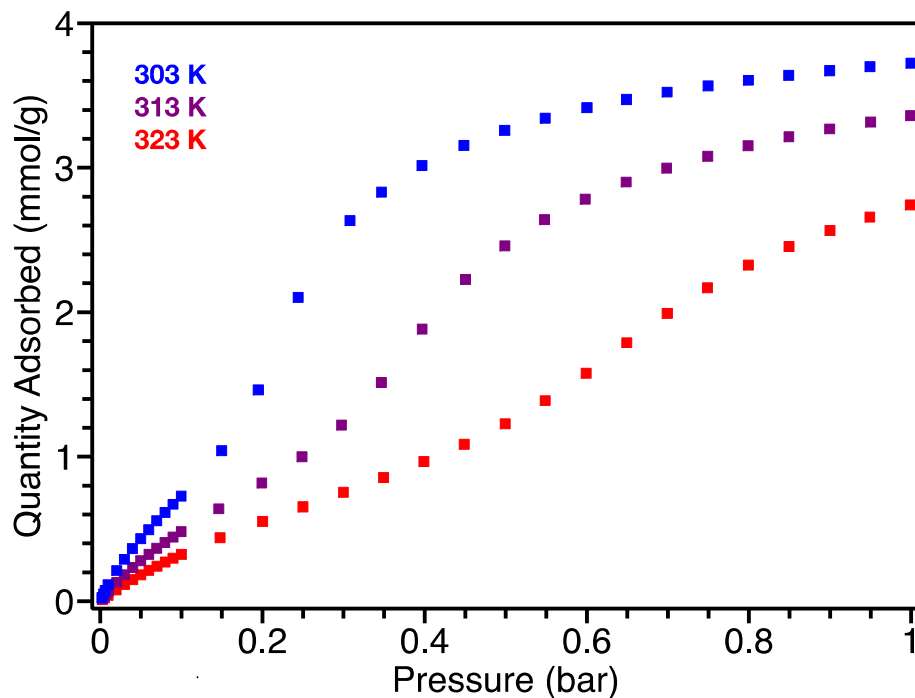


**Figure 3.20:** Fe<sup>II</sup>(H<sub>2</sub>gallate) C<sub>2</sub>H<sub>4</sub> gas adsorption isotherms (squares) measured at 303 K (blue, top), 313 K (purple, middle), and 323 K (red, bottom).

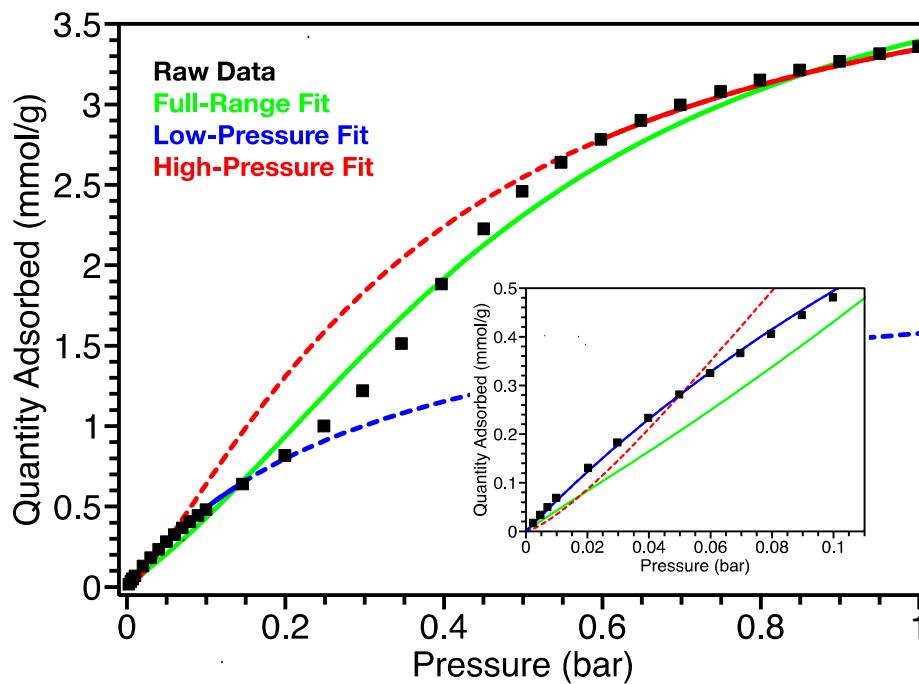


**Figure 3.21:** Fe<sup>II</sup>(H<sub>2</sub>gallate) C<sub>2</sub>H<sub>4</sub> gas adsorption isotherm measured at 313 K (black squares), dual-site Langmuir-Freundlich fits for the full pressure range (green solid line), high-pressure range (red solid line), and low-pressure range (blue solid line), with projections in dashed lines and low pressure inset.

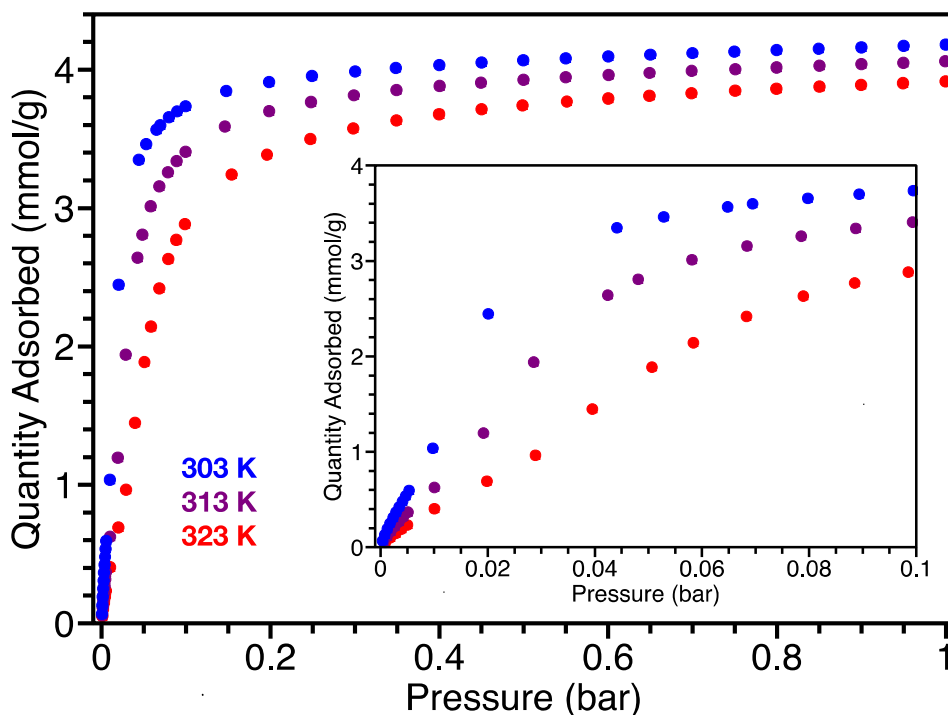


**Figure 3.22:**  $\text{Fe}^{\text{II}}(\text{H}_2\text{gallate})$   $\text{C}_2\text{H}_2$  gas adsorption isotherms (circles) measured at 303 K (blue, top), 313 K (purple, middle), and 323 K (red, bottom), with low pressure inset.

The large disparity between  $\text{Fe}^{\text{II}}(\text{H}_2\text{gallate})$ 's ethylene adsorption and ethane adsorption indicates that it should be highly selective for ethylene and thus have possible industrial applications, despite its high sensitivity to oxygen (**Figure 3.23**). The gold standard for calculation of selectivities has been the use of IAST.<sup>40,41</sup> As described in Chapter 1, IAST is a model for predicting multicomponent gas adsorption behavior. As it is derived from single component isotherms, it is much more experimentally accessible than measuring multicomponent isotherms for arbitrary mixtures. Additionally, the model has been experimentally shown to predict selectivities well for mixed gas streams.<sup>42-44</sup> Mg, Co, and Ni( $\text{H}_2\text{gallate}$ ) are reported to have IAST of 37, 52, and 17, respectively, for 50/50 ethylene/ethane at 1 bar and 298 K. Co( $\text{H}_2\text{gallate}$ )'s IAST selectivity of 52 is currently the highest value reported in the literature. The ethylene isotherms of the reported materials were all fit over their entire measured pressure range with dual site Langmuir-Freundlich equations; treating  $\text{Fe}^{\text{II}}(\text{H}_2\text{gallate})$  in this same manner leads to an exceptionally high calculated IAST value of 131.

As mentioned before, however, these fits do not accurately represent adsorption in  $\text{Fe}^{\text{II}}(\text{H}_2\text{gallate})$ . In fact, close inspection of supplementally published ethylene isotherms for the three isostructural analogs reveals that all three materials also display inflection points consistent with phase changes. This is consistent with the authors' report that Mg( $\text{H}_2\text{gallate}$ ) distorts when activated. If this phase change is in fact occurring, then not only do these violate an assumption of the Langmuir adsorption model, but also an assumption of IAST: the adsorbent maintains constant surface area across a given pressure range.

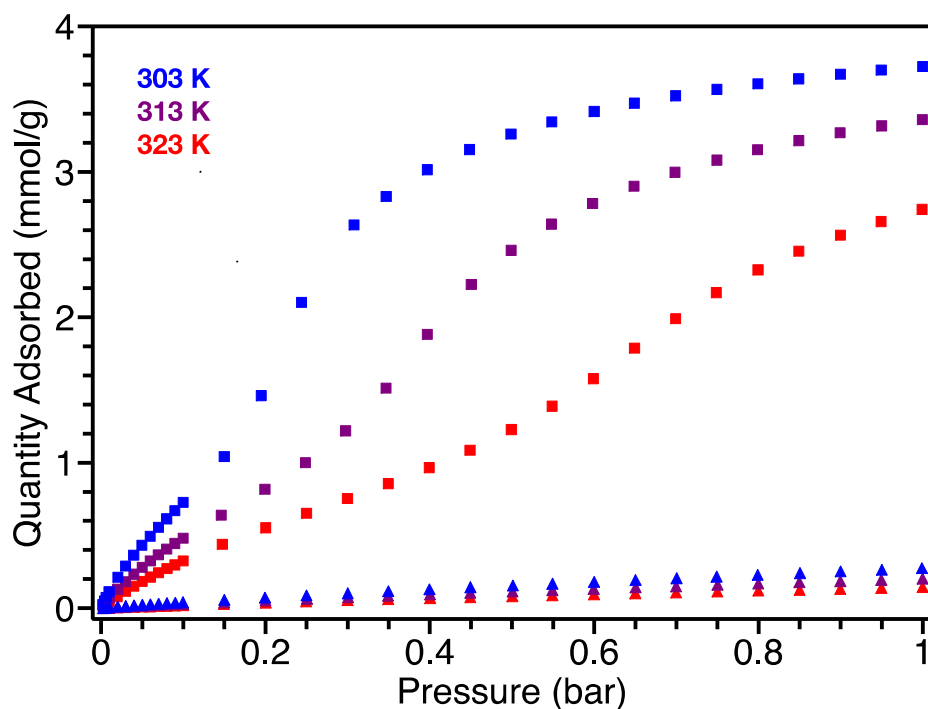


**Figure 3.23:** Comparison of  $\text{Fe}^{\text{II}}(\text{H}_2\text{gallate})$  gas adsorption isotherms for  $\text{C}_2\text{H}_4$  (squares) and  $\text{C}_2\text{H}_6$  (triangles) measured at 303 K (blue, top), 313 K (purple, middle), and 323 K (red, bottom).

Although IAST cannot be rigorously applied to the full data set, the claim of exceptional selectivity might still be valid. For example, because the inflection point for  $\text{Fe}^{\text{II}}(\text{H}_2\text{gallate})$  with ethylene at 303 K occurs at  $\sim 250$  mbar, well below the 500 mbar of partial pressure in a 50/50 1 bar mixture, the material should be entirely composed of the higher-pressure phase. If the material is one phase under the given conditions and at equilibrium, then the spreading pressure of an adsorbate should be dictated by the thermodynamics of adsorption in the given phase and not dependent on the properties of a nonexistent phase or the phase transition. This is to say that a model that accurately reproduces the high-pressure regions of the ethylene isotherms will more accurately represent the spreading pressure exerted by ethylene in the material. As long as the adsorption of ethane does not change in the presence of the high-pressure ethylene phase, then IAST could still model the selectivity of the system.

One of the issues with extrapolating low-pressure behavior from high pressure data is that very slight differences in low-pressure data can cause dramatic differences in calculating spreading pressure and thus IAST values. Nevertheless, using this predictive approach can allow for a comparison between  $\text{Fe}^{\text{II}}(\text{H}_2\text{gallate})$  and the reported  $\text{Co}(\text{H}_2\text{gallate})$  (**Figure 3.24**). Using data extracted from supplemental figures, the high-pressure-phase regions of  $\text{Co}(\text{H}_2\text{gallate})$  isotherms can be fit to a dual-site Langmuir-Freundlich equation. Taking this fit and applying IAST with the reported ethane behavior yields a selectivity of 63, a modest improvement over 52. Treating  $\text{Fe}^{\text{II}}(\text{H}_2\text{gallate})$  in the same manner with a similar quality fit gives a selectivity of 190, almost four times the current best non-metal-gallate framework selectivity (49 for NOTT-300<sup>45</sup>).

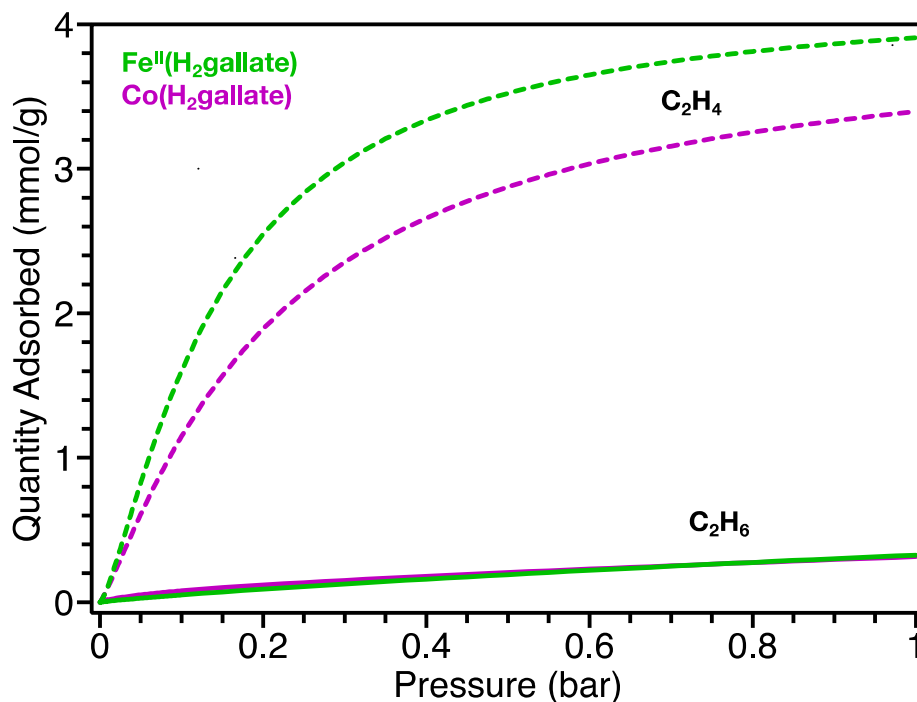


**Figure 3.24:** Modeled dual-site Langmuir-Freundlich isotherms for C<sub>2</sub>H<sub>4</sub> (dashed lines) and C<sub>2</sub>H<sub>6</sub> (solid lines) in Fe<sup>II</sup>(H<sub>2</sub>gallate) (green) and Co(H<sub>2</sub>gallate) (purple) at 298 K.

While Fe<sup>II</sup>(H<sub>2</sub>gallate)'s modeled IAST selectivity seems very high, I would argue that it is not as high as the physical multicomponent test might give. Evidence suggests that ethane cannot fit into the pore of the M(H<sub>2</sub>gallate) structure. If the material can only adsorb one gas out of a binary mixture, its selectivity should be infinite. While it is possible that ethane could adsorb to defect sites in a framework, the vast majority of adsorption in M(H<sub>2</sub>gallate) should occur on the external surface of particles. Any ethane adsorption should therefore be dependent on the external surface area of M(H<sub>2</sub>gallate). Ethylene adsorption on the other hand will be dependent on the strong binding that occurs on the internal surface area. As I discussed in Chapter 1, this violates one of the key assumptions of IAST, because each adsorbate is not exerting spreading pressure over the same area. Nonetheless, I believe IAST selectivities can be used as a qualitative indicator of the materials' properties. Certainly, they should not be given as a quantitative measure or a predictor of performance.

In the case of Fe<sup>II</sup>(H<sub>2</sub>gallate), it can be inferred that the material's selectivity for ethylene over ethane is the highest among reported M(H<sub>2</sub>gallate) frameworks. It has a larger capacity for ethylene with almost no change in the capacity for ethane. Additionally, fitting the higher-pressure-phase data for ethylene predicts steeper adsorption in Fe<sup>II</sup>(H<sub>2</sub>gallate) than Co(H<sub>2</sub>gallate). Because of this isostructural series' promising selectivities, these frameworks should be quantitatively tested in an actual multicomponent separation. If the IAST predictions hold true, I believe that only then would it be justifiable to claim the highest reported ethylene/ethane selectivity over the previous record holder NOTT-300.<sup>45</sup> Until such results are obtained, I can conclude for now that gas adsorption data implies that the steep and high capacity adsorption of ethylene compared to ethane in Fe<sup>II</sup>(H<sub>2</sub>gallate) should make it an exceptionally selective adsorbent.

### Activation and Gas Sorption Properties of Oxidized Iron–Gallate

The possibility of applying a new synthetic handle, framework redox state, to tune gas sorption properties is truly tantalizing. Oxidation of a framework typically corresponds to a reduction in unit cell and pore size; however, the removal of a proton and change in charge distribution within the pore could lead to substantial changes in adsorbate interactions. It is not possible to know a priori how these two effects will change gas sorption properties. Theoretical calculations of accessible surface area for  $\text{Fe}^{\text{III}}(\text{H}_x\text{gallate})$  using the crystal structure for  $\text{Fe}^{\text{III}}(\text{H}_x\text{gallate}) \cdot 2\text{H}_2\text{O}$  with water molecules removed, show that across a range of probe sizes, it has very similar porosity to  $\text{Fe}^{\text{II}}(\text{H}_2\text{gallate})$  (**Table 3.5**). Unfortunately, all attempts to date of accessing activated  $\text{Fe}^{\text{III}}(\text{H}_x\text{gallate})$  have been unsuccessful. Whether due to decreased chemical stability, decreased structural stability, or a combination thereof, the material loses all crystallinity upon activation. Fortunately, the mixed-valent analogue of the framework accessed by partial chemical oxidation can be activated. When activated,  $\text{Fe}^{\text{II/III}}(\text{H}_x\text{gallate})$  does not exhibit any reduction of symmetry as seen in  $\text{Fe}^{\text{II}}(\text{H}_2\text{gallate})$  (**Figure 3.25**). If this diverging diffraction behavior is consistent with  $\text{Fe}^{\text{II/III}}(\text{H}_x\text{gallate})$  retaining a more open structure it could be due to the presence of more rigid  $\text{Fe}^{\text{III}}$  metal sites.<sup>46</sup>

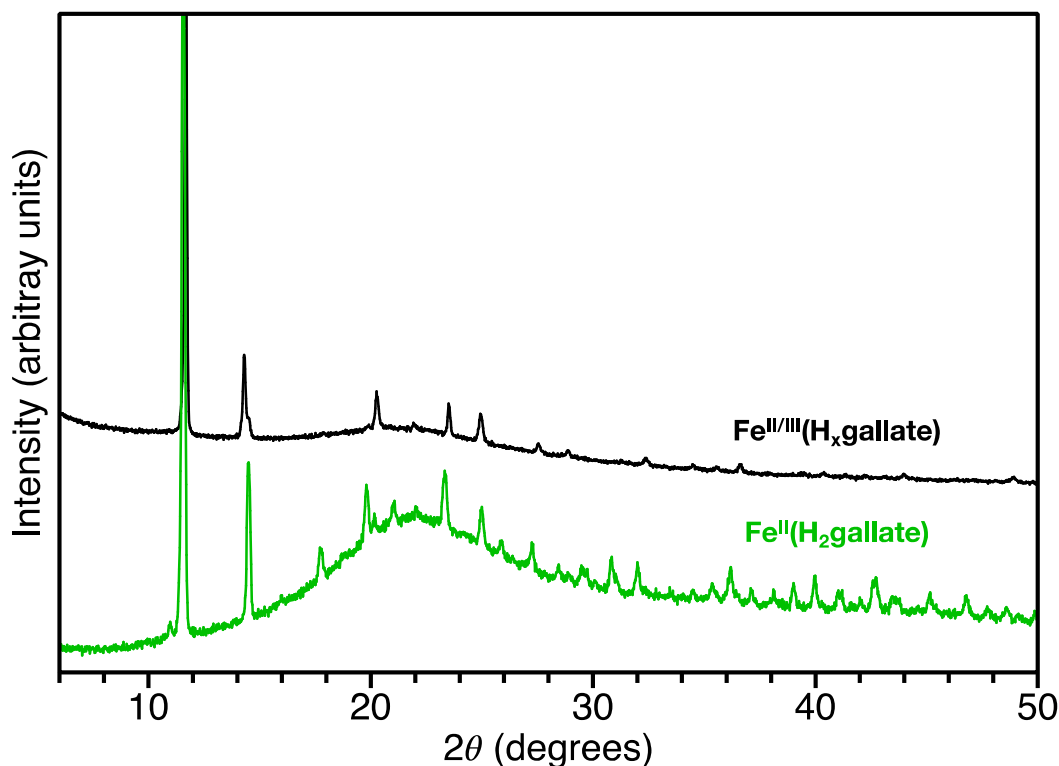


**Figure 3.25:** X-ray powder diffraction pattern of sealed capillaries of activated  $\text{Fe}^{\text{II}}(\text{H}_2\text{gallate})$  (green, bottom) and activated  $\text{Fe}^{\text{II/III}}(\text{H}_x\text{gallate})$  (black, top). There is no observable decrease in symmetry in  $\text{Fe}^{\text{II/III}}(\text{H}_x\text{gallate})$ .

While there is a contraction in the unit cell compared to  $\text{Fe}^{\text{II}}(\text{H}_2\text{gallate})$ , the partially oxidized phase does however still exhibit permanent porosity with a 195 K  $\text{CO}_2$  BET surface area of  $219 \text{ m}^2/\text{g}$  and Langmuir surface area of  $350 \text{ m}^2/\text{g}$  (**Figure 3.26**). Interestingly, there is no indication of a phase change under increasing gas pressure during the  $\text{CO}_2$  isotherm, consistent with

$\text{Fe}^{\text{II/III}}(\text{H}_x\text{gallate})$  maintaining the same structure under activation and solvation conditions. Because of this apparent structural rigidity, it is possible to measure a 77K  $\text{N}_2$  isotherm for  $\text{Fe}^{\text{II/III}}(\text{H}_x\text{gallate})$ , giving a BET surface area of  $76 \text{ m}^2/\text{g}$ . While these surface areas are substantially below those predicted for  $\text{Fe}^{\text{II}}(\text{H}_2\text{gallate})$  and  $\text{Fe}^{\text{III}}(\text{Hgallate})$ , I believe there are at least two plausible explanations. The degradation caused by the chemical oxidation could have induced more defects and/or blocked pores; in a material with one-dimensional pores, blocked pores dramatically lower accessible porosity.<sup>47</sup> As the exact structure is not known, it is also possible that the material when partially oxidized and activated distorts slightly, changing the internal surface area.

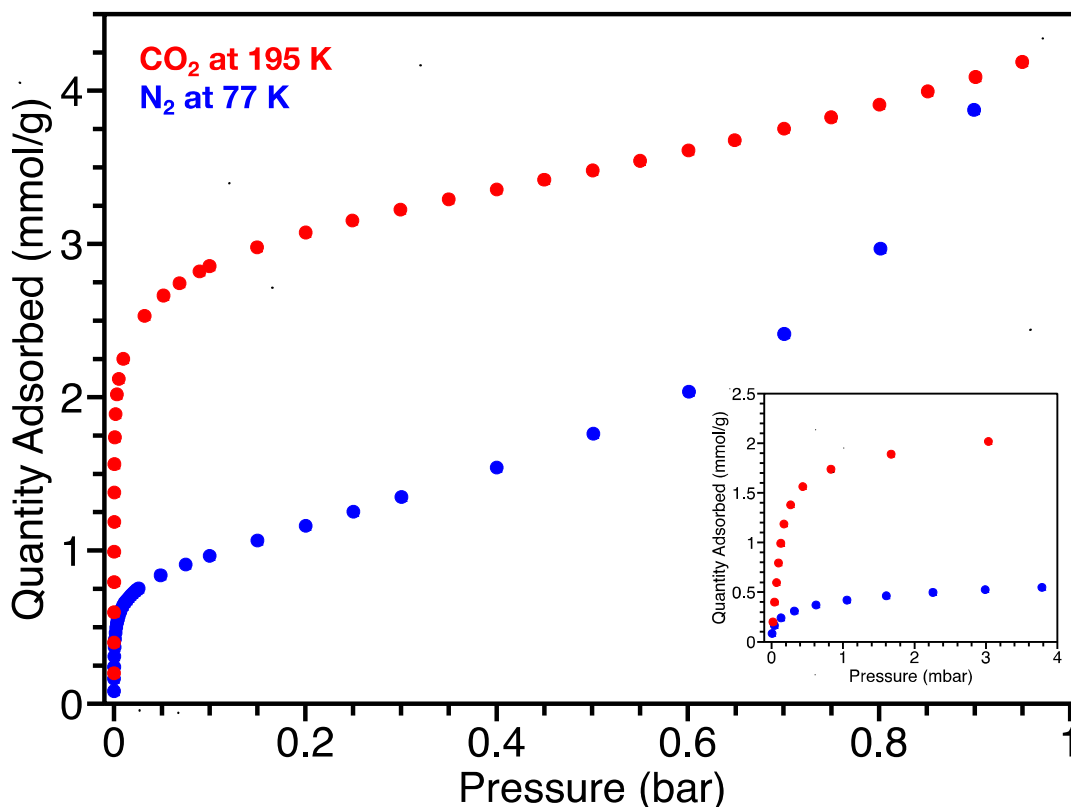


**Figure 3.26:** Gas adsorption isotherms for  $\text{N}_2$  at 77 K (blue circles, bottom) and  $\text{CO}_2$  (red circles, top) in  $\text{Fe}^{\text{II/III}}(\text{H}_x\text{gallate})$  with no discernible low-pressure phase change.

Due to its stability under activation conditions, it was possible to measure adsorption isotherms for  $\text{Fe}^{\text{II/III}}(\text{H}_x\text{gallate})$  with acetylene, ethylene, and ethane at 303, 313, and 323 K (**Figure 3.27**). In line with diminished surface area,  $\text{Fe}^{\text{II/III}}(\text{H}_x\text{gallate})$  exhibits decreased ethylene capacity compared to  $\text{Fe}^{\text{II}}(\text{H}_2\text{gallate})$ . However, as with  $\text{CO}_2$ , there is no pressure-induced phase change in  $\text{Fe}^{\text{II/III}}(\text{H}_x\text{gallate})$  in the presence of higher pressures of ethylene. Instead, the adsorption can be readily fitted to a three-site Langmuir-Freundlich equation (**Figure 3.28**). It is not unreasonable to expect there to be a larger variety of binding sites in the material now that some of the ligands have lost an additional proton, and there could be some local inhomogeneity in the distribution of charge states, giving rise to different binding sites. Despite the decrease in capacity, the thermodynamics of ethylene adsorption between the unoxidized and oxidized framework are quite similar.

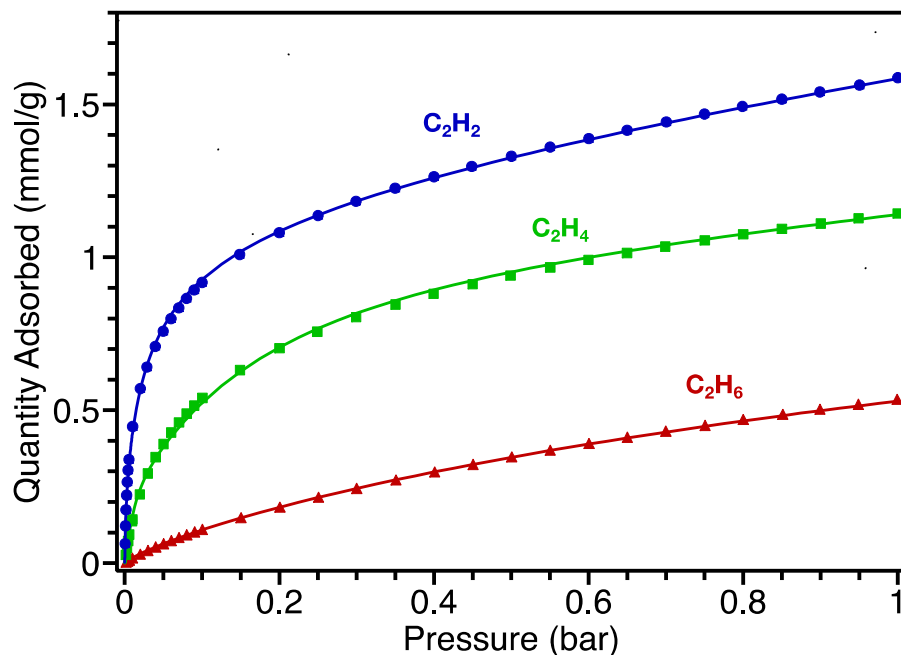


**Figure 3.27:** Example gas adsorption isotherms for  $C_2H_2$  (blue circles),  $C_2H_4$  (green squares), and  $C_2H_6$  (red triangles) in  $Fe^{III}(H_xgallate)$  at 313 K, fit to multi-site Langmuir-Freundlich isotherms (solid lines).

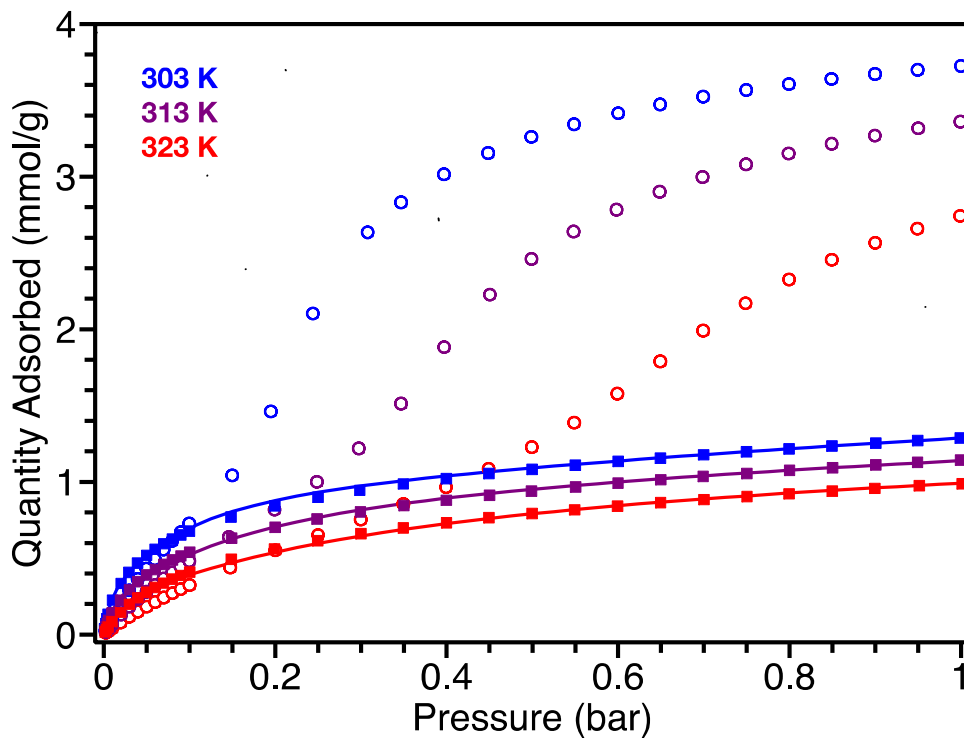


**Figure 3.28:** Comparison of gas adsorption isotherms for  $C_2H_4$  in  $Fe^{III}(H_xgallate)$  (solid squares) and  $Fe^{II}(H_2gallate)$  (empty circles) measured at 303 K (blue), 313 K (purple), and 323 K (red), with multi-site Langmuir-Freundlich fits for  $Fe^{III}(H_xgallate)$  (solid lines).

Ethane isotherms for  $\text{Fe}^{\text{II/III}}(\text{H}_x\text{gallate})$  are particularly interesting because they no longer appear to show just weak external surface adsorption. Instead, relatively steep isotherms are observed with more than double the capacity seen for  $\text{Fe}^{\text{II}}(\text{H}_2\text{gallate})$ , despite the decrease in surface area (**Figure 3.29**). While additional in situ probes are needed to verify this, the data strongly implies that ethane is now entering the pores of  $\text{Fe}^{\text{II/III}}(\text{H}_x\text{gallate})$ . I posit two possible explanations: 1. the loss of internal protons increases both pore apertures and binding sites sufficiently to allow ethane to enter. 2. the non-distorted or higher-pressure phase of metal–gallate frameworks may actually be porous to ethane, but ethane is merely incapable of converting the distorted or lower-pressure activated phase to the more porous higher-pressure phase under tested conditions. The latter explanation would be potentially problematic for the application of these materials to separate ethylene from ethane; if ethane can bind in the higher-pressure phase induced by ethylene, then the selectivity of the material will greatly diminish.

The phenomena of flexible framework exhibiting different phase transition pressures for different gases has been well documented, but interestingly there is an example of a framework maintaining selectivity by still excluding one gas molecule in the presence of another.<sup>48</sup>  $\text{Co}(\text{bdp})$  ( $\text{bdp} = 1,4\text{-benzenedipyrazolate}$ ) has been shown to flex open in the presence of  $\text{CO}_2$  but not  $\text{CH}_4$  and still selectively adsorb  $\text{CO}_2$  from a mixture of the two. Because the step pressure in flexible materials decreases with lower temperature, if  $\text{Fe}^{\text{II}}(\text{H}_2\text{gallate})$  has a phase transition with ethane it will occur more readily at lower temperature. To this end, a 195 K ethane isotherm was measured for  $\text{Fe}^{\text{II}}(\text{H}_2\text{gallate})$  (**Figure 3.30**). Rather than a step, there is incredibly shallow binding at low pressures and a gradual increase in adsorption at higher pressures consistent with mesoporous condensation. If under such forcing conditions, ethane is still incapable of inducing a phase change, then it seems unlikely that it is capable of fitting in to the framework pore. Thus, we are left with the first explanation, the removal of protons from the pore environment of iron–gallate removes the spatial obstacle that prevents ethane from entering the pore. Despite appreciable adsorption of ethane,  $\text{Fe}^{\text{II/III}}(\text{H}_x\text{gallate})$  is still selective for ethylene, albeit with a much more modest IAST selectivity of 12.

Acetylene adsorption in  $\text{Fe}^{\text{II/III}}(\text{H}_x\text{gallate})$  similarly does not show any phase change. As with the other  $\text{C}_2$  gases, acetylene isotherms can also be readily fit by a multi-site Langmuir-Freundlich equation. Unexpectedly, the partial oxidation of the framework appears to have dramatically changed the nature of acetylene adsorption; the binding enthalpy appears to have decreased by 20–30 kJ/mol (**Figure 3.31**). While its capacity for acetylene is still greater than that of ethylene, the decreased binding enthalpy lowers  $\text{Fe}^{\text{II/III}}(\text{H}_x\text{gallate})$ 's acetylene/ethylene IAST selectivity to just 5, compared to 17 for  $\text{Fe}^{\text{II}}(\text{H}_2\text{gallate})$ . Further studies such as in situ infrared spectroscopy and in situ diffraction measurements could help elucidate the cause of this difference in gas adsorption properties.

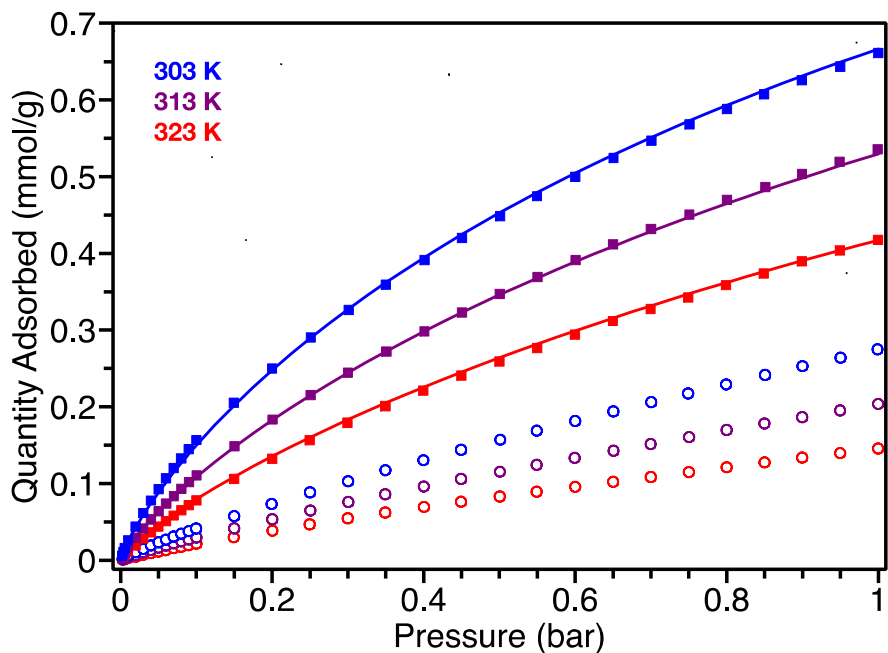


**Figure 3.29:** Comparison of gas adsorption isotherms for  $C_2H_6$  in  $Fe^{III}(H_xgallate)$  (solid squares) and  $Fe^{II}(H_2gallate)$  (empty circles) measured at 303 K (blue, top), 313 K (purple, middle), and 323 K (red, bottom), with multi-site Langmuir-Freundlich fits for  $Fe^{III}(H_xgallate)$  (solid lines).

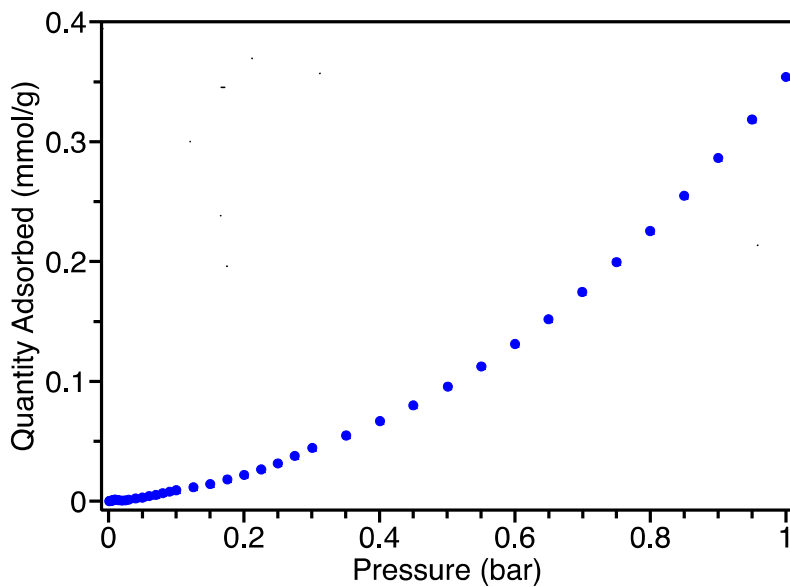


**Figure 3.30:** Gas adsorption isotherms for  $Fe^{II}(H_2gallate)$  in the presence of  $C_2H_6$  at 195 K (blue circles) exhibiting mesoporous condensation.

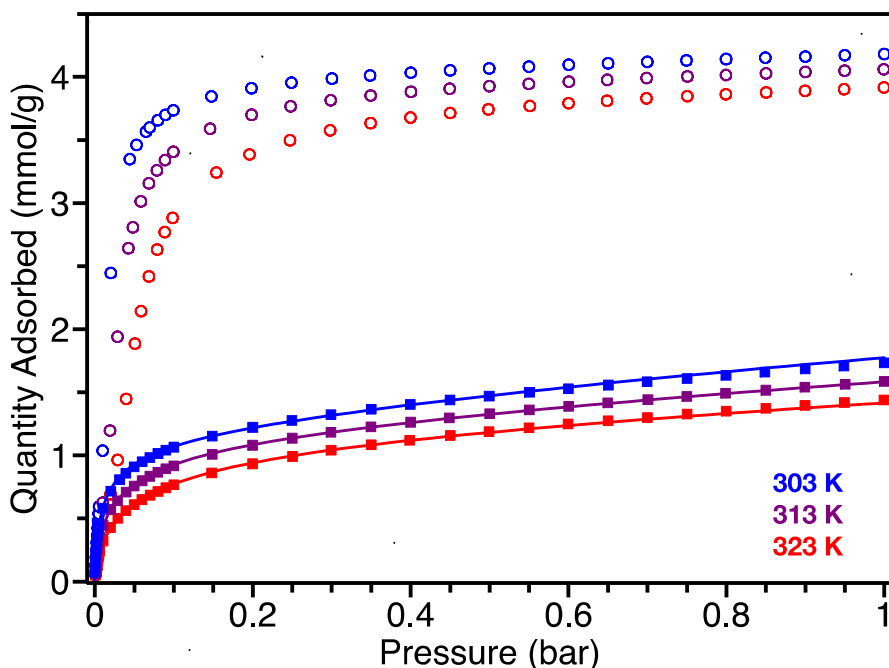


**Figure 3.31:** Comparison of gas adsorption isotherms for C<sub>2</sub>H<sub>2</sub> in Fe<sup>III</sup>(H<sub>x</sub>gallate) (solid squares) and Fe<sup>II</sup>(H<sub>2</sub>gallate) (empty circles) measured at 303 K (blue), 313 K (purple), and 323 K (red), with multi-site Langmuir-Freundlich fits for Fe<sup>III</sup>(H<sub>x</sub>gallate) (solid lines).

### 3.4 Conclusions and Outlook

The newly isolated and characterized framework, Fe<sup>II</sup>(H<sub>2</sub>gallate), exhibits a unique confluence of properties in metal–organic frameworks. Evidence suggests that Fe<sup>III</sup>(Hgallate)·*x*H<sub>2</sub>O forms as Fe<sup>II</sup>(H<sub>2</sub>gallate)·2H<sub>2</sub>O and oxidizes in situ. Understanding the roles of the valence state of reagents as well as the presence of oxidants and reductants during synthesis is critical to the formation of redox-active metal-organic frameworks. The gas adsorption behavior of Fe<sup>II</sup>(H<sub>2</sub>gallate) suggests an unprecedented selectivity for ethylene over ethane. The observance of a phase change under various gasses and subsequent impact on selectivity calculations highlights the important role of frequently disregarded or unacknowledged assumptions in adsorption models. Accurate control over crystallite morphology could also help elucidate the origin of ethane adsorption in metal–gallate frameworks and whether in fact it is dependent on external surface area and defect sites. Lastly, as the library of synthesized metal–organic frameworks continues to expand, the possibility of utilizing framework protonation state for charge balance in redox chemistry should not be overlooked. As indicated by the change in adsorption properties of Fe<sup>III</sup>(H<sub>x</sub>gallate), this underutilized phenomenon could be seen as another tool for tuning the properties of an isorecticular system, along with mixed-metal and mixed-linker approaches.

### 3.5 Acknowledgments

Material synthesis was funded by NSF Award No. DMR-1611525 and material characterization was funded by the U.S. Department of Energy, Office of Science, Basic Energy Sciences (the Center for Gas Separations, an Energy Frontier Research Center, DE-SC0001015). R.M.T. was funded by National Science Foundation (NSF) Graduate Research Fellowship Program and University of California-Berkeley Chancellor's Fellowship. I thank James Breen for design and fabrication of glassware, Miguel I. Gonzalez for single-crystal X-ray diffraction measurements, Khetspakorn Chakarawat for  $^{57}\text{Fe}$  Mössbauer measurements, and Kristen A. Colwell for SEM imaging.

### 3.6 References and Supplementary Figures

- (1) Cooper, L.; Hidalgo, T.; Gorman, M.; Lozano-Fernández, T.; Simón-Vázquez, R.; Olivier, C.; Guillou, N.; Serre, C.; Martineau, C.; Taulelle, F.; Damasceno-Borges, D.; Maurin, G.; González-Fernández, Á; Horcajada, P.; Devic, T. *Chem. Commun.* **2015**, 51 (27), 5848.
- (2) Feller, R. K.; Cheetham, A. K. *Solid State Sci.* **2006**, 8 (9), 1121.
- (3) Saines, P. J.; Yeung, H.; Hester, J. R.; Lennie, A. R.; Cheetham, A. K. *Dalton Trans.* **2011**, 40 (24), 6401.
- (4) Weber, R.; Bergerhoff, G. *Z. Krist.-Cryst. Mater.* **1991**, 195, 87.
- (5) Wunderlich, C. -H.; Weber, R.; Bergerhoff, G. *Z. Anorg. Chem.* **1991**, 598 (1), 371.
- (6) Pliny the Elder. *Naturalis Historia.* **77-79**.
- (7) Capella, M. *De nuptiis Philologiae et Mercurii.*
- (8) Ponce, A.; Brostoff, L. B.; Gibbons, S. K.; Zavalij, P.; Viragh, C.; Hooper, J.; Alnemrat, S.; Gaskell, K. J.; Eichhorn, B. *Anal. Chem.* **2016**, 88 (10), 5152.
- (9) Lerf, A.; Wagner, F. *Hyperfine Interact.* **2016**, 237 (1), 36.
- (10) Wagner, F. E.; Lerf, A. *Z. Anorg. Chem.* **2015**, 641 (14), 2384.
- (11) Huskić, I.; Pekov, I. V.; Krivovichev, S. V.; Friščić, T. *Sci. Adv.* **2016**, 2 (8), e1600621.
- (12) Metal-organic frameworks with appreciable electronic conductivity are always reported as darkly colored in appearance, most likely stemming from the excitation of a large quantity of charge carriers over a range of different hopping-barriers.
- (13) Sun, L.; Hendon, C. H.; Park, S. S.; Tulchinsky, Y.; Wan, R.; Wang, F.; Walsh, A.; Dincă, M. *Chem. Sci.* **2017**, 8 (6), 4450.
- (14) Aubrey, M. L.; Wiers, B. M.; Andrews, S. C.; Sakurai, T.; Reyes-Lillo, S. E.; Hamed, S. M.; Yu, C.; Darago, L. E.; Mason, J. A.; Baeg, J.; Grandjean, F.; Long, G. J.; Seki, S.; Neaton, J. B.; Yang, P.; Long, J. R. *Nat. Mater.* **2018**, 17, 625.
- (15) Park, J. G.; Aubrey, M. L.; Oktawiec, J.; Chakarawat, K.; Darago, L. E.; Grandjean, F.; Long, G. J.; Long, J. R. *J. Am. Chem. Soc.* **2018**, 140 (27), 8526.
- (16) Zheng, F.; Wang, L. *Energ. Environ. Sci.* **2019**, 12 (4), 1219.
- (17) Oniki, T.; Takahama, U. *J. Wood Sci.* **2004**, 50 (6), 545.
- (18) Caregnato, P.; vid Gara, P.; Bosio, G. N.; Gonzalez, M. C.; Russo, N.; del Michelini, M.; Mártire, D. O. *J. Phys. Chem.* **2008**, 112 (6), 1188.
- (19) Badhani, B.; Sharma, N.; Kakkar, R. *RSC Adv.* **2015**, 5 (35), 27540.
- (20) Bao, Z.; Wang, J.; Zhang, Z.; Xing, H.; Yang, Q.; Yang, Y.; Wu, H.; Krishna, R.; Zhou, W.; Chen, B.; Ren, Q. *Angew. Chem. Int. Ed.* **2018**, 57 (49), 16020.
- (21) Sholl, D. S.; Lively, R. P. *Nat. News* **2016**, 532 (7600), 435.

- (22) Othmer, D.; Naphtali, L. *Ind. Eng. Chem. Chem. Eng. Data Series* **1956**, *1* (1), 6.
- (23) Fritz, J.; Fuget, C. *J. Ind. Eng. Chem.* **1956**, *1* (1), 10.
- (24) Technically acidic protons can act as an oxidizing species in the generation of H<sub>2</sub> gas but a hexaaquo Fe<sup>II</sup> species or a Fe<sup>II</sup> in a similarly weak field coordination environment should not be reducing enough for this to occur.
- (25) Lu, Z.; Godfrey, H. G.; da Silva, I.; Cheng, Y.; Savage, M.; Manuel, P.; Rudić, S.; Ramirez-Cuesta, A. J.; Yang, S.; Schröder, M. *Chem. Sci.* **2018**, *9* (13), 3401.
- (26) Bloch, E. D.; Murray, L. M.; Queen, W. L.; Chavan, S.; Maximoff, S. N.; Bigi, J. P.; Krishna, R.; Peterson, V. K.; Grandjean, F.; Long, G. J.; Smit, B.; Bordiga, S.; Brown, C. M.; Long, J. R. *J. Am. Chem. Soc.* **2011**, *133*, 14814.
- (27) Liao, P.-Q.; Zhu, A.-X.; Zhang, W.-X.; Zhang, J.-P.; Chen, X.-M. *Nat. Commun.* **2015**, *6* (1), 6350.
- (28) Tu, B.; Pang, Q.; Xu, H.; Li, X.; Wang, Y.; Ma, Z.; Weng, L.; Li, Q. *J. Am. Chem. Soc.* **2017**, *139*, 7998.
- (29) Xiao, D. J.; Gonzalez, M. I.; Darago, L. E.; Vogiatzis, K. D.; Haldoupis, E.; Gagliardi, L.; Long, J. R. *J. Am. Chem. Soc.* **2016**, *138*, 7161.
- (30) Tulchinsky, Y.; Hendon, C. H.; Lomachenko, K. A.; Borfecchia, E.; Melot, B. C.; Hudson, M. R.; Tarver, J. D.; Korzyński, M. D.; Stubbs, A. W.; Kagan, J. J.; Lamberti, C.; Brown, C.M.; Dincă, M. *J. Am. Chem. Soc.* **2017**, *139* (16), 5992.
- (31) Anderson, J. S.; Gallagher, A. T.; Mason, J. A.; Harris, D. T. *J. Am. Chem. Soc.* **2014**, *136* (47), 16489.
- (32) Sekutowski, D. G.; Stucky, G. D. *J. Chem. Educ.* **1976**, *53* (2), 110.
- (33) Leorand, J.; Lygo, B.; Procter, G. *Advanced Practical Organic Chemistry*, 3rd Ed. Routledge, **2013**.
- (34) Connelly, N. G.; Geiger, W. E. *Chem. Rev.* **1996**, *96* (2), 877.
- (35) Yousefinejad, S.; Honarasa, F.; Solhjoo, A. *J. Chem. Eng. Data* **2016**, *61* (1), 614.
- (36) Material degradation from an inevitably imperfect oxygen-free atmosphere could also lead to addition Fe<sup>III</sup> presence.
- (37) While the unit cell parameters are similar, direct comparison of the structures is not possible as the authors have yet to submit a .cif of their powder neutron diffraction structure, which should have been required by the editor.
- (38) Mahajan, O. P. *Carbon* **1991**, *29* (6), 735.
- (39) The CO<sub>2</sub> isotherms are plotted in almost the same way as **Figure 3.17**, but without a low pressure insert. At this scale, the low-pressure region appears completely vertical. It is possible that lower-pressure deviations were attributed to noise/instrument error, but any such discussion was omitted.
- (40) Walton, K. S.; Sholl, D. S. *AIChE J.* **2015**, *61* (9), 2757.
- (41) Myers, A.; Prausnitz, J. *AIChE J.* **1965**, *11* (1), 121.
- (42) Rother, J.; Fieback, T. *Adsorption* **2013**, *19* (5), 1065.
- (43) Harlick, P.; Tezel, F. *Separ. Sci. Technol.* **2002**, *37* (1), 33.
- (44) Ahmadpour, A.; Wang, K.; Do, D. *AIChE J.* **1998**, *44* (3), 740.
- (45) Yang, S.; Ramirez-Cuesta, A. J.; Newby, R.; Garcia-Sakai, V.; Manuel, P.; Callear, S. K.; Campbell, S. I.; Tang, C. C.; Schröder, M. *Nat. Chem.* **2015**, *7* (2), 121.
- (46) van Eldik, R.; Hubbard, C. D. *Advances in Inorganic Chemistry: Inorganic Reaction Mechanisms*. Elsevier, **2003**.

- (47) Kärger, J.; Ruthven, D. M.; Theodorou, D. N. Diffusion in Nanoporous Materials. Wiley-VCH Verlag GmbH & Co. KGaA, **2012**.
- (48) Taylor, M. K.; Runčevski, T.; Oktawiec, J.; Bachman, J. E.; Siegelman, R. L.; Jiang, H.; Mason, J. A.; Tarver, J. D.; Long, J. R. *J. Am. Chem. Soc.* **2018**, *140* (32), 10324.

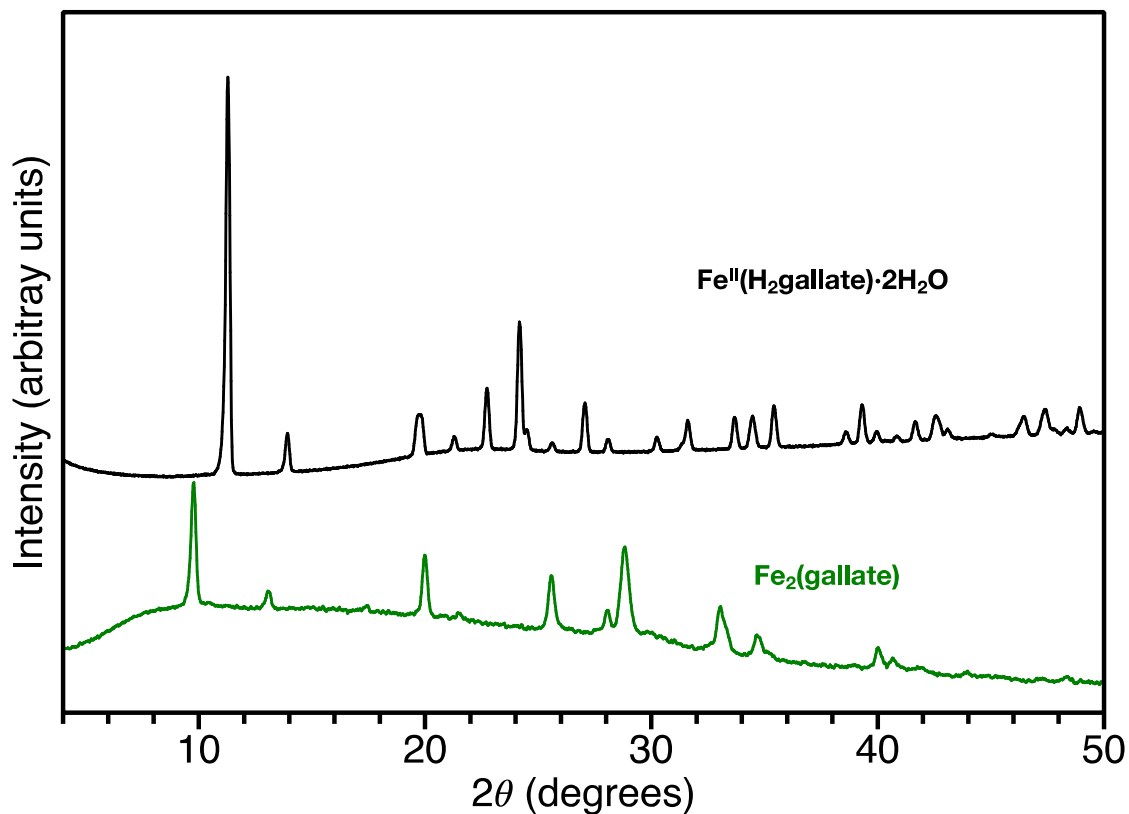


**Figure 3.S1:** Comparison of powder X-ray diffraction patterns of  $\text{Fe}_2(\text{gallate})$  (green, bottom), vs  $\text{Fe}^{\text{II}}(\text{H}_2\text{gallate})\cdot 2\text{H}_2\text{O}$  (black, top).  $\text{Fe}_2(\text{gallate})$  was obtained as a green powder from the reaction of stoichiometric equivalents of  $\text{FeCl}_2$  and gallic acid in a 3:1 DMF: $\text{H}_2\text{O}$  solution in a sealed tube at  $120^\circ\text{C}$  for 1 day.

# Chapter 4: Solvent-Free Synthetic Routes Towards Redox-Active Metal–Organic Frameworks

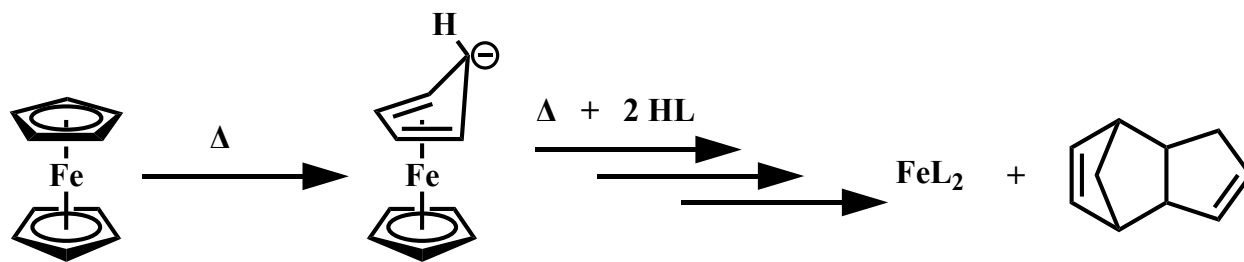
## 4.1 Introduction

The vast majority of synthetic routes for the formation of metal–organic frameworks are solution-based procedures which rely upon the formation of an enthalpically favored product via a pseudo-reversible process to yield a crystalline solid.<sup>1</sup> Reversibility of framework formation is often indirectly controlled by the gradual deprotonation of organic ligands. This deprotonation is commonly performed via the thermal decomposition of an amide-based solvent,<sup>2</sup> but in some cases it is facilitated by simply introducing a base at ambient<sup>3</sup> or elevated temperatures.<sup>4</sup> While solution-based syntheses have given rise to tens of thousands of metal–organic frameworks,<sup>5</sup> they are inherently limited to a portion of reaction space where the reagents are stable in solution but not so stable as to prevent framework formation. In some cases, metal cations in solution interact so strongly with a target ligand that essentially irreversible bonding between the two leads to precipitation of an amorphous solid when a crystalline phase would be lower in free energy. At the other end of the spectrum, a reaction can result in little to no solid, with the reagents either forming molecular species or merely remaining as solvated species without reacting. These two scenarios (amorphous product or no product) are rarely described in the literature because they do not yield an isolable or easy to characterize material, yet they occur so frequently that any researcher that performs reaction screens for metal–organic frameworks is bound to encounter them. In the broader field of coordination solids, over the last few decades numerous “solvent-free” synthetic methods have been developed to aid in obtaining new materials that for one reason or another are not accessible via solution-based chemistry. Two particularly promising approaches are the use of “melts” at high temperature (typically  $\geq 150$  °C),<sup>6</sup> and the use of mechanochemistry to synthesize metal–organic frameworks.<sup>7</sup>

As the name suggests, melt reactions broadly speaking involve heating a mixture of solid reagents above the melting point of one or more components to create a liquid environment where a desired reaction may proceed. While the reaction can still be thought of as occurring in solution, now the solvent is constituted solely of reagents. These reactions typically rely on the formation of thermodynamically favored products, but careful control of heating, cooling, and reaction duration can lead to the isolation of kinetic products. Melt reactions are applied in a variety of fields such as solid-state chemistry, in the formation of dense inorganic solids from salts,<sup>8</sup> and organic chemistry, i.e. the Newman-Kwart rearrangement.<sup>9,10</sup>

As they pertain to coordination solids, melt reactions rely on organic ligands with high thermal stability and relatively low melting points. While there are melt reactions that have been reported with neutral ligands,<sup>11</sup> the reactions that are most analogous to metal–organic framework syntheses are ones performed with protic ligands that are incorporated into a coordination solid product in a deprotonated state. In one common approach, the thermal decomposition of ferrocene is used to gradually introduce a base (**Scheme 4.1**),<sup>6,12–18</sup> analogous to the thermal decomposition of N,N-dimethylformamide (DMF) in solvothermal reactions. At elevated temperatures ( $\geq 150$  °C) the cyclopentadienyl ligands in ferrocene become more labile and can dearomatize. Once partially dissociated, these ligands can function as a Bronsted base and deprotonate other reaction species, leading to complete dissociation. This process gradually introduces  $\text{Fe}^{2+}$  ions into liquid media of

both protonated and deprotonated ligands, allowing a crystalline solid to be formed with dicyclopentadiene as the only byproduct.



**Scheme 4.1:** The cyclopentadienyl (Cp) ligands in ferrocene can rearomatize when heated to sufficiently high temperature ( $\sim 150\text{ }^{\circ}\text{C}$ ) exposing a highly basic carbanion. This basic species then deprotonates a ligand (L) leading to dissociation of HCp, which readily dimerizes ( $\text{H}_2\text{Cp}_2$ ). This process is repeated with the other Cp ligand as  $\text{Fe}^{2+}$  ions are eventually incorporated into a coordination solid with L.

Melt reactions in coordination solids have been strictly limited to n-heterocyclic ligands, due to their thermal and chemical stability (**Figure 4.1**). Moreover, other common framework forming moieties, such as carboxylates, generally decompose long before melting.<sup>19</sup> The most common ligands used for these melts are imidazole-derived species. In the field of metal–organic frameworks, materials made from purely imidazolate-based ligands fall primarily under the umbrella term of zeolitic imidazolate frameworks (ZIFs). Coined by Yaghi et al. in 2006,<sup>20</sup> this phrase is meant to highlight the topological similarities between ZIFs and zeolites; since then, this subsection of metal–organic frameworks has expanded dramatically to encompass a wide variety of structures and topologies not found in zeolites.<sup>21–24</sup>

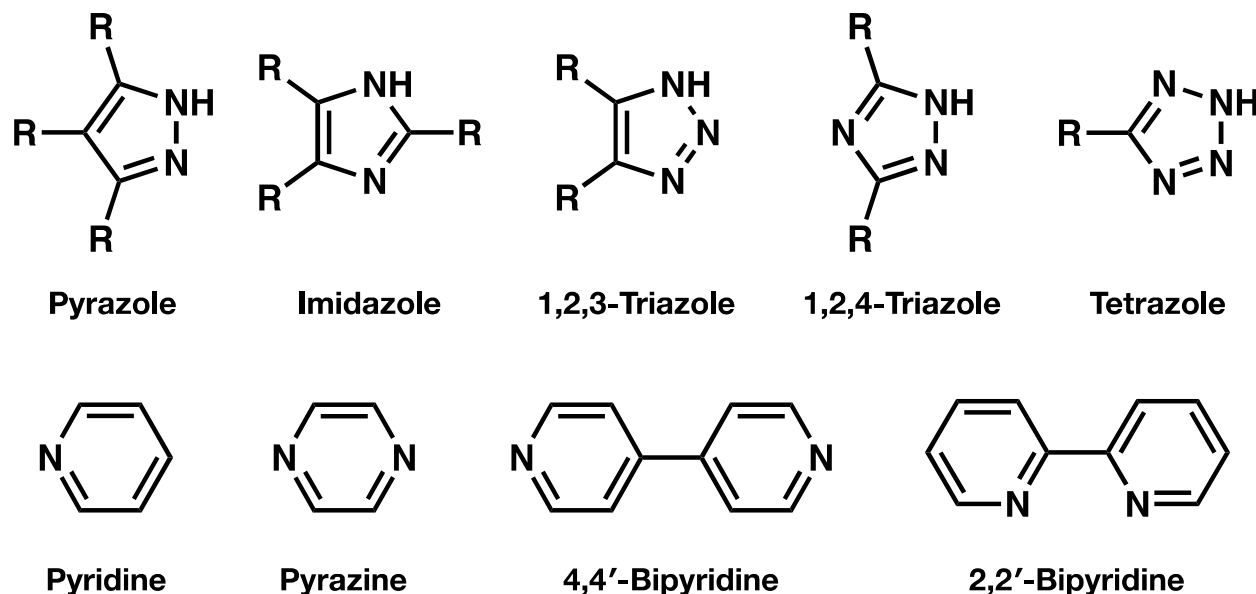
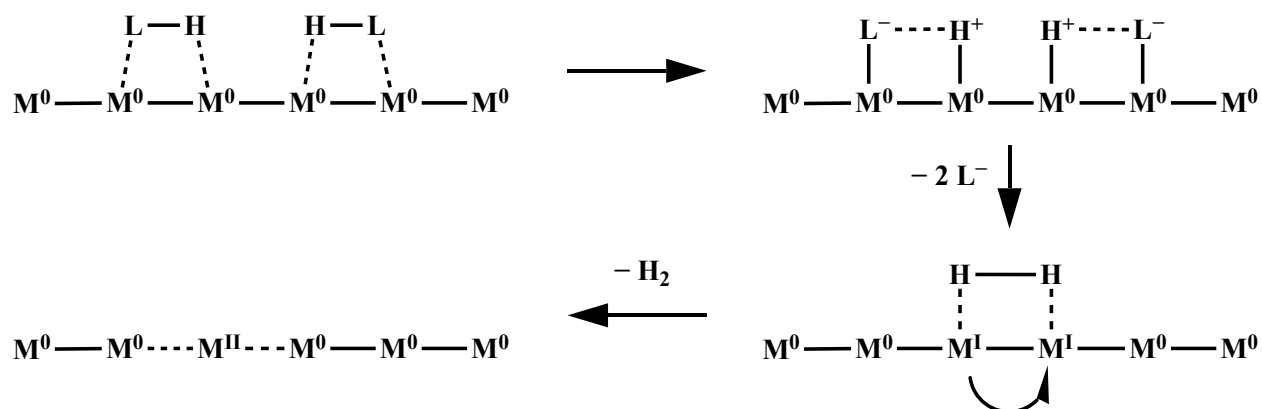


**Figure 4.1:** Five-membered n-heterocycles which can be used to form coordination solids (top) with a large number of variable substituents (R) and neutral six-membered n-heterocycles (bottom) which can occasionally be incorporated into coordination solids.

ZIFs have also been the target of numerous studies in the formation of metal–organic framework glasses, and liquid-MOFs.<sup>25–28</sup> In these studies, crystalline ZIFs are heated to induce phase transitions, a process that is only possible due to the same thermal stability that is leveraged in melt reactions. ZIFs, however, have been primarily limited to Zn<sup>2+</sup>, with some Co<sup>2+</sup> and Cd<sup>2+</sup> species, and a sparse selection of other metal analogues. Until very recently, iron was noticeably absent from these series, even though it can readily adopt the tetrahedral coordination environment ubiquitous in ZIFs. The first reported porous iron-ZIF (Fe-ZIF-8) was recently synthesized using a melt reaction.<sup>6</sup> The use of melt reactions could therefore lead to the isolation of new iron-ZIFs that have not yet been achieved via solvothermal routes or other traditional methods.

The requisite use of *n*-heterocyclic ligands such as imidazoles in melt reactions should not be seen as a limitation. Strong *d*–*p* orbital interactions between a metal and the delocalized  $\pi$ -system in *n*-heterocycles via metal-bound nitrogens can engender strong electronic communication between metal sites. Such communication has been seen not only in classic mixed valent systems such as the Creutz–Taube ion,<sup>29,30</sup> but also in imidazolate bridged species.<sup>31</sup> How such interactions correlate to bulk properties in extended networks remains poorly understood, primarily due to a lack of available materials. In what was one of the first examples of electrical conductivity in metal–organic frameworks, iron–triazolate (Fe(tri)<sub>2</sub>, tri<sup>−</sup> = 1,2,3-triazolate) exhibited a substantial increase in conductivity upon oxidation;<sup>32</sup> this phenomenon was later investigated further through careful sub-stoichiometric oxidations.<sup>33</sup> Such examples of conductive *n*-heterocycle-based metal–organic frameworks are almost entirely limited to redox-active iron systems.<sup>34,35</sup> For many of these materials there are isostructural analogues, but they are primarily made with later transition metals with much more limited redox activity, and poor spatial and energetic orbital matching with the linkers.<sup>32</sup> In general, early transition metals with large diffuse orbitals capable of accessing multiple redox states, such as titanium, vanadium, and chromium, are rarely found in metal–organic frameworks. This scarcity is in part due to the instability of these transition metal ions in solution under solvothermal conditions and ligand incompatibility. Solvent-free approaches such as melt reactions could be leveraged to obtain these more exotic materials, as was demonstrated recently in the isolation of a dense, highly conductive coordination solid containing chromium and pyrazine radicals via a melt reaction.

A more recent and somewhat niche area of research in coordination solid melts has been in the reactivity of elemental metal with organic molecules to yield metal–organic frameworks or denser phases.<sup>36–44</sup> At substantially elevated temperatures (~250–300 °C) metal surfaces can reduce even mildly acidic protons on an organic ligand yielding H<sub>2</sub>(gas) and an anionic ligand (**Scheme 4.2**). As this process continues, metal cations dissolve into an increasingly basic solution of the ligand, eventually affording a coordination solid of the two reagents. I think of this approach as “minimalist” chemistry because if the reaction proceeds correctly, the only byproduct is an elemental gas. There is no counterion, base, or otherwise unused component, just metal (solid) + organic molecule (liquid) = metal–organic material (solid) + H<sub>2</sub> (gas). In some cases, however, the metal source can have diminished reactivity due to the presence of a small but relatively stable oxide layer; this can be overcome by the addition of a small amount of mercury, which forms an amalgam with all known metals and can destabilize passivating oxides. While this approach has been applied to cobalt<sup>36</sup> and some lanthanides,<sup>37–44</sup> such reactivity with other transition metals is entirely unreported. Application of this facet of melt reactions to iron or earlier first row transition metals could be another possible route to the formation of new metal–organic materials.



**Scheme 4.2:** A simplified depiction of the reduction of acidic protons on ligands (L) on a metal surface (M) leading to the formation of H<sub>2</sub> gas. As the metal surface continues to oxidize, divalent or higher oxidation state ions dissociate.

Mechanochemistry presents an interesting alternative route for the synthesis of metal–organic frameworks, utilizing local heating and/or pressure from friction and/or impacts to provide energy to overcome reaction barriers. Numerous well-known metal–organic frameworks have been later synthesized via mechanochemical routes.<sup>45–51</sup> It is often touted as a greener, high yield synthesis, as it does not require toxic or expensive solvents and reaction yields can be near quantitative.<sup>52</sup> Additionally, with the development of special X-ray beamline-compatible apparatuses, mechanochemistry has been used as an in situ technique to study intermediate phases that form during framework syntheses.<sup>47,53</sup> However, the critical weakness of this synthetic approach is a lack of standardizable reaction parameters. There are numerous different instrumentations and approaches that fall under the umbrella of mechanochemistry, from ball mills, to disk mills, to even a manually operated mortar and pestle. Reaction times using one technique cannot be readily converted to another. Because of its ubiquitous use in the literature, I will limit further mechanochemistry discussion hereafter to ball milling.<sup>52</sup>

There are two general configurations for ball milling: shaker and planetary ball mills. Shaker mills move reaction jars back and forth rapidly causing a ball(s), also known as a charge(s), to impact and scrape reactants against each other and the inner walls of the jar. In planetary ball mills, on the other hand, a large assembly is rotated rapidly in one direction while individual jars on the assembly are spun in the opposite direction. As in shaker ball mills, balls are used to impart force on the contents of the jars, in this case large centrifugal forces. Planetary mills can provide larger energetic inputs to ball mill reactions; however, they are substantially more expensive than shakers and are therefore less frequently used in the literature. The most frequently used instrumentation, and consequentially the one used for reactions reported in this chapter, is the Retsch MM-400 ball mill. In a typical ball mill reaction, dry reagents react analogously to salt metathesis reactions (**Scheme 4.3**). This reactivity has been leveraged to form frameworks from oxides or in the presence of other basic species.<sup>45–53</sup> In the following sections of this chapter I will discuss several new results in the use of ball milling as well as melt reactions as alternative solvent-free synthetic routes towards redox-active metal–organic frameworks.



**Scheme 4.3:** Ball milling typical functions as a form of salt metathesis; in this generic example, a metal halide  $\text{MX}_2$  reacts with the alkali salt (A) of an anionic base (B) and a protonated ligand ( $\text{H}_n\text{L}$ ) to yield the coordination solid  $\text{M}_{n/2}\text{L}$ , conjugate acid (HB), and salt (AX).

## 4.2 Experimental

### Melt Reactions

All metallocenes and n-heterocycles used for melt reactions were sublimed before use (ferrocene was sublimed three times). Iron-based melt reactions were prepared in air by loading solid reagents into 1/2" or 1/4" glass tubes, attaching a Breen adapter, freezing in liquid  $\text{N}_2$ , evacuating, and then flame-sealing. Chromocene and vanadocene reaction tubes were prepared in an analogous manner but the reagents were initially loaded in an Ar glove box. Tubes were typically heated in an oven at 150 °C for three days before being transferred into an Ar glove box and opened. Samples were typically washed three times with acetonitrile at room temperature for one day each.  $\text{Fe}(\text{bzimid})_2$  was synthesized by reacting 60 mg of ferrocene (0.32 mmol, 1 eq.) with 116 mg of benzimidazole (0.98 mmol, 3 eq.) in a 1/2" tube as described above to yield a light pink/tan solid. Cr–bzimid was synthesized by reacting 60 mg of chromocene (0.33 mmol, 1 eq.) with 116 mg of benzimidazole (0.98 mmol, 3 eq.) in a 1/2" tube as described above to yield a dark purple powder V–bzimid was synthesized by reacting 60 mg of vanadocene (0.33 mmol, 1 eq.) with 116 mg of benzimidazole (0.98 mmol, 3 eq.) in a 1/2" tube as described above to yield a olive green powder.

### Solvothermal reactions

Parallel solvothermal reactions were performed in air by mixing reagents in 1-2 mL of DMF, or desired solvent mixture, transferring to a 1/2" glass tube, attaching a Breen adapter, freezing in liquid  $\text{N}_2$ , evacuating, and then flame-sealing. Tubes were then heated in an oven at temperatures from 120–150 °C for 1–3 days before being opened and filtered in air.

### Minimalist Reactions

In a general procedure for minimalist reactions, <10  $\mu\text{m}$  diameter metal powder was mixed with the desired ligand(s) inside an Ar glovebox in a predetermined stoichiometry. 25 mg or less of this mixture was added to a 1/4" glass tube, topped with a Breen adapter, transferred out of the glovebox and onto a Schlenk line, frozen in liquid  $\text{N}_2$ , evacuated, and then flame-sealed. Tubes were then heated in an oven at 300 °C for 5 days. Tubes that did not undergo a "sudden unplanned depressurization" and that did not have any visual cracks were transferred back into an Ar glovebox and opened.

$\text{Fe}(\text{imid})_2$  was synthesized by first loading a 1/2" sealed tube with 50 mg iron powder (0.90 mmol, 1 eq.) with 183 mg of imidazole (2.69 mmol, 3 eq.) inside an Ar glove box and flame sealing it as previously mentioned. The tube was then heated in an oven at 300 °C for 5 days resulting in the formation of a large quantity of fluffy white  $\text{Fe}(\text{imid})_2$

## Ball Mill Reactions

All ball milling reactions were performed with Restch MM-400 shaker ball mill, in stainless steel jars with Teflon gaskets, at room temperature, with 1–2 stainless steel balls, and oscillated at 30 Hz. For ball milling melt screens, 5 mL jars were used.  $\text{Fe}^{\text{II}}(\text{H}_2\text{gallate})\cdot 2\text{H}_2\text{O}$  was synthesized by first loading 452 mg of anhydrous  $\text{FeCl}_2$  beads (3.56 mmol, 1 eq.), 142 mg of powdered sodium hydroxide (3.56 mmol, 1 eq.), and 670 mg of gallic acid monohydrate (3.56 mmol, 1eq.) into a 25 mL stainless steel jar with a single 13.6 g stainless steel ball. The jar was sealed using specially designed Retsch tools, inside an aqueous compatible glovebox, before then being transferred out of the glovebox, shaken in a ball mill, and transferred back into the glovebox. Reaction shaken times were 45 min for phase impure iron–gallate and 90 minutes for phase pure  $\text{Fe}^{\text{II}}(\text{H}_2\text{gallate})\cdot 2\text{H}_2\text{O}$ . Inside the glove box, jars were opened using the same Retsch tools, and the contents were rinsed out of the jars using water, left to soak for one hour and then filtered. For 90 minutes reaction  $\sim 390$  mg of  $\text{Fe}^{\text{II}}(\text{H}_2\text{gallate})\cdot 2\text{H}_2\text{O}$  was obtained (1.50 mmol, 42% yield)

$\text{Ni}(\text{H}_2\text{gallate})\cdot 2\text{H}_2\text{O}$  was synthesized in an analogous manner by loading 539 mg of gallic acid monohydrate (2.86 mmol, 1 eq.) and 713 mg of nickel acetate tetrahydrate (2.86 mmol, 1 eq.) into a 25 mL stainless steel jar with a single 13.6 g stainless steel bar, either in air or in an aqueous compatible glovebox and shaken in a ball mill for 45 mins. As with iron-gallate samples

## Powder X-ray Diffraction Measurements

Laboratory powder X-ray diffraction patterns were collected using a Bruker AXS D8 Advance diffractometer with  $\text{Cu K}\alpha$  radiation ( $\lambda = 1.5418 \text{ \AA}$ ). In the case of air-sensitive materials, samples were loaded into 1.0 mm diameter borosilicate capillaries inside a glovebox under an Ar or  $\text{N}_2$  atmosphere and flame-sealed. High-resolution powder X-ray diffraction data for Cr–bzimid and V–bzimid were collected at Beamline 12.2.2 at the Lawrence Berkeley National Lab Advanced Light Source ( $\lambda = 0.4972 \text{ \AA}$ ).

## Infrared Spectroscopy Measurements

Infrared spectra were obtained using a Perkin Elmer Avatar Spectrum 400 FTIR spectrometer equipped with a Pike attenuated total reflectance accessory. Air-free measurements were performed by encasing the in the sample holder in a  $\text{N}_2$  purged glove bag.

## 4.3 Results and Discussion

### Ferrocene-Based Melt Reactions

The process of performing a melt reaction with ferrocene is not dramatically more difficult than typical metal–organic framework solvothermal reactions. Ferrocene and a desired ligand can be loaded into a glass tube under ambient conditions, at which point the tube is evacuated, flame sealed, and heated in an oven. Additionally, purification of reagents is relatively trivial, as ferrocene and many n-heterocycles sublime readily. Some consideration must be made to prevent such sublimation from occurring during the reaction due to uneven heating, but otherwise numerous reaction screens can be readily set up. However, the primary barrier in screening melt reactions is the isolation of product. Melt reactions can result in the formation of a very dense resin-like matrix of unreacted ligand, unreacted ferrocene, dicyclopentadiene, and the desired coordination solid product. Adding to this synthetic quagmire is the air sensitivity of the product. All such ferrocene-derived products that I synthesized eventually exhibited an irreversible color

change when exposed to O<sub>2</sub>, consistent with oxidation of Fe<sup>II</sup> centers to Fe<sup>III</sup>. Therefore, while ferrocene melt reactions can be prepared under ambient conditions, any work up or manipulation of the products must be performed under inert atmosphere. While unreacted reagents can be removed via sublimation, this process is slow, subjects the products to additional heat, and is not easily applied to a large number of samples simultaneously without cross contamination. Instead, following procedures reported by Thompson et al.,<sup>14–16,54,55</sup> the washing the reactions with acetonitrile can lead to the dissolution of unreacted starting material. This process is slow and can often leave a small amount of residual ligand and invariably some dicyclopentadiene, which is notoriously in inorganic chemistry for being difficult to completely remove.

I have been able to isolate crystalline phases in spite of these hurdles, and in some cases single crystals were obtained from ferrocene melts. I was able to obtain multiple known phases such as Fe(2-methylimidazolate)<sub>2</sub> via established literature procedures.<sup>15</sup> My efforts to expand reaction screens to unreported iron-ligand combinations were less successful, with one clear exception. The melt reaction of ferrocene with a large excess of benzimidazole (Hbzimid) at 150 °C for three days in a sealed tube yielded a light pink/tan solid. Close inspection of acetonitrile- washed product afforded crystals sufficiently large enough for single-crystal X-ray diffraction (**Figure 4.2**). The structure was found to be stacked two-dimensional sheet rather than a three-dimensional connected solid. Each sheet consists of distorted tetrahedral Fe<sup>II</sup> centers bridged by benzimidazolate for an empirical formula of Fe(bzimid)<sub>2</sub> (Expected: 58.0% C, 3.5% H, 19.3% N, Measured: 58.4% C, 4.1% H, 18.7% N). Interestingly, the four benzimidazolate ligands around a single iron center are in coplanar pairs, with two protruding above the sheet in one direction, and the other two protruding below the sheet in another. Visually this results in an arrangement comparable to two sets of Venetian blinds rotated 90° to each other. Each Fe(bzimid)<sub>2</sub> sheet is rotated and translationally offset from the sheets above and below, such that the phenyl rings of the benzimidazolate form a herringbone-like pattern. This arrangement is presumably the thermodynamic minimum due to strong edge–face  $\pi$ -interactions between the phenyl rings. While I isolated this phase in July 2016, it was convergently discovered and reported in October 2018.<sup>18</sup> Coronado et al. were able to synthesize Fe(bzimid)<sub>2</sub>, as well as a few substituted analogues, exfoliate individual sheets and subsequently measure magnetic properties. Additionally, an isorecticular analogue of this phase was previously reported with zinc, but in that case the material was synthesized solvothermally.<sup>56</sup>

Thermodynamic driving force for Fe(bzimid)<sub>2</sub> under melt conditions appears to be so great that attempts to synthesize mixed-imidazolate materials (as has been utilized in obtaining new ZIFs<sup>57–60</sup>) invariably leads to the formation of Fe(bzimid)<sub>2</sub> as the sole crystalline product if benzimidazole was used. The addition of neutral ligands to a melt reaction has been reported to stabilize pore environments and lead to the formation of a ZIF topology.<sup>6</sup> Attempts to synthesize a three-dimensionally connected benzimidazole-containing structure such as ZIF-7<sup>61</sup> through the use of neutral pillaring n-heterocycles such as pyrazine and 4,4'-bipyridine also only yielded Fe(bzimid)<sub>2</sub> sheets. Despite what appears to be a strong thermodynamic driving force for formation, this phase could not be formed solvothermally. Numerous solvothermal screens with varying iron salt, metal:ligand ratio, solvent, reaction temperature/time, etc. yielded no isolable precipitate. While it is unclear if the solvation of iron ions by strongly coordinating solvent molecules, such as DMF, is the reason for no precipitate formation, this large difference in chemical reactivity between solvothermal and melt reactions underscores the potential for forming new iron containing materials by using ferrocene as a starting material.

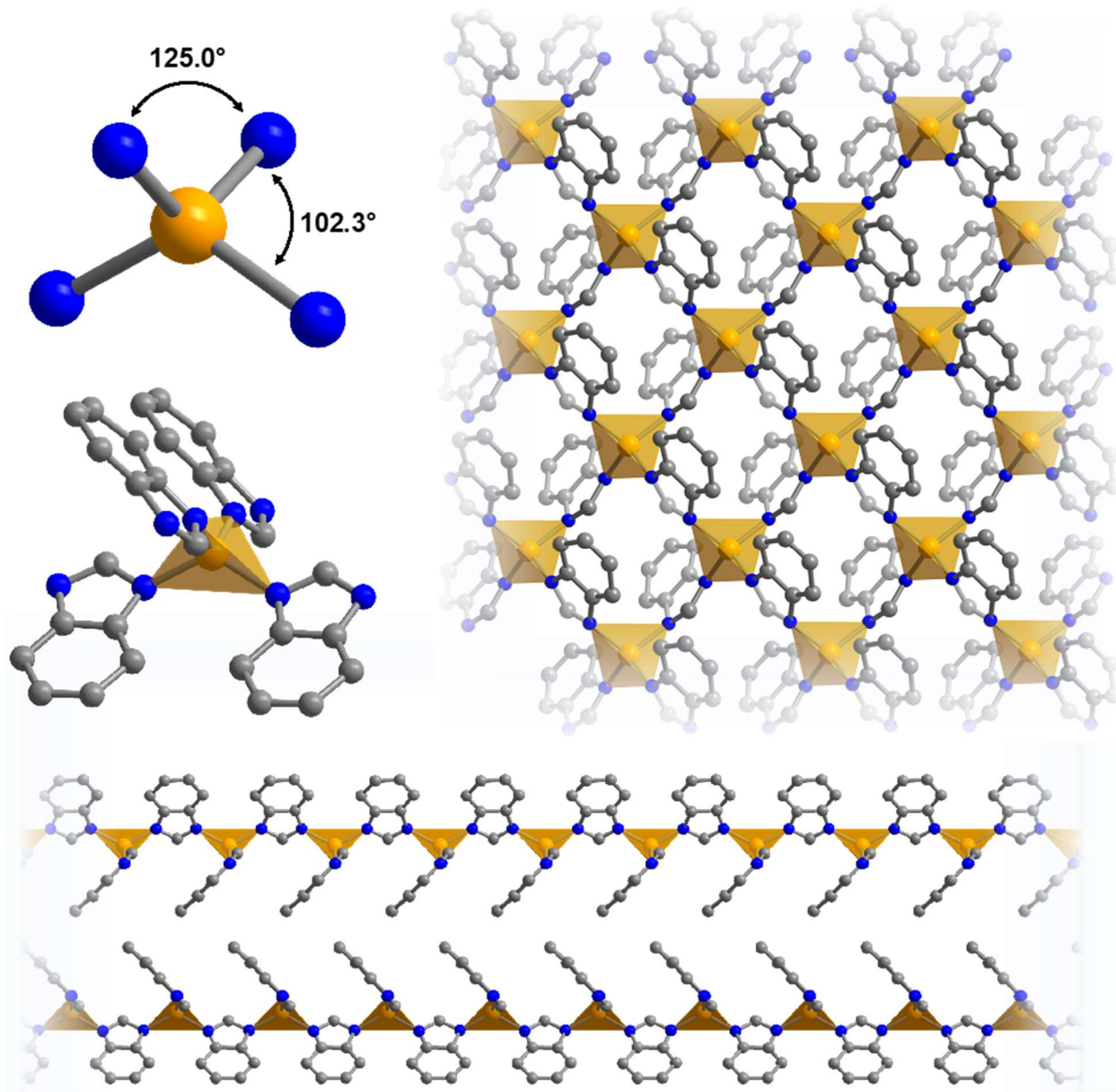


**Figure 4.2:** Single-crystal structure of  $\text{Fe}(\text{bzimid})_2$  with hydrogen atoms omitted for clarity. Distorted tetrahedral iron site (top left), coplanar benzimidazolate ligand pairs around an iron center (middle left), view of a single two-dimensional sheet from the  $c$  axis (top right) and view of herringbone-like stacking of two  $\text{Fe}(\text{bzimid})_2$  sheets (bottom).

### Expanding Melt Reactions Beyond Ferrocene

While ferrous metal–organic frameworks or coordination solids are interesting in their own right, the application of melt chemistry to other oxidation states or other transition metals could broaden its applicability and lead to the generation of entirely new materials. As ferrocenium  $[\text{Fe}^{\text{III}}\text{Cp}_2]^+$  salts are readily commercially available these were the target of initial screens to access ferric metal–organic compounds. Unfortunately, any melt reaction performed with ferrocenium

salts invariably led to amorphous products and/or starting materials, which usually dissolved readily in acetonitrile or other solvents. While the exact cause of these failures is unclear, dearomatization of the cyclopentadienyl ligands in ferrocenium should have a larger barrier and as such would require higher temperatures and longer reaction times. Alternatively, when  $\text{Fe}^{3+}$  cations are introduced in to the melt solution, their decreased lability<sup>62</sup> results in the irreversible formation of amorphous solid.

An unreported molecular species,  $\text{Fe}^{\text{II}}(\text{acac})_2(\text{Himid})_2$  (acac = acetylacetonate and Himid = imidazole) was found while running solvothermal reaction screens in parallel to the melt reactions for the sake of comparison. As is consistent with the reactivity of ferrocenium salts and imidazolate- or triazololate-based ligand melts, solvothermal reaction of  $\text{Fe}^{\text{III}}$  salts either yielded amorphous material or no precipitate. One peculiar exception to this was the formation of very large dark red crystals from a reaction of ferric acetylacetonate,  $\text{Fe}(\text{acac})_3$ , and imidazole in DMF at 150 °C. Despite having a high-intensity low-angle X-ray powder diffraction peak, a common feature in large unit cell frameworks, single crystal diffraction revealed the crystals consisted of  $\text{Fe}^{\text{II}}(\text{acac})_2(\text{Himid})_2$  molecules (**Figure 4.3**). This neutral divalent-metal complex has been reported for multiple other transition metals.<sup>63</sup> Curiously, this molecule is a  $\text{Fe}^{\text{II}}$  species but was synthesized from a  $\text{Fe}^{\text{III}}$  metal source. It has been proposed that at elevated temperatures, formate, which is formed in solvothermal reactions via the hydrolysis of DMF, can act as a reductant, liberating a proton and  $\text{CO}_2$ . This reactivity, which can complicate the valence state of solvothermally synthesized redox-active materials, is absent from melt reactions.

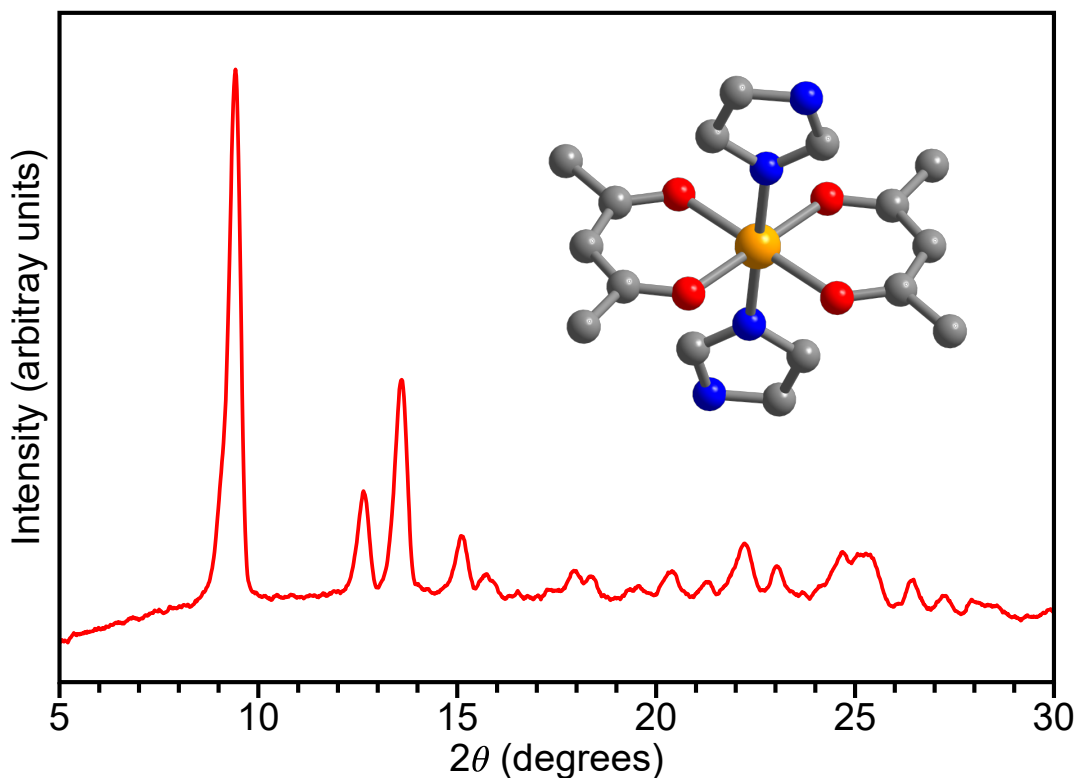


**Figure 4.3:** Powder X-ray diffraction pattern for  $\text{Fe}^{\text{II}}(\text{acac})_2(\text{Himid})_2$  obtained solvothermally from  $\text{Fe}^{\text{III}}(\text{acac})_3$  with imidazole in DMF, and structural model of the molecular complex (inset).

While the use of ferrocenium or other ferric sources did not yield crystalline materials, endeavors with different metallocenes were more fruitful. Chromocene and vanadocene are both commercially available, and similar to ferrocene, purification via sublimation is readily achieved. These materials are noticeably air-sensitive, as is consistent with their low reduction potentials.<sup>64</sup> Screens performed with chromocene and benzimidazole yielded a highly crystalline dark purple phase (**Figure 4.4**). The material decomposes in air but is stable to a variety of deoxygenated/anhydrous solvents such as methanol and acetonitrile. This phase does not appear to be isostructural to  $\text{Fe}(\text{bzimid})_2$ . Attempts to index this diffraction pattern were unsuccessful and indicate that there are most likely multiple phases present. Utilizing vanadocene instead of chromocene similarly yields a highly crystalline mixed-phase material (**Figure 4.4**). This olive-green colored solid is also air-sensitive and is also stable to multiple solvents. Elemental analysis, after solvent washing, for both materials is consistent with a 3:1 benzimidazolate:metal ratio with residual dicyclopentadiene accounting for excess carbon and hydrogen content (**Table 4.1**). These phases, Cr–bzimid and V–bzimid are the first known examples of metal–organic materials formed from chromocene and vanadocene, respectively. Further work is required to isolate these materials phase pure and determine their structures, but their formation gives hope to the use of melt reactions in forming novel early transition metal frameworks.

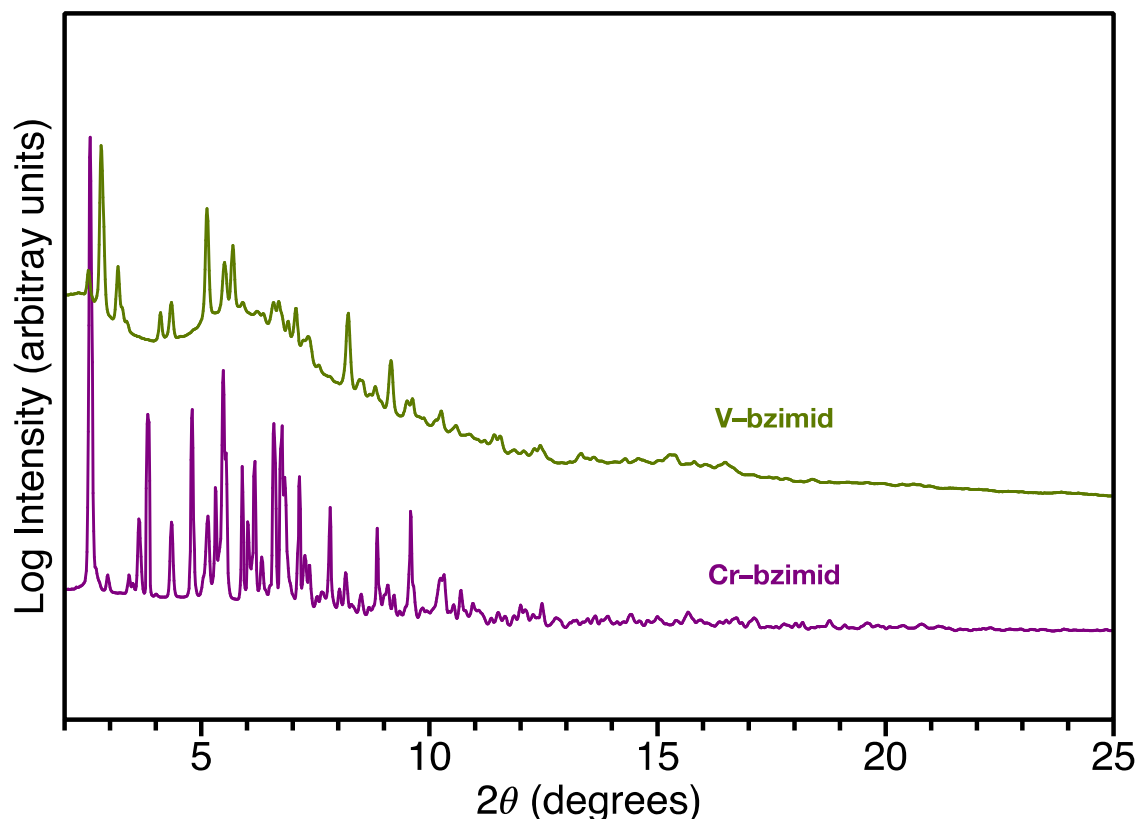


**Figure 4.4:** Powder X-ray diffraction pattern of highly crystalline but phase impure coordination polymers Cr–bzimid (purple, bottom) and V–bzimid (green, top) collected with 0.4972 Å X-rays.

**Table 4.1:** Elemental analysis of Cr–bzimid and V–bzimid with predicted composition for a modeled mixture of  $M(\text{bzimid})_3$  and  $\text{H}_2\text{Cp}_2$ .

		%C	%H	%N
Cr–bzimid $\text{Cr}(\text{bzimid})_3(\text{H}_2\text{Cp}_2)_{0.32}$	Predicted	64.9	4.2	18.7
	Found	64.3	4.6	18.6
V–bzimid $\text{V}(\text{bzimid})_3(\text{H}_2\text{Cp}_2)_{0.40}$	Predicted	67.0	4.5	18.7
	Found	67.0	4.6	17.8

### “Minimalist” Chemical Reactions

The successful reaction of n-heterocyclic ligands with metals at high temperatures requires multiple experimental considerations: 1. reactions should not be performed in metal containers so as to not introduce other metal impurities, 2. small mesh metal particles should be used so as to increase reactive surface area and decrease reaction time, 3. reactions should be prepared in an air/water-free environment to avoid the formation of reaction-inhibiting metal oxides, and 4. precautions should be taken to account for increased pressure caused by the formation of stoichiometric quantities of hydrogen gas. These last two considerations were the most critical in obtaining a crystalline product.

Using Breen adapters, iron powder and the desired azolate ligand were loaded into ¼” glass tubes inside an argon glove box, evacuated on a Schlenk line, and flame sealed. Despite performing screens with <25 mg of reagents, the failure rate of sealed tubes was exceptionally high. Sealed tubes occasionally fractured at the flame seal, but more often only contaminated glass shards were recovered from ovens. Because of this high failure rate, glass tubes were first annealed overnight in a glass kiln at 500 °C to decrease stress in the glassware cause by initially sealing one end. Additionally, after flame sealing, the recently sealed end of tubes was supplementally annealed using a methane torch where the flame was gradually decreased in intensity. With all of these considerations, one screen in particular out of dozens of reactions of iron powder with n-heterocyclic ligands yielded an isolable crystalline phase.

The reaction of iron powder with 2.5 equivalents of imidazole at 300 °C for 5 days yielded a metallic grey powder. While the initial coloration of the product appeared promising due to the prospect of a highly conductive metal–organic framework, it was determined that the origin of the color was simply from small residual unreacted iron particles, as evident via powder X-ray diffraction. Close inspection of the glass tube led to the identification of a small fissure that most likely led to the evaporation/sublimation of much of the imidazole, preventing the reaction from going to completion. I therefore endeavored to isolate this material cleanly, without any such fracturing of the reaction vessel. After more than a dozen attempts, a pristine sample was obtained: a large quantity of white powder (**Figure 4.5**). This material exhibited incredibly high crystallinity, and elemental analysis found that it was consistent with the empirical formula  $\text{Fe}(\text{imid})_2$

(Expected: 37.9% C, 3.2% H, 29.5% N, Measured: 38.2% C, 3.3% H, 29.6% N). This predicted formula explains the dramatic increase in volume of the product from the initial reagents, as is to be expected when converting two very dense reagents into a less dense coordination solid.

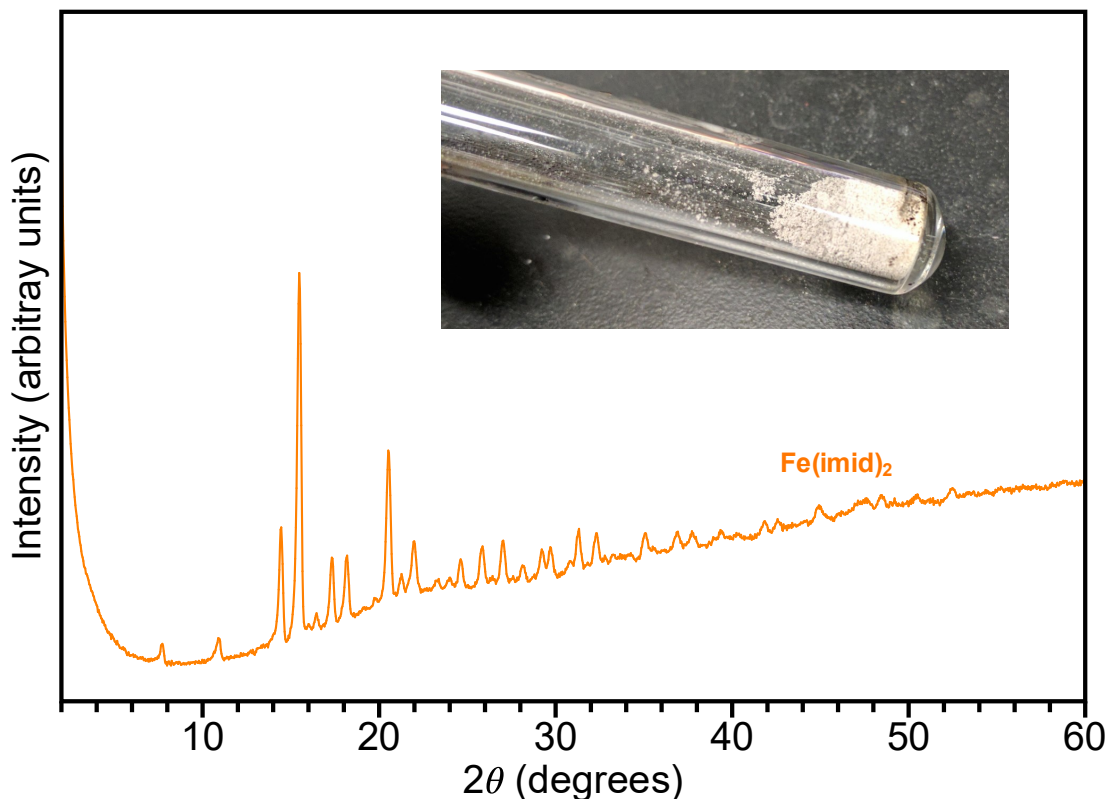


**Figure 4.5:** Powder X-ray diffraction pattern for  $\text{Fe}(\text{imid})_2$  obtained as a voluminous white powder (inset) via a minimalist reaction.

Comparison of the powder pattern for  $\text{Fe}(\text{imid})_2$  with cobalt phases obtained via similar reaction conditions<sup>36</sup> indicated it had a different topology. Of the large abundance of known ZIF structures, only one matched the powder pattern of  $\text{Fe}(\text{imid})_2$  (Figure 4.6):  $\text{Co}(\text{imid})_2$  (Figure 4.6).<sup>65</sup> The synthetic route for this coordination solid, which predates metal-organic frameworks by several decades, also happens to be a solvent-free melt. The highly unusual reagent of bis(tetracarbonyl cobalt)mercury<sup>66</sup> ( $\text{Hg}[\text{Co}(\text{CO})_4]_2$ ) is reacted with liquid imidazole at 200°C to yield “auberginefarbener” crystals of  $\text{Co}(\text{imid})_2$ . This material is composed of nearly-perfect tetrahedral metal nodes in a very compact tetragonal crystal system with no appreciable void space (Figure 4.7). The fascinatingly complex topology of this material exhibits phenomena such as filled octagonal pores formed by triple helices (Figure 4.S1). While the iron analog of this material,  $\text{Fe}(\text{imid})_2$  is inherently very thermally robust and stable to most solvents, it, like many other ferrous materials, degrades rapidly in the presence of  $\text{O}_2$ , losing crystallinity and turning dark brown. However, the validation of  $\text{Fe}(\text{imid})_2$  makes it the first example of an iron-organic material made via such a “minimalist” approach. While additional crystalline phases were obtained with other n-heterocycles and iron powder, these could not be isolated cleanly, preventing further characterization.

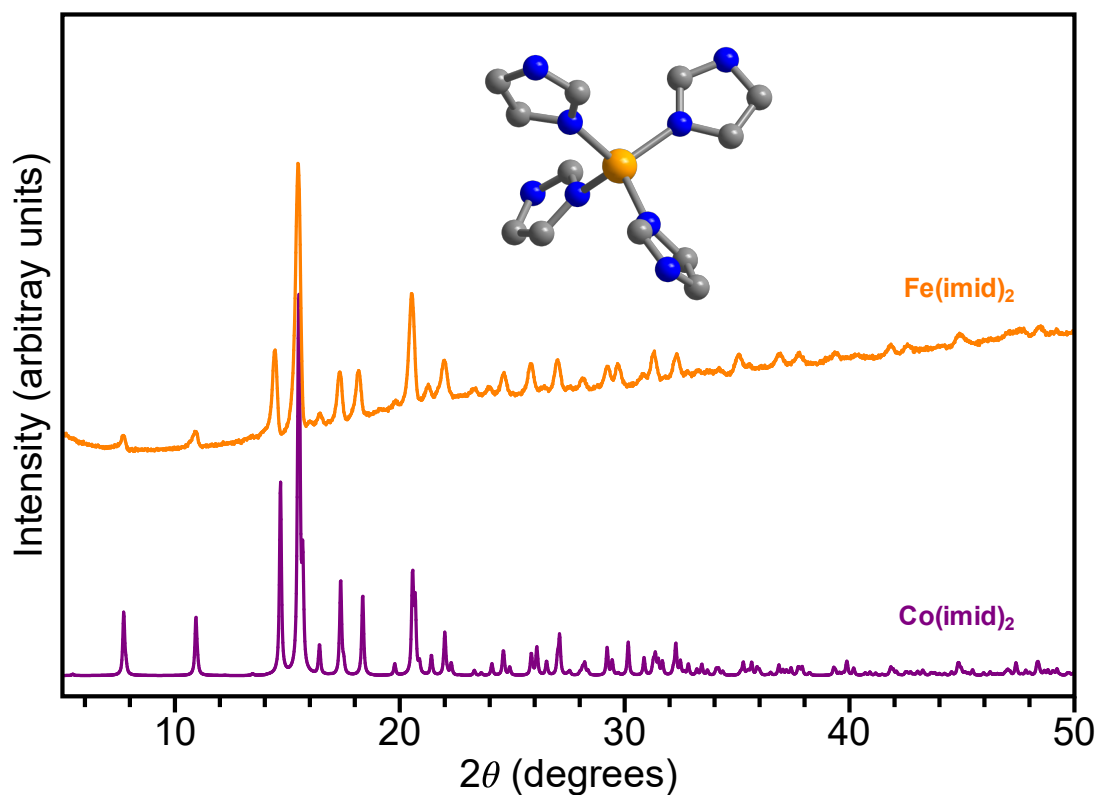


**Figure 4.6:** Comparison of experimentally measured  $\text{Fe}(\text{imid})_2$  powder X-ray diffraction pattern (orange, top) with a pattern predicted for  $\text{Co}(\text{imid})_2$  (purple, bottom) from a reported single crystal structure,<sup>65</sup> with a representative tetrahedral metal site from the predicted structure of  $\text{Fe}(\text{imid})_2$  (inset).

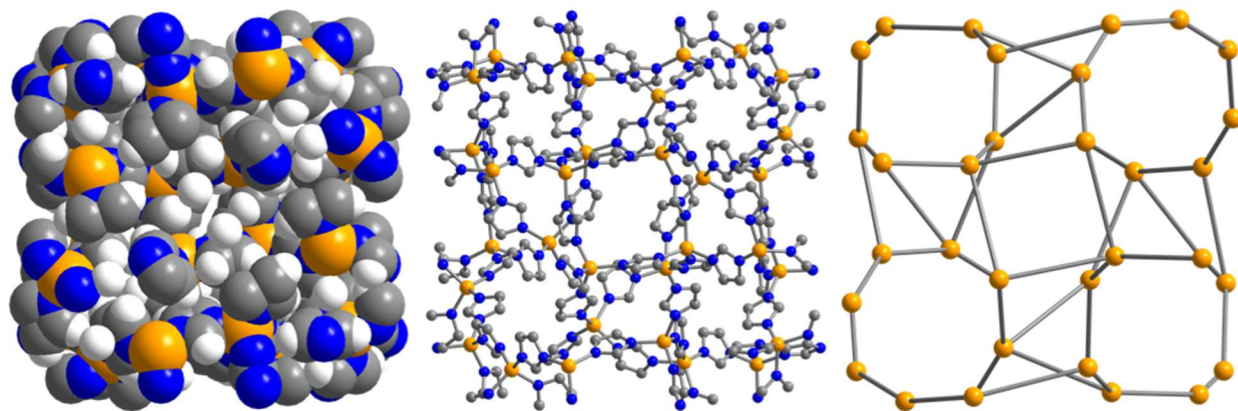


**Figure 4.7:** The highly complex unit cell of the assumed structure of  $\text{Fe}(\text{imid})_2$ . A space filling representation (left) shows the visual porosity for a ball and stick model with hydrogens omitted (middle) is nonexistent. A wireframe structure of only metal centers connected to adjacent metal centers (right) reveals the interesting topology of octagonal pores, which are filled by bridging imidazolates.

Applying the minimalist chemistry approach to earlier transition metals, as was done with melt reactions, will require further investigation as reaction screens led to unpredicted reactivity. Reactions with iron powder that didn't rupture typically yielded a free flowing solid (albeit often with unreacted metal powder or weak crystallinity), but reactions of titanium, vanadium, or chromium powder with n-heterocycle ligands consistently yielded amorphous black residues coating the sides of the glass tubes. While it is possible that some of these failed reactions were caused by unnoticed failures of the glass seal, uniformity across multiplicate screens suggests an underlying cause. A unifying and more likely explanation is that the ligands simply decompose in the presence of such reducing metals and at such elevated temperatures. Although the actual reduction potential of these metals will be different under these experimental conditions, their standard electrode potentials can give a qualitative comparison for the tested series compared to iron.<sup>67-69</sup> Additionally, these early transition metals have multiple accessible oxidation states, and available data for the divalent cations indicates that they are almost as reducing as Fe<sup>0</sup>. Therefore, if a minimalist synthetic approach is to be applied to early transition metals, more redox-limiting conditions will need to be explored.

### **Mechanochemistry Reactions**

Mechanochemistry, specifically ball milling, presents an interesting alternative path for the solvent-free synthesis of metal-organic framework. An obvious first approach would be attempting to apply mechanochemistry to the aforementioned solvent-free approaches. Before I discuss the results of synthetic screens performed via mechanochemistry, there are several limitations to ball milling worth discussing. Because the process of ball milling involves impacting a charge or ball against jar, it is not a question of whether impurities are introduced but rather how much is introduced. Using jars and charges of the same material and using harder materials such as stainless steel or agate can minimize the amount of impurity introduced. Additionally, while jars typically have a Teflon gasket that allows them to seal tightly, they are not explicitly designed to neither maintain an inert atmosphere nor withstand large pressures. Potential reactivity with the jar material, and safety concerns about the generation of highly pressurized container preclude the use of mechanochemistry to react metal powder with organic molecules. Careful sealing of jars using specially designed tools and frequent replacement of Teflon gaskets does allow air sensitive reactions to be performed via ball milling. Reactions were therefore loaded and sealed inside a glove box, reacted outside the glove box in a ball mill, and cycled back in for extraction of product.

Multiple ferrocene-based melt reactions were attempted via ball milling. Due to the large quantities of reagents required for an individual ball mill reaction (> 200 mg), screens were limited to ferrocene because of its relative affordability, especially compared to chromocene or vanadocene. Even with reaction times of up to several hours, only starting materials were obtained from ball milling screens, indicating the reactions did not proceed. While it is very difficult to directly quantify both the forces imparted and local temperature during the mixing, studies have shown that other shaker ball mills can reach local temperatures as high as 100 °C during ball milling.<sup>70</sup> The dearomatization and subsequent protonation of cyclopentadienyl in melt reactions typical requires a temperature of around 150 °C. Certainly, the forces imparted in ball milling cannot be simplified to just a temperature, but if the shaker ball mill used is incapable of imparting a similar amount of energy as those supplied during the melt reactions, then it follows that these ball-milling reactions would not proceed. This does not mean that ferrocene or by extension other metallocenes cannot be used as metal and base sources in ball mill reactions, only that this particular experiment configuration is not amenable to the approach. It stands to reason that by

imparting more energy, reactivity could be induced; this could be accomplished either heating the system slightly while ball milling or through the use of a planetary ball mill, which can achieve temperatures as high as 200 °C.<sup>70</sup>

Solid state reactions are perhaps better suited for ball milling, rather than applying solvent-free routes that liquify and only proceed at high temperature. Since ball milling has been successfully applied to the synthesis of metal–organic frameworks with near quantitative yields, it could potentially be utilized to improve the yields of solvothermally obtained frameworks. The gallate frameworks, in particular iron–gallate, suffer from a synthetic limitation of exceptionally low yield (see Chapter 3).<sup>71–74</sup> Solvothermal reactions afford only 10% yield due to acidification of the solution, while beginning with a more basic initial state leads to excessive formation of iron hydroxide and amorphous material. Utilizing an aqueous-compatible glove box for the pre- and post-reaction handling of ball mill jars led to the development of a “solvent-free” synthetic route for  $\text{Fe}^{\text{II}}(\text{H}_2\text{gallate})\cdot 2\text{H}_2\text{O}$ . Ball milling anhydrous ferrous chloride with gallic acid monohydrate (the reagents used for the solvothermal reaction) would inherently have to produce two equivalents of HCl as a byproduct if it formed  $\text{Fe}^{\text{II}}(\text{H}_2\text{gallate})$ , corroding the stainless-steel jar and most likely dissolving the framework. Instead, a base can be added to allow the reaction to proceed. Thus, ball milling iron chloride, gallic acid, and an equivalent of sodium hydroxide led to the formation of a pure white crystalline solid (**Figure 4.8**).

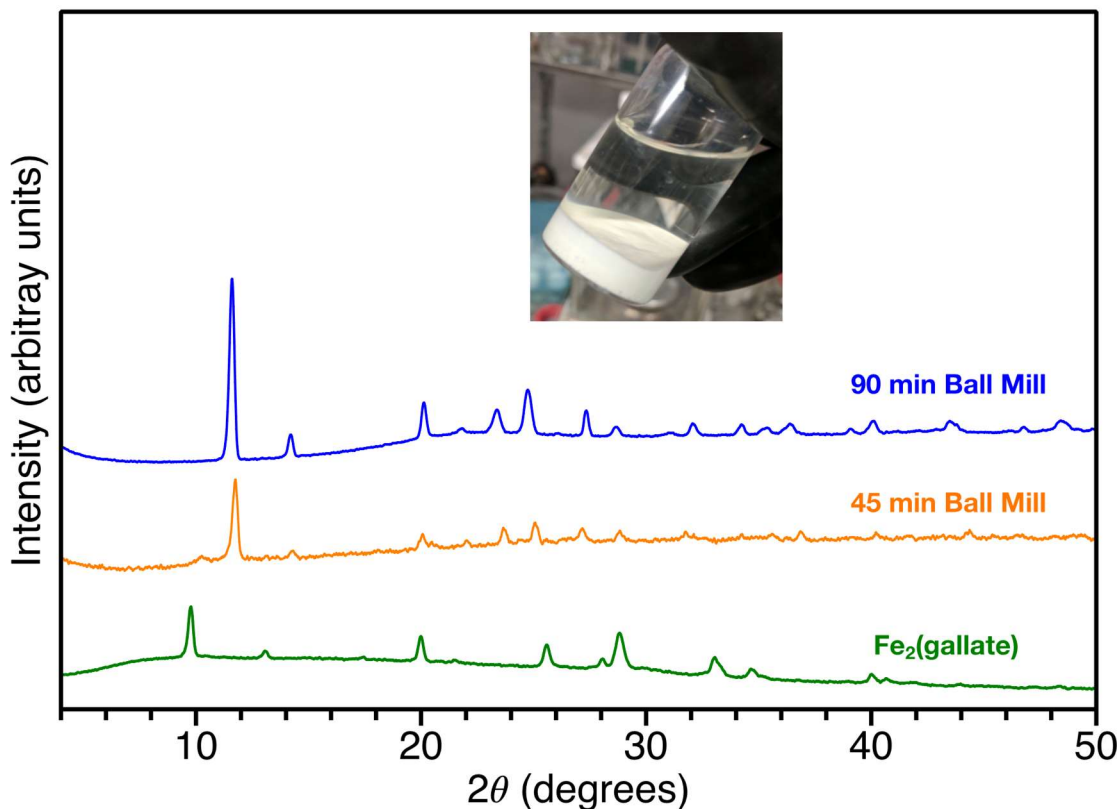


**Figure 4.8:** Powder X-ray diffraction of phase impure  $\text{Fe}^{\text{II}}(\text{H}_2\text{gallate})\cdot 2\text{H}_2\text{O}$  obtained via 45 minutes of ball milling (orange, middle), possible impurity  $\text{Fe}^{\text{II}}_2(\text{gallate})$  (green, bottom), and phase pure  $\text{Fe}^{\text{II}}(\text{H}_2\text{gallate})\cdot 2\text{H}_2\text{O}$  obtained via 90 minutes of ball milling (blue, top) with picture of white 90 min product (inset).

This material is  $\text{Fe}^{\text{II}}(\text{H}_2\text{gallate})\cdot 2\text{H}_2\text{O}$ , as is evident from the powder X-ray diffraction pattern. However, there is also a small phase impurity which corresponds to the proposed material  $\text{Fe}^{\text{II}}_2(\text{gallate})$  (see Chapter 3). The formation of  $\text{Fe}^{\text{II}}_2(\text{gallate})$ , however, should be unfavorable under more acidic environments as all the oxo functionalities are deprotonated in this phase. The quantity of sodium hydroxide used, one equivalent per ligand, was consistent with the solution-based reaction, but it should be insufficient to allow complete conversion of the gallic acid to  $\text{H}_2\text{gallate}^{2-}$ , let alone fully deprotonate it to  $\text{gallate}^{4-}$ . Allowing the reaction to proceed for a longer period of time appears to resolve this issue, presumably by allowing the  $\text{pH}^*$  of the system to more fully equilibrate, leading to dissolution of the trace  $\text{Fe}_2(\text{gallate})$  impurity. At these longer reaction times, phase pure  $\text{Fe}^{\text{II}}(\text{H}_2\text{gallate})\cdot 2\text{H}_2\text{O}$  may be obtained. It should be noted that while no additional solvent was added to this ball mill reaction, some amount of water should be released, one equivalent from the neutralization of sodium hydroxide and one equivalent from gallic acid, as the monohydrate was used. In this case, this adventitious water is almost certainly beneficial to the framework synthesis by stabilizing the pore and being incorporated in the final product:  $\text{Fe}^{\text{II}}(\text{H}_2\text{gallate})\cdot 2\text{H}_2\text{O}$ . This material is noticeably less colorful than when it is obtained via solvothermal routes. Even rigorously air-free solvothermal syntheses of  $\text{Fe}^{\text{II}}(\text{H}_2\text{gallate})\cdot 2\text{H}_2\text{O}$  have some slight green coloration to an otherwise white material. As discussed in Chapter 3 this coloration is believed to originate from trace iron hydroxide impurities. For ball milled  $\text{Fe}^{\text{II}}(\text{H}_2\text{gallate})\cdot 2\text{H}_2\text{O}$ , the solid is completely white. Despite the large amount of hydroxide ions present in the ball mill reaction mixture, no visual or diffraction indication of iron hydroxide was observed in the isolated product. One of the most important results for this synthetic approach is the dramatically improved yield, 42% compared to 10% solvothermally and in only 90 minutes compared to 24 hrs. This yield could be further improved by the addition of more sodium hydroxide; however, this would increase the likelihood of  $\text{Fe}_2(\text{gallate})$  formation and could require further extending the reaction time to reach phase purity.

This solvent-free ball milling approach can also be applied to other members of the isostructural gallate family. Nickel–gallate, for example can be synthesized analogously to the iron analogue, by simply removing the water from the known solvothermal approach<sup>73</sup> and ball milling the solid reagents (**Figure 4.9**). The material is highly crystalline, more so even than ball milled iron–gallate, and the yield is also higher (62% vs. 37% solvothermally). Both of these phenomena can be explained by the anion used in the nickel synthesis: acetate. Unlike the chloride anions found in the iron-gallate reaction, acetate should actually function as a base and facilitate deprotonation of gallic acid, allowing the formation of more  $\text{Ni}(\text{H}_2\text{gallate})$  before the reaction mixture becomes too acidic. An additional factor could be the larger amount of adventitious water present in the reaction mixture as the nickel salt used in the tetrahydrate form. With three times the amount of water in the ball mill jar as compared to the iron reaction, the reaction could be progressing more rapidly, as liquid assisted grinding has been shown to induce more reactions faster than just dry ball milling.<sup>75</sup>

Of particular interest here is that if this reaction is performed rigorously oxygen-free, as ferrous-gallate reactions were, the visual color of the material is incongruous with the solvothermal reaction. Nickel–gallate formed solvothermally in air is dark green, while nickel–gallate formed via ball milling air-free is mint green. Unlike the iron–gallate syntheses, the nickel–gallate divergence is most likely caused by oxidation of the gallate linker, rather than the formation of metal hydroxide. In addition to previous reports of the ligand’s redox activity, a simple basic solution of the ligand exposed to air rapidly darkens due to ligand oxidation. Because the

metal–gallate frameworks should be able to readily accommodate different material redox states by charge balancing with protons, it is within reason that Ni(H<sub>2</sub>gallate) could actually be Ni(H<sub>x</sub>[gallate<sup>-(2+x)</sup>]) (x < 2) when synthesized in air.

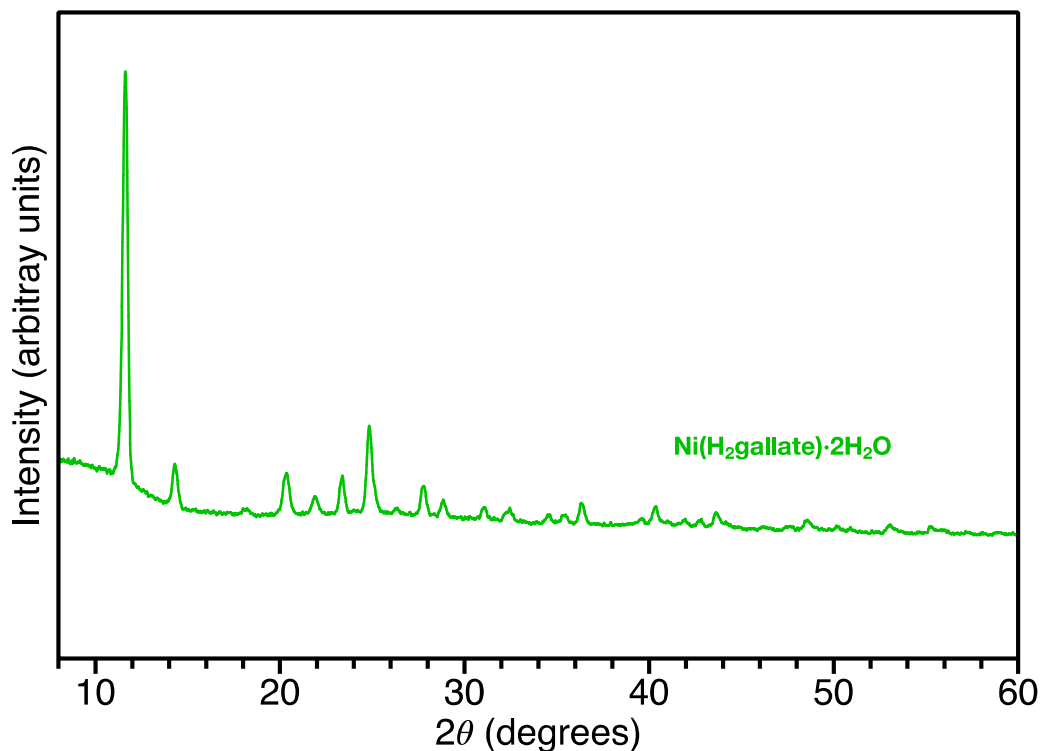


**Figure 4.9:** Powder X-ray diffraction pattern of Ni(H<sub>2</sub>gallate)·2H<sub>2</sub>O obtained via ball milling.

In fact, when the mint green air-free synthesized nickel–gallate is exposed to air there is a rapid color change to dark green, similar to the as-synthesized material. Comparison of nickel–gallate synthesized in air vs air-free reveals dramatic spectroscopic differences. ATIR measurements reveal a noticeable difference in the 1100–900 cm<sup>-1</sup> region of the spectra (**Figure 4.10**). Air-free Ni(H<sub>2</sub>gallate) exhibits several strong features at 1005 cm<sup>-1</sup> and 1042 cm<sup>-1</sup> consistent with C–O vibrational modes. Upon exposure to air, these features shift to higher energy, 1058 cm<sup>-1</sup>, consistent with a strengthening of the C–O bond as would be caused by oxidation of the linker. The spectra of the recently exposed air-free nickel–gallate parallels that of the nickel–gallate synthesis in air. This result, which stemmed from ball milling reactions, implies that the gallate ligand in metal–gallate framework could be exhibiting redox-active, even in systems where the metal is not redox-active.

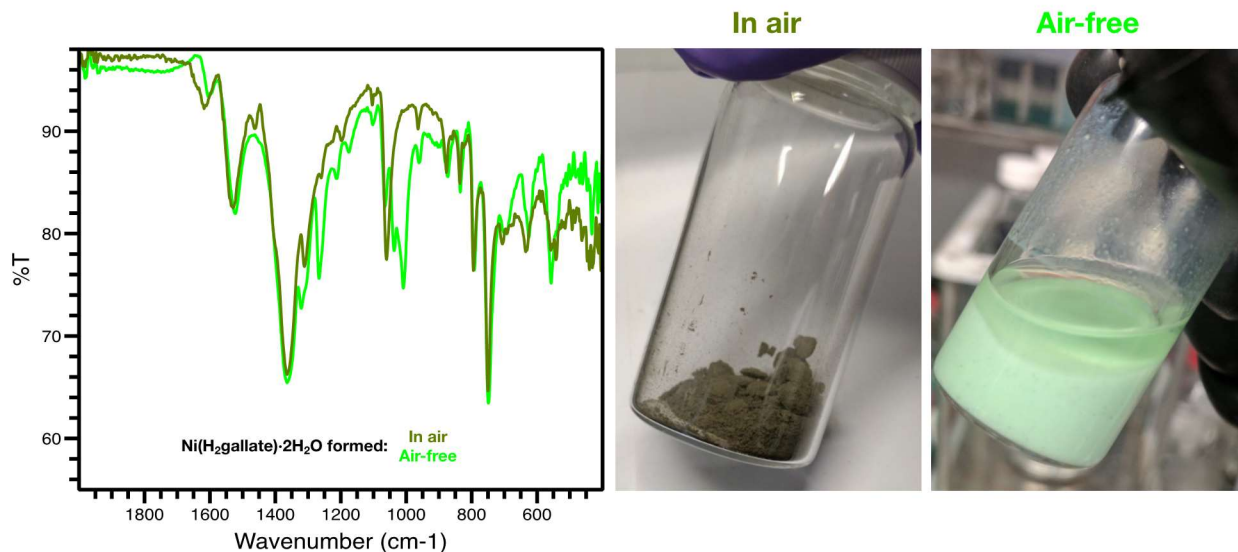


**Figure 4.10:** ATIR spectra (left) for  $\text{Ni}(\text{H}_2\text{gallate})\cdot 2\text{H}_2\text{O}$  synthesized via ball milling in air (dark green) and air-free (light green), with pictures of in air synthesized (middle) and air-free synthesized (right).

## 4.4 Conclusions and Outlook

Herein I have reported three different solvent-free synthetic routes and explored their efficacy for obtaining new and/or improved materials. Melt reactions can be used to obtain air-sensitive crystalline phases from ferrocene in the case of the novel two-dimensional solid  $\text{Fe}(\text{bzimid})_2$ , and from chromocene and vanadocene in the case of  $\text{Cr}\text{-bzimid}$  and  $\text{V}\text{-bzimid}$ , respectively. While further exploration of reaction parameters is necessary for the isolation of phase pure chromium and vanadium materials, these results validate the use of metallocenes for synthesizing early transition metal frameworks. Titanocene dicarbonyl or other titanocene-derived species could potentially be used as a titanium source for melt reactions. Higher temperatures could also be utilized to induce melt reactivity with ferrocenium salts as could the addition of *n*-heterocycles that are more amenable to trivalent frameworks, such as pyrazolate. Exploration of the melt reactivity of substituted metallocenes will undoubtedly lead to the isolation of new and/or more crystalline phases as substituents on the cyclopentadienyl ligands should alter both the barrier for dearomatization and the basicity of the dissociated species.

I have shown that minimalist chemistry can be applied to iron-based materials for the first time. While crystalline material can be obtained, the failure rate for minimalist reactions remains quite high. Better experimental apparatus, such as thicker or better sealed glass tubing, could help decrease leak rates. With higher pressure resistant vessels,  $M^0$  precursors such as metal carbonyls could be utilized to perform minimalist reactions rigorously water free and without having to overcome passivating oxide layers with mercury. Lowering reaction temperature for early transition metal reactions could help prevent ligand decomposition. Even further exploratory techniques such as initially pressuring reaction vessels with hydrogen gas could be used to prevent over oxidation of very reducing metals by protons. If the proper apparatus could be designed, research in both minimalist reactions and melt reactions would be greatly aided by the use of in situ diffraction to follow reaction progression.

Despite unsuccessful attempts to synthesize new phases via ball milling, I still hold hope for the future of this technique in exploratory metal–organic framework synthesis. While limited quantification and reporting of reaction variables is inhibiting to the development of new ball milling reactions, the same can be said for almost any field of research. Heated ball mill jars could allow for screening of melt type reactions. Salt metathesis-based routes could open a new direction for the solvent-free of frameworks, relying on large enthalpies of formation to drive reactions. As I have shown that ball milling can be utilized to rapidly obtain improved yields of highly air-sensitive materials, this technique could be applied to other low yielding and/or air sensitive syntheses. Oxygen-free ball milling is a dramatically underexplored field, and to the best of my knowledge its application to metal–organic frameworks is entirely nonexistent. Lastly, combining air-free ball milling with high-throughput techniques could allow for much more rapid screening of redox-active frameworks.

## 4.5 Acknowledgments

Material synthesis and characterization was funded by National Science Foundation (NSF) Award No. DMR-1611525 R.M.T. was funded by the NSF Graduate Research Fellowship Program and the University of California-Berkeley Chancellor’s Fellowship. Powder X-ray diffraction performed at the Advanced Light Source was supported by the Office of Science, Office of Basic Energy Sciences, of the U. S. DOE under Contract No. DE-AC02-05CH11231. I thank Lucy Darago for powder X-ray diffraction measurements, Khetsakorn Chakarawat for  $^{57}\text{Fe}$  Mössbauer measurements, and Kristen A. Colwell and Mike Aubrey for helpful discussion.

## 4.6 References and Supplementary Figures

- (1) Stock, N.; Biswas, S. *Chem. Rev.* **2012**, *112* (2), 933.
- (2) Lee, Y.-R.; Kim, J.; Ahn, W.-S. *Korean J. Chem. Eng.* **2013**, *30* (9), 1667.
- (3) Pakamorè, I.; Rousseau, J.; Rousseau, C.; Monflier, E.; Szilágyi, P. *Green Chem.* **2018**, *20* (23), 5292.
- (4) Avci-Camur, C.; Perez-Carvajal, J.; Imaz, I.; MasPOCH, D. *ACS Sustain. Chem. Eng.* **2018**, *6* (11), 14554.
- (5) Furukawa, H.; Cordova, K. E.; O’Keeffe, M.; Yaghi, O. M. *Science* **2013**, *341* (6149), 1230444.
- (6) López-Cabrelles, J.; Romero, J.; Abellán, G.; Giménez-Marqués, M.; Palomino, M.; Valencia, S.; Rey, F.; Espallargas, G. *J. Am. Chem. Soc.* **2019**, *141* (17), 7173.
- (7) Friščić, T. Mechanochemical Approaches to Metal-Organic Frameworks. *Encyclopedia of Inorganic and Bioinorganic Chemistry*, **2014**.
- (8) Liu, X.; Fechler, N.; Antonietti, M. *Chem. Soc. Rev.* **2013**, *42* (21), 8237.
- (9) Newman, M. S.; Karnes, H. A. *J. Org. Chem.* **1966**, *31* (12), 3980.
- (10) Kwart, H.; Evans, R. E. *J. Org. Chem.* **1966**, *31* (2), 410.
- (11) Pedersen, K. S.; Perlepe, P.; Aubrey, M. L.; Woodruff, D. N.; Reyes-Lillo, S. E.; Reinholdt, A.; Voigt, L.; Li, Z.; Borup, K.; Rouzières, M.; Samohvlov, D.; Wilhelm, F.; Rogalev, A.; Neaton, J.B.; Long, J.R.; Clérac, R.. *Nature Chem.* **2018**, *10* (10), 1056.
- (12) Lehnert, R.; Seel, F. *Z. Anorg. Chem.* **1978**, *444* (1), 91.
- (13) Spek, A. L.; Duisenberg, A. J. M.; Feiters, M. C. *Acta Crystallogr. C* **1983**, *39* (9), 1212.

- (14) Rettig, S. J.; Storr, A.; Summers, D. A.; Thompson, R. C.; Trotter, J. *J. Am. Chem. Soc.* **1997**, *119* (37), 8675.
- (15) Rettig, S. J.; Storr, A.; Summers, D. A.; Thompson, R. C.; Trotter, J. *Can. J. Chem.* **1999**, *77* (4), 425.
- (16) Rettig, S. J.; Sánchez, V.; Storr, A.; Thompson, R. C.; Trotter, J. *J. Chem. Soc., Dalton Trans.* **2000**, 3931.
- (17) López-Cabrelles, J.; Giménez-Marqués, M.; Espallargas, G.; Coronado, E. *Inorg. Chem.* **2015**, *54* (21), 10490.
- (18) López-Cabrelles, J.; Mañas-Valero, S.; Vitorica-Yrezábal, I.; Bereciartua, P.; Rodríguez-Velamazán, J.; Waerenborgh, J.; Vieira, B.; Davidovikj, D.; Steeneken, P.; van der Zant, H.; Espallargas, G.M.; Coronado, E. *Nat Chem* **2018**, *10* (10), 1001.
- (19) Kubitschke, J.; Lange, H.; Strutz, H. Ullmann's Encyclopedia of Industrial Chemistry. **2014**.
- (20) Park, K.; Ni, Z.; Côté, A. P.; Choi, J.; Huang, R.; Uribe-Romo, F. J.; Chae, H. K.; O'Keeffe, M.; Yaghi, O. M. *Proc. National Acad. Sci.* **2006**, *103* (27), 10186.
- (21) Banerjee, R.; Phan, A.; Wang, B.; Knobler, C.; Furukawa, H.; O'Keeffe, M.; Yaghi, O. M. *Science* **2008**, *319* (5865), 939.
- (22) Phan, A.; Doonan, C. J.; Uribe-Romo, F. J.; Knobler, C. B.; O'Keeffe, M.; Yaghi, O. M. *Accounts Chem. Res.* **2010**, *43* (1), 58.
- (23) Pimentel, B. R.; Parulkar, A.; Zhou, E.; Brunelli, N. A.; Lively, R. P. *ChemSusChem* **2014**, *7* (12), 3202.
- (24) Chen, B.; Yang, Z.; Zhu, Y.; Xia, Y. *J. Mater. Chem. A* **2014**, *2* (40), 16811.
- (25) Longley, L.; Collins, S. M.; Zhou, C.; Smales, G. J.; Norman, S. E.; Brownbill, N. J.; Ashling, C. W.; Chater, P. A.; Tovey, R.; Schönlieb, C.-B.; Headen, T.F.; Terrill, N.J.; Yue, Y.; Smith, A.J.; Blanc, F.; Keen, D.A.; Midgley, P.A.; Bennett, T.D. *Nat. Commun.* **2018**, *9* (1), 2135.
- (26) Qiao, A.; Bennett, T. D.; Tao, H.; Krajnc, A.; Mali, G.; Doherty, C. M.; Thornton, A. W.; Mauro, J. C.; Greaves, N. G.; Yue, Y. *Sci. Adv.* **2018**, *4* (3), eaao6827.
- (27) Tuffnell, J. M.; Ashling, C. W.; Hou, J.; Li, S.; Longley, L.; Gómez, M.; Bennett, T. D. *Chem. Commun.* **2019**, 55, 8715.
- (28) Frenzel-Beyme, L.; Kloss, M.; Kolodzeiski, P.; Pallach, R.; Henke, S. *J. Am. Chem. Soc.* **2019**. <https://doi.org/10.1021/jacs.9b05558>.
- (29) Zhang, L.; Ko, J.; Ondrechen, M. *J. Am. Chem. Soc.* **1987**, *109* (6), 1666
- (30) Creutz, C.; Taube, H. *J. Am. Chem. Soc.* **1969**, *91* (14), 3988.
- (31) Bechlars, B.; D'Alessandro, D. M.; Jenkins, D. M.; Iavarone, A. T.; Glover, S. D.; Kubiak, C. P.; Long, J. R. *Nature Chem.* **2010**, *2* (5), 362.
- (32) Gándara, F.; Uribe-Romo, F. J.; Britt, D. K.; Furukawa, H.; Lei, L.; Cheng, R.; Duan, X.; O'Keeffe, M.; Yaghi, O. M. *Chem. – Euro. J.* **2012**, *18* (34), 10595.
- (33) Park, J. G.; Aubrey, M. L.; Oktawiec, J.; Chakarawet, K.; Darago, L. E.; Grandjean, F.; Long, G. J.; Long, J. R. *J. Am. Chem. Soc.* **2018**, *140* (27), 8526.
- (34) Xie, L. S.; Sun, L.; Wan, R.; Park, S. S.; DeGayner, J. A.; Hendon, C. H.; Dincă, M. *J. Am. Chem. Soc.* **2018**, *140* (24), 7411.
- (35) Aubrey, M. L.; Wiers, B. M.; Andrews, S. C.; Sakurai, T.; Reyes-Lillo, S. E.; Hamed, S. M.; Yu, C.; Darago, L. E.; Mason, J. A.; Baeg, J.; Grandjean, F.; Long, G. J.; Seki, S.; Neaton, J. B.; Yang, P.; Long, J. R. *Nat. Mater.* **2018**, *17*, 625.
- (36) Müller-Buschbaum, K.; Schönfeld, F. *Z. Anorg. Chem.* **2011**, *637* (7-8), 955.

- (37) Zurawski, A.; Mai, M.; Baumann, D.; Feldmann, C.; Müller-Buschbaum, K. *Chem. Commun.* **2010**, 47 (1), 496.
- (38) Rybak, J.-C.; Tegel, M.; Johrendt, D.; Müller-Buschbaum, K. *Z. Krist.-Cryst. Mater.* **2010**, 225 (5), 187.
- (39) Müller-Buschbaum, K.; Mokaddem, Y. *Solid State Sci.* **2008**, 10 (4), 416.
- (40) Müller-Buschbaum, K.; Mokaddem, Y.; Schappacher, F. M.; Pöttgen, R. *Angew. Chem. Int. Ed.* **2007**, 46 (23), 4385.
- (41) Müller-Buschbaum, K.; Gomez-Torres, S.; Larsen, P.; Wickleder, C. *Chem. Mater.* **2007**, 19 (4), 655.
- (42) Müller-Buschbaum, K.; Quitmann, C. C. *Inorg Chem* **2006**, 45 (6), 2678.
- (43) Müller-Buschbaum, K. *Z. Anorg. Chem.* **2005**, 631 (5), 811.
- (44) Müller-Buschbaum, K.; Mokaddem, Y. *Chem. Commun.* **2006**, 2060.
- (45) Užarević, K.; Wang, T. C.; Moon, S.-Y.; Fidelli, A. M.; Hupp, J. T.; Farha, O. K.; Friščić, T. *Chem. Commun.* **2015**, 52 (10), 2133.
- (46) Beldon, P. J.; Fábíán, L.; Stein, R. S.; Thirumurugan, A.; Cheetham, A. K.; Friščić, T. *Angew. Chem. Int. Ed.* **2010**, 49 (50), 9640.
- (47) Julien, P. A.; Užarević, K.; Katsenis, A. D.; Kimber, S. A.; Wang, T.; Farha, O. K.; Zhang, Y.; Casaban, J.; Germann, L. S.; Etter, M.; Dinnebier, R.E.; James, S.L.; Halasz, I.; Friščić, T. *J. Am. Chem. Soc.* **2016**, 138 (9), 2929.
- (48) Zhang, R.; Tao, C.-A.; Chen, R.; Wu, L.; Zou, X.; Wang, *JNanomaterials-Basel* **2018**, 8 (12), 1067.
- (49) Wei, F.; Chen, D.; Liang, Z.; Zhao, S.; Luo, Y. *RSC Adv.* **2017**, 7 (73), 46520.
- (50) Prochowicz, D.; Sokołowski, K.; Justyniak, I.; Kornowicz, A.; Fairen-Jimenez, D.; Friščić, T.; Lewiński, J. *Chem. Commun.* **2015**, 51 (19), 4032.
- (51) Ayoub, G.; Karadeniz, B.; Howarth, A. J.; Farha, O. K.; Đilović, I.; Germann, L. S.; Dinnebier, R. E.; Užarević, K.; Friscic, T. *Chem. Mater.* **2019**.  
<https://doi.org/10.1021/acs.chemmater.9b01068>.
- (52) Do, J.-L.; Friščić, T. *ACS Central Sci* **2016**, 3 (1), 13.
- (53) Friščić, T.; Halasz, I.; Beldon, P. J.; Belenguer, A. M.; Adams, F.; Kimber, S.; Honkimäki, V.; Dinnebier, R. E. *Nature Chem.* **2013**, 5 (1), 66.
- (54) Storr, A.; Summers, D. A.; Thompson, R. C. *Can. J. Chem.* **1998**, 76 (8), 1130.
- (55) Rettig, S. J.; Storr, A.; Summers, D. A.; Thompson, R. C.; Trotter, J. *Can. J. Chem.* **1997**, 75 (7), 949.
- (56) Peng, Y.; Li, Y.; Ban, Y.; Jin, H.; Jiao, W.; Liu, X.; Yang, W. *Science* **2014**, 346 (6215), 1356.
- (57) Ban, Y.; Li, Y.; Liu, X.; Peng, Y.; Yang, W. *Micropor. Mesopor. Mat.* **2013**, 173, 29.
- (58) Liao, Y.-T.; Dutta, S.; Chien, C.-H.; Hu, C.-C.; Shieh, F.-K.; Lin, C.-H.; Wu, K. *J. Inorg. Organomet. Polym.* **2015**, 25 (2), 251.
- (59) Thompson, J. A.; Blad, C. R.; Brunelli, N. A.; Lydon, M. E.; Lively, R. P.; Jones, C. W.; Nair, S. *Chem. Mater.* **2012**, 24 (10), 1930.
- (60) Hillman, F.; Zimmerman, J. M.; Paek, S.-M.; Hamid, M. R.; Lim, W.; Jeong, H.-K. *J. Mater. Chem. A* **2017**, 5 (13), 6090.
- (61) Arami-Niya, A.; Birkett, G.; Zhu, Z.; Rufford, T. E. *J. Mater. Chem. A* **2017**, 5 (40), 21389.
- (62) van Eldik, R.; Hubbard, C. D. *Advances in Inorganic Chemistry: Inorganic Reaction Mechanisms.* Elsevier, **2004**.

- (63) Döring, M.; Ludwig, W.; Uhlig, E.; Wočadlo, S.; Müller, U. *Z. Anorg. Chem.* **1992**, *611* (5), 61.
- (64) Kotz J.C. (1986) The Electrochemistry of Transition Metal Organometallic Compounds. In: Fry A.J., Britton W.E. (eds) *Topics in Organic Electrochemistry*. Springer, Boston, MA.
- (65) Sturm, M.; Brandl, F.; Engel, D.; Hoppe, W. *Acta Crystallogr. B* **1975**, *31* (10), 2369.
- (66) Seyferth, D.; Spohn, R. J. *Trans. New York Acad. Sci.* **1971**, *33* (6 Series II), 625.
- (67) Standard Potentials in Aqueous Solutions. Bard, A.J.; Parsons, R.; Jordan, J., Ed. IUPAC: New York and Basel, **1985**.
- (68) Milazzo, G.; Caroli, S.; Sharma, V. *Tables of Standard Electrode Potentials*. John Wiley & Sons: Chichester, New York, **1978**.
- (69) Swift, E.; Butler, E. *Quantitative Measurements and Chemical Equilibria*. W.H. Freeman and Co., San Francisco, **1972**.
- (70) Takacs, L.; McHenry, J. *J. Mater. Sci.* **2006**, *41* (16), 5246.
- (71) Bao, Z.; Wang, J.; Zhang, Z.; Xing, H.; Yang, Q.; Yang, Y.; Wu, H.; Krishna, R.; Zhou, W.; Chen, B.; Ren, Q. *Angew. Chem. Int. Ed.* **2018**, *57* (49), 16020.
- (72) Cooper, L.; Hidalgo, T.; Gorman, M.; Lozano-Fernández, T.; Simón-Vázquez, R.; Olivier, C.; Guillou, N.; Serre, C.; Martineau, C.; Taulelle, F.; Damasceno-Borges, D.; Maurin, G.; González-Fernández, Á.; Horcajada, P.; Devic, T. *Chem. Commun.* **2015**, *51* (27), 5848.
- (73) Feller, R. K.; Cheetham, A. K. *Solid State Sci.* **2006**, *8* (9), 1121.
- (74) Saines, P. J.; Yeung, H.; Hester, J. R.; Lennie, A. R.; Cheetham, A. K. *Dalton Trans.* **2011**, *40* (24), 6401.
- (75) Friščić, T.; Reid, D. G.; Halasz, I.; Stein, R. S.; Dinnebier, R. E.; Duer, M. J. *Angew. Chem. Int. Ed.* **2010**, *49* (4), 712.

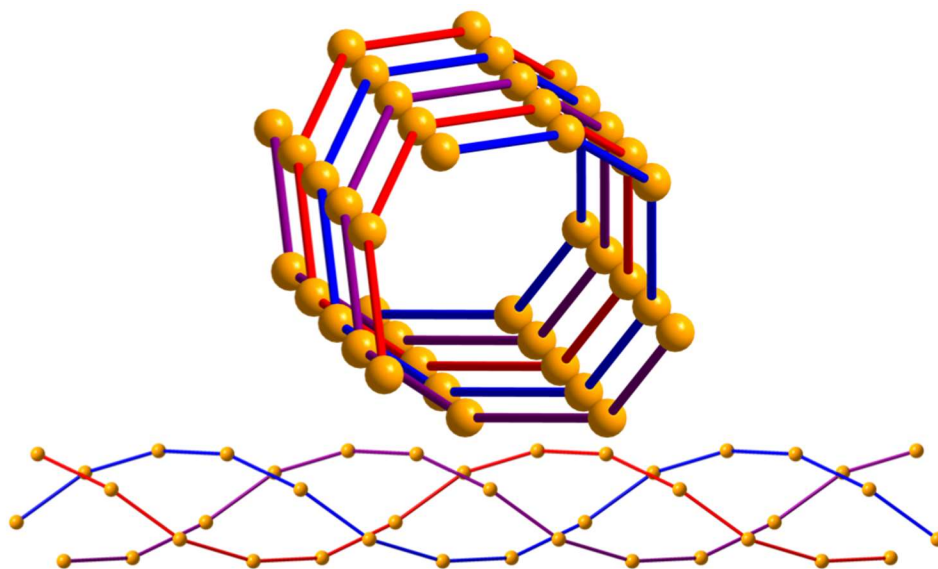


**Figure 4.S1:** Wire-frame representation of an octagonal filled pore in  $\text{Fe}(\text{imid})_2$  which has a triple helix structure, with a view down the  $c$  axis (top) and perpendicular to the  $c$  axis (bottom). All atoms except Fe are removed and only adjacent metal centers are attached for clarity.

# Appendix A: The Breen Sealed-Tube Adapter

## A.1 Design

The Breen adapter (**Figure A.1**) was created out of a necessity to perform aqueous sealed-tube reactions with highly oxygen-sensitive reagents, as discussed in Chapter 3. Precipitating from a conversation between myself and James Breen, the College of Chemistry's inhouse glassblower, in July 2015, he proposed the combination of a Chemglass Chem-Cap Teflon valve (CG-960-01) with a Chemglass Chem-Thread adapter (CG-350-06) and a simple glass hose barb to yield a sealed-tube adapter that is both compatible with Schlenk chemistry and capable of achieving noticeably lower vacuum pressures than other sealed-tube adapters (down to  $10^{-6}$  torr). A  $\frac{1}{2}$ " glass tube can be passed through the screw cap and o-ring and into the glass adapter; as the cap is tightened the o-ring is compressed and an air-tight seal is formed. The Chem-Cap Teflon valve can be used to seal the other end of the adapter, or alternatively be replaced with a rubber septum under positive pressure for cannula-based transfers. These adapters can readily be used to prepare sealed-tube reactions in an inert atmosphere glove box and then transfer them out of the glove box via a small antechamber, thanks to the compactness of the adapter. These tubes can then be evacuated on a Schlenk line, and flame sealed, all without exposing the reaction to air. Following their introduction, use of Breen adapters for preparing sealed-tubes rapidly became common practice in lab. This design is generalizable to other size tubing, and  $\frac{1}{4}$ " Breen adapters have also been frequently used for smaller scale sealed-tube reactions. While this combination of parts or the underlying principal may not be unheard of before now, I believe that the sizable impact that the Breen adapter has had on my research and that of my peers in metal-organic framework and related areas merits its recognition and discussion.



**Figure A.1:** A  $\frac{1}{2}$ " Breen adapter (left), and the adapter disassembled into its four components (right).

## A.2 Application to Metal–Organic Frameworks

In addition to facilitating synthetic screens for metal–organic frameworks, Breen adapters can also be utilized to improve the activation of metal–organic frameworks, one of the critical barriers for research in this field. Solvated porous frameworks are normally activated (desolvated) by heating under flow of a gas and/or heating under dynamic vacuum. While materials are typically exposed to a turbomolecular pump for final activation before measurements are performed, they must be almost entirely desolvated prior to this point, lest an expensive pump be damaged, or a different sample be ruined in the case simultaneous activation of samples. Prior to the advent of the Breen adapter, a typical procedure for framework activation involved heating an exhaustively solvent-washed material inside a glass vessel under vacuum on a Schlenk line, transferring into a solvent-free glove box, losing an enormous portion of material to static adherence to the glass vessel, losing and addition portion while adding it into an ASAP tube, and then final activation on an instrument before measurement.

The extensive loss of valuable material through multiple transfers can be avoided by activating samples directly in ASAP tubes. Previously this was performed by attaching a septum onto the end of an ASAP tube containing solvated powder, piercing the septa with a long needle, and flowing an inert gas over the sample while heating it. In addition to the possible loss of small material particulates, if the flow was not carefully controlled, there was no route to sealing the tube with a Micromeritics *Transeal* without at least temporarily exposing the tube to air. As ASAP tubes often come in ½” diameter tubing, a Breen adapter can provide the possibility of removing the purging needle under positive pressure and thus maintaining inert atmosphere (**Figure A.2**); the seal is sufficiently good to allow for transfer into a glovebox if desired.



**Figure A.2:** Attachment of a Breen adapter onto a ½” ASAP tube.

Breen adapters are better utilized for ASAP though in combination with a *Transeal*. Because the adapter narrows from the ½” Chem-Thread adapter to the Chem-Cap valve, it can be used to open and close the spring-loaded valve in *Transeals* by pressing or withdrawing the tube from the inner wall of the adapter (**Figure A.3**). The o-ring in the adapter can provide sufficient force to prevent movement of the ASAP tube, allowing the *Transeal* to remain in the position it was last placed. With this combination of Breen adapter and *Transeal*, metal–organic framework samples can be activated directly in ASAP tubes and transferred onto an instrument, with no appreciable sample loss or exposure to air. Consequentially, this technique has become invaluable to the study of air-sensitive metal–organic frameworks.

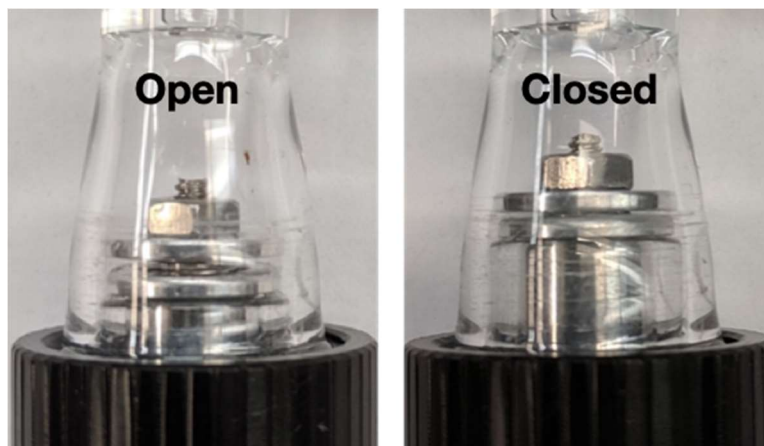


**Figure A.3:** Magnified image of a Breen adapter with a Micromeritics *Transeal* in the open position (left) and the closed position (right).

### **A.3 Acknowledgements**

I would like to thank James Breen for his clever glassware design and high-quality craftsmanship in not only the fabrication of Breen adapters but also in the multiple glass related projects and repairs that were necessary during the course of my graduate career.